ACCELERATION FEEDBACK CONTROL STRATEGIES FOR ACTIVE AND SEMI-ACTIVE CONTROL SYSTEMS: MODELING, ALGORITHM DEVELOPMENT, AND EXPERIMENTAL VERIFICATION

A Dissertation
Submitted to the Graduate School of the University of Notre Dame
in Partial Fulfillment of the Requirements for the Degree of
Doctor of Philosophy
by

Shirley Jane Dyke, B.S., A.A.E.

Department of Civil Engineering and Geological Sciences

Notre Dame, Indiana

July 1996

ACCELERATION FEEDBACK CONTROL STRATEGIES FOR ACTIVE AND SEMI-ACTIVE CONTROL SYSTEMS: MODELING, ALGORITHM DEVELOPMENT, AND EXPERIMENTAL VERIFICATION

Abstract

by

Shirley J. Dyke

Most of the current research on active structural control for aseismic protection has been based on either full state feedback strategies or velocity feedback strategies. However, accurate measurement of the necessary displacements and velocities of the structure is difficult to achieve directly, particularly during seismic activity. Because accelerometers are inexpensive and can readily provide reliable measurement of the structural accelerations, development of control methods based on acceleration feedback is an ideal solution to this problem.

The focus of this dissertation is the development and experimental verification of acceleration feedback strategies for seismically excited structures. Both active and semi-active control systems are considered. Three different active control configurations are considered, including an active bracing system, an active tendon system, and an active mass driver system. The system identification procedure used in these studies is presented, and the effects of control-structure interaction are incorporated into the models. H_2/LQG control strategies are applied to design the control systems. In addition to the active control experiments, one semi-active system employing a promising new semi-active device known as a magnetorheological (MR) damper is studied. The device is employed to control a three-story test structure. A phenomenological model that is based on a Bouc-Wen

hysteresis model is proposed and shown to effectively portray the behavior of a typical MR damper. System identification techniques and acceleration feedback control strategies which are appropriate for semi-active control systems are developed and applied. The studies discussed herein demonstrate that acceleration feedback control strategies are effective and practically implementable for active and semi-active structural control applications.

Table of Contents

List of Figures

CHAPTER 1

CHAPTER 2

CHAPTER 3

CHAPTER 4

CHAPTER 5

CHAPTER 6

CHAPTER 7

CHAPTER 8

CHAPTER 9

List of Tables

CHAPTER 10

CHAPTER 3

CHAPTER 4

CHAPTER 5

CHAPTER 6

CHAPTER 7

CHAPTER 8

CHAPTER 9

Acknowledgements

I would like to first thank my advisor, Professor Bill Spencer, for his advise, encouragement, support and friendship throughout my time at Notre Dame. I also would like to thank Professor Michael Sain for sharing his experience in the field of control theory, and for his thought provoking discussions over the years, and Professor Nicos Makris and Professor Ahsan Kareem for reading this dissertation and offering constructive comments.

Professor Larry Bergman at the University of Illinois offered much appreciated advise and guidance. I would like to thank Peter Quast and Dan Kaspari for their assistance and friendship. My fellow graduate students provided companionship and encouragement throughout this effort.

Finally, I would like to thank my parents for their advise and encouragement, and for instilling in me the importance of hard work and persistence. This work would not have been possible without the love and support of my family.

Financial support for this work has come from a number of sources, including the National Science Foundation Graduate Research Traineeship, the Clare Booth Luce Fellowship, the National Science Foundation Supplemental Fellowship, the Graduate Assistance in Areas of National Need Program, and the Department of Civil Engineering at the University of Notre Dame. This research is also partially funded by National Science Foundation Grants Nos. BCS 90-06781 and BCS 93-01584.

CHAPTER 1

Introduction

In the U.S., the concept of employing active control systems in civil engineering structures to minimize the vibrational response was originally suggested by Yao (1972). In the years since, significant progress has been made in the design, development and verification of such systems to mitigate the effects of environmental loads such as high winds and earthquakes. Recently, active and hybrid control systems have even been implemented in a number of structures in Japan. However, the engineering community is not yet ready to fully accept structural control systems to reduce the effects of natural hazards on structures. This lack of acceptance arises, in part, from questions of stability, cost effectiveness, reliability, power requirements, *etc*.

New control devices and strategies are continually being developed to address these issues in an effort to increase the acceptance of structural control systems. Prior to implementation on actual structures, extensive experimental verification of these systems must be performed to provide insight and expose difficulties which are not encountered in computer simulations. Additionally, knowledge and experience acquired during these studies aid in the development of improved models of the control devices and systems that may be used to construct more sophisticated simulations.

Many agree that the next generation of control research for civil engineering applications must focus on developing systems that are more implementable (Housner, *et al.*, 1994a; Kobori, 1994). One necessary condition for a control strategy to be implementable is that it must use available measurable responses to determine an appropriate control action. Most of the previous research in the control of civil engineering structures has assumed that all of the structure's states can be directly measured (*i.e.*, full state feedback). However, this situation rarely occurs in practice. Usually, the number and type of structural responses that can be readily obtained is quite limited.

Of the structural responses that can be directly observed, one of the easiest to obtain is acceleration. Accelerometers can readily provide inexpensive and reliable measurements of the accelerations at strategic locations on the structure. Moreover, in contrast to displacement and velocity measurements, acceleration measurements are independent of the inertial reference frame in which they are taken. Thus, for practical implementation, absolute structural acceleration measurements are ideal outputs to use for determination of the control action. Controllers that are based on partial measurement of the states, or linear combinations of the states as in the case of absolute acceleration feedback, are termed output feedback controllers.

The focus of this dissertation is the development and experimental verification of acceleration feedback control strategies for seismically excited structures. Both active and semi-active control systems are considered. In each of the experiments, accelerometers located on the floors of the model structures provided the primary measurements of the structural response used for determination of the control action. Using the acceleration feedback strategies, three different active control actuator configurations are considered,

including an active bracing system, an active tendon system, and an active mass driver system. Acceleration feedback strategies proposed by Spencer *et al*. (1991, 1994), Suhardjo (1990) and Suhardjo *et al.* (1992) are employed in the control studies. The analytical results presented therein indicated that acceleration feedback strategies would be effective for active control applications, but a number of challenges had to be overcome for successful experimental implementation. These challenged are addressed herein.

In addition to the active control studies, a semi-active control system employing a promising new device known as a magnetorheological (MR) damper is investigated. Appropriate control-oriented system identification techniques and semi-active control strategies based on acceleration feedback are developed and applied in the analysis. The investigations discussed in this dissertation are designed to demonstrate that acceleration feedback control strategies are effective and practically implementable for active and semi-active structural control applications.

1.1 Literature Review

Structural control systems fall into four basic categories: passive, active, hybrid, and semi-active. Passive systems, including base isolation, viscoelastic dampers and tuned mass dampers, employ supplemental devices which respond to the motion of the structure to dissipate vibratory energy in the structural system. These systems are well understood and are accepted by the engineering community as a means for mitigating the effects of dynamic loadings such as strong earthquakes and high winds. However, these passive-device methods have the limitation of not being able to adapt to structural changes and to varying usage patterns and loading conditions. Active, hybrid and semi-active control systems have the ability to adapt to various operating conditions. In the remainder of this sec-

tion, previously reported research on the various types of active, hybrid, and semi-active control systems will be discussed.

1.1.1 Active Structural Control

Active control strategies have been developed as one means by which to minimize the effects of these environmental loads (see Soong, 1990; Housner and Masri, 1990, 1993; Housner, *et al.*, 1994a). Active control systems operate by using external energy supplied by actuators to impart forces on the structure. The appropriate control action is determined based on measurements of the structural responses. For approximately two decades, researchers have investigated the possibility of using active control methods to improve upon passive approaches to reduce structural responses.

A variety of active control mechanisms have been suggested. These mechanisms include the active tendon system (Roorda 1975; Yang and Giannopoulos 1978; Abdel-Rohman and Leipholz 1978a), the active bracing system (Reinhorn, *et al.*, 1989b), the active tuned mass damper/driver (Abdel-Rohman and Leipholz 1983; Chang and Soong 1980), and the active aerodynamic appendage mechanism (Soong and Skinner 1981; Abdel-Rohman 1984). To evaluate the effectiveness of active structural control systems for earthquake hazard mitigation, the National Center for Earthquake Engineering Research (NCEER) has conducted extensive experiments on scale models of buildings. Chung, *et al*. (1988) applied linear quadratic regulator theory to a SDOF structure equipped with an active tendon system and later extended this work to a three degree-of-freedom structure in Chung, *et al*. (1989). Reinhorn, *et al*. (1989b) also applied active control algorithms to a six-story model structure.

Various control algorithms for active systems have been considered. Output feedback strategies using absolute acceleration measurements were developed by Spencer *et al.*, (1991, 1994), Suhardjo *et al.*, (1992) and Suhardjo (1990). Control algorithms which account for the force and stroke limitations of control actuators have been investigated (Asano and Nakagawa, 1993; Tamura, *et al*. 1994; Indrawan and Higashihara, 1993). Nonlinear control algorithms have also been considered in an effort to increase the effectiveness of these active systems (Gattulli and Soong, 1994). Other types of control algorithms that have been suggested for active control system include fuzzy control (Chameau, *et al.*, 1991; Furuta *et al.*, 1994), neural-based control (Casciati, *et al*., 1993; Shoureshi, *et al*., 1994), and sliding mode control (Yang, *et al.*, 1994b). Additionally, a number of strategies for active control systems were discussed and compared by Casciati and Yao (1994).

Issues associated with the successful implementation of these control systems when they are applied to actual structures have also been studied. Housner *et al.* (1994b) stressed the importance of system integration in the design and development of active control systems. Not only is it necessary to consider the individual components of a control system, but the system as a whole must be understood, including the structure, control devices, sensors, and computer control system. In this regard, Soong and Reinhorn (1993) discussed these issues in more detail and examined two case studies including an active bracing system and an active mass driver system. Additionally, the effects of control-structure interaction and actuator dynamics have been considered by Dyke *et al.* (1995), and digital control implementation issues were addressed by Quast *et al*. (1995).

The first implementation of an active control system to a full-scale building was the Kyobashi Seiwa building in 1989 (Kobori 1994; Sakamoto, *et al*., 1994), as shown in Fig.

1.1. Two active mass drivers were installed on the top floor to reduce structural vibrations due to moderate earthquakes and strong winds, and to increase the comfort level of the building's occupants. A primary AMD (4 tons) was employed to control the lateral motion and the secondary AMD (1 ton) controls the torsional motion. Active and hybrid structural control systems have subsequently been installed in over twenty buildings and utilized during the construction of more than ten bridges.

Even though a large amount of analytical and experimental research has been conducted in the last twenty years, and a number of full-scale structures in Japan have been equipped with active control systems, there are no full-scale, active control implementations in the U.S. This is partially due to the lack of standardized analysis and testing procedures for the control systems and devices. Moreover, the U.S. construction industry appears to be conservative and reluctant to employ new technologies. Before active control can gain general acceptance, a number of challenges must be addressed. According to Fujino *et al*., (1996), these challenges include: (i) reduction of capital cost and mainte-

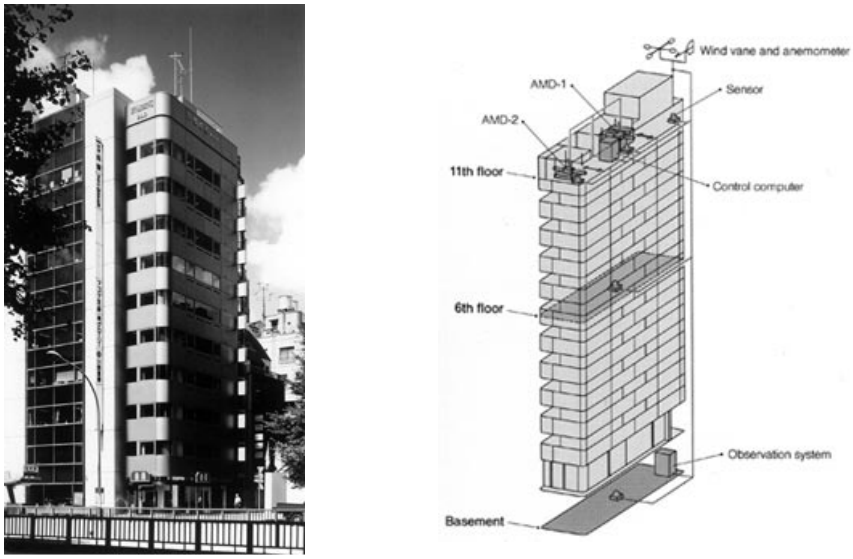

Figure 1.1 Kyobashi Seiwa Building with an AMD System.

nance, (ii) eliminating reliance on external power, (iii) increasing system reliability and robustness, and (iv) gaining acceptance of nontraditional technology.

Although a number of questions still exist regarding the application of active control systems to civil engineering structures, the future is promising. Hybrid and semi-active control strategies appear to have the potential to address a number of the challenges to this technology. The following sections discuss some of the hybrid control systems, which are more mature, and recently proposed semi-active control systems, employing devices that potentially offer the reliability of passive devices, yet maintain the versatility and adaptability of fully active systems.

1.1.2 Hybrid Structural Control Systems

Hybrid control strategies have been investigated by many researchers to exploit their potential to increase the overall reliability and efficiency of the controlled structure (Soong and Reinhorn, 1993). A hybrid control system is typically defined as one which employs a combination of two or more passive or active devices. Because multiple control devices are operating, hybrid control systems can alleviate some of the restrictions and limitations that exist when each system is acting alone. Thus, higher levels of performance may be achievable. Additionally, the resulting hybrid control system can be more reliable than a fully active system, although it is also often more complicated. Research in the area of hybrid control systems has focused on two classifications of systems: i) hybrid mass damper systems, and ii) active base isolation.

The hybrid mass damper (HMD) is the most common control device employed in full-scale civil engineering applications. The HMD is a combination of a tuned mass

damper (TMD) and an active control actuator. The ability of this device to reduce structural responses relies mainly on the natural motion of the TMD. The forces from the control actuator are employed to increase the efficiency of the HMD and to increase its robustness to changes in the dynamic characteristics of the structure. The energy and forces required to operate a typical HMD are far less than those associated with an fully active mass driver system of comparable performance.

Many researchers have made significant contributions toward development of HMDs that are compact, efficient and practically implementable. A number of innovative, compact, long-period devices have been reported. For example, Tanida, *et al*. (1991) developed an arch-shaped HMD that has been employed in a variety of applications, including bridge tower construction, building response reduction and ship roll stabilization. An arch-shaped hybrid mass damper (see Fig. 1.2) was used during construction of the bridge tower (height = 119m) of the Rainbow suspension bridge in Tokyo to reduce large-amplitude vortex-induced vibration expected to occur at a wind speed of 7m/s (Tanida, *et al*. 1991; Tanida 1995). The mass ratio for the hybrid damper used for the Rainbow bridge tower was 0.14% of the first modal mass of a structure, whereas a comparable passive TMD would require a 1% mass ratio to achieve a similar level of perfor-

Figure 1.2 Rainbow Bridge Tower While under Construction.

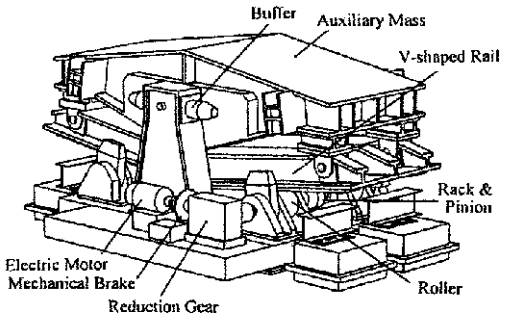

Figure 1.3 V-Shaped Hybrid Mass Damper.

mance. Figure 1.3 shows an extension of the arch-shaped HMD, the V-shaped HMD (Koike, *et al*., 1994), which has the advantage of an easily adjustable fundamental period. Three of these devices were installed in the Shinjuku Park Tower, the largest, in terms of square footage, building in Japan. Two multi-step pendulum HMDs (Yamazaki, *et al*., 1992; Yamazaki, *et al*., 1995) have been developed and installed in the Yokahoma Landmark Tower, the tallest building in Japan. Additionally, the DUOX HMD (Kobori, 1994), which attains high control efficiency with a small actuator force, has been proposed and employed in two buildings (see Fig. 1.5). Devices similar to the DUOX HMD were also

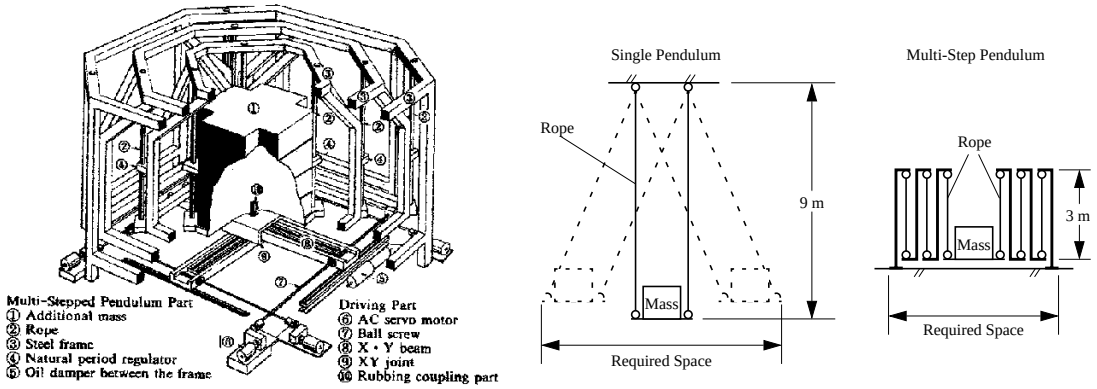

Figure 1.4 Multi-Step Pendulum Damper Used in the Yokohama Landmark Tower.

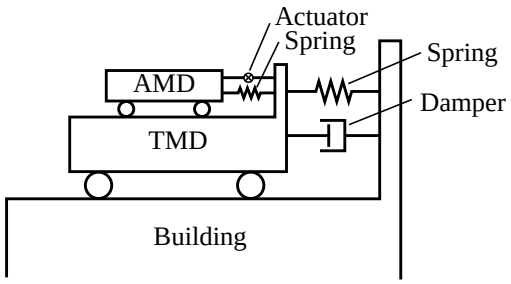

Figure 1.5 Concept of the DUOX System.

studied by Iemura and Izuno (1994) and Ohrui, *et al*. (1994). Otsuka, *et al*. (1994) conducted experiments in which a roller-pendulum based HMD was applied to control a tower experiencing seismic excitation. Cheng, *et al*. (1994) proposed to use an HMD system, combining a control actuator with a passive tuned liquid damper to control wind-induced vibration of the Nanjing tower in Nanjing, China. Information regarding other full-scale structural control implementations employing HMDs have been documented (*e.g.*, see Hirai, *et al*., 1993; Higashino and Aizawa 1993; Sakamoto, *et al*., 1994; Ohyama, *et al*., 1994; Suzuki, *et al*., 1994; Fujino 1994; Fujino and Yamaguchi 1994; Fujita, *et al*., 1994a,b; Koike, *et al*., 1994; Nakamura, *et al*., 1994; Shiba, *et al*., 1994; Yamamoto and Aizawa 1994).

A number of researchers have investigated various control methods for HMDs. For example, Shing, *et al*., (1994), Kawatani, *et al*. (1994), Petti, *et al*. (1994), Suhardjo, *et al*. (1992) and Spencer, *et al*. (1994) have considered optimal control methods for HMD controller design. Tamura, *et al*. (1994) proposed a gain scheduling technique in which the control gains vary with the excitation level to account for stroke and control force limitations. Similarly, Niiya, *et al*. (1994) proposed an ad hoc control algorithm for HMDs to

account for the limitations on the stroke. Adjikari and Yamaguchi (1994) and Nonami, *et al*. (1994) applied sliding mode theory to control structures with HMD systems.

Another class of hybrid control systems which has been investigated by a number of researchers is found in the active base isolation system, consisting of a passive base isolation system combined with a control actuator to supplement the effects of the base isolation system. Base isolation systems have been implemented on civil engineering structures worldwide for a number of years because of their simplicity, reliability and effectiveness. Excellent review articles of base isolation systems are presented by Kelly (1981, 1986), Buckle and Mayes (1990), and Soong and Constantinou (1994). However, base isolation systems are passive systems and are limited in their ability to adapt to changing demands for structural response reduction. With the addition of an active control device to a base isolated structure, a higher level of performance can be potentially achieved without a substantial increase in the cost (Reinhorn, *et al*., 1987).

Through simulations, Yoshida, *et al*. (1994) investigated the use of LQG and H_∞ control strategies with hybrid base isolation systems. Additionally, several small-scale experiments have been performed to verify the effectiveness of these systems in reducing the structural responses. Reinhorn and Riley (1994) performed analytical and experimental studies of a small-scale bridge with a sliding hybrid isolation system in which a control actuator was employed between the sliding surface and the ground to supplement the base isolation system.

Also mentioned in this context is another type of *hybrid* base isolation system which employs a semi-active friction-controllable fluid bearing in the isolation system. Feng, *et al*. (1993) employed such bearings in a hybrid base isolation system in which the pressure

in the fluid could be varied to control the amount of friction at the isolation surface. Yang, *et al*. (1994a) investigated the use of continuous sliding mode control and variable structure system for a base isolated structure with friction-controllable bearings.

Because base isolation systems often exhibit nonlinear behavior, researchers have developed various nonlinear control strategies including fuzzy control (Nagarajaiah, 1994), neural network based control (Venini and Wen, 1994) and adaptive nonlinear control (Rodellar, *et al.*, 1994). In addition, Inaudi, *et al.* (1993) studied the use of frequency domain shaping techniques in designing controllers.

1.1.3 Semi-Active Structural Control Systems

Semi-active control devices have received a great deal of attention in recent years because they offer the adaptability of active control devices without requiring the associated large power sources. In fact, many can operate on battery power, which is critical during seismic events when the main power source to the structure may fail. According to presently accepted definitions, a semi-active control device is one that cannot increase the mechanical energy in the controlled system (*i.e.*, including both the structure and the device), but has properties which can be dynamically varied to optimally reduce the responses of a structural system. Therefore, in contrast to active control devices, semi-active control devices do not have the potential to destabilize the structural system (in the bounded input/bounded output sense). Preliminary studies indicate that appropriately implemented semi-active systems perform significantly better than passive devices and have the potential to achieve, or even surpass, the performance of fully active systems, thus allowing for the possibility of effective response reduction during a wide array of dynamic loading conditions. Examples of such devices include variable-orifice fluid

dampers, controllable friction devices, variable stiffness devices, controllable liquid dampers and controllable fluid dampers.

One means of achieving a variable damping device is to use an electromechanically-variable orifice to alter the resistance to flow of a conventional hydraulic fluid. A schematic of such a device is given in Fig. 1.6. The concept of applying this type of variable damping devices to control the motion of bridges experiencing seismic motion was first discussed by Feng and Shinozuka (1990) and by Kawashima, *et al*. (1992). Variable-orifice dampers have been studied at the National Center for Earthquake Engineering Research in Buffalo, N.Y. (Shinozuka, *et al*., 1992; Constantinou and Symans, 1992; Constantinou, *et al*., 1993, 1994; Symans and Constantinou, 1995). Sack and Patten (1994) conducted experiments in which a hydraulic actuator with a controllable orifice was applied to a single-lane test bridge to dissipate the energy induced by vehicle traffic (see also Patten, *et al*., 1994a). The effectiveness of devices in controlling seismically excited buildings has been demonstrated through both simulation and small-scale experimental studies (Sack, *et al*., 1994; Patten, *et al*., 1994b; Kurata, *et al*., 1994). Kamagata and

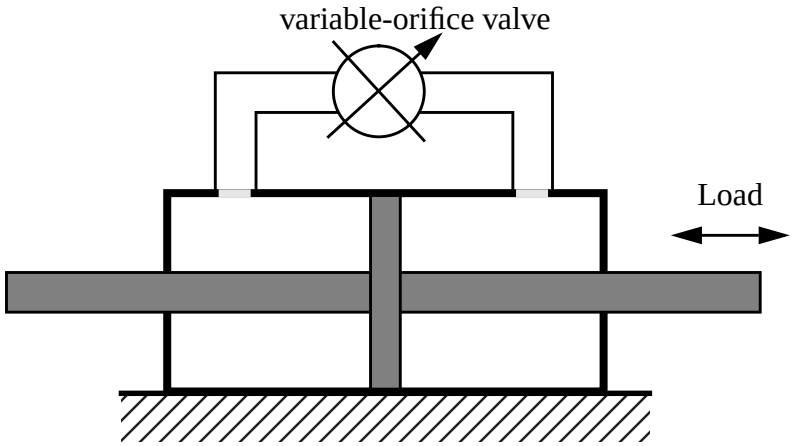

Figure 1.6 Schematic of a Variable-Orifice Damper.

Kobori (1994) employed a variable-orifice damper to investigate adaptive control methods for an active variable stiffness system at the Kobori Research Complex. The results of these analytical and experimental studies indicate that this device is effective in reducing structural responses.

Various semi-active devices have been proposed which utilize forces generated by surface friction to dissipate vibratory energy in a structural system. Akbay and Aktan (1990, 1991) and Kannan *et al.* (1995) proposed variable friction devices which consists of a friction shaft which is rigidly connected to the structural bracing. The force at the frictional interface was adjusted to allow controlled slippage. A similar device was considered at the University of British Columbia (Dowdell and Cherry, 1994a,b; Cherry, 1994). Through analytical studies, the ability of these semi-active devices to reduce the interstory drifts of a seismically excited structure was investigated (Dowdell and Cherry, 1994b). In addition, a semi-active friction-controllable fluid bearing has been employed in parallel with a seismic isolation system in Feng, *et al*. (1993), Nagarajaiah (1993), Yang, *et al*. (1994), and Fujita *et al.*, (1995).

Another type of semi-active control device utilizes the dynamic motion of a sloshing fluid or a column of fluid to reduce the responses of a structure. These liquid dampers are based on the passive tuned sloshing dampers (TSD) and tuned liquid column dampers (TLCD). As in a tuned mass damper (TMD), the TSD uses the liquid in a sloshing tank to add damping to the structural system. Similarly, in a TLCD, the moving mass is a column of liquid which is driven by the vibrations of the structure. Because these passive systems have a fixed design, they are not very effective for a wide variety of loading conditions, and researchers are looking toward semi-active alternatives for these devices to improve

their effectiveness in reducing structural responses (Kareem, 1994). Lou, *et al*. (1994) proposed a semi-active device based on the passive TSD, in which the length of the sloshing tank could be altered to change the properties of the device. Haroun, *et al*. (1994) presented a semi-active device based on a TLCD with a variable-orifice.

All of the semi-active control devices discussed until now in this section have employed some electrically controlled valves or mechanisms. Such mechanical components can be problematic in terms of reliability and maintenance. Another class of semi-active devices uses controllable fluids. The advantage of controllable fluid devices is that they contain no moving parts other than the piston, which makes them very reliable.

Two fluids that are viable contenders for development of controllable dampers are: (i) electrorheological (ER) fluids and (ii) magnetorheological (MR) fluids. The essential characteristic of controllable fluids is their ability to reversibly change from a free-flowing, linear viscous fluid to a semi-solid with a controllable yield strength in milliseconds when exposed to an electric (for ER fluids) or magnetic (for MR fluids) field. Although the discovery of both ER and MR fluids dates back to the late 1940's (Winslow 1947; Winslow 1949; Rabinow 1948), research programs have to date concentrated primarily on ER fluids. A number of ER fluid dampers have recently been developed, modeled, and tested for civil engineering applications (Ehrgott and Masri, 1994; Gavin, *et al*., 1994a,b; Gordaninejad, *et al*., 1994; Makris, *et al*., 1995, 1996; McClamroch and Gavin, 1995). One type of controllable fluid damper is shown conceptually in Fig. 1.7, although a variety of designs have been investigated.

Recently developed MR fluids appear to be an attractive alternative to ER fluids for use in controllable fluid dampers (Carlson 1994; Carlson and Weiss 1994; Carlson, *et al.*

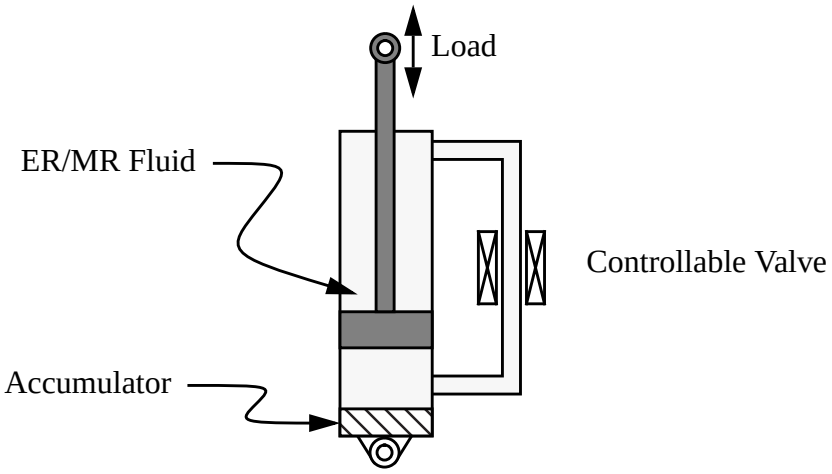

Figure 1.7 Schematic of a Controllable Fluid Damper.

1995; see also: *http://www.rheonetic.com/mrfluid/*). MR fluids typically consist of micron-sized, magnetically polarizable particles dispersed in a carrier medium such as mineral or silicone oil. When a magnetic field is applied to the fluid, particle chains form, and the fluid becomes a semi-solid and exhibits viscoplastic behavior similar to that of an ER fluid. Transition to rheological equilibrium can be achieved in a few milliseconds, allowing construction of devices with high bandwidth. Additionally, Carlson and Weiss (1994) indicated that the achievable yield stress of an MR fluid is an order of magnitude greater than its ER counterpart and that MR fluids can operate at temperatures from –40 to 150^{o}C with only slight variations in the yield stress. Moreover, MR fluids are not sensitive to impurities such as are commonly encountered during manufacturing and usage, and little particle/carrier fluid separation takes place in MR fluids under common flow conditions. Further, a wider choice of additives (surfactants, dispersants, friction modifiers, anti-wear agents, *etc.*) can generally be used with MR fluids to enhance stability, seal life, bearing life, *etc*, since electro-chemistry does not affect the magneto-polarization mechanism. The MR fluid can be readily controlled with a low voltage (*e.g.*, ~12–24V), current-driven

power supply outputting only ~1–2 amps. Table 1.1 provides a comparison between the key physical characteristics of the MR and ER fluids. The future of MR devices for civil engineering applications appears to be quite bright (Spencer, *et al*., 1996a–d; Dyke, *et al*., 1996c–f).

Because all of these semi-active devices are intrinsically nonlinear, one of the main challenges is to develop control strategies that can optimally reduce structural responses. Various nonlinear control strategies have been developed to take advantage of the particular characteristics of the semi-active devices, including bang-bang control (McClamroch and Gavin, 1995), clipped-optimal control (Patten, *et al*., 1994a,b; Dyke, *et al*., 1996c–f), bi-state control (Patten, *et al*., 1994a,b), fuzzy control methods (Sun and Goto, 1994), and adaptive nonlinear control (Kamagata and Kobori, 1994).

Table 1.1 Summary of the Physical Characteristics of MR and ER Fluids.

Property	MR Fluids	ER Fluids
Yield Stress, τ_y	> 80 kPa	3.0 – 3.5 kPa
Operable Temperature Range	–50 to 150^{o}C	–25 to 125^{o}C
Plastic Viscosity, η_p	0.10 to 0.70 Pa-sec	0.10 to 0.70 Pa-sec
Stability	Not affected by most chemical impurities	Cannot tolerate impurities
$\eta_p/\tau^2_{y(field)}$	$\approx 5\times10^{-11}$ sec/Pa	$\approx 5\times10^{-8}$ sec/Pa
Power Supply	12-24V, ~1A	~4000V, ~1 mA
Response Time	milliseconds	milliseconds
Particle Sedimentation	Little	Little
Raw Materials	nontoxic & environmentally safe	nontoxic & environmentally safe

1.2 Overview of the Dissertation

The focus of this dissertation is the experimental verification of the acceleration feedback strategies developed by Spencer *et al.* (1991, 1994), Suhardjo (1990) and Suhardjo *et al.* (1992) for seismically excited structures. Both active and semi-active control systems are considered.

Chapter 2 presents a number of topics that will be used in the later chapters for the design, development and experimental verification of the proposed structural control strategies. The discussion will include: techniques and equipment used for reliable data acquisition and processing, system identification procedures employed to develop control-oriented mathematical models of the active and semi-active systems, acceleration feedback control design methods, and issues related to digital control implementation.

The effects of control-structure interaction and actuator dynamics, as they apply to active control systems, are addressed in Chapter 3. First, the phenomenon of control-structure interaction will be discussed and specific models are developed for hydraulic actuators typical of those used in many active control situations. Next, through illustrative examples, the consequences of neglecting, or only partially accounting for, actuator dynamics and control-structure interaction are demonstrated.

In Chapters 4–6, experimental verification of acceleration feedback strategies is presented for three active control systems. In the first active control experiment, a three-story test structure at the Structural Dynamics and Control/Earthquake Engineering Laboratory (SDC/EEL) at the University of Notre Dame (*http://www.nd.edu/~quake/*) is configured with an active bracing system (Chapter 4). This experiment constitutes the first successful experimental implementation of acceleration feedback control strategies. To demonstrate

the validity of the acceleration feedback control strategies for larger scale structures, the second verification of these methods is performed on the 1:4 scale, tendon-controlled, three-story test structure at the National Center for Earthquake Engineering Research (NCEER) at SUNY-Buffalo (Chapter 5). Because of the large number of full-scale implementations of active and hybrid mass driver systems in Japan, the final verification for active control systems is performed on the three-story test structure at the SDC/EEL configured with an active mass driver (AMD) on the top floor (Chapter 6).

In the latter portion of the dissertation, acceleration feedback strategies are developed and experimentally verified for semi-actively controlled structures. In this study, a prototype MR damper, obtained from the Lord Corporation of Cary, North Carolina, is employed to control the three-story test structure at the SDC/EEL. The MR damper is chosen for this study because of its mechanical simplicity, low operating power requirements, environmental robustness, and demonstrated potential for developing forces sufficient for full-scale applications.

To experimentally verify the acceleration feedback strategies for this semi-active system, the first step is to develop a high fidelity model of the MR damper for use in control design and analysis. This task is challenging because the MR damper, like most semi-active control means, is a highly nonlinear device. A phenomenological model of the MR damper is proposed in Chapter 7 which effectively models the behavior of the MR damper over a wide range of operating conditions. A clipped-optimal control strategy based on acceleration feedback methods is developed in Chapter 8 and, through numerical example, shown to be effective for structural response reduction. Experimental verification of the acceleration feedback methods for the semi-active system is presented in Chapter 9.

CHAPTER 2

Background

In this chapter, a number of topics are discussed that are used in later chapters for system modeling, control design, and control implementation. Because accurate data acquisition and processing techniques are important for the development of effective models of the structural systems as well as the reliable evaluation of system performance, some issues associated with these subjects are presented first. The system identification procedures used to develop mathematical models of the structural systems are then presented. Next, H_2/LQG frequency domain control design methods, which utilize the structural acceleration responses (Suhardjo, 1990; Suhardjo *et al.*, 1992; Spencer, *et al.*, 1991, 1994) are discussed. Subsequently, a description of the hardware and software employed for the controller implementation is provided, including a discussion of the supervisory features designed to monitor operation of the control system. In the last section, several issues associated with digital control implementation are addressed.

2.1 Data Acquisition and Processing

Accurate data acquisition and processing techniques are important in the effective modeling and reliable evaluation of structural control systems. Often models are identified based on experimentally obtained data, and the quality of the resulting model is closely linked to the quality of the data on which it is based. Inaccurate recording of the system responses may lead to modeling errors and control designs which are ineffective or even

unstable when implemented. Additionally, to evaluate the performance of a control system, it is necessary to obtain an accurate record of the structural responses. To obtain high-quality data, a good understanding of the sampling process and certain phenomena associated with processing the data is important. In this section, the source of these phenomena are explained, the techniques used to minimize the errors in processing the data are presented, and the data acquisition instrumentation used in the experiments discussed herein is described.

2.1.1 Phenomena Associated with Sampling and Data Acquisition

Although most of the sensors used in structural control systems are analog devices, data acquisition is usually performed with a digital computer. The quality of the data obtained is heavily dependent upon the specific manner in which the data are obtained and the subsequent processing. To be recorded on a computer, the analog signals must be discretized in time and in magnitude, which inevitably results in errors in the time and frequency domain representations of the measured signals. The processing of the recorded data can also introduce additional errors. If the sources of these errors are identified and understood, the effects on the recorded data can be minimized.

Three important phenomena associated with data acquisition and digital signal processing are quantization errors, aliasing, and spectral leakage. The sources of each of these phenomena are discussed in the following sections and examples are provided which demonstrate their associated effects.

Quantization Error

The device that allows the digital computer to sample the analog signal provided by a sensor is the analog-to-digital (A/D) converter. An A/D converter can be viewed as being composed of a sampler and a quantizer. The sampler discretizes the signal in time, and the

quantizer discretizes the signal in magnitude. In sampling a continuous signal, the quantizer must truncate, or round, the magnitude of the continuous signal to a digital representation in terms of a finite number of bits. Typically, data acquisition boards have A/D converters with 8, 12, or 16 bits, corresponding to dynamic ranges of 48, 72, and 96 dB, respectively. A simple example demonstrating the effect of quantization on a sinusoidal signal is shown in Fig. 2.1. Here, the dotted line is the actual signal being measured and the solid line represents a quantized version of the signal. Each value of the signal is rounded to one of ten discrete levels, resulting in significant errors in the quantized signal.

The difference between the actual value of the signal and the quantized value is considered to be a noise which increases uncertainty in the measurement. To minimize the effect of this noise, the truncated portion of the signal should be small relative to the actual signal. Thus, the maximum value of the signal should be as close as possible to, but not exceed, the full scale voltage of the A/D converter. If the maximum amplitude of the signal is known, an input amplifier can be incorporated before the A/D converter, thus reducing the effect of quantization. Once the signal is processed by the A/D system, it can be divided numerically in the data analysis program by the same ratio that it was amplified by at the input to the A/D converter to restore the original scale of the signal.

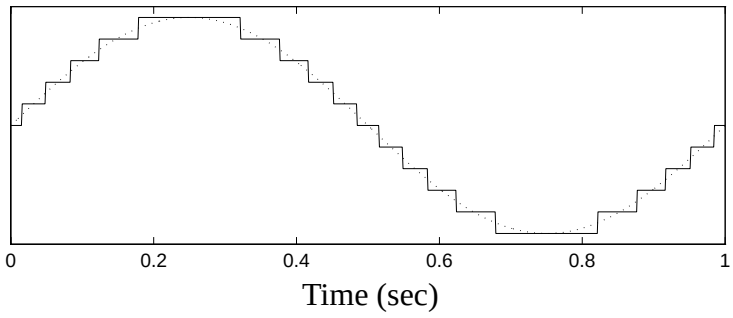

Figure 2.1 The Effect of Quantization.

Aliasing

The second component of the A/D converter is the sampler, which discretizes the analog signal in time. Often the frequency domain representation of the signal is determined (with a FFT) and errors can be introduced in the frequency domain if appropriate filtering of the signal is not performed before the signal is sampled. According to Nyquist sampling theory, the sampling rate must be at least twice the largest significant frequency component present in the signal to obtain an accurate discrete representation of the signal (Bergland, 1969). If this condition is not satisfied, the frequency components above the Nyquist frequency ($f_N = 1/(2T)$, where T is the sampling period) are *aliased* to lower frequencies. Once the signal has been sampled, it is no longer possible to identify which portion of the signal is due to the higher frequencies. The phenomenon of aliasing is demonstrated in Fig. 2.2. Two sinusoidal signals are shown with frequencies of 1 Hz and 9 Hz. If both of these signals are sampled at 10 Hz, the signals have the same values at the sampling instants. Although the two signals do not have the same frequency, the frequency domain representations of the sampled versions of the signals is identical, as shown in Fig. 2.2. To ensure that aliasing does not occur, the sampling frequency is chosen to be greater than twice the highest frequency in the measured signal.

In reality, no signal is ideally bandlimited, and a certain amount of aliasing will occur in the sampling of any physical signal. To reduce the effect of this phenomenon, analog low-pass filters are typically introduced prior to sampling to attenuate the high frequency components of the signal that would be aliased to lower frequencies. Since a transfer function is the ratio of the frequency domain representations of an output signal of a system to an input signal, it is important to use anti-aliasing filters with identical phase and amplitude characteristics for measuring both signals. Such phase/amplitude matched filters pre-

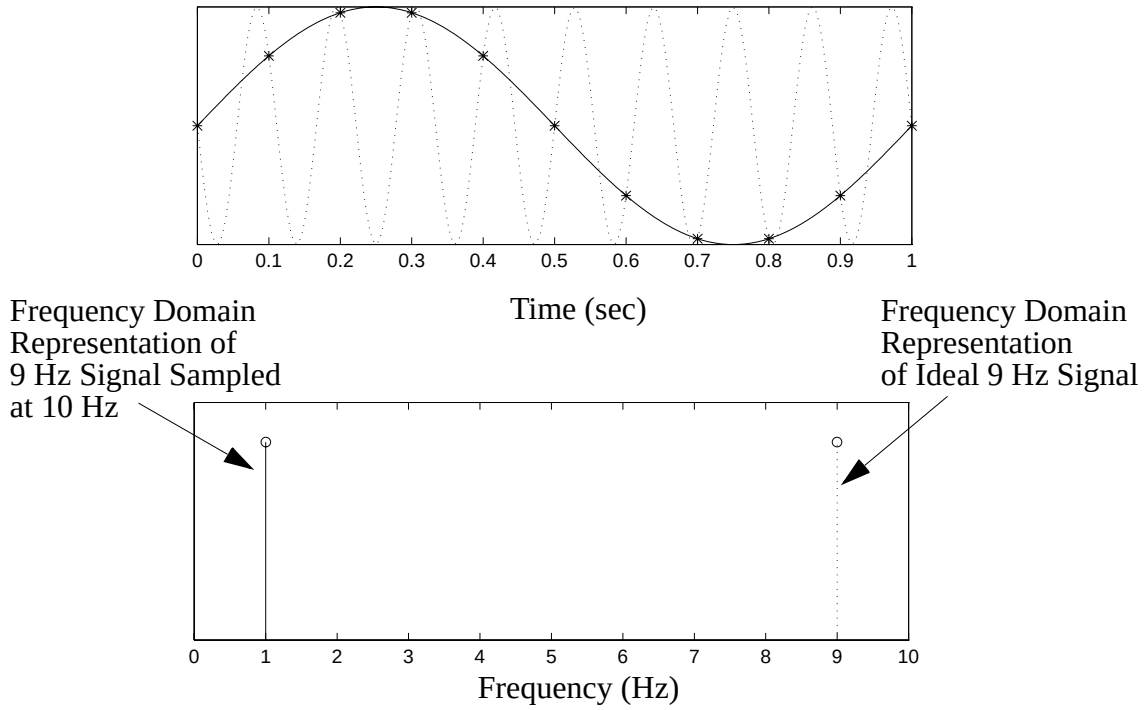

Figure 2.2 The Effect of Aliasing.

vent systematic bias errors due to the filtering process from being present in the resulting transfer functions.

Spectral Leakage

Errors may also be introduced in the frequency domain representation of a signal due to the processing of the data. In processing the discrete-time data to determine the frequency domain representation of the signal, a finite number of samples is acquired and an FFT is performed. This process introduces a phenomenon associated with Fourier analysis known as *spectral leakage* (Bergland, 1969; Harris, 1978). There are two approaches to explain the source of spectral leakage. To describe the first, more intuitive approach, recall that the discrete Fourier transform is defined only at a finite number of frequencies, as discussed in section 2.1.2. If the signal contains frequencies which are not exactly on these

spectral lines, the periodic representation of the signal will have discontinuities and the frequency domain representation of the signal is distorted. In the second description of spectral leakage, the finite duration discrete signal is considered be an infinite duration signal which has been multiplied by a rectangular window. This multiplication in the time domain is equivalent to a convolution of the frequency domain representation of the measured signal with that of the rectangular window. The Fourier transform of the rectangular window has a magnitude described by the function $\mathrm{Sinc}(fT)$ (where $\mathrm{Sinc}(fT) = \mathrm{Sin}(\pi fT)/(\pi fT)$). The result of this convolution is a distorted version of the Fourier transform of the original infinite signal.

A technique known as *windowing* is applied to minimize the amount of distortion due to spectral leakage. The sampled finite duration signal is multiplied by a function, or window, before the FFT is performed. Based on the specific type of signal considered (*e.g.*, narrow-band random, periodic, impulse response), this time domain function is chosen with frequency domain characteristics to reduce the amount of distortion in the frequency domain representation of the signal.

The effect of spectral leakage is illustrated in Fig. 2.3. The spectrum of a finite sample of a 2 Hz signal is compared to the spectrum of the same signal multiplied by a Hanning window, given by

$$w_H(nT) = \begin{cases} \alpha + (1-\alpha)\cos(2\pi/(N-1)) & for \ |n| \le (N-1)/2 \\ 0 & otherwise \end{cases} . \qquad (2.1)$$

where $\alpha = 0.5$ and N is the number of points in the FFT. The frequency domain representation of the Hanning window has reduced side lobes (the peaks on either side of the main peak) compared to those of the rectangular window, which decreases the amount of distortion in the frequency domain representation. Notice that the frequency domain representation of the raw signal contains nonzero components on either side of the main peak,

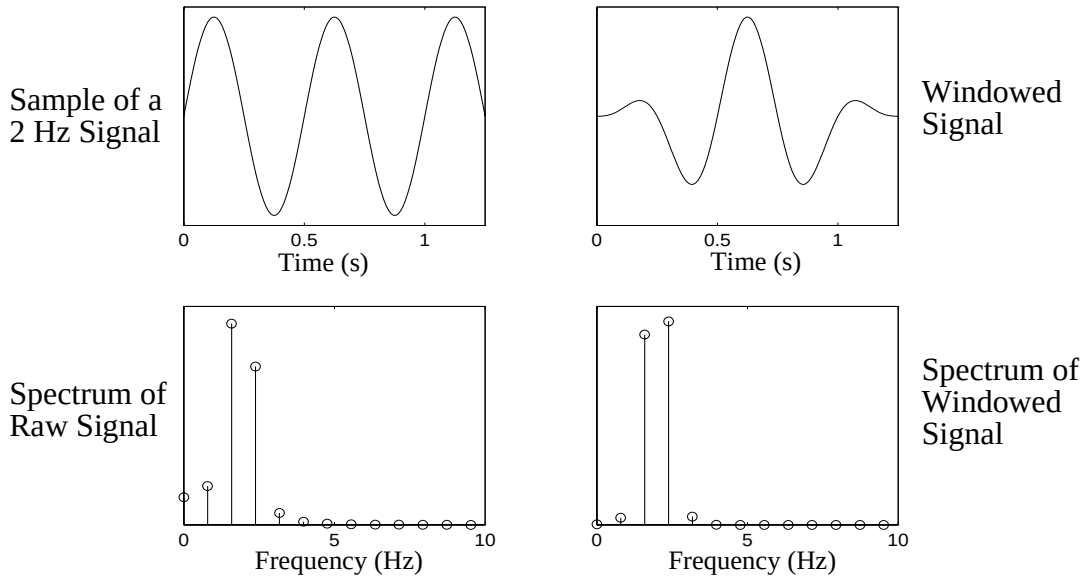

Figure 2.3 The Effect of Spectral Leakage.

while the windowed signal has less leakage. The Hanning window, which was used in the analysis of each of the experiments discussed herein, is often recommended for narrow-band, random signals such as occur in vibration testing.

2.1.2 Experimental Determination of Transfer Functions

In the identification of linear systems, it is often useful to obtain transfer functions (also termed frequency response functions) which portray the input/output behavior of the system in the frequency domain (see section 2.2). Methods for experimental determination of transfer functions can be classified in two fundamental types: (i) swept-sine, and (ii) broadband approaches using fast Fourier transforms (FFT). While both methods can produce accurate transfer function estimates, there are advantages and limitations to each approach. The swept-sine approach is helpful in recognizing and characterizing nonlinearities which may be present in the system, but it is rather time consuming because it analyzes the system one frequency at a time. Furthermore, noise in the measurements can

produce significant errors in the results. The broadband approach estimates the transfer function simultaneously over a band of frequencies, and the effects of noise and nonlinearities are reduced. Herein the structural system is assumed to remain approximately linear, and the broadband approach is employed to determine the experimental transfer functions.

To experimentally determine a transfer function using the broadband approach, the first step is to excite the system input over the frequency range of interest. Assuming the two continuous signals (input, *u*, and output, *y*) are stationary, the transfer function is determined by dividing the cross-spectral density of the two signals by the autospectral density of the input signal (Bendat and Piersol, 1980) as in

$$H_{yu}(j\omega) = \frac{S_{uy}(\omega)}{S_{uu}(\omega)} . \tag{2.1}$$

Experimental transfer functions are determined in a discrete sense. The continuous time records of the specified system input and the resulting responses are sampled at N discrete time intervals, yielding the finite duration, discrete-time representations of each signal, $u(nT)$ and $y(nT)$, where T is the sampling period and $n = 0, 1, \ldots, (N-1)$ is an integer representing the discrete time variable. A periodic representation of this signal (with period NT) is then formed as

$$u_p(nT) = \sum_{r=-\infty}^{\infty} u(nT + rNT) . \tag{2.2}$$

An *N*-point FFT is performed on the periodic discrete-time signal to compute the discrete Fourier transform given by

$$U(jk\Omega) = \sum_{n=0}^{N-1} u_p(nT) W^{-nk}, \qquad k = 0, \ldots, N-1 , \tag{2.3}$$

where $W = e^{2\pi j/N}$, $\Omega = \omega_s/N$, and ω_s is the sampling frequency (Antoniou, 1993). The discrete form of the autospectral density of each input signal and of the cross-spectral density of each pair of input and output signals are then determined by

$$S_{uu}(k\Omega) = cU^*(jk\Omega)U(jk\Omega) \tag{2.4}$$

$$S_{uy}(k\Omega) = cU^*(jk\Omega)Y(jk\Omega) \tag{2.5}$$

where c is a normalization constant defined as $c = T/N$, and '*' indicates the complex conjugate. For the discrete case, Eq. (2.1) can be written as

$$H_{yu}(jk\Omega) = \frac{S_{uy}(k\Omega)}{S_{uu}(k\Omega)} . \tag{2.6}$$

This discrete frequency transfer function can be thought of as a frequency sampled version of the continuous transfer function in Eq. (2.1).

In practice, one collection of samples of length N does not produce very accurate results due to inherent noise in the measurements. Better results are obtained by averaging the spectral densities of a number of collections of samples of the same length (Bendat and Piersol, 1980). Given that the number of collections of samples is M, the equations corresponding to (2.4) through (2.6) are

$$\bar{S}_{uu}(k\Omega) = \frac{1}{M}\sum_{i=1}^{M} S_{uu}^{i}(k\Omega) \tag{2.7}$$

$$\bar{S}_{uy}(k\Omega) = \frac{1}{M}\sum_{i=1}^{M} S_{uy}^{i}(k\Omega) \tag{2.8}$$

$$\bar{H}_{yu}(jk\Omega) = \frac{\bar{S}_{uy}(k\Omega)}{\bar{S}_{uu}(k\Omega)} \tag{2.9}$$

where S^i denotes the spectral density of the ith collection of samples and the overbar represents the ensemble average. Here, the input and output of the system are assumed to be

ergodic processes. Therefore, the ensemble averages may be calculated by computing the corresponding time averages of the functions.

2.1.3 Description of Data Acquisition Equipment

To develop high quality models and evaluate the structural control systems, two separate systems are available in the SDC/EEL to collect the experimental data. In the following paragraphs the two systems are described and the advantages of each system are discussed.

Tektronix Fourier Analyzer

A 4-channel Tektronix 2630 Fourier Analyzer is available to perform on-line calculations of the experimental transfer functions. This instrument greatly simplifies the tasks of obtaining and processing experimental data. Both analog and digital anti-aliasing filters are employed and adjustable input amplifiers for the A/D converters are provided to minimize the errors due to quantization. Voltage ranges span 55 mV to 10 V in 16 steps of 3 dB. This instrument has 12 base-band frequency ranges from DC-5 Hz to DC-20 kHz, 9 zoom ranges from 5 Hz to 2 kHz and built-in anti-aliasing signal conditioners. The dynamic range is 75 dB, and the real-time bandwidth is 10 kHz. The system also has a built-in signal generator and a digital record/playback feature that provides high-speed, bidirectional transfer of digitized input signal between the 2630 and the PC's hard disk. Various windowing options are available, including a Hanning window, which is recommended when a broadband excitation is used,. However, one of the limitations of this system is that it only has four channels.

Data Acquisition System

An eight channel data acquisition system was also employed to collect reliable measurement of the structural responses. This data acquisition system consists of eight Sym-

inex XFM82 3-decade programmable antialiasing filters, an Analogic LSDAS-16-AC-mod2 data acquisition board, an Analogic CTRTM-05 counter-timer board, and the Snap-Master software package written by HEM Data Corporation, driven by a Gateway 2000 P5-90 Computer. This high-quality system can be employed to record the time responses of the systems and the subsequent processing is then performed in MATLAB (1994).

The XFM82 series filters offer programmable pre-filter gains to amplify the signal into the filter, programmable post-filter gains to adjust the signal so that it falls in the correct range for the A/D converter, and analog antialiasing filters which are programmable up to 25 kHz. The high-quality elliptic low-pass filters have a 0.001 dB pass-band ripple, a stop band magnitude of -90 dB, and a 90 dB/oct roll-off above the cutoff frequency. The filters on all 8-channels are magnitude/phase matched to within 0.1 dB/1 degree to 90% of the cutoff frequency. In addition, each channel has a sample-and-hold device to allow simultaneous measurement of all signals. Simultaneous sample-and-hold (SSH) is necessary to eliminate systematic bias in the phase of the transfer functions.

The Analogic LSDAS-16-AC-mod2 data acquisition board is a high speed, high precision multifunction board featuring 50 kHz sampling and 16 bits of A/D resolution. The LSDAS-16-AC-mod2 can measure up to 8 channels in the differential input mode. This mode is recommended for noise rejection and resistance to ground loops. To take full advantage of the SSH ability of the XFM82 filters, the sample-and-hold and A/D conversion are triggered with an external clock source supplied by an Analogics CTRTM-05 counter-timer board which generates the appropriate timing signals.

Snap-Master for Windows provides the necessary drivers for the antialiasing filters, counter-timer board and data acquisition board. Snap-Master also has the required time and frequency domain functions which can be used to analyze the data during testing or post processing. Additionally, Snap-Master allows the user to create custom instruments.

2.2 System Identification

One of the most important and challenging tasks in control synthesis and analysis is the development of an accurate mathematical model of the structural system under consideration, including the structure and control devices. There are several methods by which to accomplish this task. One approach is to analytically derive the system input/output characteristics through physically-based modeling. Often this technique results in complex models that do not correlate well with the observed response of the actual system.

Alternatively, measured input/output data from the system can be employed directly to construct a mathematical model that replicates observed behavior. This approach is termed *system identification* and consists of the following steps: collection of high-quality input/output data, computation of the best model within the class of systems considered, and evaluation of the adequacy of the model's properties.

System identification techniques fall into two categories: time domain and frequency domain. Time domain techniques such as the recursive least squares (RLS) system identification method (Friedlander, 1982) are superior when limited measurement time is available or nonlinearities are present in the system. Frequency domain techniques are generally preferred when significant noise is present in the measurements and the system is assumed to be linear and time invariant.

While linear system identification techniques are fairly well established (Schoukens and Pintelon, 1991), general approaches for identification of nonlinear systems, such as result from a semi-actively controlled structure, are not readily available (Bendat and Piersol, 1990; Billings, 1984). In the three active control experiments to be discussed, a frequency domain approach to system identification which will be discussed in section 2.2.1 is applied. In these experiments the structural system, including the test structure and the control devices, is assumed to remain in the linear region. In section 2.2.2, a new approach

is developed to identify the semi-actively controlled structure, and this approach is applied in Chapter 9 to identify a model of a test structure configured with a semi-active magnetorheological damper.

2.2.1 Frequency Domain Approach to System Identification

In the frequency domain approach to system identification, the first step is to experimentally determine the transfer functions from each of the system inputs to each of the outputs. Subsequently, each of the experimental transfer functions is modeled as a ratio of two polynomials in the Laplace variable *s* and then used to determine a state space representation for the structural system. This frequency domain system identification approach will be employed herein for the development of a mathematical model of the structural system.

A block diagram of a typical structural system to be identified is shown in Fig. 2.4 The structural system includes the structure to be controlled, as well as the control actuators and any structural components employed to connect the actuators to the structure (*e.g.*, in the case of an active tendon system in Chapter 5, the tendons and the frame connecting the actuator to the tendons). Although in general, the disturbance to the system would be represented as a vector, the procedure is presented for the case in which there is a single ground excitation given by $\ddot{x}_g$. Extending this approach to multiple excitations is straightforward. Thus, the inputs to the system are the ground excitation $\ddot{x}_g$ and the vector of actuator command signals $\mathbf{u} = [u_1\ u_2 \ldots u_l]'$. The vector of system outputs, $\mathbf{y} = [y_1\ y_2 \ldots y_m]'$, includes any measurements which are used for feedback in the control system. Thus, a $m \times (l + 1)$ transfer function matrix, given as

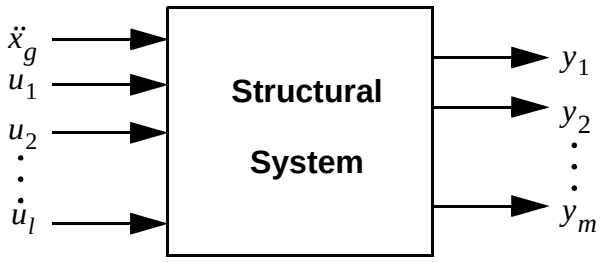

Figure 2.4 System Identification Block Diagram.

$$\mathbf{G} = \begin{bmatrix} G_{y_1\ddot{x}_g} & G_{y_1u_1} & \cdots & G_{y_1u_l} \\ G_{y_2\ddot{x}_g} & \ddots & & \vdots \\ \vdots & & & \\ G_{y_m\ddot{x}_g} & G_{y_mu_1} & \cdots & G_{y_mu_l} \end{bmatrix} \tag{2.10}$$

must be identified to describe the characteristics of the system in Fig. 2.4.

Experimental Determination of Transfer Functions

The first step in the frequency domain approach is to independently excite each of the system inputs over the frequency range of interest. Exciting the system at frequencies outside this range is typically counterproductive; thus, the excitation should be band-limited (*e.g.*, pseudo-random, chirps, *etc*.). The transfer functions from the ground acceleration to each of the measured responses (the first column of the transfer functions matrix in Eq. (2.10)) are obtained by exciting the structure with a band-limited white noise ground acceleration with the actuator command set to zero. Similarly, the experimental transfer functions from each of the actuator command signals to each of the measured outputs (the remaining columns of the transfer functions matrix) are determined by applying a band-limited white noise to each actuator command while the earthquake simulator is held fixed.

Mathematical Modeling of the Transfer Functions

Once the experimental transfer functions have been obtained, the next step in the system identification procedure is to model the transfer functions as a ratio of two polynomials in the Laplace variable *s*. This task was accomplished via a least squares fit of the ratio of numerator and denominator polynomials, evaluated on the $j\omega$ axis, to the experimentally obtained transfer functions (Schoukens and Pintelon, 1991). The algorithm requires the user to input the number of poles and zeros to use in estimating the transfer function, and then determines the location for the poles/zeros and the gain of the transfer function for a best fit. This algorithm is used in each experiment to fit each of the transfer functions.

To effectively identify a structural model, a thorough understanding of the significant dynamics of the structural system is required. For example, because the transfer functions represent the input/output relationships for a single physical system, a common denominator should be assumed for the elements of each column of the transfer function matrix. The curve fitting routine, however, does not necessarily yield this result. Thus, the final locations of the poles and zeros are then adjusted as necessary to more accurately represent the physical system. A MATLAB (1994) computer code was written to automate this process.

Another important phenomenon that should be consistently incorporated into the identification process is control-structure interaction. Most of the current research in the field of structural control does not explicitly take into account the effects of control-structure interaction in the analysis and design of protective systems. In Chapter 3 the phenomenon of control-structure interaction is examined and it is demonstrated through three illustrative examples that neglecting the effects of control-structure interaction can result in decreased performance and even instability in the controlled system (Dyke, *et al.*, 1993, 1995). By including the actuator in the structural system, the actuator dynamics and con-

trol-structure interaction effects are automatically taken into account in the system identification procedure.

Of course, the structural system is actually a continuous system and will have an infinite number of vibrational modes. One of the jobs of the control designer is to ascertain which of these modes are necessary to model for control purposes. The system model must then be accurate in this frequency range. A consequence of this decision is that significant control effort should not be applied at frequencies outside this frequency range. The techniques used to roll-off the control effort at higher frequencies are presented in section 2.3. In the subsequent chapters, more details will be provided regarding the specific modeling requirements of each experiment.

State-Space Realization

The system is then assembled in a state space form using the analytical representation of the transfer functions (*i.e.*, the poles, zeros and gain) for each individual transfer function. Because the systems under consideration are multi-input/multi-output systems (MIMO), such a construction is not straightforward.

First, a number of separate systems are formed, each with a single input corresponding to one of the inputs to the system. Thus, a total of $l + 1$ systems must be formed, each corresponding to a column of the transfer function matrix. The state equations modeling the input/output relationship between the disturbance, $\ddot{x}_g$, and the measured outputs can be realized as

$$\begin{aligned} \dot{\mathbf{x}}_1 &= \mathbf{A}_1\mathbf{x}_1 + \mathbf{B}_1\ddot{x}_g, \\ \mathbf{y} &= \mathbf{C}_1\mathbf{x}_1 + \mathbf{D}_1\ddot{x}_g, \end{aligned} \tag{2.11}$$

where $\mathbf{A}_1$, $\mathbf{B}_1$, $\mathbf{C}_1$, and $\mathbf{D}_1$ are in controller canonical form, $\mathbf{x}_1$ is the state vector, and $\mathbf{y}$ is the vector of measured structural responses.

The second set of state equations, modeling the input/output relationship between the command to each actuator u_i for $i = 1, 2, \ldots, l$ and the responses $\mathbf{y}$ are given by

$$\begin{aligned} \dot{\mathbf{x}}_{2i} &= \mathbf{A}_{2i}\mathbf{x}_{2i} + \mathbf{B}_{2i}u_i, \\ \mathbf{y} &= \mathbf{C}_{2i}\mathbf{x}_{2i} + \mathbf{D}_{2i}u_i. \end{aligned} \tag{2.12}$$

where $\mathbf{A}_{2i}$, $\mathbf{B}_{2i}$, $\mathbf{C}_{2i}$, and $\mathbf{D}_{2i}$ are in controller canonical form, and $\mathbf{x}_{2i}$ are the state vectors for system corresponding to each input u_i. These systems typically contains all of the poles corresponding to the building modes, plus additional dynamics required to model the actuators. Because the transfer function characteristics from the ground to the building response are dominated by the dynamics of the building, the system in Eq. (2.11) typically requires fewer states, corresponding to the dominant modes of the building, to accurately model the experimental transfer functions over the frequency range of interest.

Once both of the component system state equations have been identified, the MIMO system can be formed by stacking the states of the two individual systems. By defining a new state vector, $\mathbf{x} = [\mathbf{x}_1' \ \mathbf{x}_{21}' \ \mathbf{x}_{22}' \ldots \mathbf{x}_{2l}']'$, the state equation for the (l+1)-input/m-output system is written

$$\dot{\mathbf{x}} = \begin{bmatrix} \mathbf{A}_1 & \mathbf{0} \\ \mathbf{0} & \mathbf{A}_2 \end{bmatrix} \mathbf{x} + \begin{bmatrix} \mathbf{0} \\ \mathbf{B}_2 \end{bmatrix} \mathbf{u} + \begin{bmatrix} \mathbf{B}_1 \\ \mathbf{0} \end{bmatrix} \ddot{x}_g \, , \tag{2.13}$$

and the measurement equation becomes

$$\mathbf{y} = \begin{bmatrix} \mathbf{C}_1 & \mathbf{C}_2 \end{bmatrix} \mathbf{x} + \mathbf{D}_2\mathbf{u} + \mathbf{D}_1\ddot{x}_g \, . \tag{2.14}$$

However, this is not a minimum realization of the system. The dynamics of the test structure itself are redundantly represented in this combined state space system, thus the system given in Eqs. (2.13) and (2.14) has repeated eigenvalues for which the eigenvectors are not linearly independent (*i.e.*, the associated modes are not linearly independent). Thus, a balanced realization of the system given in Eqs. (2.13) and (2.14) is found and a model reduc-

tion is performed (Moore, 1981; Laub, 1980) to eliminate the redundant states corresponding to the building dynamics.

For robust stability and performance of the controlled system, it is important to have an accurate model from each of the control inputs to the measured responses in the frequency range of interest. Therefore, in performing the model reduction, weightings can be applied to the columns of the transfer function matrix **G** corresponding to the control inputs to the measured responses (Eq. (2.12)), to specify their relative importance in the model reduction. As the respective weightings increase, the transfer functions of the reduced order model for the corresponding column of the transfer function matrix remain similar to the transfer functions of the original model.

The state space representation of the reduced model is given by

$$\begin{aligned} \dot{\mathbf{x}}_r &= \mathbf{A}\mathbf{x}_r + \mathbf{B}\mathbf{u} + \mathbf{E}\ddot{x}_g, \\ \mathbf{y} &= \mathbf{C}_y\mathbf{x}_r + \mathbf{D}_y\mathbf{u} + \mathbf{F}_y\ddot{x}_g + \mathbf{v}, \end{aligned} \tag{2.15}$$

where **v** represents the measurement noise. To ensure that information is not lost in the model reduction, the transfer functions of the reduced order system will be compared to the transfer functions of the original model. In the subsequent chapters, verification of the reduced order model is provided for each experiment.

2.2.2 Identification of Semi-Actively Controlled Systems

In this section, an approach to the identification of semi-actively controlled structures is developed. This approach will be used in Chapter 9 to identify a model of a test structure which is controlled with a semi-active MR damper. Because accurate measurement of displacements and velocities is difficult to achieve directly in full-scale applications, emphasis is placed on the identified models being appropriate for synthesis of acceleration feedback control strategies. Attention is restricted to the case in which the structure is con-

figured with a single semi-active control device, although extension to the multiple-device case is straightforward.

Consider a seismically excited structure configured with a single semi-active control device, where the semi-active controller is assumed to be adequate to keep the response of the primary structure in the linear range. A block diagram of this problem is shown in Fig. 2.5, where v is the command signal to the semi-active device, f is the force generated in the semi-active device, $\ddot{x}_g$ is the ground acceleration, $\mathbf{y} = [\mathbf{y}_1' \ \mathbf{y}_2']'$ is the vector of measured outputs, and $\mathbf{y}_1$ is the portion of the measured output vector that accounts for feedback interaction with the semi-active device. As indicated here, the inputs $\mathbf{y}_1$ and v to the semi-active device are required to be measurable quantities to directly apply the proposed approach.

The proposed system identification algorithm simplifies the problem by decoupling the identification of the nonlinear semi-active device from that of the primary structure. The approach consists of four steps: (i) identification of a model for the semi-active control device, (ii) identification of a model for the primary structure, (iii) integration and optimization of the device and structural models, and (iv) validation of the integrated model of the system. Therefore, the primary structure can be identified using standard lin-

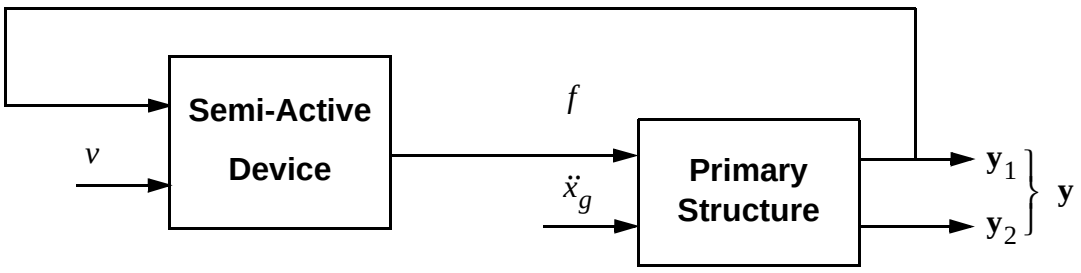

Figure 2.5 Block Diagram of a Semi-Actively Controlled Structure.

ear system identification techniques, although nonlinear identification means must still be employed to identify the semi-active control device.

The first step in the identification process is to develop an input/output of the semi-active device which can effectively predict the behavior of the semi-active device. In the literature both nonparametric and parametric models have been considered to model the observed behavior of various semi-active devices (Stanway *et al.*, 1985, 1987; Gamota and Filisko, 1991; Ehrgott and Masri, 1992, 1994; Sack *et al.*, 1994; Patten *et al.*, 1994a,b; Makris *et al.*, 1995; 1996; Burton *et al.*, 1996; Constantinou and Symans, 1996). In chapter 7, a parametric model based on a simple mechanical idealization is proposed to model the behavior of the MR damper. To obtain the optimal values for the model parameters, a least-squares output-error method is employed in conjunction with a constrained nonlinear optimization. The optimization is performed using the sequential quadratic programming algorithm available in MATLAB (1994).

To identify a model of the structure, the frequency domain approach to system identification of linear systems, presented previously in section 2.2.1, is applied. In this approach, the transfer functions from each of the inputs to each of the outputs must first be experimentally determined. The inputs to the structure are the ground acceleration $\ddot{x}_g$ and the control force f applied by the semi-active device, as shown in Fig. 2.5. The system outputs are the measured responses given by $\mathbf{y}$. Each of the transfer functions is modeled as a ratio of two polynomials in the Laplace variable s, the individual state vectors of the two models are stacked to form one combined system, a model reduction is performed, and the model is verified.

Because the semi-active device may be functioning at a different operating point when it is installed in the structure than during the initial experiments when the device is tested alone, it may be necessary to update the parameters of the model for the semi-active

device. To identify the new set of parameters, tests should be conducted to measure the response of the structure with the semi-active device in place. The updated parameters can then be determined based on the response of the semi-active device when it is installed in the structure. An integrated model of the semi-actively controlled structure is then formed by connecting the models of semi-active device and the structure as shown in Fig. 2.5.

The procedure outlined in this section will be used to identify an integrated model of the MR damper/test structure in Chapter 9. Verification of this integrated system model is provided therein.

2.3 Control Design

Many of the control strategies that have been studied for civil engineering applications assume that the full state vector can be measured. However, as discussed in Chapter 1, this is not typically the case and output feedback strategies must be considered. Because of this requirement, and the stochastic nature of earthquake ground excitations, H_2/LQG methods are advocated herein. In Spencer *et al.*, (1991, 1994) and Suhardjo *et al.* (1992), output feedback control strategies which utilize structural accelerations in determining the control action have been systematically developed based on H_2/LQG methods. An overview of the H_2/LQG control design is given in this section.

2.3.1 Control Algorithm

A block diagram of the general structural control problem is shown in Fig. 2.6. Here, **y** is the output vector of measured structural responses, **z** is the vector of system responses to be controlled, **u** is the control input vector, and **d** is the input vector of excitations. The measured output vector **y** includes the accelerations of the floors of the test structure and any additional measurements which are used for feedback in the control system. The regulated output vector **z** may consist of any linear combination of the states of the system and

components of the control input vector **u**, thus allowing for a broad range of control objectives by appropriately choosing the elements of **z**.

In the H_2/LQG method, the control design is performed in the frequency domain, while the associated control calculations are computed in the time domain. Because the dynamic behavior of structures is often characterized with frequency domain functions (*e.g.*, transfer functions), a frequency domain approach to control design is natural. The frequency domain approach is considered to be versatile, because it provides a clear way to incorporate frequency domain weighting functions into the design. Weighting functions can be applied to the elements of **z** to specify the frequency range over which each element of **z** is minimized, or used to shape the input excitation vector **d**. The "structural system" in Fig. 2.6 then contains the test structure, actuator, any structural fixtures between the actuator and structure, plus filters and weighting functions in the frequency domain. The frequency domain approach can then be solved in the time domain by appending the appropriate filters to the state equations of the structural system, and solving the equivalent LQG problem.

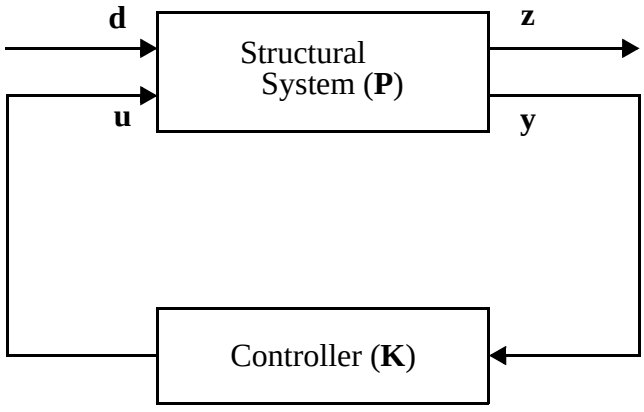

Figure 2.6 General Structural Control Block Diagram.

The goal of the H_2 control problem is to design a stablizing controller **K,** that minimizes the H_2 norm of the closed loop transfer function matrix from the disturbance $\mathbf{d}$, to the regulated output vector $\mathbf{z}$, given by $\mathbf{H_{zd}}$. By definition, the H_2 norm of a stable transfer function matrix $\mathbf{H}$ is (Boyd and Barratt, 1991)

$$\|\mathbf{H}\|_2 \equiv \sqrt{\text{trace}\left\{\frac{1}{2\pi}\int_{-\infty}^{\infty}\mathbf{H}(j\omega)\mathbf{H}^*(j\omega)d\omega\right\}}. \tag{2.16}$$

To better understand the H_2 norm of $\mathbf{H_{zd}}$, notice that the value of the H_2 norm of $\mathbf{H_{zd}}$, $\|\mathbf{H_{zd}}\|_2$, represents the root mean square (*rms*) value of the regulated output vector $\mathbf{z}$ of the closed loop system when the input, $\mathbf{d}$, is a unit intensity white noise (*i.e.,* when the spectral density of $\mathbf{d}$, $S_{\mathbf{dd}}(\omega) = \mathbf{I}$). The *rms* output vector is defined by

$$\|\mathbf{z}\|_{rms} = \sqrt{\lim_{\tau\to\infty}\frac{1}{2\tau}\int_{-\tau}^{\tau}\mathbf{z}^T(t)\mathbf{z}(t)dt}\ . \tag{2.17}$$

When $\mathbf{z}(t)$ is a vector of ergodic stochastic process, the *rms* output vector is defined by

$$\|\mathbf{z}\|_{rms} = \sqrt{\sum_i E[z_i^2(t)]}\ , \tag{2.18}$$

where $E[\cdot]$ is the expected value operator and z_i are the components of $\mathbf{z}$. Thus, minimizing the value of $\|\mathbf{H_{zd}}\|_2$ corresponds to minimizing the *rms* output vector for a unit intensity white noise input.

Following Spencer, *et al.* (1994), refer to Fig. 2.6 to obtain the closed loop transfer function matrix $\mathbf{H_{zd}}$. First, partition the transfer function matrix of the structural system $\mathbf{P}$, as in

$$\mathbf{P} = \begin{bmatrix}\mathbf{P_{zd}} & \mathbf{P_{zu}}\\ \mathbf{P_{yd}} & \mathbf{P_{yu}}\end{bmatrix}. \tag{2.19}$$

The transfer function matrix **P** is assumed to be strictly proper, however one should note that **P** includes the weighting functions employed in the control design. Therefore systems of the form of Eq. (2.15) which are not strictly proper can be readily handled through appropriately chosen weighting functions. The transfer function matrix of the closed loop system from $\mathbf{d}$ to $\mathbf{z}$ can then be written as (Suhardjo, 1990)

$$\mathbf{H_{zd}} = \mathbf{P_{zd}} + \mathbf{P_{zu}K}(\mathbf{I} - \mathbf{P_{yu}K})^{-1}\mathbf{P_{yd}}. \tag{2.20}$$

Also note that the inverse in Eq. (2.20) must exist.

As mentioned previously, an advantage of the H_2 approach is that frequency domain functions may be incorporated into the design process, allowing the designer to focus the control effort on a particular frequency range or to roll-off the control effort in other regions. This approach is illustrated in the block diagram representation of a linear structure subjected to a one-dimensional earthquake excitation $\ddot{x}_g$ shown in Fig. 2.7. Here, the excitation vector $\mathbf{d}$ includes the input disturbance $\mathbf{w}$ and the measurement noise vector $\mathbf{v}$. The matrix weighting functions $\mathbf{W}$ and $\mathbf{F}$ are generally frequency dependent. The disturbance shaping filter, $\mathbf{F}$, shapes the spectral content of the earthquake excitation, $\ddot{x}_g$, and the scalar parameter k is used to indicate a relative preference of minimizing $\|\mathbf{H_{zw}}\|_2$ (the norm of the closed loop transfer function matrix from $\mathbf{w}$ to $\mathbf{z}$) over minimizing $\|\mathbf{H_{zv}}\|_2$ (the norm of the closed loop transfer function matrix from $\mathbf{v}$ to $\mathbf{z}$). The output filters $\mathbf{W}$, weights the components of the regulated response vector $\mathbf{z}$.

The structural system in Fig. 2.7, which includes the structure, the actuator and any fixtures and components required to apply the control force, can be represented in state space form as

$$\dot{\mathbf{x}} = \mathbf{Ax} + \mathbf{Bu} + \mathbf{E}\ddot{x}_g \tag{2.21}$$

$$\mathbf{y} = \mathbf{C_y x} + \mathbf{D_y u} + \mathbf{v} \tag{2.22}$$

where **x** is the state vector of the system, **y** is the vector of measured responses, **z** is the regulated output vector, and **v** represents the noise in the measurements. Thus, the transfer function **G** in Fig. 2.7 is

$$\mathbf{G} = (s\mathbf{I} - \mathbf{A})^{-1}\underset{\sim}{\mathbf{B}} = (s\mathbf{I} - \mathbf{A})^{-1}[\mathbf{B}\ \mathbf{E}] = [\mathbf{G}_1\ \mathbf{G}_2] \tag{2.23}$$

From the block diagram in Fig. 2.7, the partitioned elements of the system transfer function matrix **P** in Eq. (2.19) can be given as

$$\mathbf{P_{zd}} = \begin{bmatrix}\mathbf{P_{zw}} & \mathbf{P_{zv}}\end{bmatrix} = \begin{bmatrix}k\mathbf{W}\mathbf{C_z}\mathbf{G}_2\mathbf{F} & \mathbf{0}\end{bmatrix}, \tag{2.24}$$

$$\mathbf{P_{zu}} = \begin{bmatrix}\mathbf{W}(\mathbf{C_z}\mathbf{G}_1 + \mathbf{D_z})\end{bmatrix}, \tag{2.25}$$

$$\mathbf{P_{yu}} = \mathbf{C_y}\mathbf{G}_1 + \mathbf{D_y}, \tag{2.26}$$

and

$$\mathbf{P_{yd}} = \begin{bmatrix}\mathbf{P_{yw}} & \mathbf{P_{yv}}\end{bmatrix} = \begin{bmatrix}k\mathbf{C_y}\mathbf{G}_2\mathbf{F} & \mathbf{I}\end{bmatrix}. \tag{2.27}$$

Equations (2.24)–(2.27) can then be substituted into Eq. (2.20), yielding an explicit expression for the closed loop transfer function matrix $\mathbf{H_{zd}}$. The H_2 control problem is

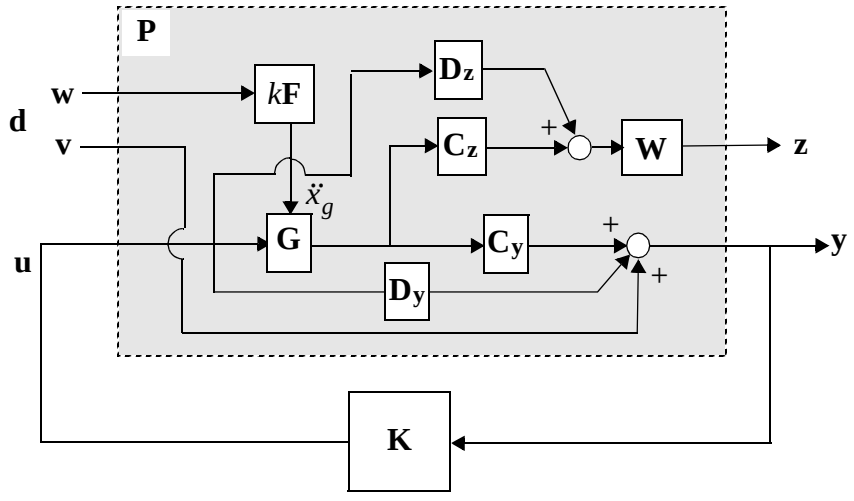

Figure 2.7 Typical Structural Control Block for a Seismically Excited Structure.

then solved by determining the controller $\mathbf{K}$ which minimizes the H_2 norm of this transfer function matrix.

As stated previously, the control calculations are performed in the time domain by solving an equivalent infinite horizon LQG problem (Suhardjo, 1990; Spencer, *et al.*, 1994). In the LQG approach to optimal control design, the problem is to find the controller that minimizes the infinite horizon performance index (also called a cost function) given by

$$J = \lim_{\tau \to \infty} \frac{1}{\tau} \mathrm{E}\left[\int_0^\tau \{\mathbf{z}'\mathbf{z}\} dt\right] \tag{2.28}$$

Note that minimization of this performance index corresponds to minimizing both the regulated structural responses and the control action, because $\mathbf{z}$ is a linear combination of the states of the system and components of the control input vector **u**. The excitation vector **d** is assumed to consist of unit intensity, statistically independent Gaussian white noise processes.

To better understand these ideas, consider a structure experiencing a single seismic excitation given by w. Thus, the state space representation for the structural system, including the model of the structural system, plus the weighting k, and the frequency dependent weighting functions $\mathbf{F}$ and $\mathbf{W}$, is given by

$$\dot{\mathbf{x}}_\mathbf{p} = \mathbf{A}_\mathbf{p}\mathbf{x}_\mathbf{p} + \mathbf{B}_\mathbf{p}\mathbf{u} + \mathbf{E}_\mathbf{p}w \tag{2.29}$$

$$\mathbf{y} = \mathbf{C}_{\mathbf{yp}}\mathbf{x}_\mathbf{p} + \mathbf{D}_{\mathbf{yp}}\mathbf{u} + \mathbf{F}_{\mathbf{yp}}w + \mathbf{v} \tag{2.30}$$

$$\mathbf{z} = \mathbf{C}_{\mathbf{zp}}\mathbf{x}_\mathbf{p} + \mathbf{D}_{\mathbf{zp}}\mathbf{u} + \mathbf{v} \tag{2.31}$$

where $\mathbf{x}_\mathbf{p}$ is the state vector of the system $\mathbf{P}$.

Because the measurement vector $\mathbf{y}$ is not the full state vector, an estimator must be designed to produce an optimal estimate of the states of the system model based on the

measured responses. The separation principle allows the control and estimation problems to be considered separately, yielding a controller of the form (Stengel 1986; Skelton 1988)

$$\mathbf{u} = -\mathbf{K}\hat{\mathbf{x}}_{\mathbf{p}} \tag{2.32}$$

where $\hat{\mathbf{x}}_p$ is the Kalman Filter estimate of the state vector. By the certainty equivalence principle (Stengel 1986; Skelton 1988), $\mathbf{K}$ is the full state feedback gain matrix for the deterministic regulator problem given by

$$\mathbf{K} = \tilde{\mathbf{R}}^{-1}(\tilde{\mathbf{N}}' + \mathbf{B}_{\mathbf{p}}'\tilde{\mathbf{S}}) \tag{2.33}$$

where $\tilde{\mathbf{S}}$ is the solution of the algebraic Riccati equation given by

$$\mathbf{0} = \tilde{\mathbf{S}}\tilde{\mathbf{A}} + \tilde{\mathbf{A}}'\tilde{\mathbf{S}} - \tilde{\mathbf{S}}\mathbf{B}_{\mathbf{p}}\tilde{\mathbf{R}}^{-1}\mathbf{B}_{\mathbf{p}}'\tilde{\mathbf{S}} + \tilde{\mathbf{Q}} \tag{2.34}$$

and

$$\tilde{\mathbf{Q}} = \mathbf{C}_{\mathbf{zp}}'\mathbf{C}_{\mathbf{zp}} - \tilde{\mathbf{N}}\tilde{\mathbf{R}}^{-1}\tilde{\mathbf{N}}' \tag{2.35}$$

$$\tilde{\mathbf{N}} = \mathbf{C}_{\mathbf{zp}}'\mathbf{D}_{\mathbf{zp}} \tag{2.36}$$

$$\tilde{\mathbf{R}} = \mathbf{D}_{\mathbf{zp}}'\mathbf{D}_{\mathbf{zp}} \tag{2.37}$$

$$\tilde{\mathbf{A}} = \mathbf{A}_{\mathbf{p}} - \mathbf{B}_{\mathbf{p}}\tilde{\mathbf{R}}^{-1}\tilde{\mathbf{N}}'. \tag{2.38}$$

Note that the components of the regulated output vector $\mathbf{z}$ must be chosen appropriately such that the matrix $\tilde{\mathbf{R}}$ is positive definite. One way to ensure this property is to choose the regulated output vector $\mathbf{z}$ such that it includes a component which is an invertible linear combination of the components of the control input vector $\mathbf{u}$. For instance, if there are n control inputs, the condition can be satisfied by choosing n components of the $\mathbf{z}$ vector to be a constant matrix multiplied by the control input vector $\mathbf{u}$, as in

$$\mathbf{z} = \begin{bmatrix} \mathbf{C}_{\mathbf{zp}} & \mathbf{0} \\ \mathbf{0} & \mathbf{0} \end{bmatrix} \mathbf{x}_{\mathbf{p}} + \begin{bmatrix} \mathbf{D}_{\mathbf{zp}} \\ \mathbf{T} \end{bmatrix} \mathbf{u} \tag{2.39}$$

where the inverse of $\mathbf{T}$ exists.

The Kalman Filter optimal estimator is given by

$$\dot{\hat{\mathbf{x}}}_\mathbf{p} = \mathbf{A_p}\hat{\mathbf{x}}_\mathbf{p} + \mathbf{B_p}\mathbf{u} + \mathbf{L}(\mathbf{y} - \mathbf{C_{yp}}\hat{\mathbf{x}}_\mathbf{p} - \mathbf{D_{yp}}\mathbf{u}) \tag{2.40}$$

$$\mathbf{L} = [\underset{\sim}{\mathbf{R}}^{-1}(\mathbf{F_{yp}}\mathbf{E_p}' + \mathbf{C_{yp}}\underset{\sim}{\mathbf{S}})]' \tag{2.41}$$

where $\underset{\sim}{\mathbf{S}}$ is the solution of the algebraic Riccati equation given by

$$\mathbf{0} = \underset{\sim}{\mathbf{S}}\underset{\sim}{\mathbf{A}} + \underset{\sim}{\mathbf{A}}'\underset{\sim}{\mathbf{S}} - \underset{\sim}{\mathbf{S}}\underset{\sim}{\mathbf{G}}\underset{\sim}{\mathbf{S}} + \underset{\sim}{\mathbf{H}} \tag{2.42}$$

and

$$\underset{\sim}{\mathbf{A}} = \mathbf{A_p}' - \mathbf{C_{yp}}'\underset{\sim}{\mathbf{R}}^{-1}(\mathbf{F_{yp}}\mathbf{E_p}') \tag{2.43}$$

$$\underset{\sim}{\mathbf{G}} = \mathbf{C_{yp}}'\underset{\sim}{\mathbf{R}}^{-1}\mathbf{C_{yp}} \tag{2.44}$$

$$\underset{\sim}{\mathbf{H}} = \mathbf{E_p}\mathbf{E_p}' - \mathbf{E_p}\mathbf{F_{yp}}'\underset{\sim}{\mathbf{R}}^{-1}\mathbf{F_{yp}}\mathbf{E_p}' \tag{2.45}$$

$$\underset{\sim}{\mathbf{R}} = \mathbf{I} + \mathbf{F_{yp}}\mathbf{F_{yp}}' \tag{2.46}$$

As mentioned previously, for the experiments discussed herein, the H_2 design approach was employed and the control calculations were performed in the time domain. More details regarding the use of H_2 control methods for civil engineering applications can be found in Suhardjo (1990) Suhardjo *et al.*, 1992, and Spencer, *et al*. (1991, 1994).

2.3.2 Design Considerations and Procedure

In each experiment, to offer a basis for comparison, a number of candidate controllers are designed using H_2/LQG control design techniques and employing various performance objectives. Designs which minimize either displacements relative to the foundation, interstory displacements or absolute accelerations of the structure are considered. In some cases, control designs are also considered which directly used the measured earthquake accelerations in control action determination. In this case, the matrix in Eq. (2.27) includes an additional term due to the measurement of the disturbance.

Often the control design model is acceptably accurate below a particular frequency, but significant modeling errors occur at higher frequencies due to the presence of unmodeled dynamics. If one tries to use high authority control at frequencies where the system model is poor, catastrophic results may occur. Thus, for each of the structural systems under consideration, no significant control effort is allowed above this frequency. More details regarding the specific considerations used to design the controllers are provided in the subsequent chapters.

For the three active control experiments discussed herein, the loop gain transfer function is examined in assessing the various control designs. For a single control input u, the loop gain transfer function is defined as the transfer function of the system formed by breaking the control loop at the input to the system, as shown in Fig. 2.8. Using the plant transfer function given in Eq. (2.26), the loop gain transfer function is given as

$$\mathbf{H}_{loop} = \mathbf{K}\mathbf{P}_{yu} = \mathbf{K}(\mathbf{C}_y\mathbf{G}_1 + \mathbf{D}_y) \tag{2.47}$$

By "connecting" the measured outputs of the analytical system model to the inputs of the mathematical representation of the controller, the loop gain transfer function from the actuator command input to the controller command output is calculated.

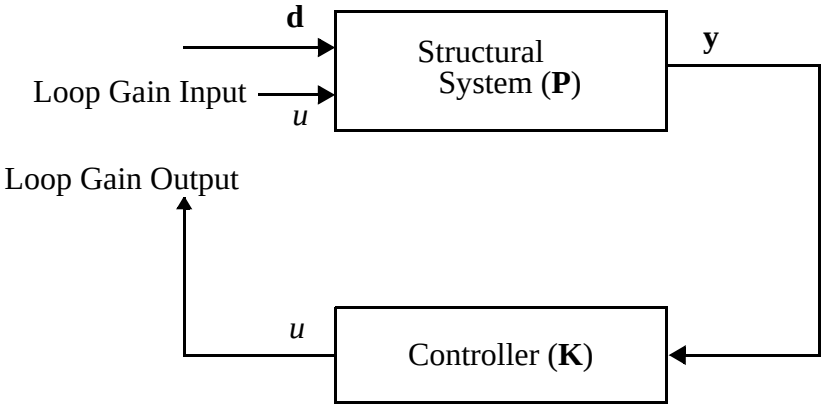

Figure 2.8 Diagram Describing the Loop Gain Transfer Function.

The loop gain transfer function is used to provide an indication of the closed-loop stability when the controller is implemented on the physical system. For stability purposes, the loop gain should be less than one at the higher frequencies where the model poorly represents the structural system. Thus, the magnitude of the loop gain transfer function should roll off steadily and be well below unity at frequencies outside of the range of interest. In the research reported in this dissertation, a control design is considered acceptable for implementation if the loop gain transfer function is below -5 dB at the higher frequencies where the modeling errors may be significant.

2.4 Control Implementation

The controllers used in these experiments are implemented on digital computers. There are many issues that must be understood and addressed to successfully implement a control design digitally. The resolution of these issues typically dictates that relatively high sampling rates need to be attained. Recently developed hardware based on dedicated DSP chips allows for very high sampling rates and offers new possibilities for control algorithm implementation.

In this section, a description of the digital control hardware used in these experiments is provided and some practical aspects of digital control implementation are considered. Additionally, the procedure employed to verify the successful implementation of the digital controller is presented.

2.4.1 Digital Controller Hardware

In the past, digital controllers were typically implemented using a data acquisition board located in one of the expansion slots in a personal computer (PC). The data acqusition board would be programmed to take samples of the measured responses at regular intervals and pass these values to the PC. The PC would then perform the required control

calculations and send the results to digital-to-analog (D/A) devices. The continuous-time control signals would then be sent to the control devices.

There are many disadvantages to this configuration. The time required to perform the control calculations, the A/D and D/A conversions, and pass values from the data acquisition board to the PC's CPU may require large sampling periods and introduce excessive time delays in the digital control system. Additionally, it is difficult to create a scheme which allows the user to unobtrusively monitor the control system while the PC is performing the control calculations.

A more desirable arrangement is obtained by using one of the available DSP boards that can be placed in an expansion slot of the PC. State-of-the-art DSP chips allow for very fast computational speeds and dedicated processing. All of the A/D and D/A conversions as well as control calculations are performed on the DSP board and which significantly increases the achievable sampling rates. In this configuration, a supervisory program running on the PC downloads the control code to the DSP board. While the DSP board runs the control algorithm, the program running on the PC can monitor the performance of the control system, monitor and display measured quantities, and allow the operator to send commands to the DSP board. This configuration allows for a very powerful and flexible implementation of a digital control system for structural control.

The digital control system employed in these experiments utilized the Real-Time Digital Signal Processor System made by Spectrum Signal Processing, Inc. It is configured on a board that plugs into a 16-bit slot in a PC's expansion bus and features a Texas Instruments TMS320C30 Digital Signal Processor chip, RAM memory and on-board A/D and D/A systems. The TMS320C30 DSP chip has single-cycle instructions, a 33.3 MHz clock, a 60 ns instruction cycle and can achieve a nominal performance of 16.7 MFLOPS. The

DSP board has two input channels and two output channels, each with 16 bit precision. The maximum sampling rate of the input channels is 200 kHz.

An expansion daughter board, which connects directly to the DSP board, provides an additional four channels of input and two channels of output, each with 12 bit precision. All four input channels share the same conversion device, which limits the achievable sampling rate. The maximum sampling rate for the daughter board is 200 kHz for one channel which decreases proportionally depending on the number of channels in use. The maximum rate for each of the two output channels on the daughter board is 300kHz. Clearly, with the high computation rates of the DSP chip and the extremely fast sampling and output capabilities, high sampling rates for the digital control system are achievable.

2.4.2 Digital Control System Design

The method of "emulation" is used for the design of the discrete-time controller (Quast, *et. al*., 1994). Using this technique, a continuous-time controller is first designed which produces satisfactory control performance. The continuous-time controller is then approximated or "emulated" with a discrete-time equivalent digital filter using the bilinear transformation (Astrom and Wittenmark, 1990). This configuration is illustrated in Fig. 2.9. The controller samples the measured outputs of the plant and passes the samples through a digital filter implemented on the DSP board. The output of the digital filter is then passed through a hold device to create a continuous-time signal which becomes the control input to the plant. The series combination of sampler, digital filter and hold emulates the operation of a continuous-time controller. Typically, with the use of emulation, if the sampling rate of the digital controller is greater than about 10-25 times the closed-loop system bandwidth, the discrete equivalent system will adequately represent the behavior

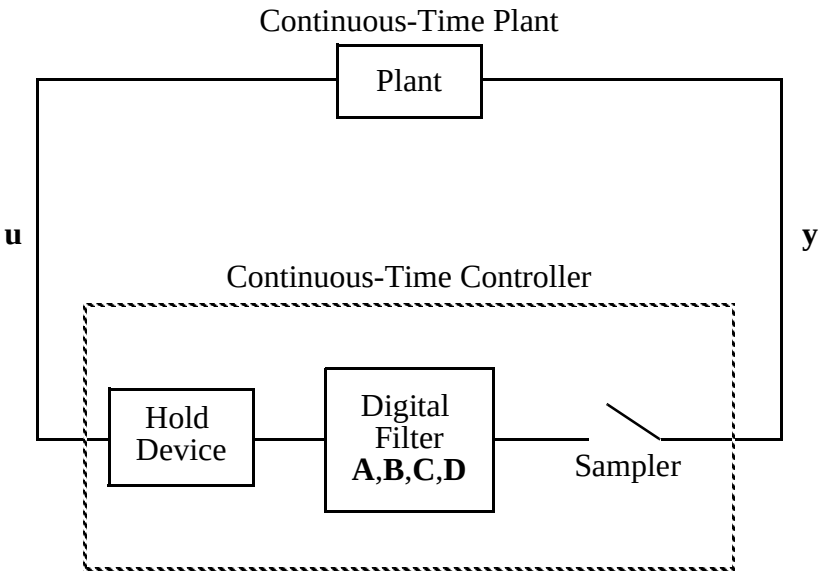

Figure 2.9 Digital Control System Design Using Emulation.

of the emulated continuous-time system over the frequency range of interest. This sampling rate is achieved by the DSP system used in these experiments.

2.4.3 Digital Control Implementation Issues

Once a filter is designed for use in the digital control system, it is implemented on a DSP system using the discrete state space form

$$\mathbf{x}(kT + T) = \mathbf{A}\mathbf{x}(kT) + \mathbf{B}\mathbf{y}(kT) \tag{2.48}$$

$$\mathbf{u}(kT) = \mathbf{C}\mathbf{x}(kT) + \mathbf{D}\mathbf{y}(kT) \tag{2.49}$$

where **y** represents the vector of measurement sampled inputs to the controller and **u** represents the vector of outputs of the digital filter. Performing the arithmetic to implement a state space realization of a digital filter is not elaborate. However, there are many practical considerations that needed to be addressed in order to successfully implement the filter, including such things as time delay and sampling rate.

Time Delay

For digital control systems, the only true time delays induced are due to latency (which results from A/D conversion time requirements and arithmetic associated with **D** matrix calculations) and the zero order hold. The delay due to latency will be reduced as the speed of the controller processor and I/O systems increases. Likewise, the delay due to the zero order hold will decrease in direct proportion to the sampling period. For the control system implemented in this experiment, the DSP processor and I/O systems were fast enough so that these time delays were on the order of 700 μ sec and small enough so as to have no significant impact on system performance.

Sampling Rate

The sampling rate that is achievable by a digital control system is limited by such things as the rate at which A/D and D/A conversions can be performed, the speed of the processor and the number of calculations required to be performed by the processor during a sampling cycle. There are many factors that must be considered when evaluating the sampling rate that is required for satisfactory performance of a digital control system. These factors include the prevention of aliasing, maintaining a sufficiently smooth control signal, and satisfactory controller performance of the controlled system with random disturbances. Accommodation of such factors usually requires a sampling rate of the controller that is 10-25 times greater than the significant frequencies in the measured responses, depending on the specific application. For this experiment, all I/O processes, control calculations, and supervisory functions were performed in less than 1 msec, allowing for sampling rates on the order of 1 kHz. Thus, the TMS320C30 DSP system readily accommodated this sampling rate guidance.

2.4.4 Software

Once the digital controller is designed, it is implemented using the Spectrum DSP board. The code for these programs can be written directly in the C programming language. An executable version of the code is created on the PC and the code is then downloaded to the DSP board through the PC.

In addition to performing the calculations for the control algorithm difference equations (Eqs. (2.48) and (2.49)), a number of other tasks are performed on the DSP board while the controller is operating. The standard deviations of the measurements are calculated, passed to the program running on the PC, and displayed to allow the operator to monitor the performance of the control system. Additionally, at each sample the values of certain measured quantities such as the actuator force and displacement are compared to a user-defined, maximum allowable values (as discussed in Soong, *et al.*, 1991; Reinhorn, *et al.*, 1993). If any of these measured values exceeds the maximum allowable value, the controller is turned off by setting the command signal to zero. The control program is also turned off if at any time the command output calculated by the control algorithm is larger enough to saturate the D/A converters. Operating the control system with a saturated output could have undesirable effects on the performance and stability of the system.

The supervisory program running on the PC allows the operator to turn the controller on and off, and monitor operation of the control system. If the control program running on the DSP board is turned off, the supervisory program on the PC displays an advisory on the monitor for the operator. This feature is designed to protect the structure and the control system from damage caused by excessive or unstable responses.

2.4.5 Verification of Digital Controller

Extensive testing is conducted for all components of the control hardware and software before each of the controlled experiments are performed. One of the final tests is to experimentally determine the loop gain transfer function by attaching the measured outputs from the structure to the inputs of the controller (*i.e.*, the DSP board). The loop gain transfer function is then calculated by exciting the actuator command input with a broadband excitation and measuring the controller output. To verify that the controller is operating correctly, the experimentally determined loop gain transfer function was compared to the analytical loop gain. In the frequency range of interest, the experimental and analytical loop gains should compare reasonably well. Outside the frequency range of interest, the magnitude of the experimental loop gain transfer function should roll off steadily and be well below unity, indicating that the closed-loop system is stable.

Note that except for built-in high frequency anti-aliasing filters on the input channels to the DSP board, no external filters are employed for either the feedback measurements or the control signal. All of the required frequency shaping is performed within the digital control algorithm.

CHAPTER 3

Control-Structure Interaction

Most of the current research in the field of structural control does not explicitly take into account the effects of control-structure interaction in the analysis and design of protective systems. Typically, the dynamics of the control actuators are integrally linked to the dynamics of the structure. Unmodeled control-structure interaction (CSI) effects can severely limit both the performance and robustness of protective systems. To study effectively the control-structure interaction problem, one must have good models for the dynamics of the associated actuators.

Many researchers studying active control of civil engineering structures have partially accounted for the dynamics of the control actuator by modeling them as a pure time delay. A phase-compensation approach has been successfully applied, with reasonable results being achieved for the state feedback situation. However, this approach does not account for control-structure interaction and does not appear to be tractable in output feedback situations. Examination of the experimentally obtained actuator transfer functions provided in the subsequent chapters shows that the actuator dynamics do not result in a pure time delay in the system. One must ensure that the effects of control-structure interaction are not neglected in obtaining a mathematical model of the experimental transfer functions. By including the actuator in the structural system, the actuator dynamics and control-structure interaction effects are automatically taken into account in the experimental data.

In contrast, the system identification procedure outlined in Chapter 2 systematically accounts for the dynamics of the actuator and the effect of control-structure interaction, resulting in a model which accurately represents the behavior of the actuator/structural system.

This chapter presents a general framework within which one can study the effects of control-structure interaction. Specific models are developed for hydraulic actuators typical of those used in many active structural control situations. A natural velocity feedback link is shown to exist, which tightly couples the dynamic characteristics of a hydraulic actuator to the dynamics of the structure to which it is attached. Neglecting this feedback interaction can produce poor, or perhaps catastrophic, performance of the controlled system due to the unmodeled or mismodeled dynamics of the actuator-structure interaction. In addition, the time lag in generation of control forces is accommodated through appropriate modeling of the actuator and the associated control-structure interaction. Experimental verification of the main concepts is presented. The implications on protective system design are illustrated through examples of seismically excited structures. Active bracing, active tendon and active mass driver (AMD) systems are considered.

3.1 Problem Formulation

Figure 3.1 provides a schematic diagram of a general active/semi-active structural control problem. The controller receives measurements from the sensors and forms a command input vector **u** to the control actuator. The control actuator then applies a force vector **f** to the structure. However, when mechanical actuators (*e.g.*, hydraulic actuators) are used to control structures, there is generally a dynamic coupling between the actuator and the structure, as represented by the dotted arrow in Fig. 3.1. This coupling indicates that it

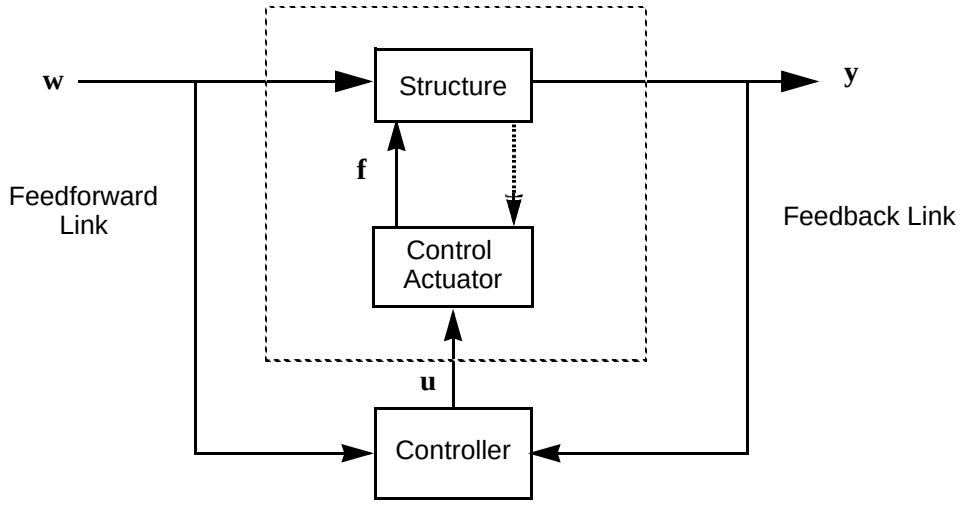

Figure 3.1 Block Diagram of Active/Semi-Active Structural Control System.

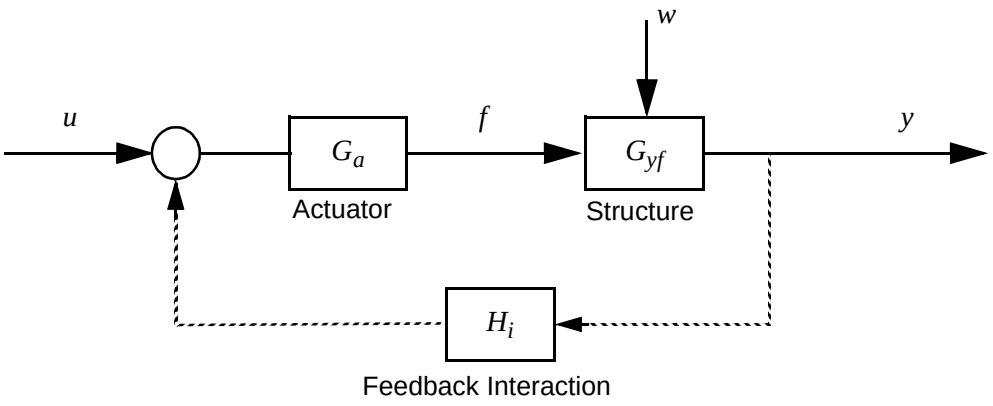

Figure 3.2 Model of Interaction Between the Actuator and the Structure.

is not possible to separate dynamical representations of the structure and the actuator, and model them as independent systems connected in series.

To understand the implications of the dynamical coupling, examine more closely the actuator and structural portions of the control system (*i.e.*, the region in Fig. 1 enclosed in the dashed box). Consider the case in which the system has one actuator, with a single command input *u* generating a single output force *f*. Fig. 3.2 provides a block diagram

description of this case, in which the interaction can be modelled from the output. Here G_a is the transfer function of the actuator, and G_{yf} is the transfer function from the force applied by the actuator to the structural responses. Because the dashed line in Fig. 3.1, representing the feedback interaction between the structure and the actuator, often has associated dynamics, these dynamics are represented by the transfer function H_i in Fig. 3.2. Thus, the overall transfer function from the control input *u* to the structural response *y* is given by

$$G_{yu} = \frac{G_{yf} G_a}{1 + G_{yf} G_a H_i} . \tag{3.1}$$

If these dynamic systems are represented by numerator and denominator polynomials in *s*, the representation of the system becomes

$$G_{yu} = \frac{n_{yu}}{d_{yu}} = \frac{n_{yf}\, n_a d_i}{d_{yf}\, d_a d_i + n_{yf}\, n_a n_i} . \tag{3.2}$$

The transfer function from the command input *u* to the force *f* applied to the structure is given by

$$G_{fu} = \frac{G_a}{1 + G_{yf} G_a H_i} . \tag{3.3}$$

From Eq. (3.3), it is clear that the dynamics of the transmission from *u* to *f* are not simply the actuator dynamics G_a, but contain dynamics due to the structure and the actuator. More insight can be gained by rewriting Eq. (3.3) in terms of the associated numerator and denominator polynomials, *i.e.*,

$$G_{fu} = \frac{n_{fu}}{d_{fu}} = \frac{d_{yf}\, n_a d_i}{d_{yf}\, d_a d_i + n_{yf}\, n_a n_i} . \tag{3.4}$$

Comparing Eqs. (3.2) and (3.4), notice that unless pole/zero cancellation occurs, the transfer functions G_{yu} and G_{fu} have the same poles, and that the poles of the structure (*i.e.*,

the poles of G_{yf}) are zeros of G_{fu}. Cancellation is most unlikely, and therefore this possibility is disregarded in the remainder of the analysis. Because the poles of the structure are zeros of G_{fu}, actuators attached to lightly damped structures will have a greatly limited ability to apply forces at the structure's natural frequencies; and if the structure is undamped, the actuator will not be able to apply a force at its natural frequencies. Also note that poles of the structure do not appear as poles in G_{yu}, because they are cancelled by the zeros in G_{fu}. These results occur regardless of how fast the dynamics of the actuator are (including the case when G_a is a constant gain).

Before closing the section, consider the effect of neglecting the interaction between the control actuator and the structure. Using the definition of G_{fu} in Eq. (3.4), an alternative block diagram to that in Fig. 3.2 can be determined as shown in Fig. 3.3. Because the dynamics of an actuator, as given in G_a, may often be fast relative to the structure, one might argue that the block G_{fu} may be reasonably represented as a constant both in phase and magnitude. However, as discussed previously, neither the phase nor the magnitude of G_{fu} will be constant in general (see Eqs. (3.3) and (3.4)). Moreover, the phase and magnitude characteristics of G_{fu} will vary depending on the structure. Neglecting phase differences between the command input *u* and the resulting force *f*, *i.e.*, neglecting the CSI, will result in an apparent time delay associated in the literature with generation of the control forces.

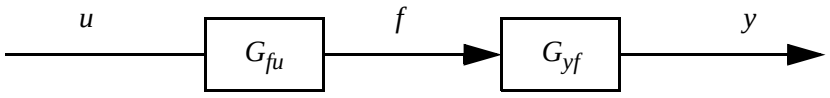

Figure 3.3 Equivalent Block Diagram Model of the Actuator/Structure.

The next section presents a simple model which shows that a feedback interaction path is always present in hydraulic actuators. Experimental verification of the model is also provided.

3.2 Hydraulic Actuator Modeling

In the case of hydraulically actuated systems, a feedback path exists between the velocity of the actuator and the command input to the actuator. From DeSilva (1989), the equations describing the fluid flow rate in an actuator can be linearized about the origin to obtain

$$\text{Valve: } q = k_q c - k_c \frac{f}{A}, \tag{3.5}$$

$$\text{Hydraulic Actuator: } q = A\dot{x} + \frac{V}{2\beta A}\dot{f}, \tag{3.6}$$

where q is the flow rate, c is the valve input, f is the force generated by the actuator, A is the cross-sectional area of the actuator, β is the bulk modulus of the fluid, V is the characteristic hydraulic fluid volume for the actuator, x is the actuator displacement, and k_q, k_c are system constants. Equating Eqs. (3.5) and (3.6) and rearranging yields

$$\dot{f} = \frac{2\beta}{V}(Ak_q c - k_c f - A^2 \dot{x}) \ , \tag{3.7}$$

which shows that the dynamics of the force applied by the actuator are dependent on the velocity response of the actuator, *i.e.*, the feedback interaction path is intrinsic to the dynamical response of a hydraulic actuator.

Figure 3.3 is a block diagram representation of the hydraulic actuator model given in Eq. (3.7) attached to a structure. Here, G_{xf} denotes the transfer function from the force generated by the actuator to the displacement of the point on the structure where the actuator is attached, and f_L is the external load on the structure. Notice the presence of the

"natural" velocity feedback in the open-loop system. Through this "natural" velocity feedback, the dynamics of the structure directly affect the characteristics of the control actuator.

The portion of the system in Fig. 3.3 identified as G_h has the following transfer function:

$$G_h = \frac{A}{\frac{V}{2\beta}s + k_c} = \frac{A/k_c}{\tau_h s + 1}, \tag{3.8}$$

where $\tau_h = V/2\beta k_c$ is the time constant of the actuator. Thus, the transfer function from the valve input *c* to the force *f* is given by

$$G_{fc} = \frac{k_q G_h}{1 + sAG_h G_{xf}}, \tag{3.9}$$

and the transfer function from the valve input *c* to the actuator displacement *x* is given by

$$G_{xc} = \frac{k_q G_h G_{xf}}{1 + sAG_h G_{xf}}. \tag{3.10}$$

Representing these transfer functions in terms of their respective numerator and denominator polynomials gives

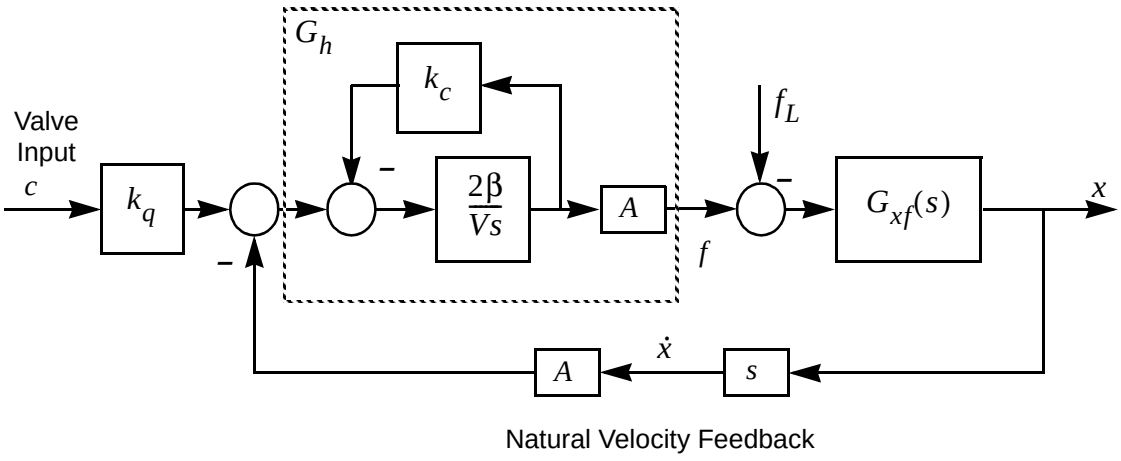

Figure 3.4 Block Diagram of Open-Loop Servovalve/Actuator Model.

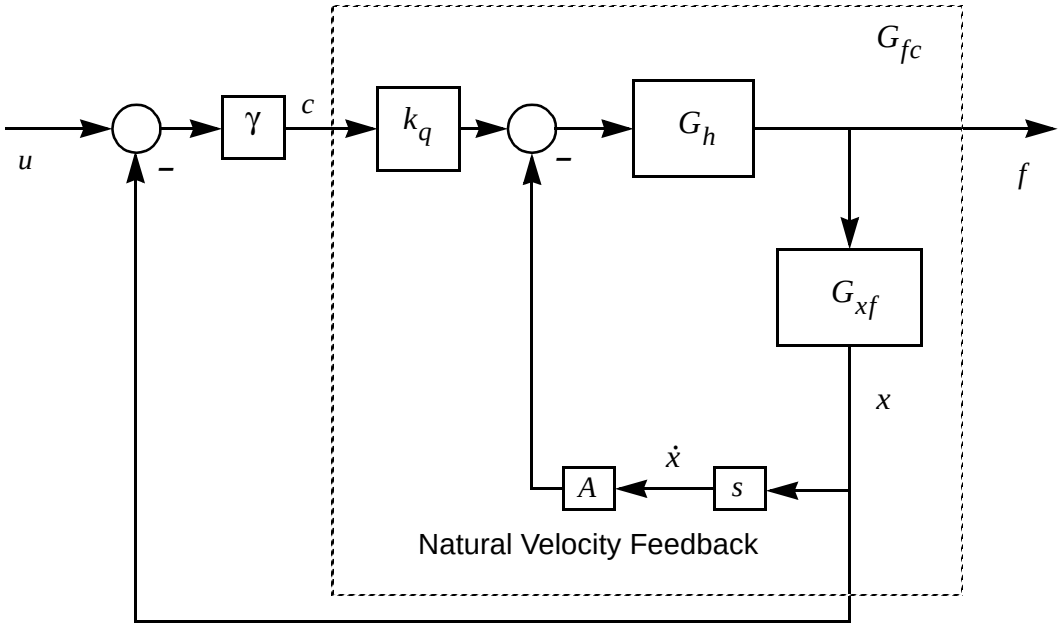

Figure 3.5 Block Diagram of Closed-Loop Servovalve/Actuator Model.

$$G_{fc} = \frac{n_{fc}}{d_{fc}} = \frac{k_q n_h d_{xf}}{d_h d_{xf} + sAn_h n_{xf}} , \tag{3.11}$$

$$G_{xc} = \frac{n_{xc}}{d_{xc}} = \frac{k_q n_h n_{xf}}{d_h d_{xf} + sAn_h n_{xf}} . \tag{3.12}$$

As discussed in the previous section, Eqs. (3.11) and (3.12) show that these two transfer functions have the same poles and that the poles of the structure (*i.e.*, the poles of G_{yf}) will be zeros of the transfer function from the input to the applied force.

Because the open-loop system identified in Fig. 3.3 is typically unstable, position, velocity and/or force feedback may be used to stabilize the system. Here, a unity-gain position feedback loop, *i.e.*, position control, is considered. Figure 3.5 is the block diagram for the hydraulic actuator with the position feedback included. This configuration is

representative of those found in active structural control systems (see, for example, Chung, *et al.*, 1988, 1989).

The transfer function from the command u to the actuator force f and to the displacement x for the system in Fig. 3.5, including the unity-gain position feedback loop, are given respectively by

$$G_{fu} = \frac{\gamma G_{fc}}{1 + \gamma G_{fc} G_{xf}} = \frac{\gamma k_q G_h}{1 + (\gamma k_q + sA) G_h G_{xf}} , \tag{3.13}$$

$$G_{xu} = \frac{\gamma G_{fc} G_{xf}}{1 + \gamma G_{fc} G_{xf}} = \frac{\gamma k_q G_h G_{xf}}{1 + (\gamma k_q + sA) G_h G_{xf}} , \tag{3.14}$$

where γ is the proportional feedback gain stabilizing the actuator. Rewriting the Eqs. (3.13) and (3.14) in terms of their numerator and denominator polynomials yields

$$G_{fu} = \frac{n_{fu}}{d_{fu}} = \frac{\gamma k_q n_h d_{xf}}{d_h d_{xf} + (\gamma k_q + sA) n_h n_{xf}} , \tag{3.15}$$

$$G_{xu} = \frac{n_{xu}}{d_{xu}} = \frac{\gamma k_q n_h n_{xf}}{d_h d_{xf} + (\gamma k_q + sA) n_h n_{xf}} . \tag{3.16}$$

Again, from Eqs. (3.15) and (3.16), the poles of the structure, G_{xf}, become zeros of the transfer function from the command u to the actuator force f, and are then cancelled in the transfer function from command to actuator position.

As an alternative to using position feedback to stabilize the hydraulic actuator, a velocity and/or force feedback loop can be added. Considering the general case in which a combination of all three measurements is used, the resulting transfer functions are

$$G_{fu} = \frac{\gamma k_q G_h}{1 + sAG_h G_{xf} + \delta \gamma k_q G_h + (\alpha + \eta s) \gamma k_q G_h G_{xf}} , \tag{3.17}$$

$$G_{xu} = \frac{\gamma k_q G_h G_{xf}}{1 + sAG_h G_{xf} + \delta \gamma k_q G_h + (\alpha + \eta s) \gamma k_q G_h G_{xf}} , \tag{3.18}$$

where α is the position feedback gain, η is the velocity feedback gain, and δ is the force feedback gain. These transfer functions can be written in terms of their respective numerator and denominator polynomials as

$$G_{fu} = \frac{n_{fu}}{d_{fu}} = \frac{\gamma k_q n_h d_{xf}}{d_h d_{xf} + sAn_h n_{xf} + \delta\gamma k_q n_h d_{xf} + (\alpha + \eta s)\gamma k_q G_h G_{xf}} \quad , \tag{3.19}$$

$$G_{xu} = \frac{n_{xu}}{d_{xu}} = \frac{\gamma k_q n_h n_{xf}}{d_h d_{xf} + sAn_h n_{xf} + \delta\gamma k_q n_h d_{xf} + (\alpha + \eta s)\gamma k_q G_h G_{xf}} \quad . \tag{3.20}$$

Similarly to the case of position control, the poles of G_{fu} are those of the overall transfer function G_{xu}, and the poles of the structure (*i.e.*, the poles of G_{xf}) are the zeros of the transfer function from the actuator command *u* to the applied actuator force *f*.

Experimental Verification

To demonstrate the validity of this model of a hydraulic actuator, the above results were compared to experimental data obtained at the Earthquake Engineering/Structural Dynamics and Control Laboratory at the University of Notre Dame. A scale model of the prototype building discussed in Chung, *et al.* (1988, 1989) was the test structure, shown in Fig. 3.6. The total mass of the floors of the model is 228 kg (500 lb), distributed evenly between the three levels, and the structure is 157.5 cm (62 in.) tall. The time scale was decreased by a factor of five, making the natural frequency of the structure five times that of the prototype. Cross-braces can be attached to the top two floors, causing the structure to respond primarily as a SDOF structure (see Fig. 3.6). This test structure and experimental setup is described further in Chapter 4. A hydraulic control actuator with a ±5.08 cm (±2 in.) stroke was placed at the first floor of the building and attached to the seismic simulator table via a rigid frame. For this system, the actuator displacement is approximately equivalent to the displacement of the first floor. Thus, a position sensor was employed to measure the displacement of the first floor and to provide feedback for the control actua-

tor. The force transmitted to the building by the control actuator was measured with a piezoelectric force ring manufactured by PCB Piezotronics, Inc.

Experimental transfer functions were found for the test structure and actuator using the Tektronix 2630 spectrum analyzer. Figure 3.7 shows the magnitude of the building and actuator transfer functions for the SDOF case (*i.e.,* with the cross-braces attached). The fundamental frequency of the structure in the SDOF configuration is 7 Hz. Examining the transfer function from the input command to the applied force, G_{fu}, it is clear that significant modeling error would be incurred if one took this transfer function to be constant (*i.e.*, neglected the actuator dynamics and the CSI). Notice that the zeros of G_{fu} coincide with the poles of the structure. Also, in the transfer function from the command input *u* to the actuator displacement *x*, G_{xu}, the poles and zeros cancel and a new complex pole pair

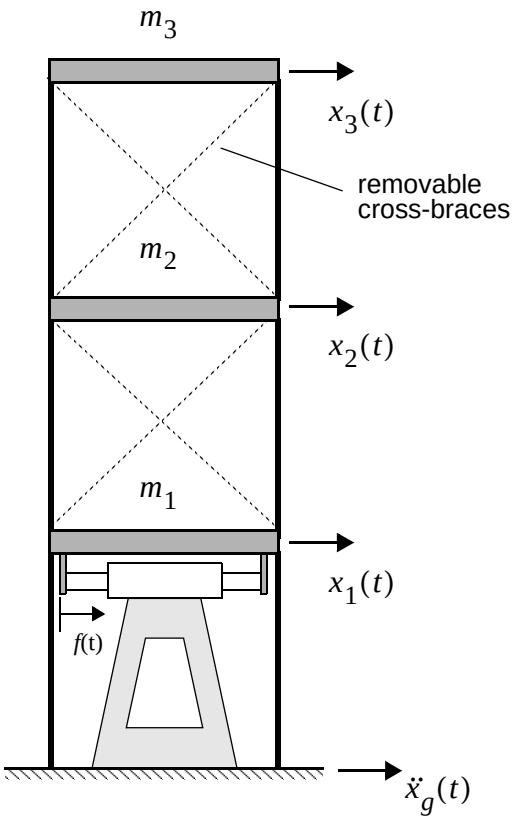

Figure 3.6 Three Degree-of-Freedom Structure with Active Bracing.

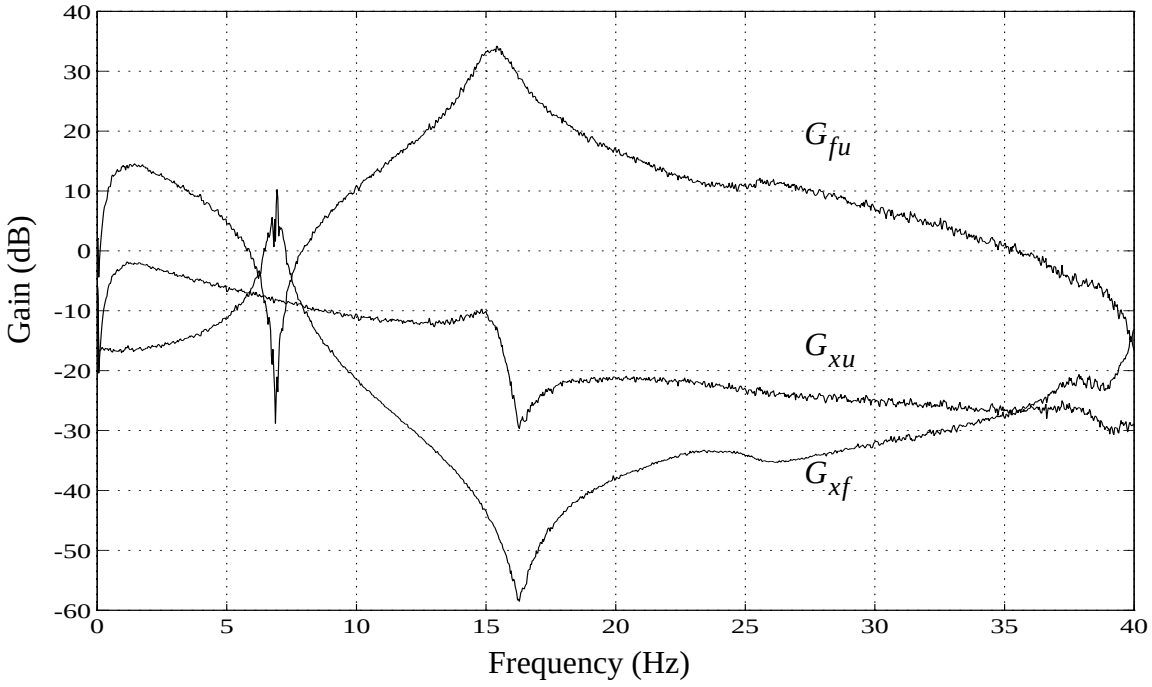

Figure 3.7 Magnitude of the Transfer Functions of the Structure, the Actuator, and the Combination for the SDOF Model.

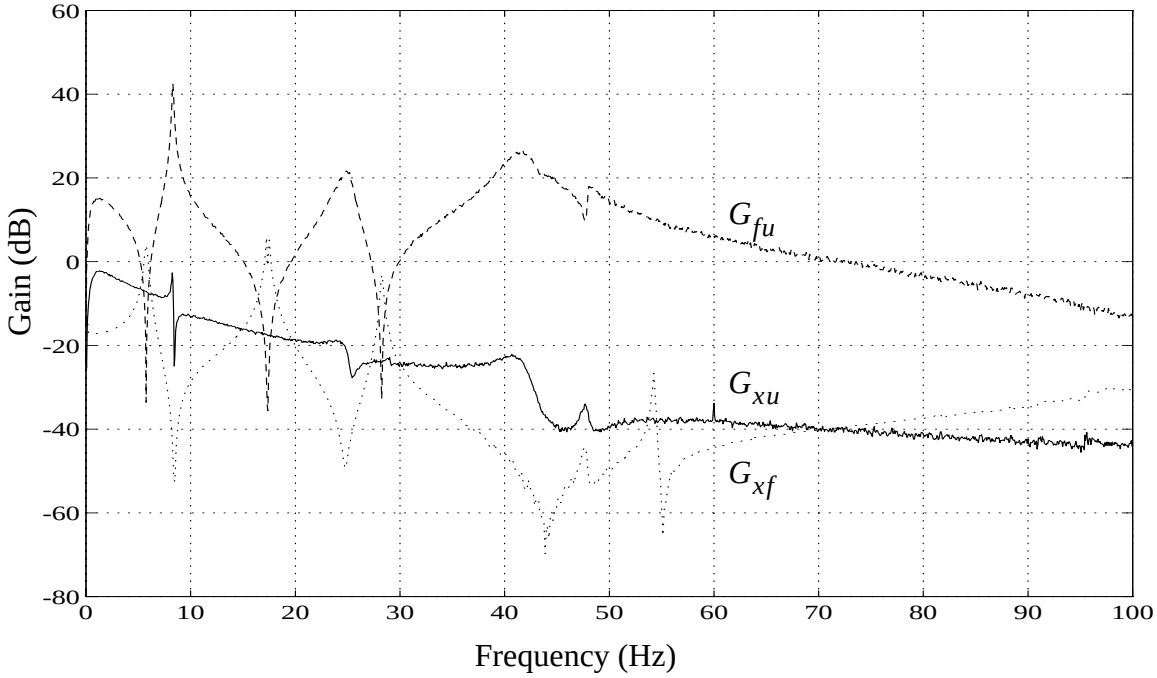

Figure 3.8 Magnitude of the Transfer Functions of the Structure, the Actuator, and the Combination for the MDOF Model.

appears at a higher frequency. This behavior is exactly what is predicted by the model presented in this section.

Figure 3.7 shows the magnitude of the building and actuator transfer functions when the braces are removed and the model is in the three degree-of-freedom configuration. The actuator transfer function G_{fu} in this case is significantly different than it is with the SDOF structure. Notice, as in the SDOF case, that the poles of the structure are cancelled by the zeros of the actuator in the transfer function from the control input *u* to the structural displacement *x*, G_{xu}, and new poles appear at poles of the actuator transfer function.

To verify the actuator model, the transfer function G_h was determined from the experimental data in the SDOF case. The proportional feedback gain stabilizing the actuator, γ, was set at 2.5. This user-defined constant can be changed through adjustment of the potentiometer of the servo-valve amplifier. By using Eq. (3.9) and the experimental data for G_{xf} and G_{fc}, A/k_q was determined as a function of frequency. Although k_q is a nonlinear parameter dependent on the operating point and the response amplitude of the hydraulic actuator (DeSilva, 1989), it can reasonably be assumed constant over the operating and frequency range of interest. The value of A/k_q which best fits the experimental data below 40 Hz was determined to be 0.15. Knowing A/k_q, ratios of the various parameters in Eq. (3.8) were determined to fit G_{fc}. The values of the ratios which define $k_q G_h$ are $k_q A/k_c = 25$ and $V/2\beta k_c = 0.015$, which determine the actuator transfer function as

$$k_q G_h = \frac{25}{0.015s + 1}. \tag{3.21}$$

Here, the value of the proportional feedback stabilizing the actuator, γ, was determined to be 2.5. Substituting Eq. (3.21) into Eq. (3.9) and using the experimentally obtained transfer function for G_{xf}, the transfer function G_{fc} can be obtained. A comparison between

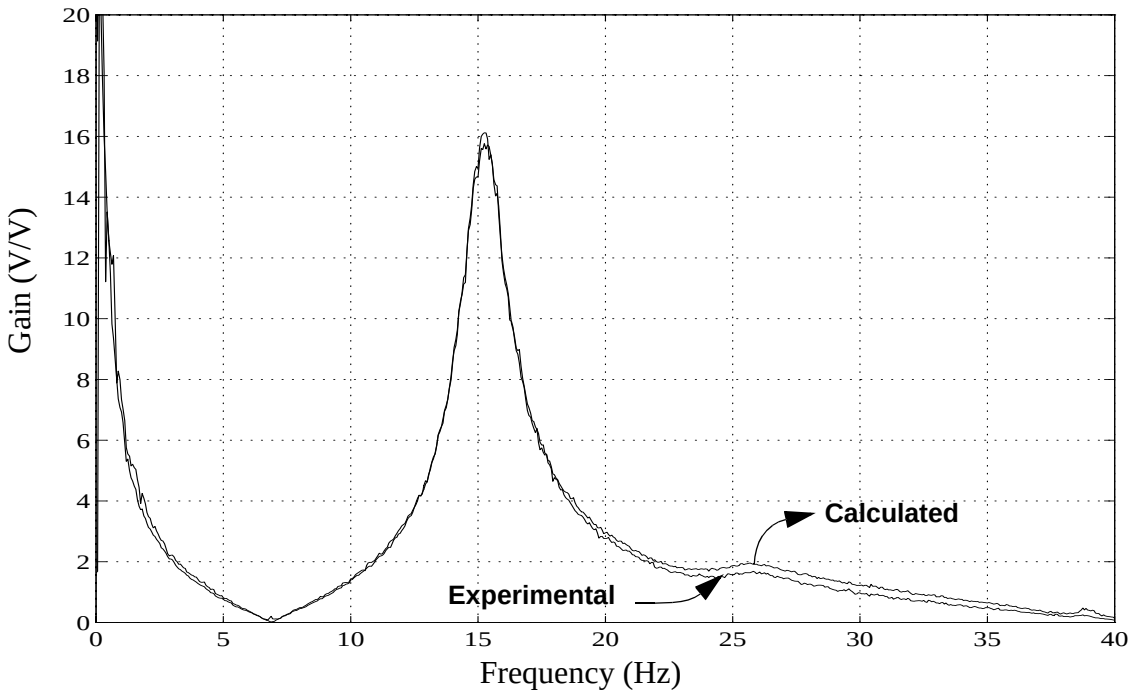

Figure 3.9 Experimental and Calculated Transfer Functions G_{fc} for SDOF Model.

these results and those obtained directly from the experimental data is given in Fig. 3.9. Notice the excellent agreement between the experimental and calculated results.

Note that the comparison of the analytical and experimental transfer functions in Fig. 3.9 is in units of Volts/Volts. Using the appropriate conversion factors for the various sensors employed, the transfer function in Eq. (3.21) can be determined as

$$k_q G_h = \frac{12500}{0.015s + 1} lb/V. \tag{3.22}$$

Because of the excellent agreement between the model and the experiment, the model of the hydraulic actuator in Eq. (3.7) is concluded to be valid.

3.3 Illustrative Numerical Examples

This section provides examples that demonstrate the importance of accounting for the interaction between the control actuator and the structure in protective system design. An active bracing, active tendon and active mass driver system are considered. Several controllers are designed for each of the example systems. Three control models are employed in the design of the various controllers. The first model, designated Model 1, uses the full equations of motion. In the second model the fluid in the hydraulic actuator was assumed to be incompressible (*i.e.*, $\dot{f} = 0$ in equation Eq. (3.7)). In this pseudo static model, designated Model 2, the hydraulic stiffness and damping terms are still included. In most studies of the control of civil engineering structures, G_{fu} is considered to be constant in magnitude and phase. This assumption is employed for the third model considered (Model 3). In each example, the value of K_0, the constant magnitude of G_{fu} used for control design, was found by determining the DC value of G_{fu} for the complete model which considers actuator dynamics and CSI (Model 1). Controllers were designed based on each of these models.

Several performance objectives were also considered. The objective for the type A controller was to minimize the relative displacements of each floor by equally weighting the relative displacement measurements in the performance function. For the type B controller, the performance objective was to minimize the absolute accelerations of each floor by equally weighting the respective absolute acceleration measurements. The identifications and descriptions for the various controllers are given in Table 3.1.

Because the measured output vector **y** is not the full state vector, the controllers are observer based and are designed using H_2/Linear Quadratic Gaussian (LQG) design methods (Spencer, *et. al.*, 1991, 1994; Suhardjo, *et. al.* 1992; Suhardjo, 1990). Both low authority (Case 1) and high authority (Case 2) controllers were considered. To allow for

direct comparison of each type of controller, the respective weightings on the displacements and accelerations are determined such that, when the ground acceleration is taken to be a given broadband excitation, the *rms* control force for each case has the same magnitude. The *rms* responses are determined through solution of the associated Lyapunov equation (Soong and Grigoriu, 1992). For all control studies, the model for which the responses are calculated is Model 1, incorporating both actuator dynamics and CSI.

Table 3.1 Controller Design Descriptions.

Model used for Controller Design	Displacement Weighting (Type A)	Acceleration Weighting (Type B)
Including CSI (Model 1)	1A	1B
Neglecting compressibility (Model 2)	2A	2B
Constant G_{fu} (Model 3)	3A	3B

Example 1: Active Bracing

Consider the three-story, single-bay building subjected to a one-dimensional earthquake excitation $\ddot{x}_g$ with active bracing as depicted in Fig. 3.6. The equations of motion are

$$\begin{bmatrix} m_1 & 0 & 0 \\ 0 & m_2 & 0 \\ 0 & 0 & m_3 \end{bmatrix} \begin{Bmatrix} \ddot{x}_1 \\ \ddot{x}_2 \\ \ddot{x}_3 \end{Bmatrix} + \begin{bmatrix} c_{11} & c_{12} & c_{13} \\ c_{12} & c_{22} & c_{23} \\ c_{13} & c_{23} & c_{33} \end{bmatrix} \begin{Bmatrix} \dot{x}_1 \\ \dot{x}_2 \\ \dot{x}_3 \end{Bmatrix} + \begin{bmatrix} k_{11} & k_{12} & k_{13} \\ k_{12} & k_{22} & k_{23} \\ k_{13} & k_{23} & k_{33} \end{bmatrix} \begin{Bmatrix} x_1 \\ x_2 \\ x_3 \end{Bmatrix}$$

$$= \begin{Bmatrix} 1 \\ 0 \\ 0 \end{Bmatrix} f - \begin{bmatrix} m_1 & 0 & 0 \\ 0 & m_2 & 0 \\ 0 & 0 & m_3 \end{bmatrix} \begin{Bmatrix} 1 \\ 1 \\ 1 \end{Bmatrix} \ddot{x}_g, \quad (3.23)$$

where x_i and m_i are the displacement relative to the ground and the mass of the *i*th floor of the building, c_{ij} and k_{ij} are the damping and stiffness coefficients, respectively, and f is the control force applied by the hydraulic actuator. Strictly speaking, m_1 includes the

weight of the actuator rod and piston. However, this additional mass is usually negligible in comparison with the first floor mass. Equation (3.23) can be written in matrix form as

$$\mathbf{M}_s\ddot{\mathbf{x}} + \mathbf{C}_s\dot{\mathbf{x}} + \mathbf{K}_s\mathbf{x} = \mathbf{B}_s f - \mathbf{M}_s\mathbf{G}_s\ddot{x}_g \,. \tag{3.24}$$

Incorporating unity gain displacement feedback into the hydraulic actuator model given in Eq. (3.7) yields

$$\dot{f} = \frac{2\beta}{V}(Ak_q\gamma(u - x_1) - k_c f - A^2\dot{x}_1) \quad , \tag{3.25}$$

where u is the control command. Defining the state vector of the system as $\mathbf{z}_1 = [\mathbf{x}' \;\; \dot{\mathbf{x}}' \;\; f]'$, the state equation is

$$\dot{\mathbf{z}}_1 = \begin{bmatrix} \mathbf{0} & \mathbf{I} & \mathbf{0} \\ -\mathbf{M}_s^{-1}\mathbf{K}_s & -\mathbf{M}_s^{-1}\mathbf{C}_s & \mathbf{M}_s^{-1}\mathbf{B}_s \\ -\dfrac{2\beta Ak_q\gamma}{V} \;\; 0 \;\; 0 & -\dfrac{2\beta A^2}{V} \;\; 0 \;\; 0 & -\dfrac{2\beta k_c}{V} \end{bmatrix}\mathbf{z}_1 + \begin{bmatrix} \mathbf{0} \\ \mathbf{0} \\ \dfrac{2\beta Ak_q\gamma}{V} \end{bmatrix} u + \begin{bmatrix} \mathbf{0} \\ -\mathbf{G}_s \\ 0 \end{bmatrix}\ddot{x}_g$$

$$= \mathbf{A}\mathbf{z}_1 + \mathbf{B}u + \mathbf{E}\ddot{x}_g \,. \tag{3.26}$$

Assuming that the actuator displacement (*i.e.*, the relative displacement of the first floor) x_1, the absolute accelerations of each floor, $\ddot{x}_{1a}, \ddot{x}_{2a}$ and $\ddot{x}_{3a}$, and the applied control force, *f*, are measured, the measurement equation is

$$\mathbf{y} = \begin{bmatrix} x_1 \\ \ddot{x}_{1a} \\ \ddot{x}_{2a} \\ \ddot{x}_{3a} \\ f \end{bmatrix} = \begin{bmatrix} 1 \;\; 0 \;\; 0 & 0 \;\; 0 \;\; 0 & 0 \\ -\mathbf{M}_s^{-1}\mathbf{K}_s & -\mathbf{M}_s^{-1}\mathbf{C}_s & \mathbf{M}_s^{-1}\mathbf{B}_s \\ 0 \;\; 0 \;\; 0 & 0 \;\; 0 \;\; 0 & 1 \end{bmatrix}\mathbf{z}_1 + \begin{bmatrix} v_1 \\ v_2 \\ v_3 \\ v_4 \\ v_5 \end{bmatrix}.$$

$$= \mathbf{C}\mathbf{z}_1 + \mathbf{v} \tag{3.27}$$

The vector **v** contains the noises in each measurement. The model given in Eqs. (3.26) and (3.27) (Model 1) includes actuator dynamics and CSI.

Model 2 for this example is found by setting $f = 0$ in Eq. (3.25). The resulting algebraic relation for the force is then given by

$$f = \frac{A\gamma k_q}{k_c}u - \frac{A\gamma k_q}{k_c}x_1 - \frac{A^2}{k_c}\dot{x}_1 \ . \tag{3.28}$$

Using the state vector $\mathbf{z}_2 = [\mathbf{x}' \ \ \dot{\mathbf{x}}']'$, the state equation reduces to

$$\dot{\mathbf{z}}_2 = \left(\begin{bmatrix} \mathbf{0} & \mathbf{I} \\ -\mathbf{M}_s^{-1}\mathbf{K}_s & -\mathbf{M}_s^{-1}\mathbf{C}_s \end{bmatrix} + \begin{bmatrix} \mathbf{0} & \mathbf{0} \\ \dfrac{-Ak_q\gamma}{m_1k_c} \ 0 \ 0 & \dfrac{-A^2}{m_1k_c} \ 0 \ 0 \\ 0 \ 0 \ 0 & 0 \ 0 \ 0 \\ 0 \ 0 \ 0 & 0 \ 0 \ 0 \end{bmatrix} \right) \mathbf{z}_2 + \begin{bmatrix} \mathbf{0} \\ \dfrac{-A\gamma k_q}{k_c}\mathbf{M}_s^{-1}\mathbf{B}_s \end{bmatrix} u + \begin{bmatrix} \mathbf{0} \\ -\mathbf{G}_s \end{bmatrix} \ddot{x}_g \, . \tag{3.29}$$

Using the same measured outputs as above, the measurement equation can be written

$$\mathbf{y} = \left(\begin{bmatrix} 1 \ 0 \ 0 & 0 \ 0 \ 0 \\ -\mathbf{M}_s^{-1}\mathbf{K}_s & -\mathbf{M}_s^{-1}\mathbf{C}_s \\ \dfrac{-Ak_q\gamma}{k_c} \ 0 \ 0 & \dfrac{-A^2}{k_c} \ 0 \ 0 \end{bmatrix} + \begin{bmatrix} 0 \ 0 \ 0 & 0 \ 0 \ 0 \\ \dfrac{-Ak_q\gamma}{m_1k_c} \ 0 \ 0 & \dfrac{-A^2}{m_1k_c} \ 0 \ 0 \\ 0 \ 0 \ 0 & 0 \ 0 \ 0 \\ 0 \ 0 \ 0 & 0 \ 0 \ 0 \\ 0 \ 0 \ 0 & 0 \ 0 \ 0 \end{bmatrix} \right) \mathbf{z}_2 + \begin{bmatrix} \mathbf{0} \\ \dfrac{-A\gamma k_q}{k_c}\mathbf{M}_s^{-1}\mathbf{B}_s \\ \dfrac{Ak_q\gamma}{k_c} \end{bmatrix} u + \mathbf{v} \, . \tag{3.30}$$

Model 3 considers G_{fu} to be constant in magnitude and phase. The constant gain, K_0 is determined from the complete model given in Eqs. (3.26) and (3.27). Using the state

vector $\mathbf{z}_3 = [\mathbf{x}' \ \dot{\mathbf{x}}']'$ and the same measurements as above, the state-space representation reduces to

$$\dot{\mathbf{z}}_3 = \begin{bmatrix} \mathbf{0} & \mathbf{I} \\ -\mathbf{M}_s^{-1}\mathbf{K}_s & -\mathbf{M}_s^{-1}\mathbf{C}_s \end{bmatrix} \mathbf{z}_3 + \begin{bmatrix} \mathbf{0} \\ \mathbf{M}_s^{-1}\mathbf{B}_s \end{bmatrix} K_0 u + \begin{bmatrix} \mathbf{0} \\ -\mathbf{G}_s \end{bmatrix} \ddot{x}_g , \tag{3.31}$$

$$\mathbf{y} = \begin{bmatrix} 1 & 0 & 0 & 0 & 0 & 0 \\ -\mathbf{M}_s^{-1}\mathbf{K}_s & & & -\mathbf{M}_s^{-1}\mathbf{C}_s & & \\ 0 & 0 & 0 & 0 & 0 & 0 \end{bmatrix} \mathbf{z}_3 + \begin{bmatrix} 0 \\ \mathbf{M}_s^{-1}\mathbf{B}_s \\ 1 \end{bmatrix} K_0 u + \mathbf{v} . \tag{3.32}$$

The structural parameters for the three degree-of-freedom model reported in Chung, *et. al.* (1989) were employed in this example with an active bracing system. The parameters associated with the control actuator were chosen to correspond to the model presented previously. Here, the ground acceleration was modeled as a broadband disturbance with a constant two-sided spectral density of magnitude $S_0 = 1.53$ cm^2/s^3 (2.37×10^{-1}in^2/s^3). The structural responses to this disturbance are shown in Table 3.2 for the type A controllers (*i.e.*, weighting the displacements of the structure) and in Table 3.3 for type B controllers (*i.e.*, weighting the accelerations of the structure). Here, the uncontrolled configuration has the active bracing system completely removed from the structure. The zeroed controller corresponds to the case in which the active bracing system is attached, but the input command signal is set equal to zero. This configuration is included because it has been used as a basis for comparison in previously reported control studies.

Examining the zeroed control case, one observes that the stiffness of the structure increases (as compared to the uncontrolled case), thus causing the first floor displacement to decrease. Notice that if the relative displacements are weighted (Table 3.2), the controller which includes actuator dynamics and CSI produces noticeably better results than either of the other two controllers. For the high authority controller (Case 2), the closed-

loop system created with Controller 3A becomes unstable before the chosen force level is reached.

When absolute accelerations are weighted, the responses using Controller 1B (*i.e.*, including actuator dynamics and CSI, and designed based on Model 1) and Controller 2B (*i.e.*, designed based on Model 2 which considers the fluid to be incompressible) are very close for both the low and high authority cases (Table 3.3). These results are considerably better than those corresponding to Controller 3B (*i.e.*, neglecting the actuator dynamics and CSI).

Table 3.2 Comparison of *RMS* Responses for Active Bracing System with Weighting on the Relative Displacements.

Configuration	σ_{x_1} (cm)	σ_{x_2} (cm)	σ_{x_3} (cm)	$\sigma_{\ddot{x}_{a1}}$ (cm/s^2)	$\sigma_{\ddot{x}_{a2}}$ (cm/s^2)	$\sigma_{\ddot{x}_{a3}}$ (cm/s^2)	σ_f (N)
(a) nominal configurations							
Uncontrolled	3.478e-1	7.087e-1	9.058e-1	249.6	199.1	243.2	—
Zeroed control	3.104e-2	2.720e-1	4.234e-1	159.6	138.0	152.7	2668
(b) Case 1: low authority controller							
Controller 1A	5.077e-2	1.135e-1	1.783e-1	269.7	126.8	101.5	2687
Controller 2A	4.140e-2	1.400e-1	2.183e-1	268.2	143.3	114.2	2687
Controller 3A	2.982e-2	2.677e-1	4.178e-1	164.5	137.7	151.7	2687
(c) Case 2: high authority controller							
Controller 1A	6.528e-2	8.669e-2	1.456e-1	415.0	141.3	109.0	3802
Controller 2A	5.169e-2	1.217e-1	1.924e-1	431.8	159.3	118.2	3802
Controller 3A	—	—	—	—	—	—	—

Table 3.3 Comparison of *RMS* Responses for Active Bracing System with Weighting on the Absolute Accelerations.

Configuration	σ_{x_1} (cm)	σ_{x_2} (cm)	σ_{x_3} (cm)	$\sigma_{\ddot{x}_{a1}}$ (cm/s^2)	$\sigma_{\ddot{x}_{a2}}$ (cm/s^2)	$\sigma_{\ddot{x}_{a3}}$ (cm/s^2)	σ_f (N)
(a) nominal configurations							
Uncontrolled	3.478e-1	7.087e-1	9.058e-1	249.6	199.1	243.2	—
Zeroed control	3.104e-2	2.720e-1	4.234e-1	159.6	138.0	152.7	2668
(b) Case 1: low authority controller							
Controller 1B	2.560e-1	3.462e-1	3.746e-1	212.6	33.86	41.33	2687
Controller 2B	2.550e-1	3.439e-1	3.716e-1	39.22	33.63	40.79	2687
Controller 3B	1.442e-1	2.437e-1	3.256e-1	141.2	105.3	108.6	2687
(c) Case 2: high authority controller							
Controller 1B	3.416e-1	4.366e-1	4.567e-1	32.46	30.20	35.43	3802
Controller 2B	3.404e-1	4.364e-1	2.562e-1	34.47	29.97	34.95	3802
Controller 3B	2.568e-1	3.426e-1	3.988e-1	138.2	103.7	106.5	3802

One should point out that the systems employing controllers designed based on Model 2 or Model 3 can quickly become unstable if one tries to reduce the *rms* responses through increasing the weighting on the relative displacements or the absolute accelerations in the performance function. However, by accounting for the actuator dynamics/CSI a significantly more authoritative control design (*i.e.*, higher performance) can be achieved without such an instability occurring.

The results given in Tables 3.2 and 3.3 indicate that, for a given level of *rms* control action, the ability of the controller to reduce the relative displacements of the structure is greatest when the relative displacements of the structure are weighted in the control performance function. Similarly, these tables indicate that the absolute accelerations of the structure are most efficiently reduced when the absolute accelerations of the structure are weighted.

Example 2: Active Tendon System

Consider the single story structure subjected to a one-dimensional earthquake excitation $\ddot{x}_g$ with an active tendon system as shown in Fig. 3.10. In this system a tendon/pulley system is used to transmit the force generated by the hydraulic actuator to the first floor of the structure. A stiff frame is included to connect the actuator to the four pretensioned tendons. The linearized equations of motion are

$$m\ddot{x} + (c + c_0 cos^2\theta)\dot{x} + (k + k_0 cos^2\theta)x + c_0(cos\theta)\dot{a} + k_0(cos\theta)a = -m\ddot{x}_g \qquad (3.33)$$

$$_0\ddot{a} + c_0\dot{a} + k_0 a + c_0 cos\theta\dot{x} + k_0 cos\theta x = -m_0\ddot{x}_g + \qquad (3.34)$$

where m is the mass of the building, m_o is the combined mass of the stiff frame and the actuator rod/piston, c and k are the damping and stiffness coefficients of the structure, respectively, c_o and k_o are the total damping and stiffness of the four tendons, x is the displacement of the building relative to the ground, a is the displacement of the actuator, and f is the force applied by the hydraulic actuator to the rigid frame. In Fig. 3.10, the force designated f_o is the force in the tendons.

Under unity gain feedback of the actuator position, the dynamics of the hydraulic system can be written as

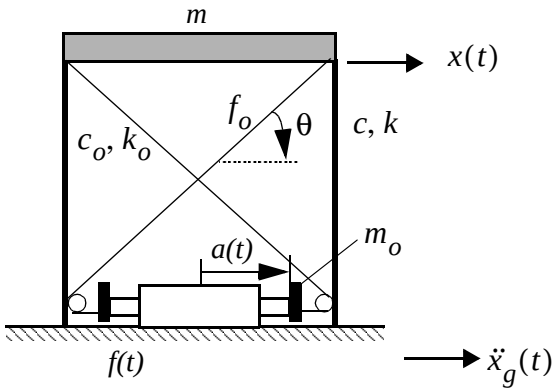

Figure 3.10 Single Story Building with Active Tendon System.

$$\dot{f} = \frac{2\beta}{V}(Ak_q\gamma(u-a) - k_c f - A^2\dot{a}) \ . \tag{3.35}$$

Defining the state vector of the system as $\mathbf{z}_1 = [a \ \ \dot{a} \ \ x \ \ \dot{x} \ \ f]'$, the state equation is

$$\dot{\mathbf{z}}_1 = \begin{bmatrix} 0 & 1 & 0 & 0 & 0 \\ -\frac{k_0}{m_0} & -\frac{c_0}{m_0} & -\frac{k_0\cos\theta}{m_0} & -\frac{c_0\cos\theta}{m_0} & \frac{1}{m_0} \\ 0 & 0 & 0 & 1 & 0 \\ -\frac{k_0\cos\theta}{m} & -\frac{c_0\cos\theta}{m} & -\frac{k_0\cos^2\theta + k}{m} & -\frac{c_0\cos^2\theta + c}{m} & 0 \\ -\frac{2\beta}{V}Ak_q\gamma & -\frac{2\beta}{V}A^2 & 0 & 0 & -\frac{2\beta}{V}k_c \end{bmatrix} \mathbf{z}_1 + \begin{bmatrix} 0 \\ 0 \\ 0 \\ 0 \\ \frac{2\beta}{V}Ak_q\gamma \end{bmatrix} u + \begin{bmatrix} 0 \\ -1 \\ 0 \\ -1 \\ 0 \end{bmatrix} \ddot{x}_g \ . \tag{3.36}$$

The measurements are chosen to include the displacement of the actuator and the absolute acceleration of the building, *i.e.*, $\mathbf{y} = [a \ \ \ddot{x}_a]'$. The measurement equation is thus

$$\mathbf{y} = \begin{bmatrix} 1 & 0 & 0 & 0 & 0 \\ -\frac{k_0\cos\theta}{m} & -\frac{c_0\cos\theta}{m} & -\frac{k_0\cos^2\theta + k}{m} & -\frac{c_0\cos^2\theta + c}{m} & 0 \end{bmatrix} \mathbf{z}_1 + \mathbf{v} \tag{3.37}$$

where the vector **v** contains the noises in each measurement. The model in Eqs. (3.36) and (3.37) includes actuator dynamics and CSI and is designated Model 1.

Model 2 is found by setting $\dot{f} = 0$ in Eq. (3.35). Using this approach will result in a controller that is equivalent to that used in Reinhorn, *et. al.* (1989a). The resulting algebraic relation for the force is then given by

$$f = \frac{Ak_q\gamma}{k_c}(u-a) - \frac{A^2}{k_c}\dot{a} \ . \tag{3.38}$$

Using the state vector $\mathbf{z}_2 = [a \ \ \dot{a} \ \ x \ \ \dot{x}]'$ and the same measured outputs as above, the state-space representation of Model 2 is

$$\dot{\mathbf{z}}_2 = \begin{bmatrix} 0 & 1 & 0 & 0 \\ -\left(\frac{k_0}{m_0} + \frac{Ak_q\gamma}{m_0k_c}\right) & -\left(\frac{c_0}{m_0} + \frac{A^2}{m_0k_c}\right) & -\frac{k_0\cos\theta}{m_0} & -\frac{c_0\cos\theta}{m_0} \\ 0 & 0 & 0 & 1 \\ -\frac{k_0\cos\theta}{m} & -\frac{c_0\cos\theta}{m} & -\frac{k_0\cos^2\theta + k}{m} & -\frac{c_0\cos^2\theta + c}{m} \end{bmatrix} \mathbf{z}_2 + \begin{bmatrix} 0 \\ \frac{Ak_q\gamma}{m_0k_c} \\ 0 \\ 0 \end{bmatrix} u + \begin{bmatrix} 0 \\ -1 \\ 0 \\ -1 \end{bmatrix} \ddot{x}_g, \tag{3.39}$$

$$\mathbf{y} = \begin{bmatrix} 1 & 0 & 0 & 0 \\ -\frac{k_0\cos\theta}{m} & -\frac{c_0\cos\theta}{m} & -\frac{k_0\cos^2\theta + k}{m} & -\frac{c_0\cos^2\theta + c}{m} \end{bmatrix} \mathbf{z}_2 + \mathbf{v} \tag{3.40}$$

Model 3 is found by assuming the transfer function G_{fu} is constant in magnitude and has zero phase. Using the state vector $\mathbf{z}_3 = [a \ \ \dot{a} \ \ x \ \ \dot{x}]'$ and the same measurements as above, the state-space representation for Model 3 is determined as

$$\dot{\mathbf{z}}_3 = \begin{bmatrix} 0 & 1 & 0 & 0 \\ -\frac{k_0}{m_0} & -\frac{c_0}{m_0} & -\frac{k_0\cos\theta}{m_0} & -\frac{c_0\cos\theta}{m_0} \\ 0 & 0 & 0 & 1 \\ -\frac{k_0\cos\theta}{m} & -\frac{c_0\cos\theta}{m} & -\frac{k_0\cos^2\theta + k}{m} & -\frac{c_0\cos^2\theta + c}{m} \end{bmatrix} \mathbf{z}_3 + \begin{bmatrix} 0 \\ \frac{K_0}{m_0} \\ 0 \\ 0 \end{bmatrix} u + \begin{bmatrix} 0 \\ -1 \\ 0 \\ -1 \end{bmatrix} \ddot{x}_g \tag{3.41}$$

$$\mathbf{y} = \begin{bmatrix} 1 & 0 & 0 & 0 \\ -\frac{k_o \cos\theta}{m} & -\frac{c_o \cos\theta}{m} & -\frac{k_0 \cos^2\theta + k}{m} & -\frac{c_0 \cos^2\theta + c}{m} \end{bmatrix} \mathbf{z}_3 + \mathbf{v} \tag{3.42}$$

In this example, the structural parameters were chosen to correspond to the SDOF test structure described in Chung, *et. al*. (1988). Their values were: m = 2,924 kg (16.69 lb-s^2/in), c = 15.8 N · s/cm (9.025 lb-s/in), k = 13,895 N/m (7934 lb/in), θ = 36 degrees, k_o = 14,879 N/m [8496 lb/in (*i.e.*, 2124×4)], and c_o = 0. The mass of the frame, m_o, was chosen to be 0.417 lb-s^2/in. The ground acceleration was modeled as a broadband excitation with a constant two-sided spectral density of magnitude S_0 = 0.2568 cm^2/s^3 (3.98×10^{-2} in^2/s^3). In all cases, the response calculations were based on the model in Eqs. (3.36) and (3.37). Here, the uncontrolled configuration refers to the case in which the tendons are present, but are fixed to the ground. The zeroed configuration refers to the case in which the actuator is attached to the tendons, but the command signal of the control actuator is set equal to zero.

The response statistics are provided in Table 3.4 for the various type A controllers (displacement weighting) and in Table 3.5 for the various type B controllers (acceleration weighting). Notice that in the case of displacement weighting (Table 3.4), a stable controller for Model 2 cannot be designed at the force levels chosen. Also, application of both the low and high authority controllers designed using Model 3 (Controller 3A) has a detrimental effect on the displacement response of the system compared to the uncontrolled system.

All of the control designs which minimize the absolute acceleration produce a significant reduction in the acceleration as well as the displacement (see Table 3.5), except the controller which is based on Model 3 (Controller 3B). The low authority controller designed based on Model 3 (Controller 3B) has little effect of the acceleration response of

the structure compared to the uncontrolled case, and the high authority controller actually increases the acceleration response. At this force level, the control design based on Model 2 (Controller 2B) performs comparably to Controller 1B, but this controller becomes unstable if the weighting on the acceleration is increased above this value. As in the previous example, the displacements are most efficiently reduced when the displacements are weighted, and the accelerations are most efficiently reduced when the accelerations are weighted.

To better understand the effects of CSI and actuator dynamics in this example, the transfer function from the actuator command to the actuator displacement is provided in Fig. 3.11 for the active tendon system. Notice that a complex pole pair is present at approximately 90 Hz due to the stabilizing position feedback. Also, the poles of the uncontrolled structure (*i.e.*, with the actuator removed and the tendons attached to the ground) have become zeros of the actuator transfer function, G_{au}. The transfer functions from the actuator command to the actuator force, G_{fu}, and to the tendon force, $G_{f_o u}$, are shown in Fig. 3.12. Comparing these two transfer functions, it is evident that the two forces are not the same. Due to the presence of a complex zero pair in G_{fu}, the two transfer functions are significantly different in magnitude at high frequencies, and above approximately 23 Hz they are 180 degrees out of phase.

Example 3: Active Mass Driver

Consider the single story structure subjected to a one-dimensional earthquake excitation $\ddot{x}_g$ with an active mass driver as shown in Fig. 3.13. The equations of motion are

$$M\ddot{x}_1 + (c_1 + c_2)\dot{x}_1 - c_2\dot{x}_2 + (k_1 + k_2)x_1 - k_2x_2 = -f - M\ddot{x}_g \ , \tag{3.43}$$

$$m\ddot{x}_2 + c_2(\dot{x}_2 - \dot{x}_1) + k_2(x_2 - x_1) = f - m\ddot{x}_g \ , \tag{3.44}$$

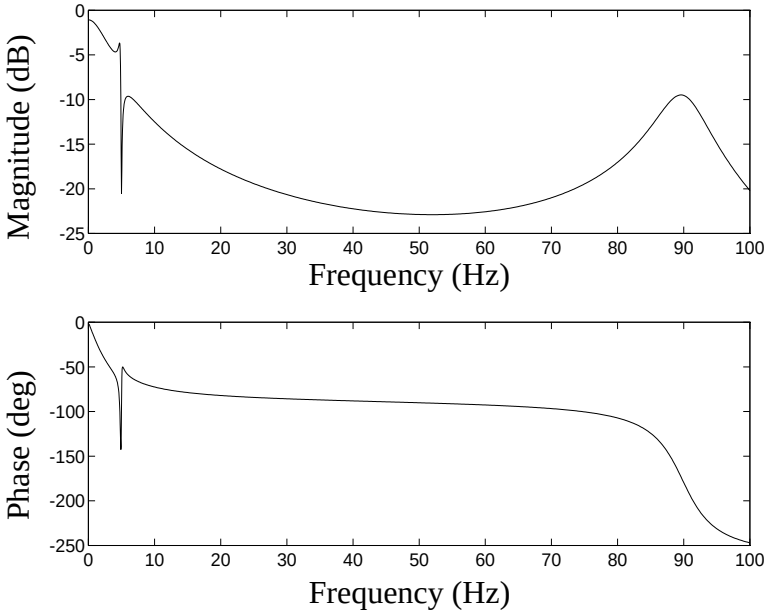

Figure 3.11 Transfer Function from Actuator Command to Actuator Displacement.

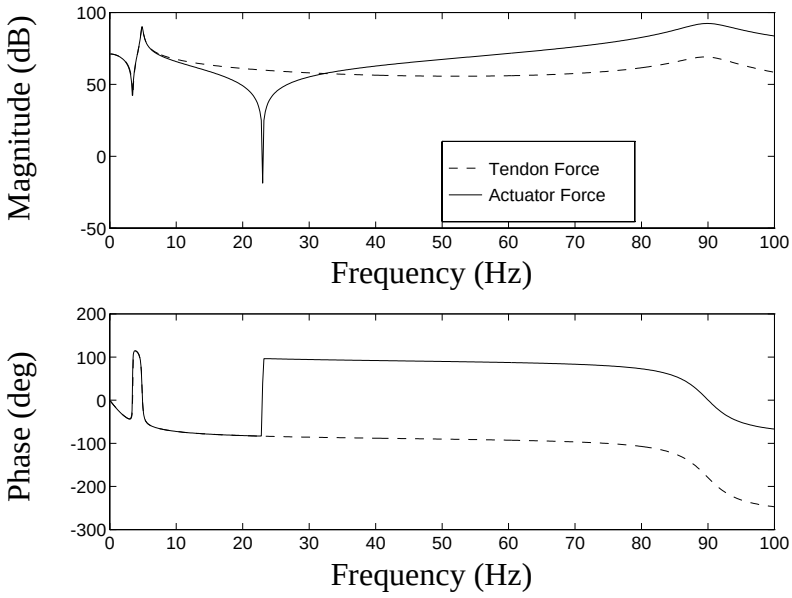

Figure 3.12 Transfer Functions from Actuator Command to Tendon Force and Actuator Force.

where *M* is the mass of the building, *m* is the mass of the AMD (including the mass of the actuator rod/piston), x_1 and x_2 are the displacement relative to the ground of the building

Table 3.4 Comparison of *RMS* Values of Controlled Responses for the Active Tendon System with Weighting on the Relative Displacement.

Configuration	σ_x (cm)	σ_a (cm)	$\sigma_{\ddot{x}_a}$ (cm/s^2)	σ_f (N)
Uncontrolled	4.295e-2	–	34.73	–
Zeroed Control	2.748e-2	3.065e-3	21.18	299.4
Case 1: Low Authority Controller				
Controller 1A	3.752e-3	2.457e-2	12.5	575.4
Controller 2A	3.692e-2	4.900e-2	21.74	575.4
Controller 3A	3.710e-2	9.324e-3	33.63	575.4
Case 2: High Authority Controller				
Controller 1A	2.744e-3	2.687e-2	12.7	1829
Controller 2A	–	–	–	–
Controller 3A	1.111e-1	3.484e-2	104.0	1829

and the moving mass, respectively, c_1 and k_1 are the damping and stiffness coefficients of the building, respectively, c_2 and k_2 are the damping and stiffness coefficients of the active mass driver system, respectively, and *f* is the control force applied by the hydraulic actuator.

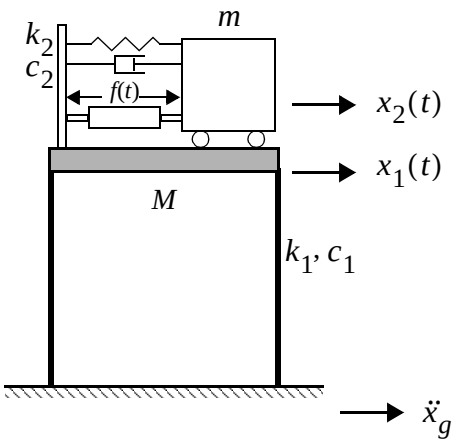

Figure 3.13 Single Story Building with Active Mass Driver.

Table 3.5 Comparison of *RMS* Values of Controlled Responses for the Active Tendon System with Weighting on the Absolute Acceleration.

Configuration	σ_x (cm)	σ_a (cm)	$\sigma_{\ddot{x}_a}$ (cm/s^2)	σ_f (N)
Uncontrolled	4.295e-2	–	34.73	–
Zeroed Control	2.748e-2	3.065e-3	21.18	299.4
Case 1: Low Authority Controller				
Controller 1B	3.748e-2	6.871e-2	3.686	575.4
Controller 2B	3.722e-2	6.845e-2	3.736	575.4
Controller 3B	3.043e-2	5.653e-2	14.84	575.4
Case 2: High Authority Controller				
Controller 1B	1.091e-1	2.111e-1	2.606	1829
Controller 2B	1.077e-1	2.086e-1	2.770	1829
Controller 3B	1.058e-1	2.061e-1	16.47	1829

From above, the equation governing the dynamics of the hydraulic system under unity-gain feedback of the actuator displacement (*i.e.*, $x_2 - x_1$) can be written as

$$\dot{f} = \frac{2\beta}{V}(Ak_q\gamma\{u-(x_2-x_1)\}-k_c f - A^2(\dot{x}_2-\dot{x}_1)) \quad . \tag{3.45}$$

Defining the state vector of the system as $\mathbf{z}_1 = [x_1 \;\; x_2 \;\; \dot{x}_1 \;\; \dot{x}_2 \;\; f]'$, the equations of motion can be written in matrix form as

$$\dot{\mathbf{z}}_1 = \begin{bmatrix} 0 & 0 & 1 & 0 & 0 \\ 0 & 0 & 0 & 1 & 0 \\ -\dfrac{(k_1+k_2)}{M} & \dfrac{k_2}{M} & -\dfrac{(c_1+c_2)}{M} & \dfrac{c_2}{M} & -\dfrac{1}{M} \\ \dfrac{k_2}{m} & -\dfrac{k_2}{m} & \dfrac{c_2}{m} & -\dfrac{c_2}{m} & \dfrac{1}{m} \\ \dfrac{2\beta A k_q \gamma}{V} & -\dfrac{2\beta A k_q \gamma}{V} & \dfrac{2\beta A^2}{V} & -\dfrac{2\beta A^2}{V} & -\dfrac{2\beta k_c}{V} \end{bmatrix} \mathbf{z}_1 + \begin{bmatrix} 0 \\ 0 \\ 0 \\ 0 \\ \dfrac{2\beta A k_q \gamma}{V} \end{bmatrix} u + \begin{bmatrix} 0 \\ 0 \\ -1 \\ -1 \\ 0 \end{bmatrix} \ddot{x}_g . \quad (3.46)$$

The measurements are chosen to include the displacement of the first floor mass relative to the ground, the displacement of the AMD relative to the first floor mass, the absolute accelerations of both masses, and the force applied by the actuator, *i.e.*, $\mathbf{y} = [x_1 \;\; (x_2 - x_1) \;\; \ddot{x}_{a1} \;\; \ddot{x}_{a2} \;\; f]'$. Thus, the measurement equation is

$$\mathbf{y} = \begin{bmatrix} 1 & 0 & 0 & 0 & 0 \\ -1 & 1 & 0 & 0 & 0 \\ -\dfrac{(k_1+k_2)}{M} & \dfrac{k_2}{M} & -\dfrac{(c_1+c_2)}{M} & \dfrac{c_2}{M} & -\dfrac{1}{M} \\ \dfrac{k_2}{m} & -\dfrac{k_2}{m} & \dfrac{c_2}{m} & -\dfrac{c_2}{m} & \dfrac{1}{m} \\ 0 & 0 & 0 & 0 & 1 \end{bmatrix} \mathbf{z}_1 + \begin{bmatrix} v_1 \\ v_2 \\ v_3 \\ v_4 \\ v_5 \end{bmatrix}, \quad (3.47)$$

where v_i is the noise in the ith measurement. This model of the AMD system accounts for both the dynamics of the actuator and CSI and is designated Model 1.

Model 2 is formed by setting $\dot{f} = 0$ in Eq. (3.45), resulting in the algebraic relation for the force given by

$$f = \frac{A\gamma k_q}{k_c}u - \frac{A\gamma k_q}{k_c}(x_2 - x_1) - \frac{A^2}{k_c}(\dot{x}_2 - \dot{x}_1) \quad . \tag{3.48}$$

Using the state vector $\mathbf{z}_2 = [x_1 \;\; x_2 \;\; \dot{x}_1 \;\; \dot{x}_2]'$ and the same measured outputs as above, the state-space representation of this model is

$$\dot{\mathbf{z}}_2 = \begin{bmatrix} 0 & 0 & 1 & 0 \\ 0 & 0 & 0 & 1 \\ -\dfrac{(k_1+k_2)+d_1}{M} & \dfrac{k_2+d_1}{M} & -\dfrac{(c_1+c_2)+d_2}{M} & \dfrac{c_2+d_2}{M} \\ \dfrac{k_2+d_1}{m} & -\dfrac{k_2+d_1}{m} & \dfrac{c_2+d_2}{m} & -\dfrac{c_2+d_2}{m} \end{bmatrix} \mathbf{z}_2 + \begin{bmatrix} 0 \\ 0 \\ \dfrac{-d_1}{M} \\ \dfrac{d_1}{m} \end{bmatrix} u + \begin{bmatrix} 0 \\ 0 \\ -1 \\ -1 \end{bmatrix} \ddot{x}_g \tag{3.49}$$

$$\mathbf{y} = \begin{bmatrix} 1 & 0 & 0 & 0 \\ -1 & 1 & 0 & 0 \\ -\dfrac{(k_1+k_2)+d_1}{M} & \dfrac{k_2+d_1}{M} & -\dfrac{(c_1+c_2)+d_2}{M} & \dfrac{c_2+d_2}{M} \\ \dfrac{k_2+d_1}{m} & -\dfrac{k_2+d_1}{m} & \dfrac{c_2+d_2}{m} & -\dfrac{c_2+d_2}{m} \\ d_1 & -d_1 & d_2 & -d_2 \end{bmatrix} \mathbf{z}_2 + \begin{bmatrix} 0 \\ 0 \\ \dfrac{-d_1}{M} \\ \dfrac{d_1}{m} \\ d_1 \end{bmatrix} u + \mathbf{v} \tag{3.50}$$

where $d_1 = A\gamma k_q / k_c$, and $d_2 = A^2 / k_c$.

Model 3 is formed by assuming G_{fu} has a constant magnitude and zero phase. Using the state vector $\mathbf{z}_3 = [x_1 \;\; x_2 \;\; \dot{x}_1 \;\; \dot{x}_2]'$ and the same measurements as above, the state-space representation for Model 3 is

$$\dot{\mathbf{z}}_3 = \begin{bmatrix} 0 & 0 & 1 & 0 \\ 0 & 0 & 0 & 1 \\ -\dfrac{(k_1+k_2)}{M} & \dfrac{k_2}{M} & -\dfrac{(c_1+c_2)}{M} & \dfrac{c_2}{M} \\ \dfrac{k_2}{m} & -\dfrac{k_2}{m} & \dfrac{c_2}{m} & -\dfrac{c_2}{m} \end{bmatrix} \mathbf{z}_3 + \begin{bmatrix} 0 \\ 0 \\ \dfrac{-1}{M} \\ \dfrac{1}{m} \end{bmatrix} K_0 u + \begin{bmatrix} 0 \\ 0 \\ -1 \\ -1 \end{bmatrix} \ddot{x}_g \tag{3.51}$$

$$\mathbf{y} = \begin{bmatrix} 1 & 0 & 0 & 0 \\ -1 & 1 & 0 & 0 \\ -\frac{(k_1 + k_2)}{M} & \frac{k_2}{M} & -\frac{(c_1 + c_2)}{M} & \frac{c_2}{M} \\ \frac{k_2}{m} & -\frac{k_2}{m} & \frac{c_2}{m} & -\frac{c_2}{m} \\ 0 & 0 & 0 & 0 \end{bmatrix} \mathbf{z}_3 + \begin{bmatrix} 0 \\ 0 \\ -\frac{1}{M} \\ \frac{1}{m} \\ 1 \end{bmatrix} K_0 u + \mathbf{v}. \tag{3.52}$$

In this example, the structural parameters were chosen to correspond to the experimental model in the SDOF configuration described in the experimental verification section. The values were: M = 245 kg (1.4 lb-s^2/in), c_1 = 3.06 N-s/m (1.75 lb-s/in), and k_1 = 4,991 N/m (2850 lb/in). The AMD was chosen such that the mass was 2% that of the structure, the stiffness k_2 = 99.8 N/m (57 lb/in) was chosen to tune the AMD to the natural frequency of the structure, and the damping c_2 was considered to be negligible and set equal to zero. Using the constants for the hydraulic actuator model presented subsequently in the experimental verification section and the above parameters, the matrices in the above models were formed. For all of the controllers, the model on which the responses calculations were based is given in Eqs. (3.46) and (3.47). In each case, the ground acceleration was modeled as a broadband excitation with a constant two-sided spectral density of magnitude S_0 = 3.83 cm^2/s^3 (5.94$\times$ 10^{-1}in^2/s^3).

Herein, the controlled response using the AMD is compared to the uncontrolled structure (*i.e.*, with the AMD removed). The zeroed control configuration is not presented for the AMD system because the results are similar to the responses of the uncontrolled configuration. The response statistics for the various type A controllers are provided in Table 3.4. For the high authority controller (Case 2), notice that while requiring the same *rms* control force, Controller 1A reduced the relative displacement of the first floor by 51.3%, whereas Controller 3A only produced a 38.5% reduction in relative displacement. The

system formed using Controller 2A became unstable before this force level was achieved. Response statistics for the three type B controllers are shown in Table 3.7. Notice that the *rms* absolute accelerations for Controllers 1B and 2B are the very close in both the high and low authority cases, and these controllers produce significantly better results than Controller 3B which considers the actuator transfer function to be constant over all frequencies. Also notice that for this example, the relative displacement response with Controller 1B (acceleration weighting) is nearly the same as for Controller 1A (displacement weighting) when the same amount of actuator force is employed. For this example, it would be slightly more beneficial to use a control strategy which weights the acceleration of the structure than one which weights the relative displacement. In addition, the controlled systems formed by using Controllers 2A, 2B, 3A, and 3B become unstable at high displacement/acceleration weighting in the performance function (*i.e.*, high authority control). If the compressibility of the hydraulic fluid is accounted for, a more authoritative (*i.e.*, higher performance) controller can be designed without such an instability occurring.

Table 3.6 Comparison of *RMS* Values of Controlled Responses for the AMD Model with Weighting on the Relative Displacement.

Configuration	σ_{x1} (cm)	$\sigma_{x_1 - x_2}$ (cm)	$\sigma_{\ddot{x}1}$ (cm/s^2)	σ_f (N)
(a) nominal configuration				
Uncontrolled	6.787e-2	—	140.1	—
(b) Case 1: low authority controller				
Controller 1A	4.321e-2	1.094e-1	86.49	27.15
Controller 2A	5.509e-2	5.100e-2	110.1	27.15
Controller 3A	5.255e-2	7.173e-2	104.1	27.15
(c) Case 2: high authority controller				
Controller 1A	3.353e-2	1.866e-1	67.51	46.84
Controller 2A	—	—	—	—
Controller 3A	4.229e-2	1.463e-1	83.01	46.84

Table 3.7 Comparison of *RMS* Values of Controlled Responses for the AMD Model with Weighting on the Absolute Acceleration.

Configuration	σ_{x1} (cm)	$\sigma_{x_1 - x_2}$ (cm)	$\sigma_{\ddot{x}1}$ (cm/s^2)	σ_f (N)
(a) nominal configuration				
Uncontrolled	6.787e-2	—	140.1	—
(b) Case 1: low authority controller				
Controller 1B	4.181e-2	1.197e-1	83.26	27.15
Controller 2B	4.181e-2	1.196e-1	83.06	27.15
Controller 3B	5.936e-2	4.338e-2	117.7	27.15
(c) Case 2: high authority controller				
Controller 1B	3.272e-2	2.004e-1	64.85	46.84
Controller 2B	3.277e-2	1.999e-1	64.92	46.84
Controller 3B	4.663e-2	1.113e-1	91.92	46.84

3.4 Summary

In this chapter, the role of control-structure interaction in the design of protective systems has been investigated, and the importance of accounting for actuator dynamics and control-structure interaction has been demonstrated. For the case of hydraulic control actuation, a natural velocity feedback interaction path has been shown to exist. This feedback, together with the stabilizing displacement (and/or force, velocity) feedback, causes control-structure interaction to be intrinsic to the device. The dynamic model presented for the hydraulic actuator was verified experimentally, as well as the predicted control-structure interaction behavior. Examples employing seismically excited structures have been provided which show that considering actuator dynamics and control-structure interaction in the design of a controller significantly improves the performance and robustness of the controlled system.

The following conclusions from this work should be emphasized:

- When the feedback interaction path is present, the poles of the structure will appear as zeros of the transfer function from the command input to the force applied to the structure. This result occurs regardless of how fast the dynamics of the actuator are (including the case when G_a is a constant gain).
- For actuators attached to lightly damped structures in which the feedback interaction path is present, the ability of the actuator to apply forces at the structure's natural frequencies is greatly limited. The actuator cannot apply a force at the natural frequencies of an undamped structure.
- Hydraulic actuators, both active and semi-active, have an implicit feedback interaction path that occurs due to the natural velocity feedback of the actuator response. This interaction occurs for actuators configured in both displacement, velocity and/or force control.
- Simple models can be employed to represent the dynamics of the hydraulic actuator and the associated control-structure interaction.
- Most researchers in the control of civil engineering structures have neglected the dynamics of the actuator, as well as the control-structure interaction effect. This approach is equivalent to assuming that the transfer function G_{fu} is constant in magnitude with zero phase. In general, neither the phase nor the magnitude of G_{fu} will be constant. Neglecting phase differences between the command input *u* and the resulting force *f*, will result in a time lag associated with generation of the control forces. Appropriate modeling of the actuator dynamics and control-structure interaction accommodates this time lag.

- In a structural control system for a given level of control action, neglecting the actuator dynamics generally results in larger responses than in the case where the control-structure interaction is considered. Also, neglecting actuator dynamics and control-structure interaction results in less achievable performance of the controller because the closed loop system more easily becomes unstable.
- Better results are obtained if the compressibility of the hydraulic fluid is taken into account than if the fluid is treated as incompressible. Also, in the latter case, the achievable performance level of the controller is significantly reduced due to instabilities created in the closed-loop system.
- For the examples of active bracing and active tendon systems considered herein, the structural response quantities are more efficiently reduced if they are directly weighted in the control performance function. Thus, to reduce the absolute structural accelerations, one should directly weight these acceleration responses in the control performance function.
- For the active mass driver example, the relative displacements and absolute accelerations are most efficiently reduced by weighting the absolute accelerations of the structure.
- In general, modeling errors resulting from neglecting actuator dynamics and control-structure interaction can be expected to decrease both the stability and performance robustness of the controlled structure.

CHAPTER 4

Active Bracing Experiment

The first experiment to verify acceleration feedback control strategies for seismically excited structures was conducted in June 1993 at the Structural Dynamics and Control/ Earthquake Engineering Laboratory (SDC/EEL) at the University of Notre Dame. The structure employed was a three-story, single-bay, model building configured with an active bracing control system. In this chapter, the experimental setup for the active bracing system is described and a control design model for the structural system is identified which incorporates the effects of control-structure interaction. An H_2/LQG controller is then designed and implemented on the system. The results show that acceleration feedback control strategies are effective for an active bracing system.

4.1 Experimental Setup

The SDC/EEL at the University of Notre Dame houses a uniaxial earthquake simulator. The earthquake simulator consists of a hydraulic actuator/servovalve assembly which drives a 48 in $\times$ 48 in (122 cm $\times$ 122 cm) aluminum slip table mounted on high-precision, low-friction, linear bearings. The actuator is a 2.5 in (6.4 cm) Nopak hydraulic cylinder with a ± 3 in $(\pm 7.6\ \text{cm})$ stroke, and the servovalve/amplifier is distributed by Continental Hydraulics. The actuator and table/bearing system are attached to a reaction massconsisting of a $30\ \text{in} \times 60\ \text{in} \times 96\ \text{in}$ sand-filled steel box. The hydraulic power unit for the simulator is a 26 gpm gear pump with nominal supply pressure of 3,000 psi. The

pump is driven by a 60 amp, 50 HP electric motor. A 2.5 gallon hydraulic accumulator is attached to the 3,000 psi supply line to the actuator. The capabilities of the simulator are: maximum displacement ±2 in (±5.1 cm), maximum velocity ±35 in/sec (±89 cm/sec), and maximum acceleration ±4gs with a 1000 lb test load. The operational frequency range of the simulator is 0-50 Hz.

The test structure (see Figs. 4.1 and 4.2) employed in this experiment is a scale-model of the prototype structure discussed in Chung *et al*., (1989). The building frame is constructed of steel, with a height of 158 cm (62 in). The floor masses of the model weigh a total of 227 kg (500 lb), distributed evenly between the three floors. The time scale factor is 0.2, making the natural frequencies of the model approximately five times those of the prototype. The first three modes of the model structural system are at 5.7 Hz, 17.3 Hz and 28.3 Hz, with associated damping ratios given, respectively, by 0.33%, 0.23%, and 0.30%. The ratio of model quantities to those corresponding to the prototype structure are: force = 1:60, mass = 1:206, time = 1:5, displacement = 4:29 and acceleration = 7:2.

The control force is applied by a servo-hydraulic control actuator with a ±2 in. (±5.1 cm) maximum stroke located just below the first floor of the building and rigidly attached to the seismic simulator table via a chevron-type brace, as shown in Figs. 4.1 and 4.2. A position sensor, rigidly connected to the actuator, provides the stabilizing position feedback for the control actuator, as well as a measurement of the first floor displacement relative to the base. Accelerometers measure the absolute acceleration of each floor as well as the ground acceleration. The force transmitted to the building by the control actuator is measured with a piezoelectric force ring manufactured by PCB Piezotronics, Inc.

Note that in this experiment the relative displacement of the actuator, the absolute acceleration measurements of the three floors of the structure, and the actuator force were employed to determine the control action (see Fig. 4.1).

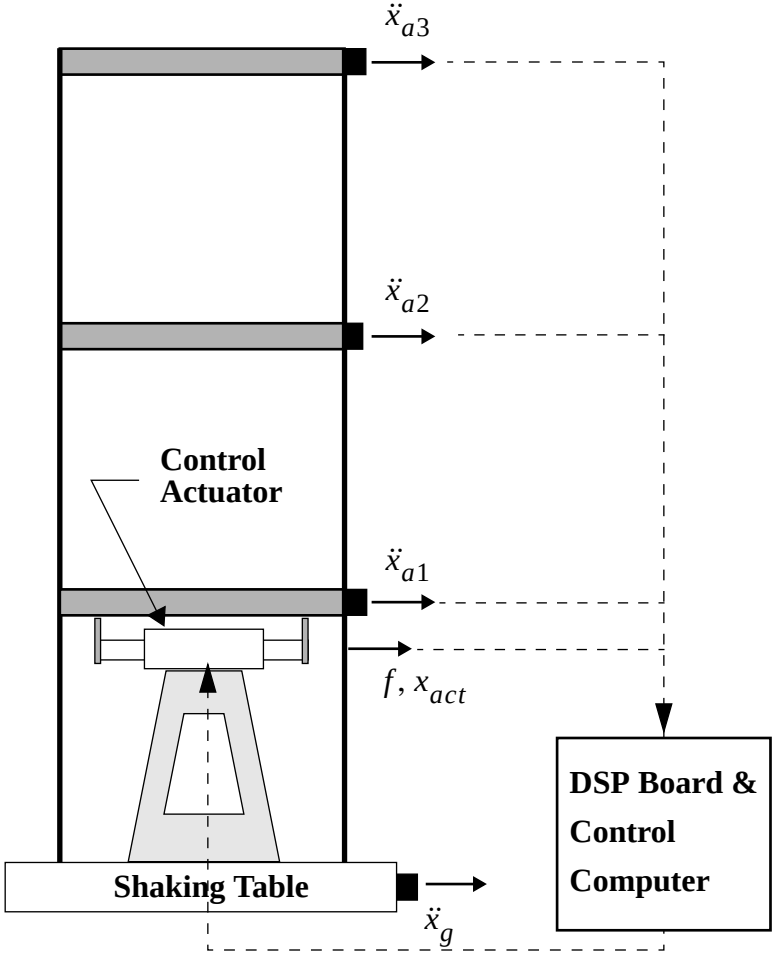

Figure 4.1 Schematic of Experimental Setup.

Figure 4.2 Three-Degree-of-Freedom Test Structure with an Active Bracing System.

4.2 System Identification and Model Validation

A block diagram of the structural system to be identified (*i.e.*, in Figs. 4.1 and 4.2) is shown in Fig. 4.3. The two inputs are the ground excitation $\ddot{x}_g$ and the command signal to the actuator u. The five measured system outputs include the relative displacement of the actuator piston, x_p, the three absolute accelerations, $\ddot{x}_{a1}$, $\ddot{x}_{a2}$, $\ddot{x}_{a3}$, of the floors of the test structure, and the control force applied to the first floor, f, (*i.e.*, $\mathbf{y} = [x_p \;\; \ddot{x}_{a1} \;\; \ddot{x}_{a2} \;\; \ddot{x}_{a3} \;\; f]'$**)**. Thus, a 5×2 transfer function matrix (*i.e.*, ten input/output relations) must be identified to describe the characteristics of the system in Fig. 4.3.

The procedure outlined in Chapter 2 was applied to determine a model of this 2-input/5-output structural system. The 4-channel Tektronix 2630 Fourier Analyzer was first used to determine the ten experimental transfer functions for the system. The transfer functions from the ground acceleration to each of the measured responses were obtained by exciting the structure with a band-limited white noise ground acceleration (0-100 Hz) with the control actuator in place and the actuator command set to zero. Similarly, the experimental transfer functions from the actuator command signal to each of the measured outputs were determined by applying a band-limited white noise (0-100 Hz) to the actuator command while the ground was held fixed.

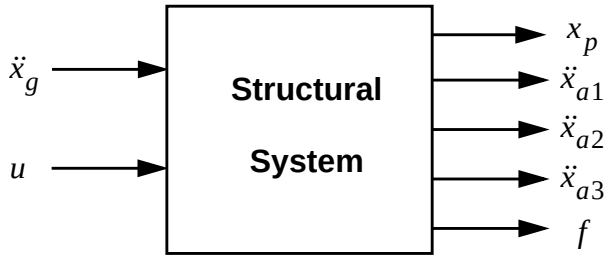

Figure 4.3 Block Diagram Representation of the Active Bracing System.

Representative magnitude and phase plots are shown in Figs. 4.4–4.6. All transfer functions were obtained using twenty averages (*i.e.*, $M = 20$ in Eqs. (2.7–2.9)). Fig. 4.4 presents the transfer function from the ground acceleration $\ddot{x}_g$ to the first floor absolute acceleration $\ddot{x}_{a1}$, with the actuator in place and the actuator command set to zero (*i.e.*, $u = 0$). Note the four distinct peaks in each transfer function at 8.28 Hz, 24.9 Hz, 41.5 Hz and 47.8 Hz, corresponding to the first four modes of the structural system (including the actuator and test structure). The transfer function from the actuator command signal u to the first floor absolute acceleration $\ddot{x}_{a1}$ is shown in Fig. 4.5, and the transfer function from the actuator command signal u to the the force applied to the structure f is shown in Fig. 4.6.

One would expect all of the eight transfer functions to have exactly the same peaks. However, notice that in the transfer functions from the ground acceleration to the structural responses, the third peak occurs at a higher frequency than the third peak in the transfer functions from the command input to the structural responses. The reason for this is not clear and requires further investigation. However, this phenomenon was only observed in the active bracing system and may be due to amplitude dependent nonlinearities in the actuator. The amplitudes of the actuator displacements when the ground is excited were significantly smaller than the displacements experienced when the actuator drives the system.

Once the experimental transfer functions have been obtained, the next step in the system identification procedure is to model the transfer functions as a ratio of two polynomials in the Laplace variable *s*. In this step, the effects of control-structure interaction should be consistently incorporated into the identification process. Thus, the zeros of the transfer function from the actuator command to the applied force are the poles of the structure (when the actuator is not attached). The resulting mathematical models of the transfer

functions are overlaid in Figs. 4.4–4.6. The quality of the mathematical models for the remaining transfer functions was similar to that depicted here.

Next, the model was assembled in state space form. Ten states were used to model the system corresponding to the ground acceleration input (Eq. 2.11) over the frequency range of interest and twelve states were used to form the second state equation (Eq. 2.12), modeling the input/output relationship between the actuator command u and the measured responses $\mathbf{y}$. Once each of the two state space systems were assembled, the states of the individual systems were stacked, as described in Chapter 2, and a model reduction was performed, reducing the twenty-two state system to a fourteenth-order system. All of the transfer functions of the reduced-order model are compared to the experimental data in Figs. 4.7–4.16.

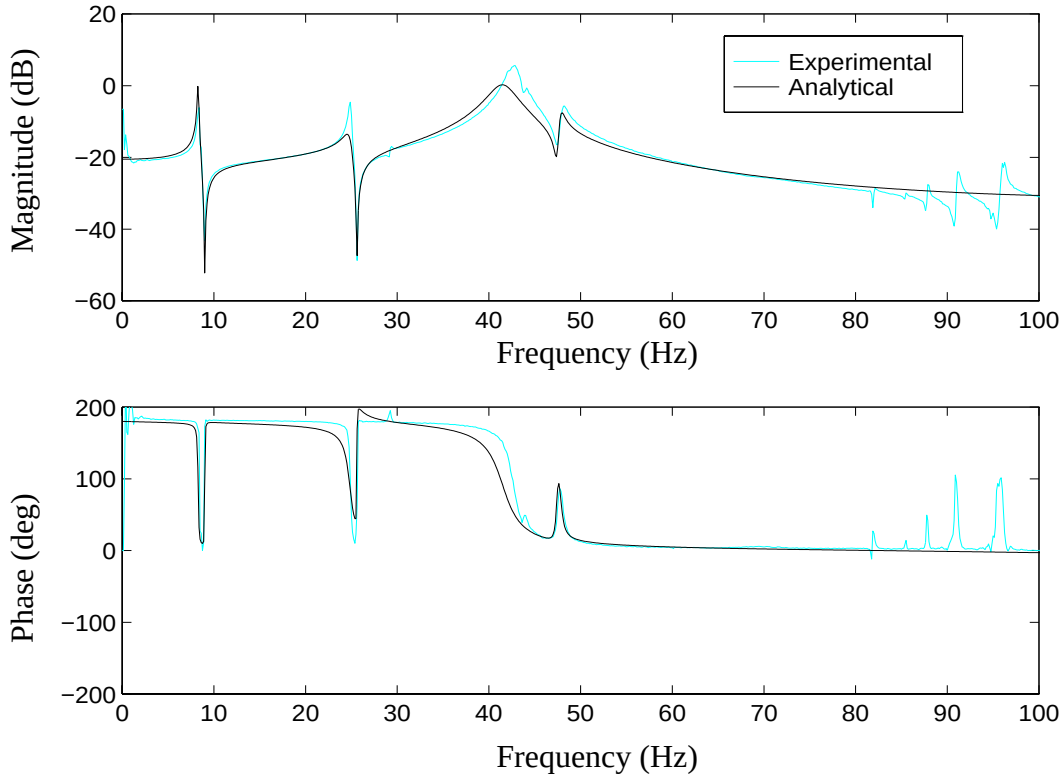

Figure 4.4 Transfer Function from Ground Acceleration to First Floor Acceleration

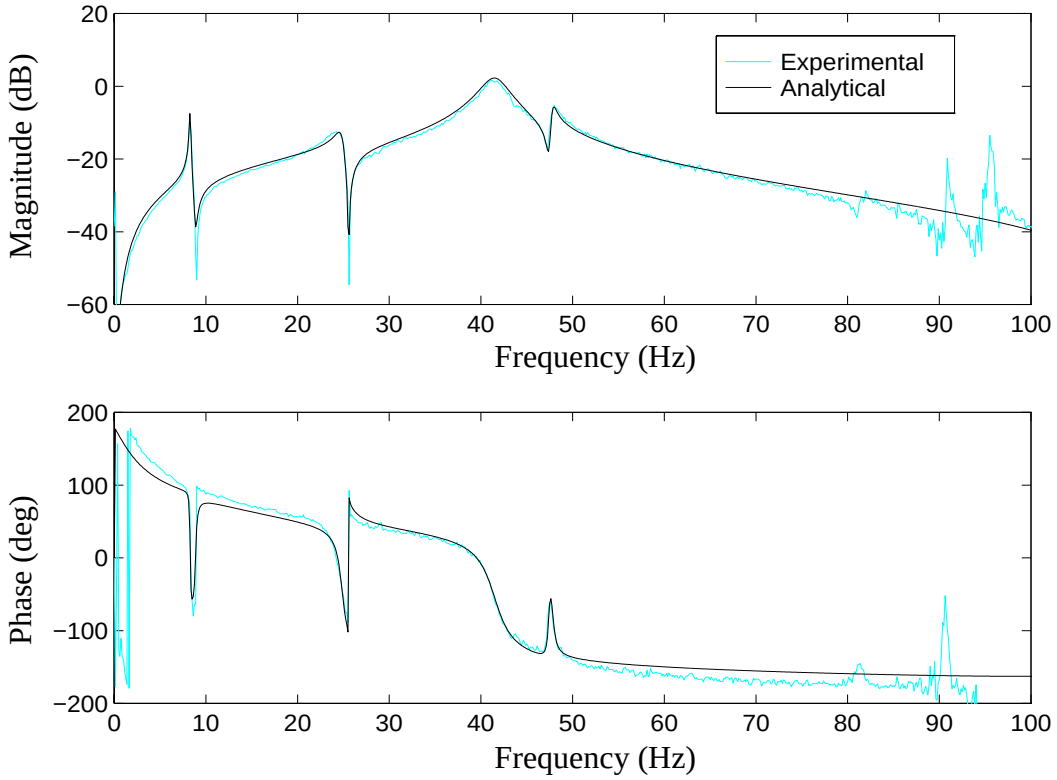

Figure 4.5 Transfer Function from Actuator Command to First Floor Acceleration.

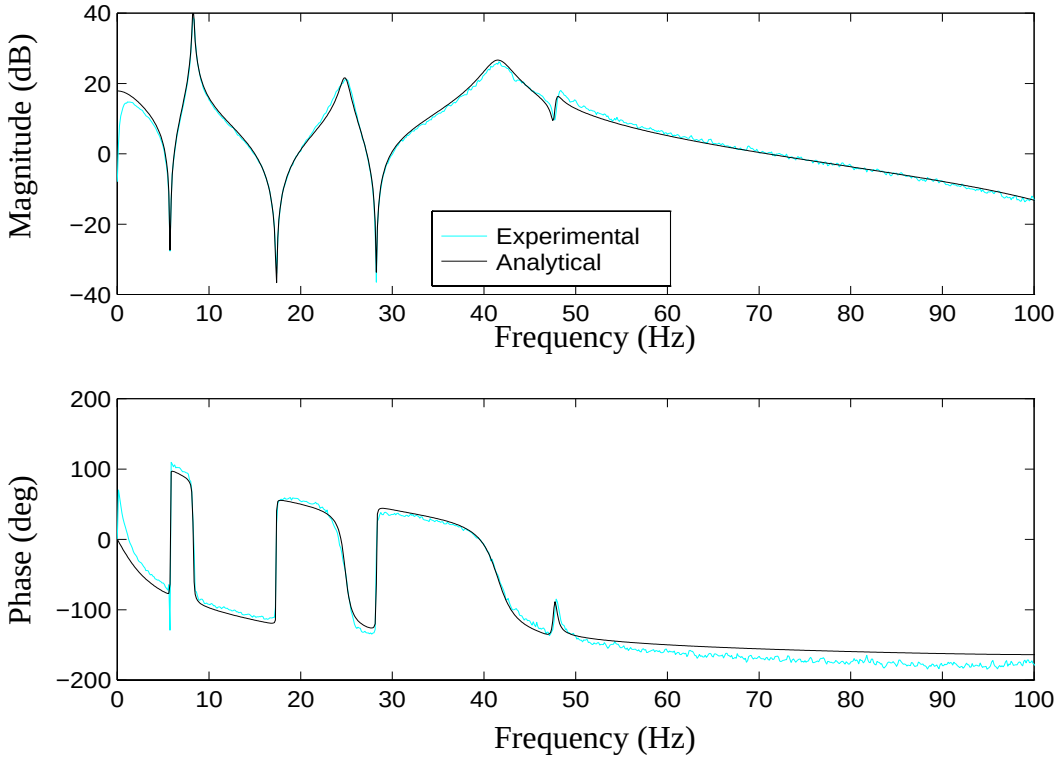

Figure 4.6 Transfer Function from Actuator Command to the Applied Force.

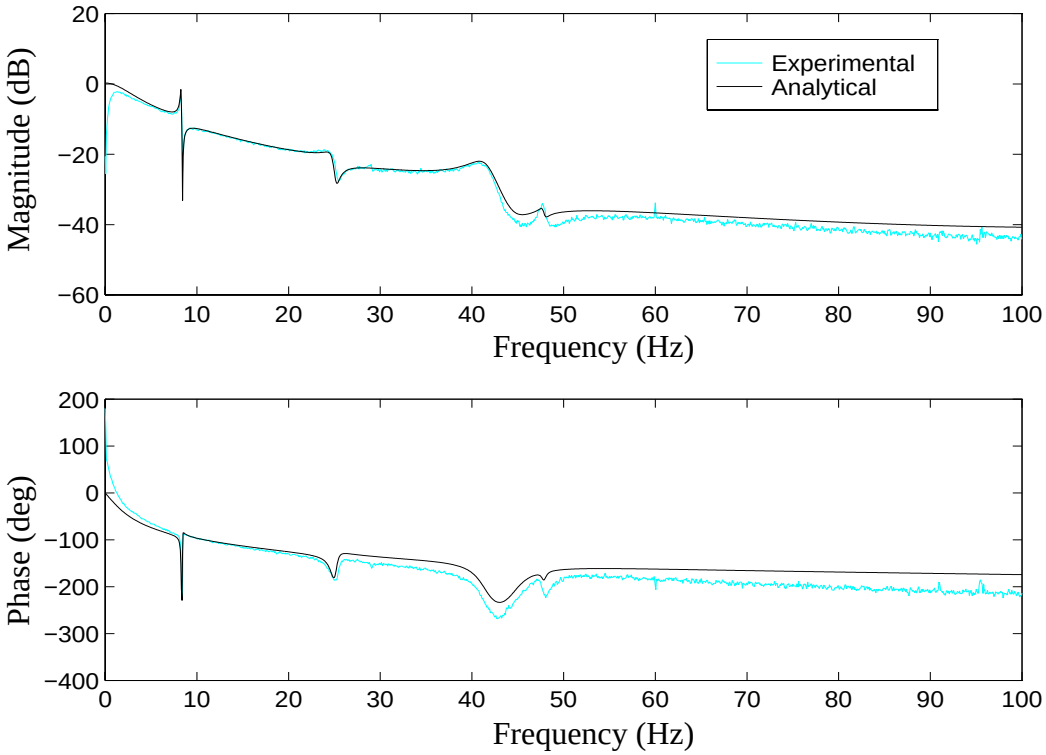

Figure 4.7 Comparison of Reduced-Order Model and Experimental Transfer Function: Actuator Command to the Actuator Displacement.

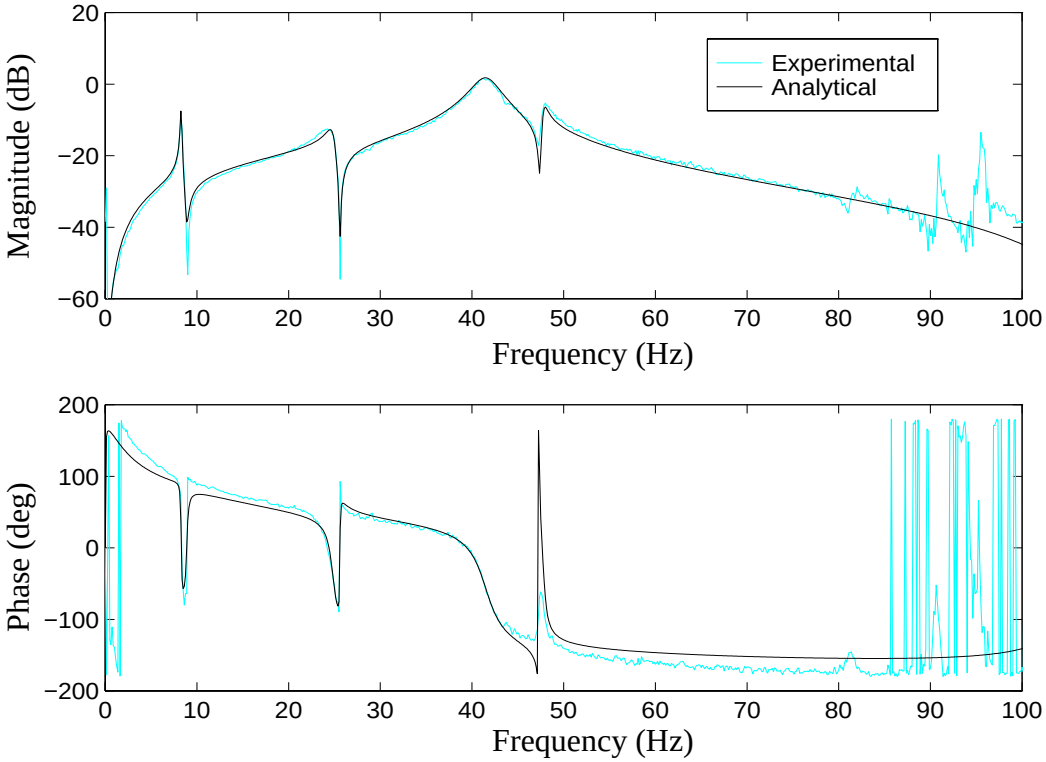

Figure 4.8 Comparison of Reduced-Order Model and Experimental Transfer Function: Actuator Command to the First Floor Absolute Acceleration.

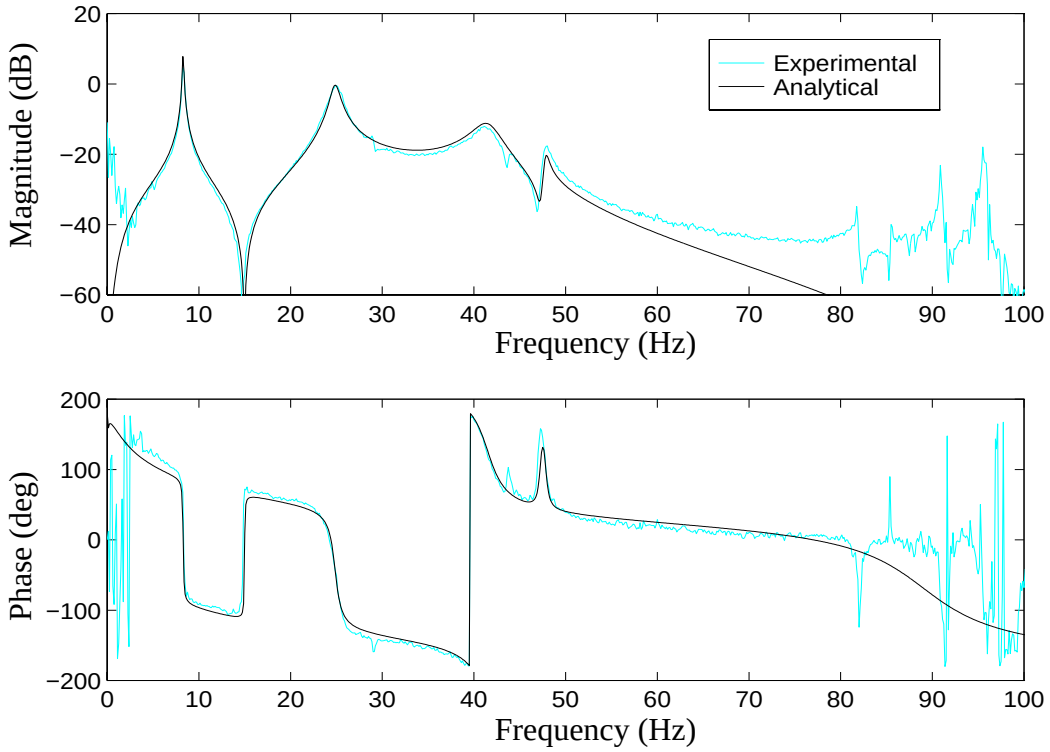

Figure 4.9 Comparison of Reduced-Order Model and Experimental Transfer Function: Actuator Command to the Second Floor Absolute Acceleration.

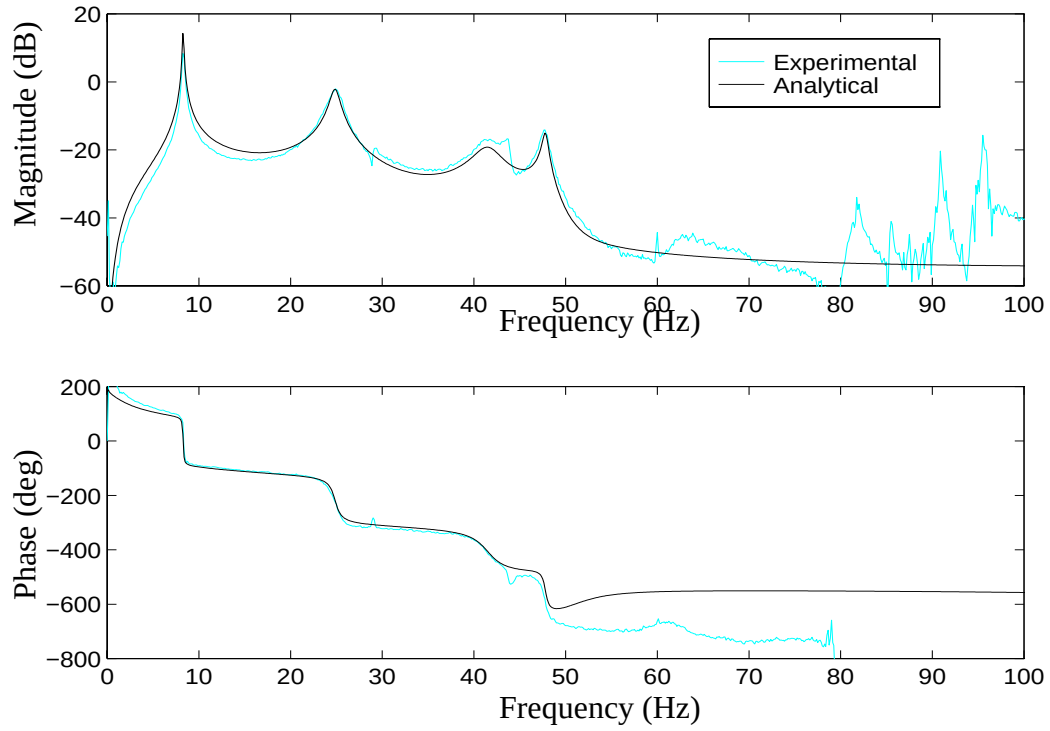

Figure 4.10 Comparison of Reduced-Order Model and Experimental Transfer Function: Actuator Command to the Third Floor Absolute Acceleration.

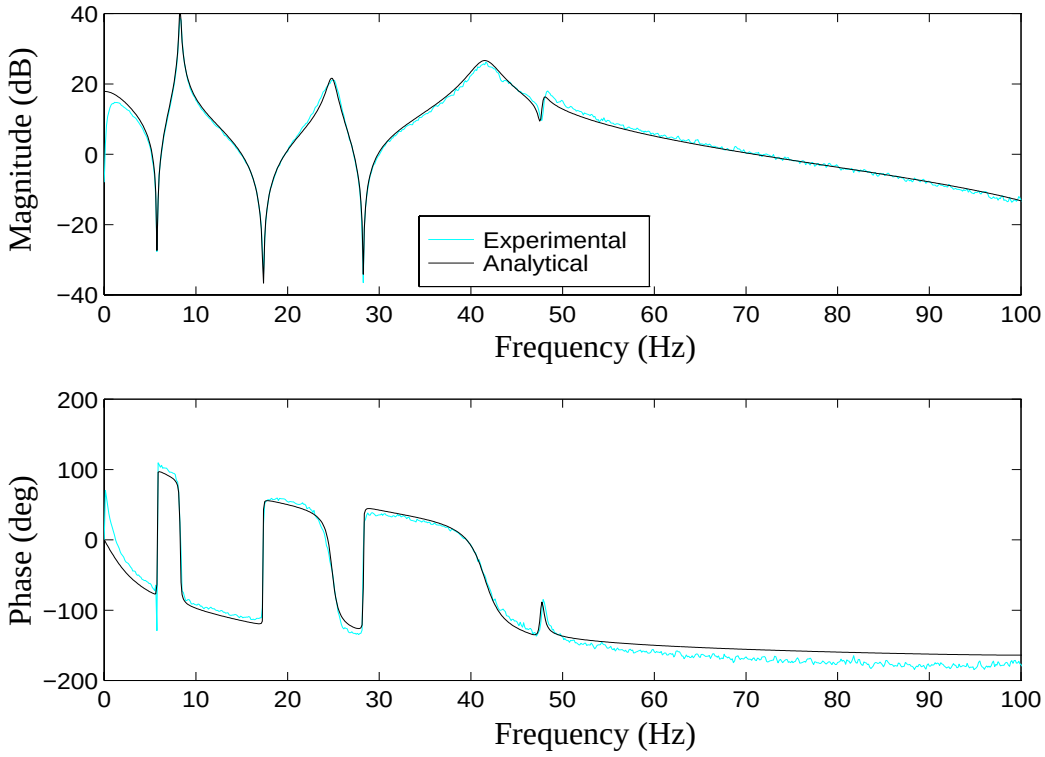

Figure 4.11 Comparison of Reduced-Order Model and Experimental Transfer Function: Actuator Command to the Applied Force.

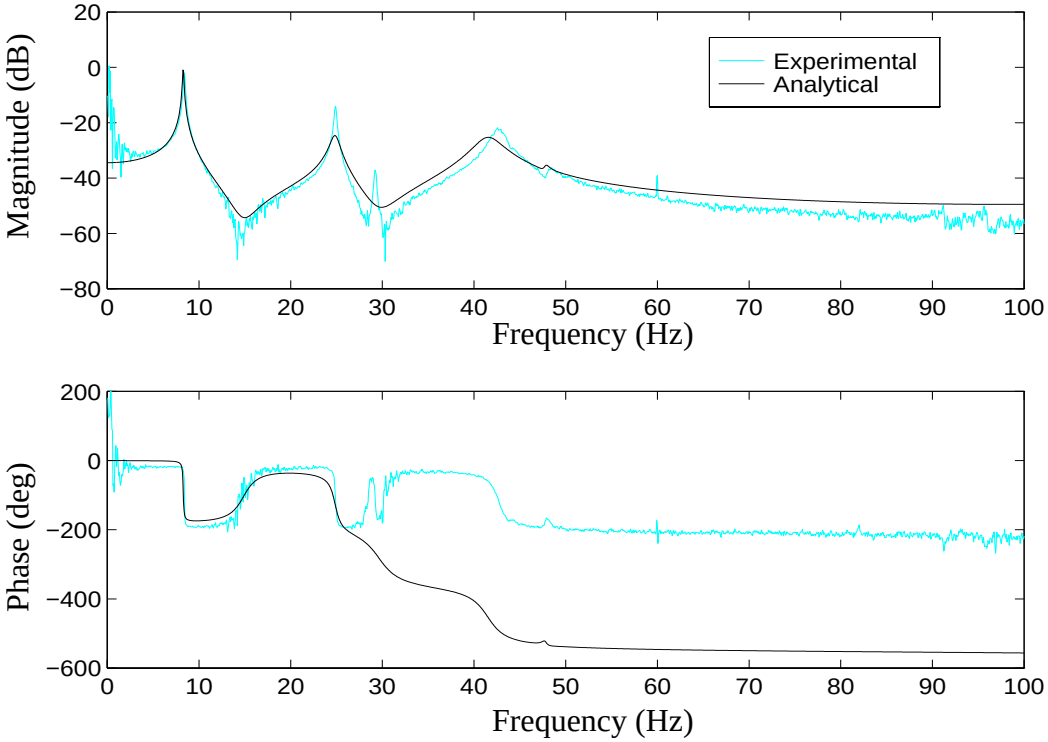

Figure 4.12 Comparison of Reduced-Order Model and Experimental Transfer Function: Ground Acceleration to the Actuator Displacement.

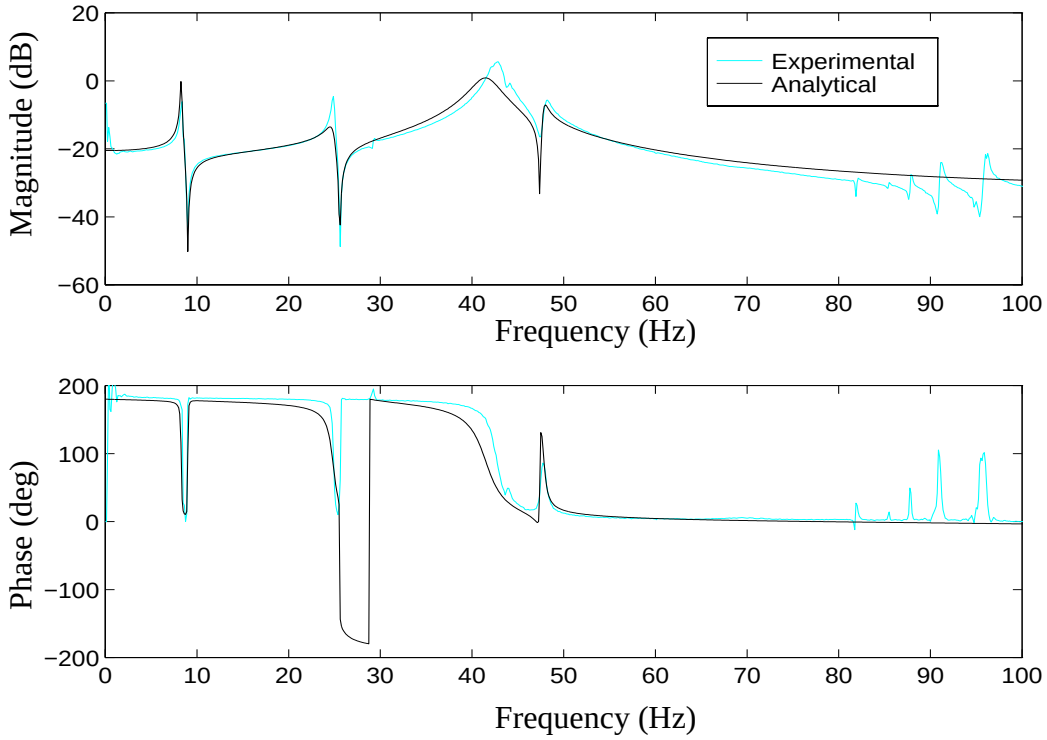

Figure 4.13 Comparison of Reduced-Order Model and Experimental Transfer Function: Ground Acceleration to the First Floor Absolute Acceleration.

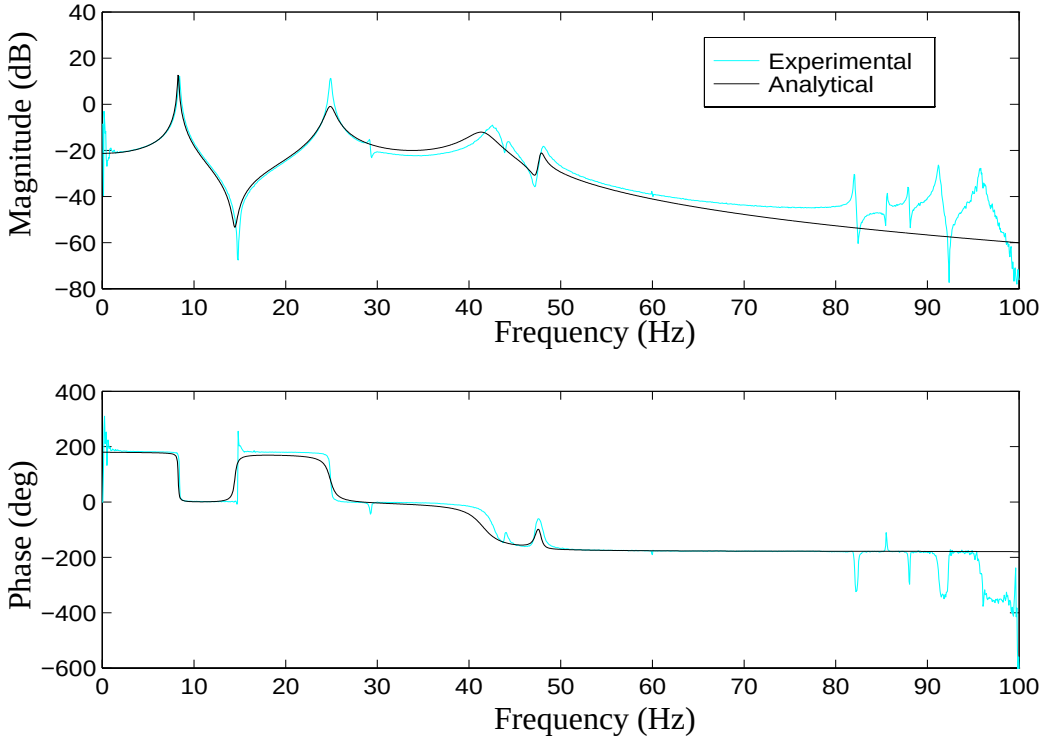

Figure 4.14 Comparison of Reduced-Order Model and Experimental Transfer Function: Ground Acceleration to the Second Floor Absolute Acceleration.

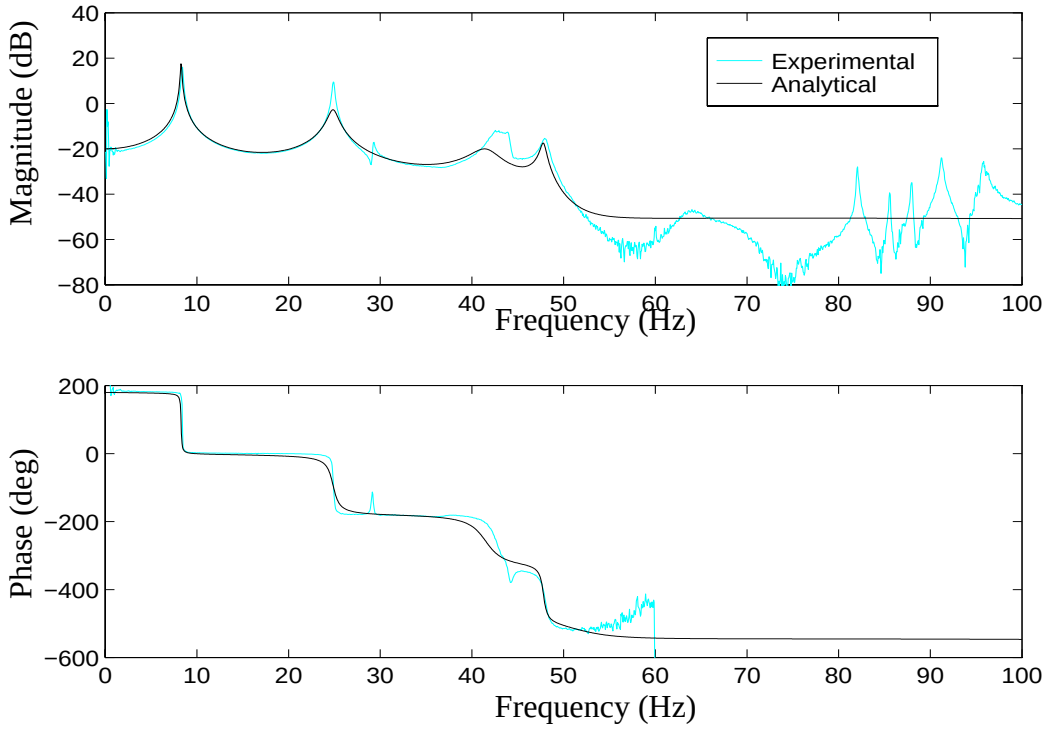

Figure 4.15 Comparison of Reduced-Order Model and Experimental Transfer Function: Ground Acceleration to the Third Floor Absolute Acceleration.

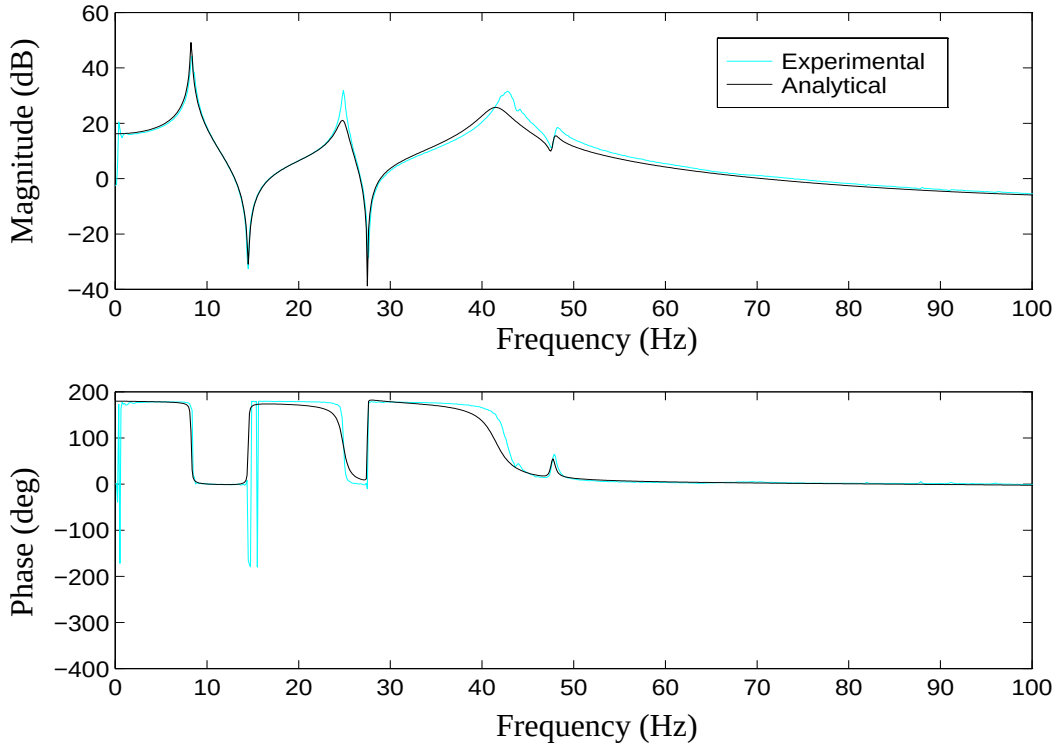

Figure 4.16 Comparison of Reduced-Order Model and Experimental Transfer Function: Ground Acceleration to the Applied Force.

Notice that the quality of the transfer functions corresponding to the actuator command input are of higher quality than those corresponding to the ground acceleration input. As discussed in Section 2.2.1, for the design of effective and robust controllers, the model should accurately predict the response of the system to the control signal. Therefore, in the system identification procedure, efforts were focused on obtaining an accurate model from the actuator command to the structural responses in the frequency range of interest.

The identified model of the structural system is used in the following section for control design and experimental verification of acceleration feedback strategies for a structure employing an active bracing system.

4.3 Control Design and Experimental Results

An acceleration feedback controller was designed for the system based on the H_2/ LQG techniques discussed in Section 2.3. The weighting functions $\mathbf{W}$ and $\mathbf{F}$, were constant matrices (*i.e.*, independent of frequency). The primary goal of the control design employed in this initial experiment was to minimize the accelerations of the three floors of the structure. Thus, an equal weighting was placed on the three absolute accelerations of the structure. The loop gain transfer function was examined in assessing the control design to provide an indication of the closed-loop stability when the controller is implemented on the physical system. For this experiment, the magnitude of the loop gain should be less than one at the frequencies above approximately 50 Hz. The analytical loop gain for the controller is compared to the experimentally obtained loop gain in Fig. 4.17.

The performance of the controller was tested by exciting the structure with a broadband ground acceleration (0-100Hz) having an *rms* value of 92.2 cm/s^2. The *rms* values of the responses for the uncontrolled and controlled configurations of the structural system

are shown in Table 4.1. The results include *rms* responses for the relative displacement of the actuator x_p (which is also a measure of the first floor relative displacement), the absolute accelerations of the three floors, $\ddot{x}_{a1}$, $\ddot{x}_{a1}$, $\ddot{x}_{a1}$, and the applied control force, f. In this experiment, displacement transducers were not available in the experimental setup, and the second and third floor displacements were not measured. Here, the *uncontrolled* configuration refers to the case in which the active bracing system is completely disconnected from the structure. The *zeroed-control* case corresponds to the case in which the actuator is attached, but the command signal is set equal to zero (*i.e.*, $u = 0$). From the response of the zeroed configuration it is shown that the "stiffness" of the actuator has a significant effect on the displacement (97.4%) and a moderate effect on the accelerations. Notice that with control, the absolute accelerations of the three floors are reduced by 37.8%, 56.4% and 61.0%, respectively, over the uncontrolled responses, and the *rms* first floor displacement is reduced by 95.6%. Also note that the controlled responses are achieved by using less force than the zeroed-control case.

The magnitude of the experimentally obtained transfer functions for the controlled system are compared to the transfer functions of the uncontrolled and zeroed systems in

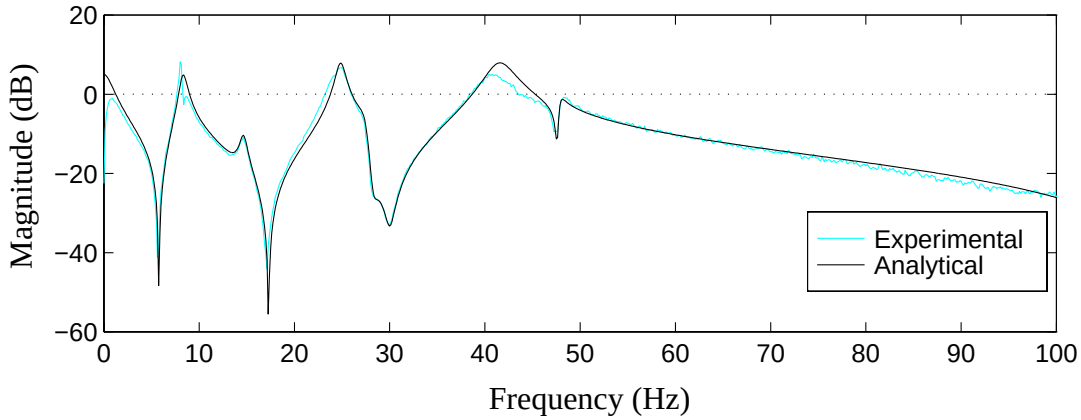

Figure 4.17 Experimental and Analytical Loop Gain Transfer Function.

Table 4.1 *RMS* Responses of Controlled System to Broadband Excitation (0-100 Hz).

	x_p, cm	$\ddot{x}_{a1}$, cm/s^2	$\ddot{x}_{a2}$, cm/s^2	$\ddot{x}_{a3}$, cm/s^2	f, N
Uncontrolled	0.693e-2	159.4	179.5	232.0	—
Zeroed-Control (% reduction)	0.197e–3 (97.4)	121.9 (23.5)	137.8 (23.2)	168.5 (27.4)	297
Controlled (% reduction)	0.310e–3 (95.6)	99.80 (37.8)	78.23 (56.4)	90.40 (61.0)	167

Figs. 4.18–4.22. Comparing the uncontrolled and zeroed transfer functions, a significant shift is observed in the natural frequencies due to the “stiffness” of the actuator (as predicted by the analysis in Chapter 3). Additionally, notice that the fourth peak which occurs near 45 Hz is not effected by the presence of the actuator. This peak is due to a torsional mode, and because the actuator is located on the centerline of test structure, it is not effected by the actuator.

Notice that the peaks of the controlled transfer functions from the ground acceleration to the structural responses are significantly smaller those of the zeroed transfer functions. Only the controlled transfer function from the ground acceleration to the actuator displacement is larger in magnitude than the zeroed response, because in the zeroed configuration the actuator attempts to remain in the locked position. In the transfer functions from the ground acceleration to the three floor accelerations, the peak in the first mode is reduced by 5–8 dB (a factor of 1.8–2.5) over the corresponding peaks in the zeroed transfer functions. In fact, notice that the controller achieves a significant reduction in all three modes in the acceleration responses. In each transfer function, the second mode is reduced by 10–15 dB (a factor of 3–5.6), and the third mode is reduced by approximately 10 dB (a factor of 3) over the zeroed response. In addition, the magnitude of the transfer function from the ground acceleration to the actuator force is significantly smaller in the controlled

case than in the zeroed case, showing again the actively controlled system achieves better performance while requiring smaller forces than the zeroed system.

To obtain a visual assessment of the effectiveness of the control strategy, a water tank was placed on the top floor of the structure. The additional mass of the water tank was negligible compared to the mass of the structure and its presence had no significant effect on the structural responses in both the uncontrolled and controlled configuration. Figure 4.23 is a photograph of the response of the uncontrolled structure to a broadband excitation. Here, large waves are present, with some of the liquid sloshing completely out of the tank. Note that the lines of the reference grid on the tank are at 2.5 cm (1 in) intervals. Figure 4.24 is a photograph of the response of the controlled structure to the broadband excitation. Here, the waves are reduced by the action of the controller.

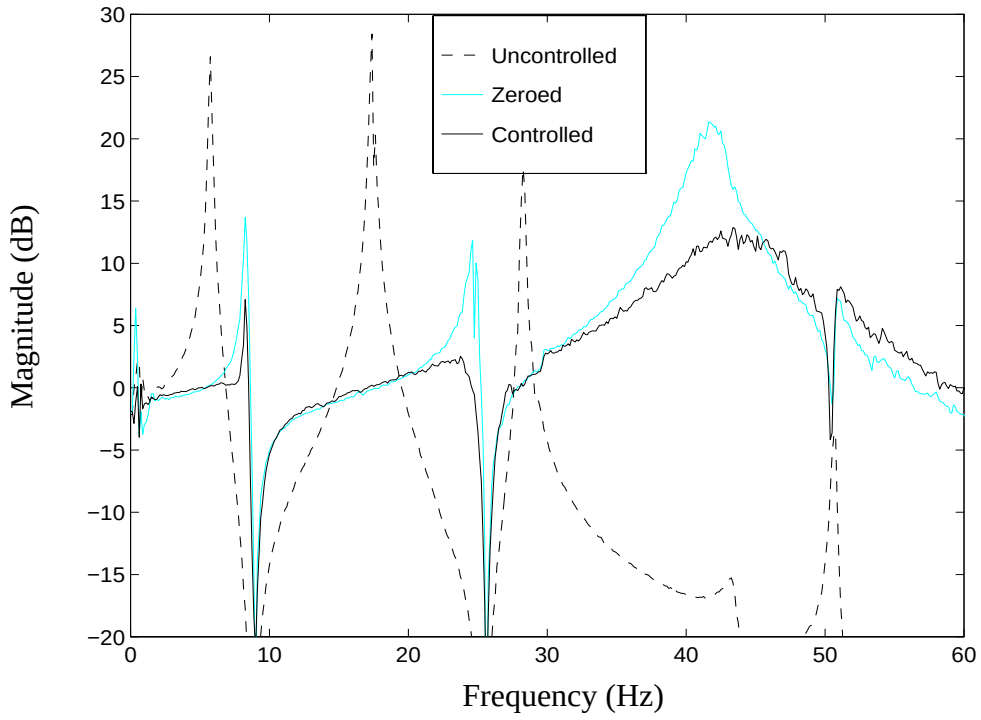

Figure 4.18 Comparison of Uncontrolled, Zeroed, and Controlled Transfer Functions: Ground Acceleration to the First Floor Absolute Acceleration.

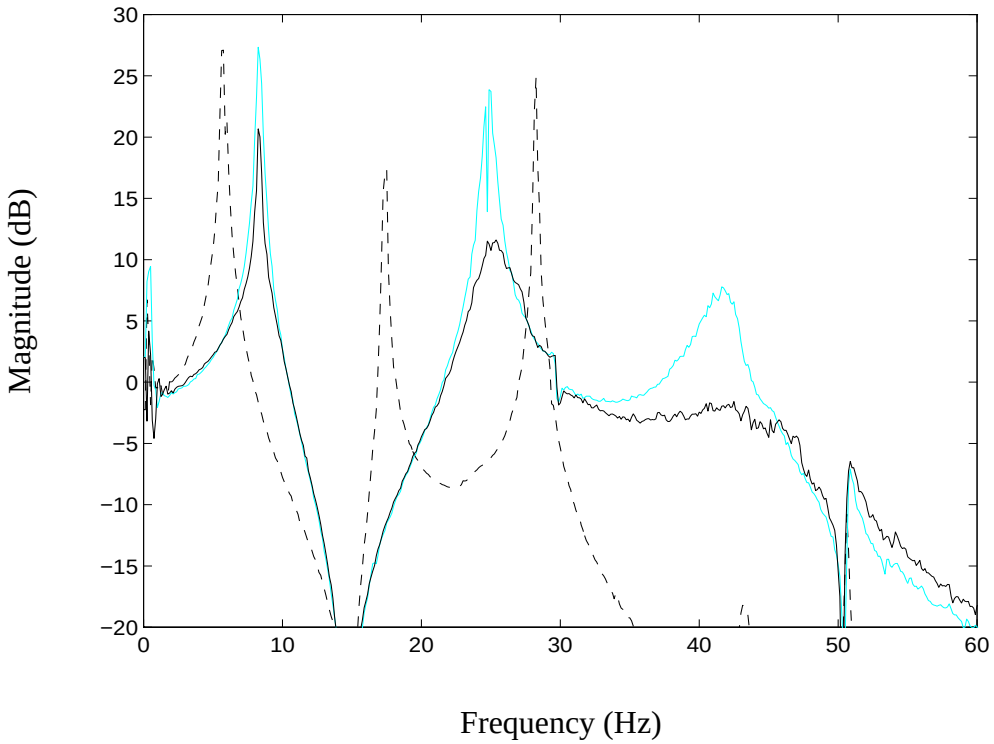

Figure 4.19 Comparison of Uncontrolled, Zeroed, and Controlled Transfer Functions: Ground Acceleration to the Second Floor Absolute Acceleration.

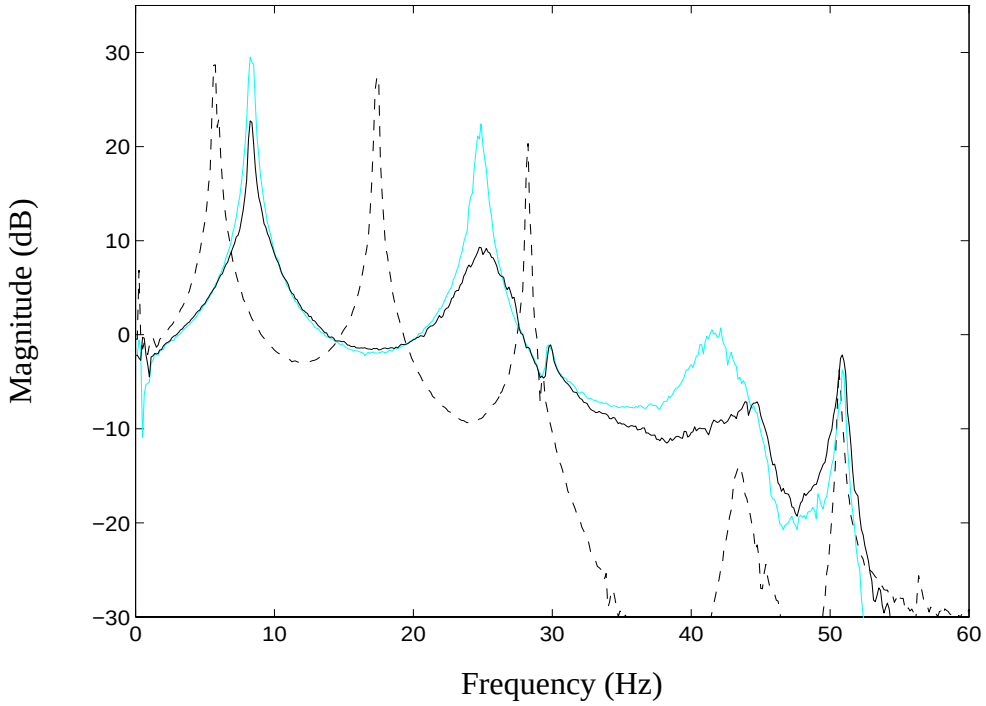

Figure 4.20 Comparison of Uncontrolled, Zeroed, and Controlled Transfer Functions: Ground Acceleration to the Third Floor Absolute Acceleration.

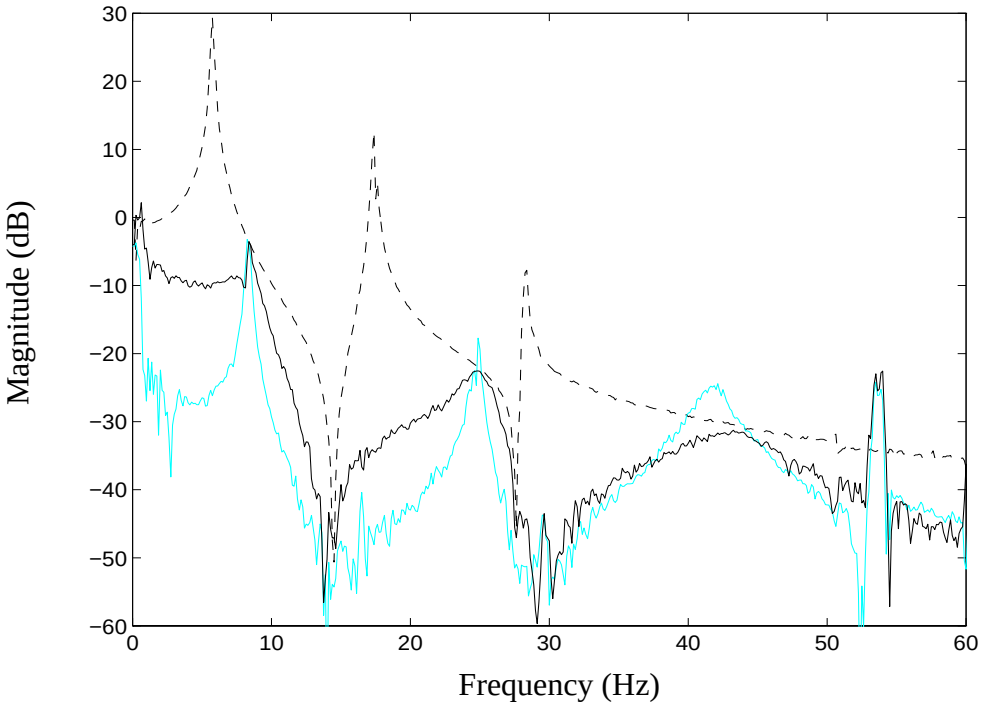

Figure 4.21 Comparison of the Uncontrolled, Zeroed and Controlled Transfer Functions: Ground Acceleration to the Actuator Displacement.

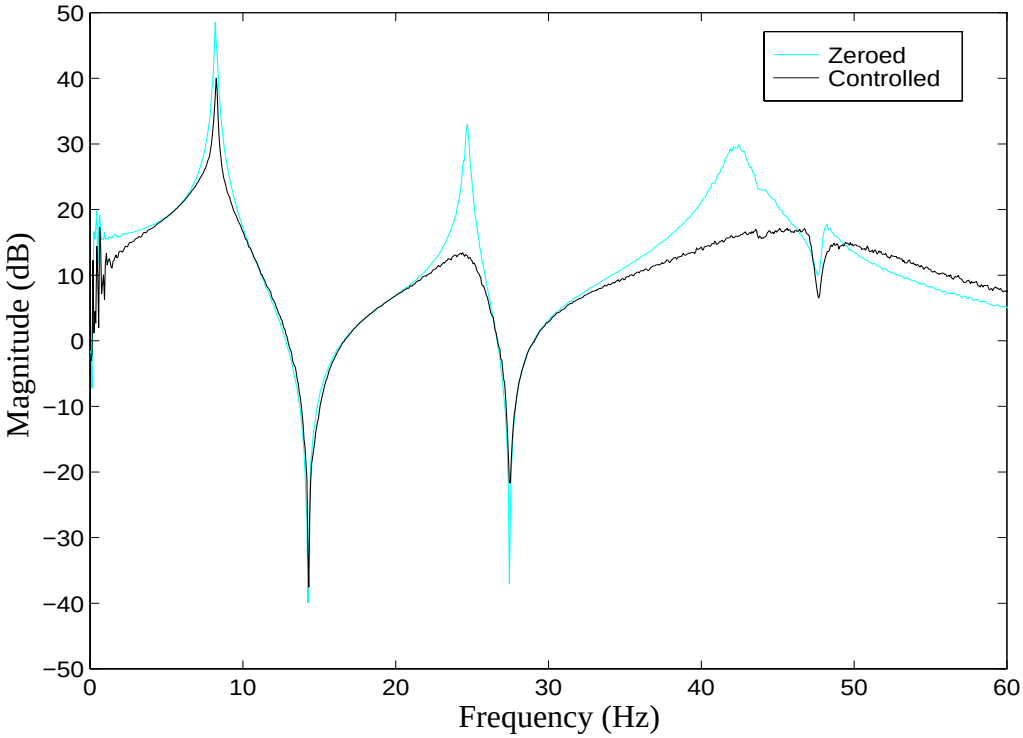

Figure 4.22 Comparison of the Zeroed and Controlled Transfer Functions: Ground Acceleration to the Applied Force.

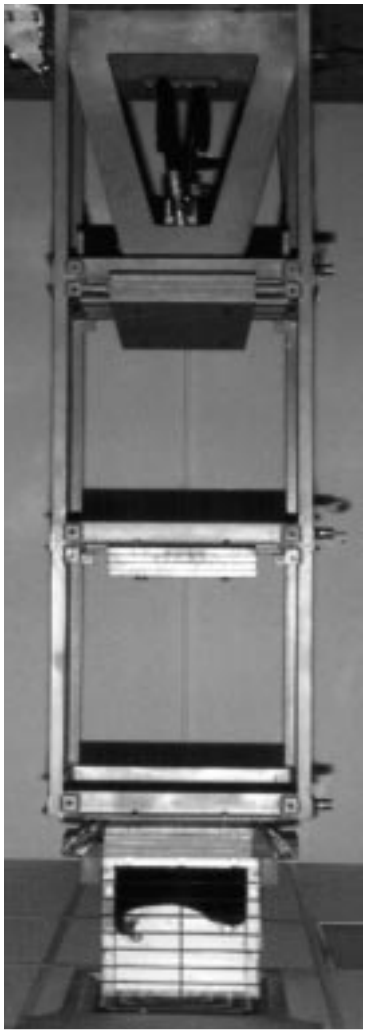

Figure 4.23 Uncontrolled Response of the Test Structure.

Figure 4.24 Controlled Response of the Test Structure.

4.4 Summary of the Active Bracing Experiment

In this experiment, acceleration feedback control strategies were successfully implemented and verified on a three-story test structure configured with an active bracing system. The system identification procedure employed implicitly incorporates the effects of control-structure interaction in the analysis by including the actuator in the identified system. When the transfer functions of the uncontrolled experiment were compared to those of the zeroed system, the effects of control-structure interaction were evident. The identified model was found to be effective for control design.

Using H_2/LQG techniques, a controller was designed for the system with the objective of reducing the accelerations of the three floors of the structure. The system was excited with a random 0-100 Hz ground excitation and the *rms* values of the responses were calculated. The controlled *rms* values of the three absolute accelerations were 37.8%, 56.4%, and 61.0% smaller than the uncontrolled values. Additionally, a comparison of the transfer functions of the uncontrolled and controlled systems demonstrated that the controller was able to achieve a significant reduction in all three modes of the structural system. Based on the experimental results, acceleration feedback control strategies should be regarded as viable and effective for a structure configured with an active bracing system.

These results consitute the first successful experimental implementation of acceleration feedback control strategies.

CHAPTER 5

Active Tendon Experiment

To demonstrate the validity of the acceleration feedback control strategies for larger scale structures, a second experiment was conducted on a 1:4 scale, tendon-controlled, three-story, test structure at the National Center for Earthquake Engineering Research (NCEER), SUNY-Buffalo. This test structure has been employed by numerous researchers to test the effectiveness of their active control strategies. First the experimental setup is described, including the test structure, the control actuator, tendons, and the sensors. A control design model for the structural system, which includes the effects of control-structure interaction, is developed and validated. The H_2/LQG frequency domain optimal control strategies discussed in Chapter 2 are employed to achieve the control objectives. The experimental results reported for the various control designs indicate that the controllers are robust and that full-state feedback performance can be effectively recovered using acceleration feedback control strategies.

5.1 Experimental Setup

Experimental verification of the acceleration feedback control strategies for an active tendon system was performed on the $12 \text{ ft.} \times 12 \text{ ft.}$ earthquake simulator at the National Center for Earthquake Engineering Research at SUNY-Buffalo. The test structure was the 1:4 scale model of a three-story building previously used by Chung, *et. al.* (1989) in state feedback experiments. The structural system consisted of the test structure, a hydraulic

control actuator and a tendon/pulley system, as shown in Figures 5.1 and 5.2. The test structure had a weight of 6,250 lbs., distributed evenly among the three floors, and was 100 in. in height.

The hydraulic control actuator, four pretensioned tendons, and a stiff frame connecting the actuator to the cables were provided to apply control forces to the test structure. The four diagonal tendons transmitted the force from the control actuator to the first floor of the structure, and the steel frame connected the actuator to the tendons. Because hydraulic actuators are inherently open-loop unstable, a feedback control system was employed to stabilize the control actuator and improve its performance. This feedback signal included a combination of the position, velocity and pressure measurements. For this actuator, an LVDT (linear variable differential transformer), rigidly mounted to the piston, provided the displacement measurement, which was the primary feedback signal. This measurement was also sent through an analog differentiator to determine the velocity measurement, and a pressure transducer across the actuator piston provided the pressure measurement.

The structure was fully instrumented to provide for a complete record of the motions undergone by the structure during testing. Accelerometers positioned on each floor of the structure measured the absolute accelerations of the model, and an accelerometer located on the base measured the ground excitation, as shown in Fig. 5.1. The displacement of the actuator was measured using the LVDT mentioned above. Additional measurements were taken to evaluate the performance of the control system. Force transducers were located on each of the four tendons and their individual outputs were combined to determine the total force applied to the structure. Displacement transducers on the base and on each floor were attached to a fixed frame (*i.e.*, not attached to the earthquake simulator) as shown in Fig. 5.1 to measure the absolute displacement of the structure and of the base. The relative

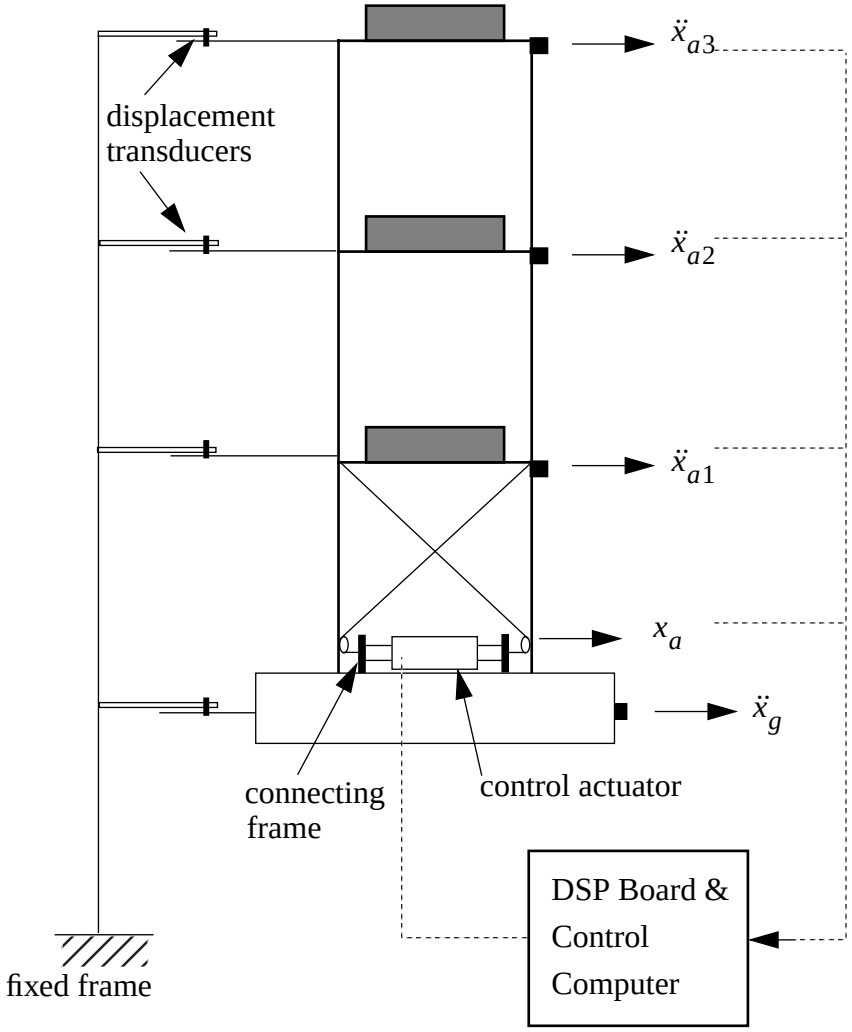

Figure 5.1 Schematic of Experimental Setup.

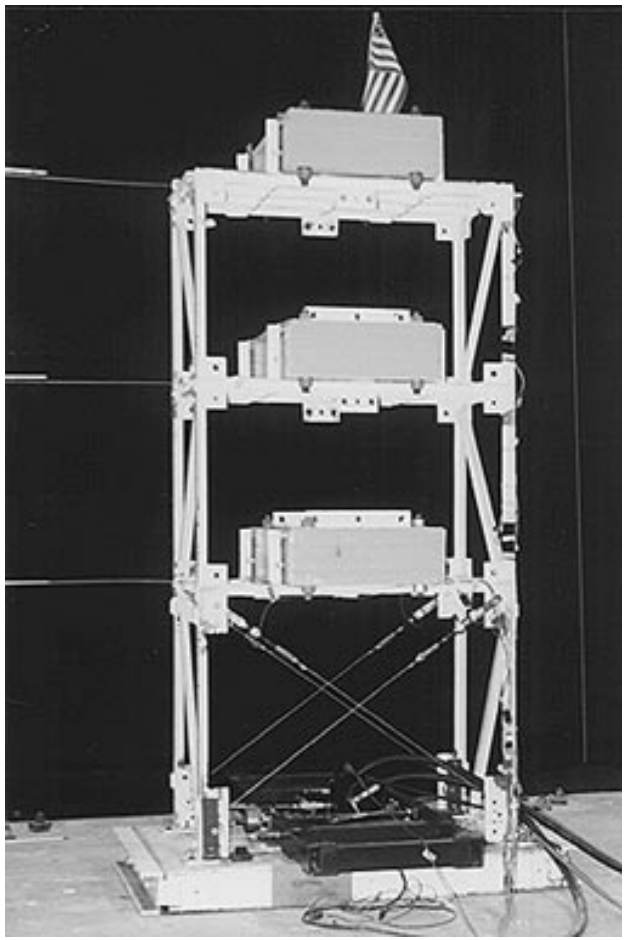

Figure 5.2 Three-Degree-of-Freedom Test Structure with an Active Tendon System.

displacements were determined by subtracting the base displacement from the absolute displacement of each floor.

Note that only acceleration measurements and the displacement of the actuator were employed in the control algorithms (see Fig. 5.1).

5.2 System Identification and Model Validation

A block diagram of the structural system to be identified (*i.e.*, in Figs. 5.1 and 5.2) is shown in Fig. 5.3. The two inputs are the ground excitation $\ddot{x}_g$ and the command signal to the actuator u. The four measured system outputs include the actuator displacement x_a and the absolute accelerations, $\ddot{x}_{a1}$, $\ddot{x}_{a2}$, $\ddot{x}_{a3}$, of the three floors of the test structure (*i.e.*, $\mathbf{y} = [x_a \;\; \ddot{x}_{a1} \;\; \ddot{x}_{a2} \;\; \ddot{x}_{a3}]'$). Thus, a 4×2 transfer function matrix (*i.e.*, eight input/output relations) must be identified to describe the characteristics of the system in Fig. 5.3.

The procedure outlined in Chapter 2 was employed to determine a model of this 2-input/4-output structural system. The Tektronix 2630 Fourier Analyzer was first used to determine the eight experimental transfer functions for the system shown in Fig. 5.3. The transfer functions from the ground acceleration to each of the measured responses were obtained by exciting the structure with a band-limited white noise ground acceleration (0-50 Hz) with the actuator and tendons in place and the actuator command set to zero. Similarly, the experimental transfer functions from the actuator command signal to each of the

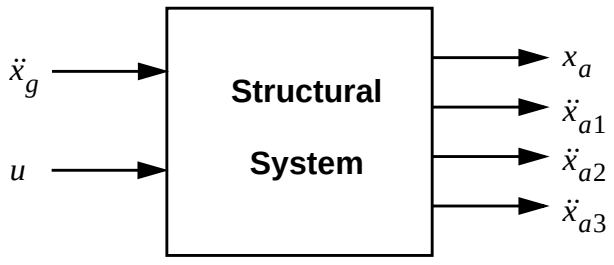

Figure 5.3 Block Diagram Representation of the Active Tendon System.

measured outputs were determined by applying a band-limited white noise (0-50 Hz) to the actuator command while the ground was held fixed.

Figures 5.4–5.6 show representative magnitude and phase plots for the experimentally determined transfer functions. All transfer functions were obtained using twenty averages (*i.e.*, $M = 20$ in Eqs. (2.7–2.8)). Figure 5.4 presents the transfer function from the ground acceleration $\ddot{x}_g$ to the first floor acceleration $\ddot{x}_{a1}$ (with the input to the control actuator set to zero). Note the three distinct, lightly-damped modes occurring in each of the transfer functions. These peaks occur at 2.33 Hz, 7.37 Hz, and 12.24 Hz and correspond to the first three modes of the structural system. Similarly, the experimental transfer function from the control command *u* to the first floor acceleration $\ddot{x}_{a1}$ (setting the input to the earthquake simulator to zero) is depicted in Fig. 5.5. Note the significant high fre-

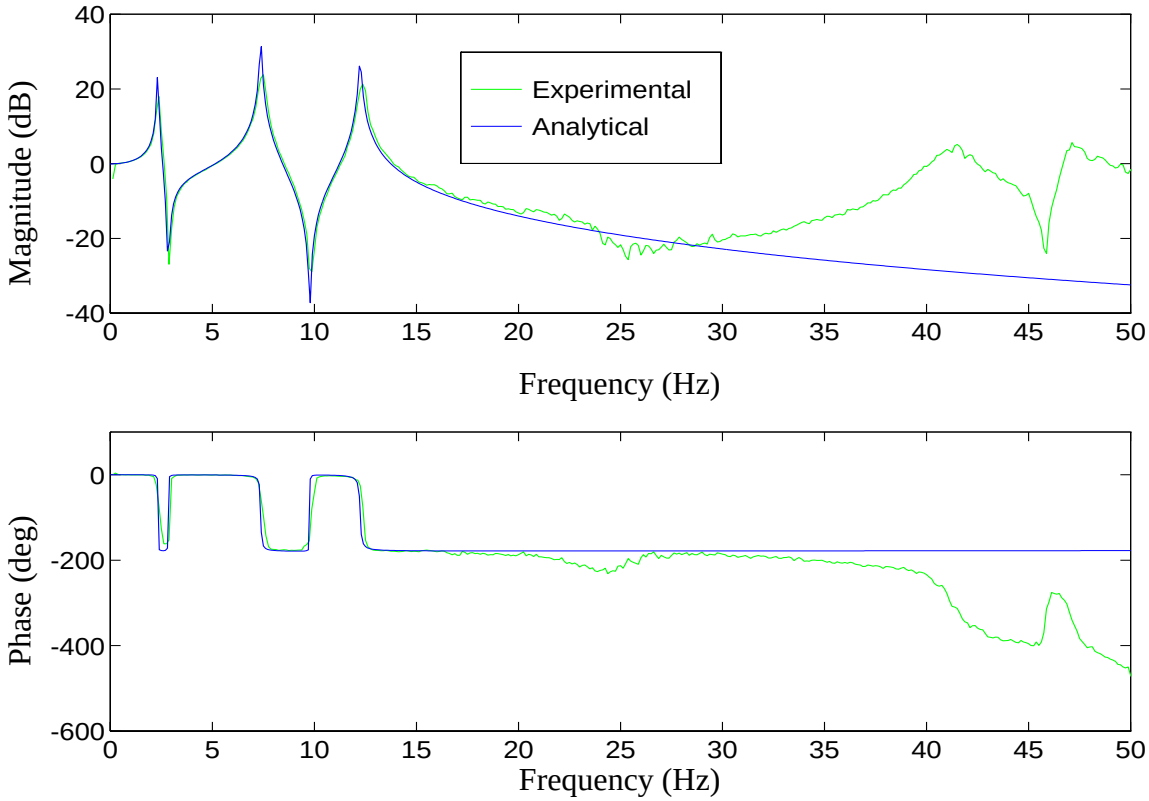

Figure 5.4 Transfer Function from Ground Acceleration to First Floor Acceleration.

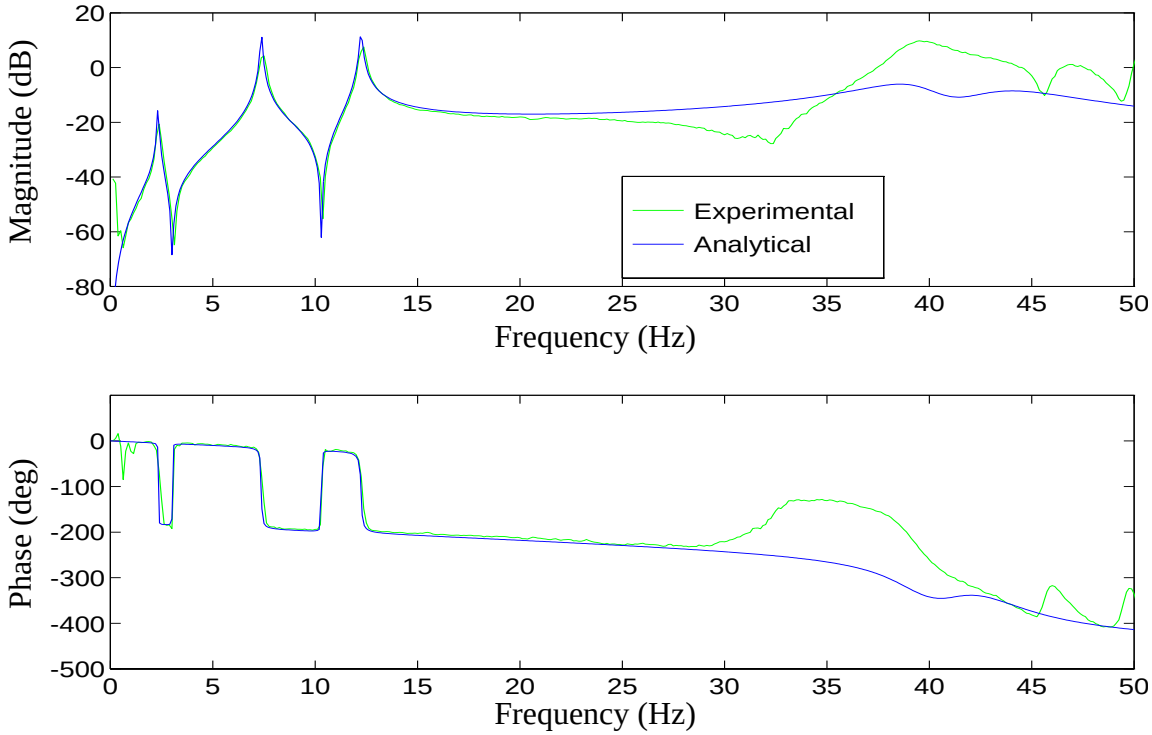

Figure 5.5 Transfer Function from Actuator Command to First Floor Acceleration.

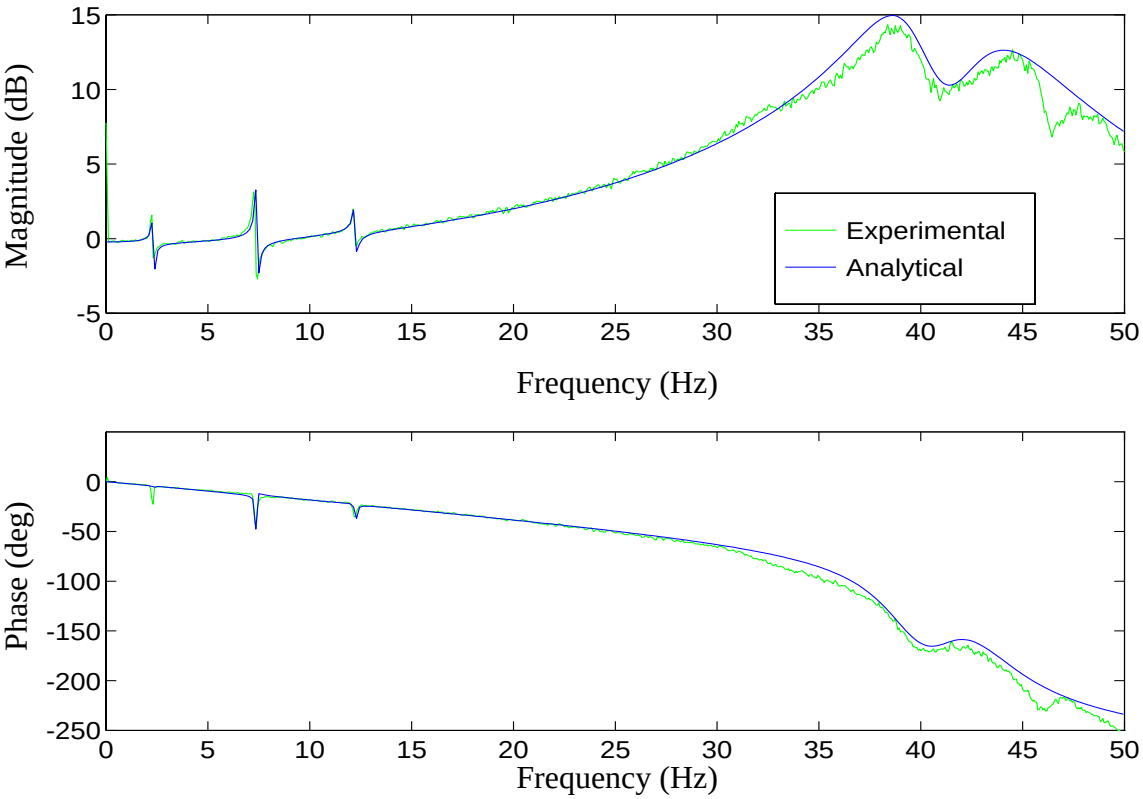

Figure 5.6 Transfer Function from Actuator Command to Actuator Displacement.

quency dynamics present; the magnitude of the transfer function at 40 Hz is as great as that corresponding to the building's primary modes. Clearly, these dynamic effects must be considered in the control design.

Figure 5.6 shows the transfer function from the actuator command *u* to the actuator displacement (*i.e.*, the actuator transfer function). As expected, this transfer function has the same three lightly damped modes of the structural system that are seen in Figs. 5.4 and 5.5. In addition, there are significant dynamics at high frequencies that correspond to actuator modes. These actuator dynamics are the primary source of the high frequency dynamics seen in the transfer functions in Figs. 5.4 and 5.5. If the gain on the stabilization loop of the hydraulic actuator is reduced, these high frequency dynamics are greatly reduced, although at the expense of a more slowly responding actuator. To observe this effect, the actuator transfer function was experimentally determined for two different feedback gains. The two transfer functions are compared in Fig. 5.7. Notice that reducing the feedback gain causes the actuator transfer function to roll off at a lower frequency and the actuator dynamics to be highly damped.

Once the experimental transfer functions have been obtained, the next step in the system identification procedure is to model the transfer functions as a ratio of two polynomials in the Laplace variable *s*. In this step, the effects of control-structure interaction should be consistently incorporated into the identification process. For the system under consideration, the results in Chapter 3 (see also Dyke, *et al*. (1993, 1995)) show that the poles of the structure (including the active tendons) will appear as zeros of the transfer function from the command input to the actuator displacement. This phenomenon occurs regardless of how fast (or slow) the actuator responds. The predicted behavior is clearly seen in Fig. 5.6, where there is nearly a pole/zero cancellation at the first three modes of the structural system. These zeros correspond to the poles of the transfer function from the actuator dis-

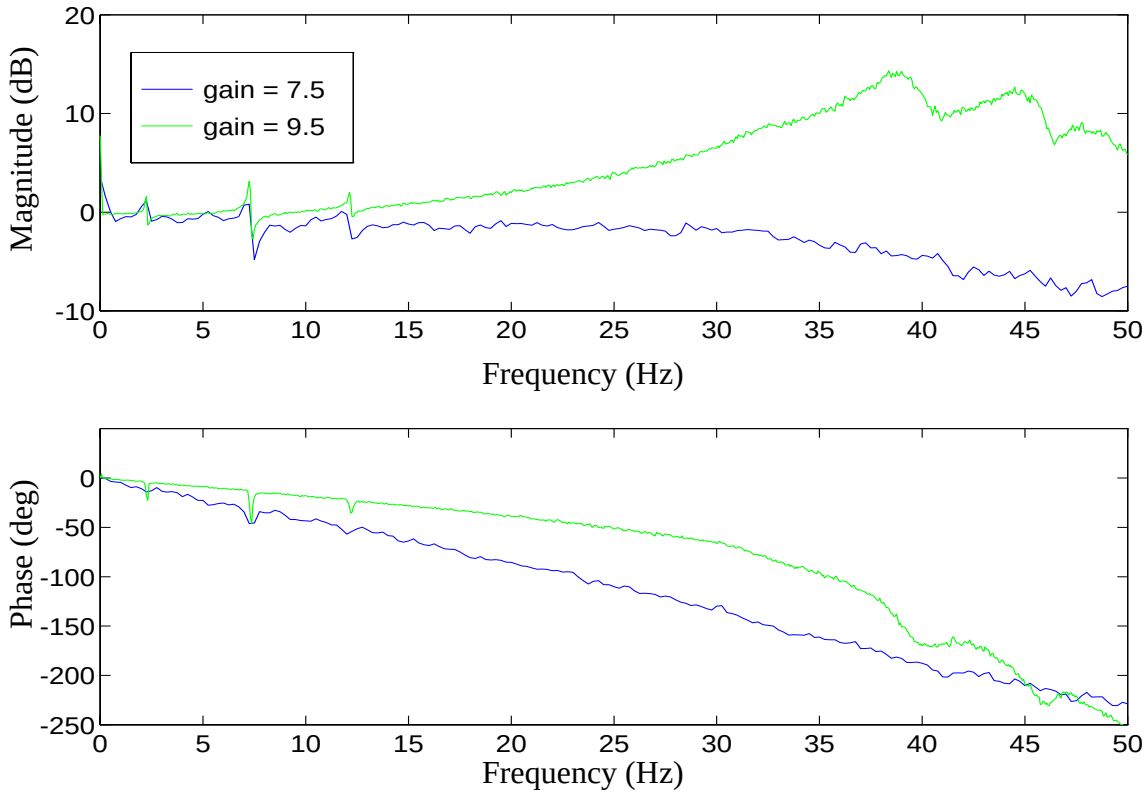

Figure 5.7 Comparison of Actuator Transfer Functions for Various Feedback Gains.

placement to the building responses. The near cancellation of these poles and zeros occurs because the tendons applying the control force to the structure are relatively flexible, as compared to the building stiffness. If one did not anticipate the effect of control-structure interaction, the transfer function for the actuator shown in Fig. 5.6 might have been assumed to be unity over the interval from 0–20 Hz. In addition, the mass of the frame connecting the tendons to the actuator is not negligible and has a significant effect on the dynamics of the system. The frame must be viewed as an additional degree-of-freedom in the system. This extra degree-of-freedom was implicitly incorporated into the system model.

Herein, it was decided that the control of the first three modes was desired; thus the model of the system needed to be accurate to approximately 20 Hz. Therefore, significant

control effort should not be applied at frequencies above 20 Hz. The techniques used to roll-off the control effort were discussed in Chapter 2.

The mathematical models of the transfer functions are overlaid in Figs. 5.4–5.6. The identified poles of the structural system are: $-0.005 \pm 2.33j$, $-0.030 \pm 7.37j$, $-0.050 \pm 12.24j$, $-2.01 \pm 39.22j$, $-3.03 \pm 43.26j$, and -140 (in Hz). The quality of the mathematical models for the remaining transfer functions was similar to that depicted in Figs. 5.4–5.6.

Next, the model was assembled in state space form. Because the transfer function characteristics from the ground to the building response were dominated by the dynamics of the building (see Fig. 5.4), the system corresponding to the ground acceleration input (Eq. 2.11) required six states, associated with the three modes of the building, to accurately model the experimental transfer functions over the frequency range of interest. The second state equation (Eq. 2.12), modeling the input/output relationship between the actuator command u and the responses **y,** had eleven states corresponding to the eleven poles identified previously. Once each of the two state space systems were assembled, the states of the individual systems were stacked, as described in Chapter 2, to form a combined system. The model reduction procedure was applied, and the seventeen state system was reduced to a tenth-order system. Six of the eliminated states corresponded to six redundant states corresponding to the building dynamics. The additional state that was eliminated corresponded to the very fast pole at 140 Hz found in the original system identification.

To ensure that information was not lost in the model reduction, the transfer functions of the reduced order system were compared to the transfer functions of the original model. All of the eight input/output relationships matched the original model well. A representative comparison of the reduced order model and the original model is shown in Figs. 5.8 (transfer function from actuator command to the first floor absolute acceleration) and 5.9

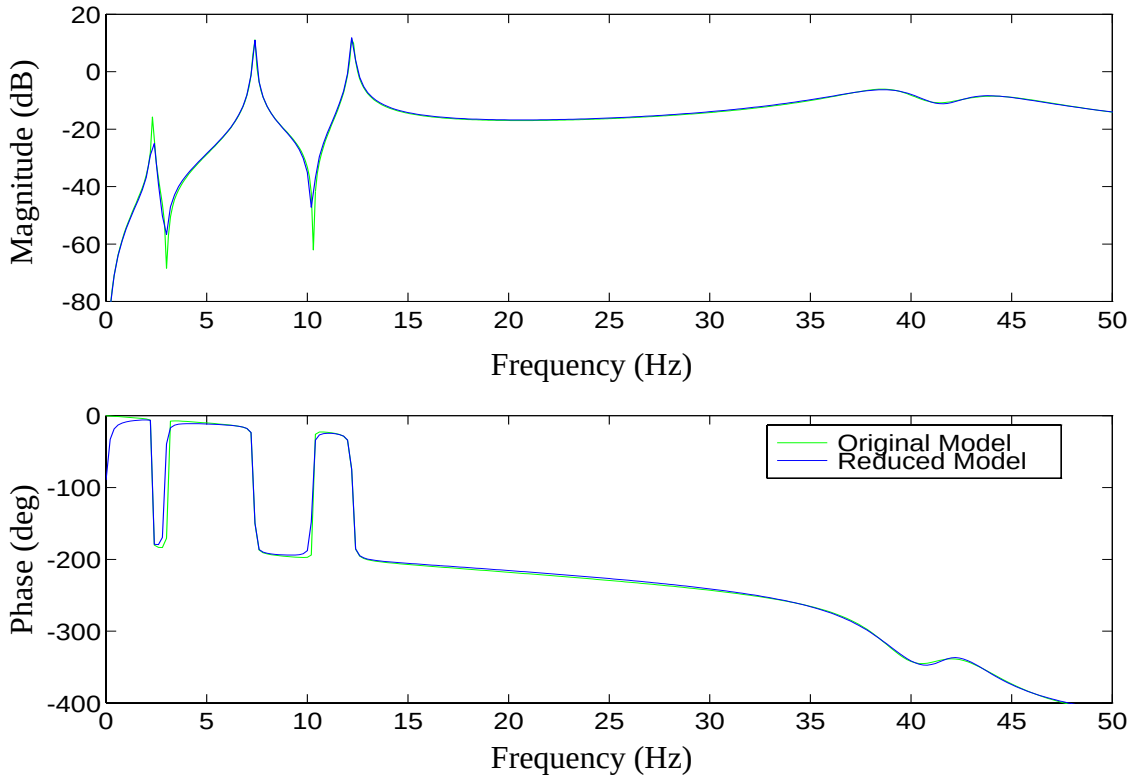

Figure 5.8 Comparison of the Reduced Order Model and Original Model Transfer Functions: Actuator Command to the First Floor Absolute Acceleration.

(transfer function from ground acceleration to the first floor absolute acceleration). In each case, the two functions are almost indiscernible, indicating that little information was lost in the model reduction. The model was used as a basis for the control designs discussed in the next section. All of the experimental transfer functions are compared to the reduced order model in Figs. 5.10 through 5.17.

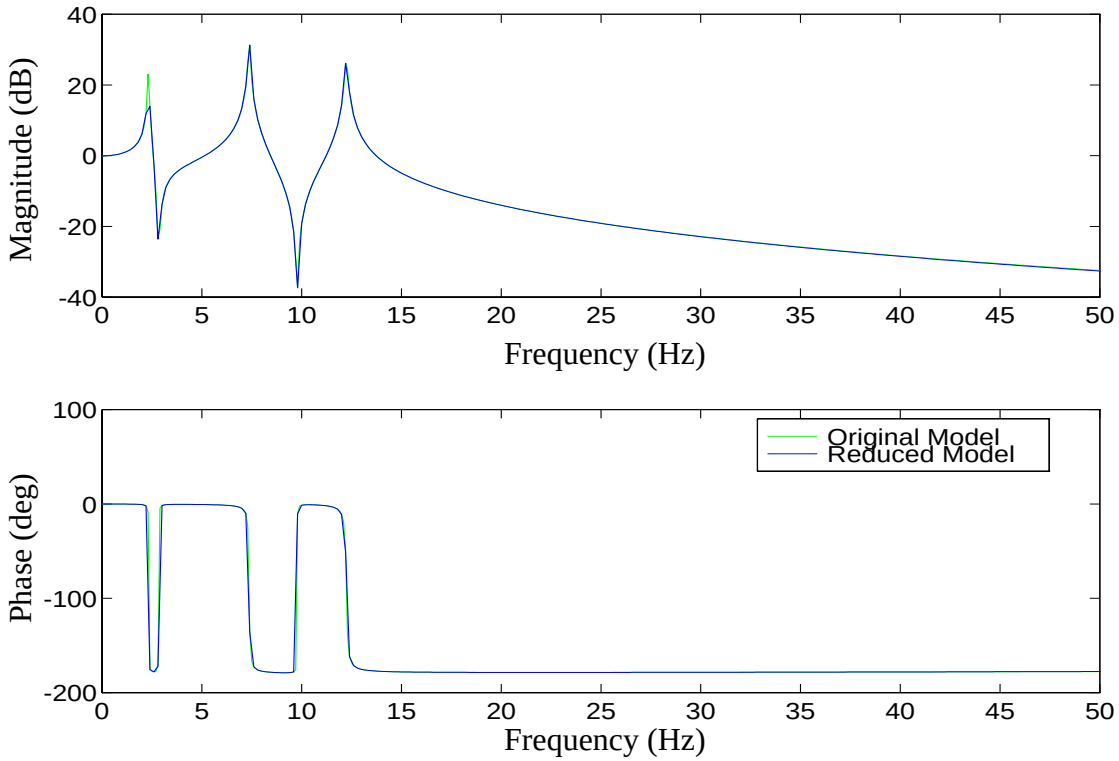

Figure 5.9 Comparison of the Reduced Order Model and Original Model Transfer Functions: Ground Acceleration to the First Floor Absolute Acceleration.

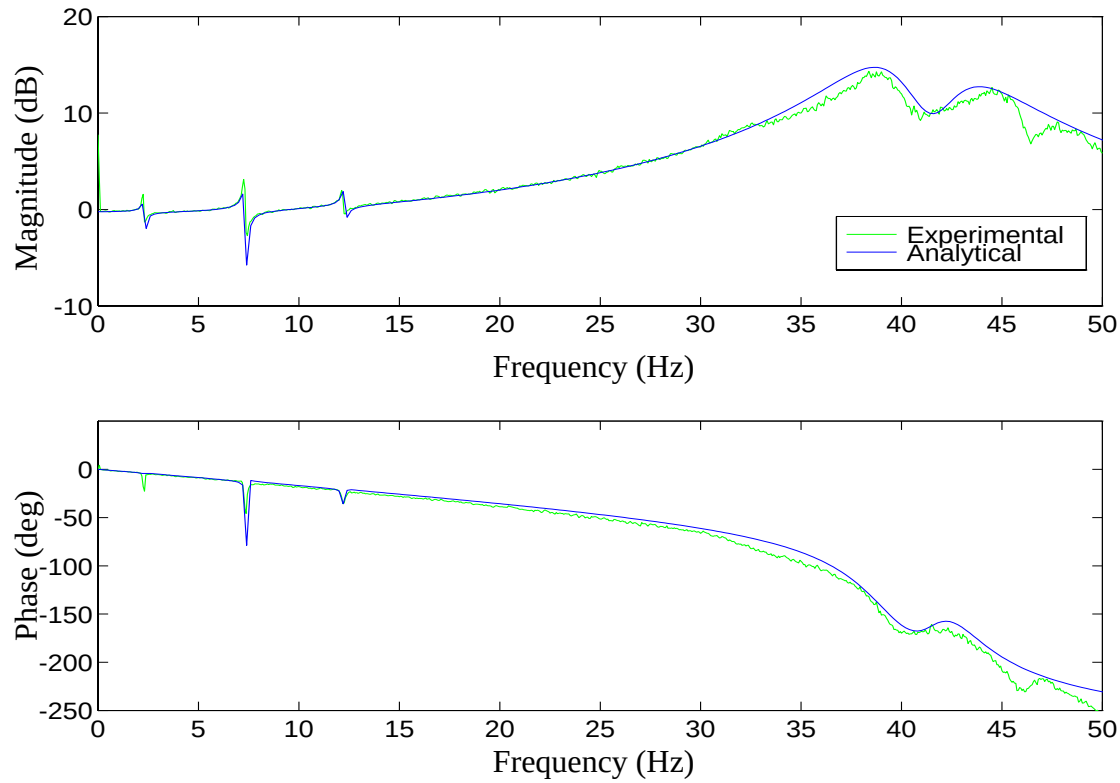

Figure 5.10 Comparison of Reduced-Order Model and Experimental Transfer Function: Actuator Command to the Actuator Displacement.

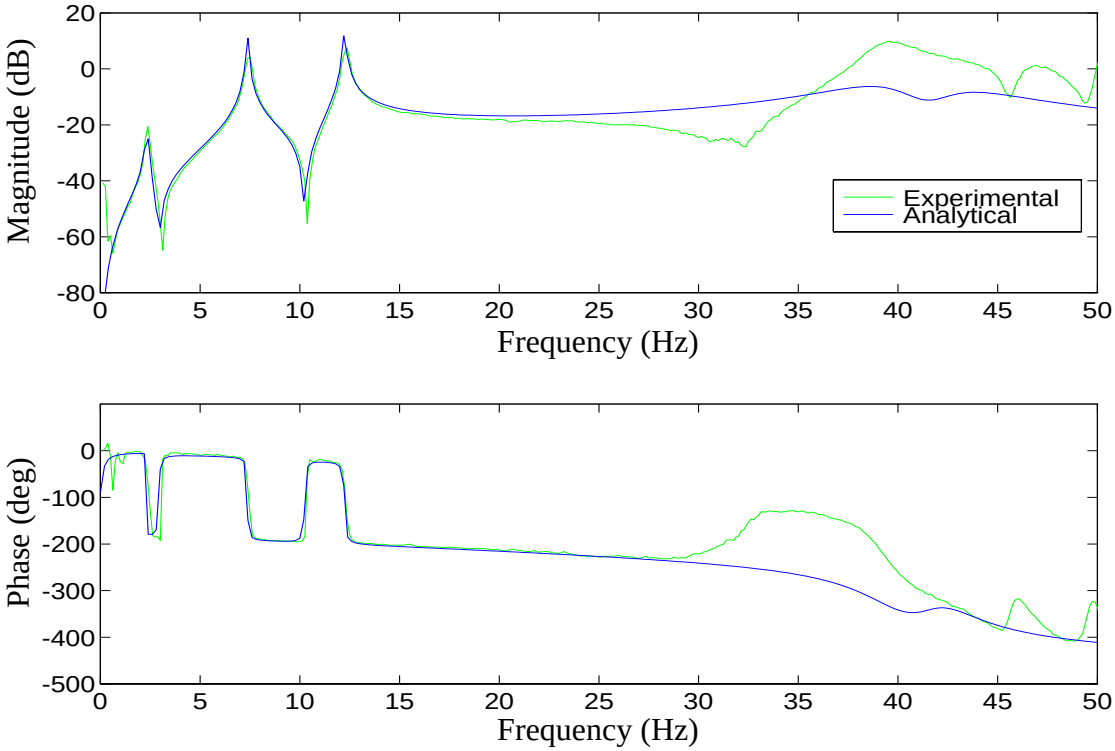

Figure 5.11 Comparison of Reduced-Order Model and Experimental Transfer Function: Actuator Command to the First Floor Absolute Acceleration.

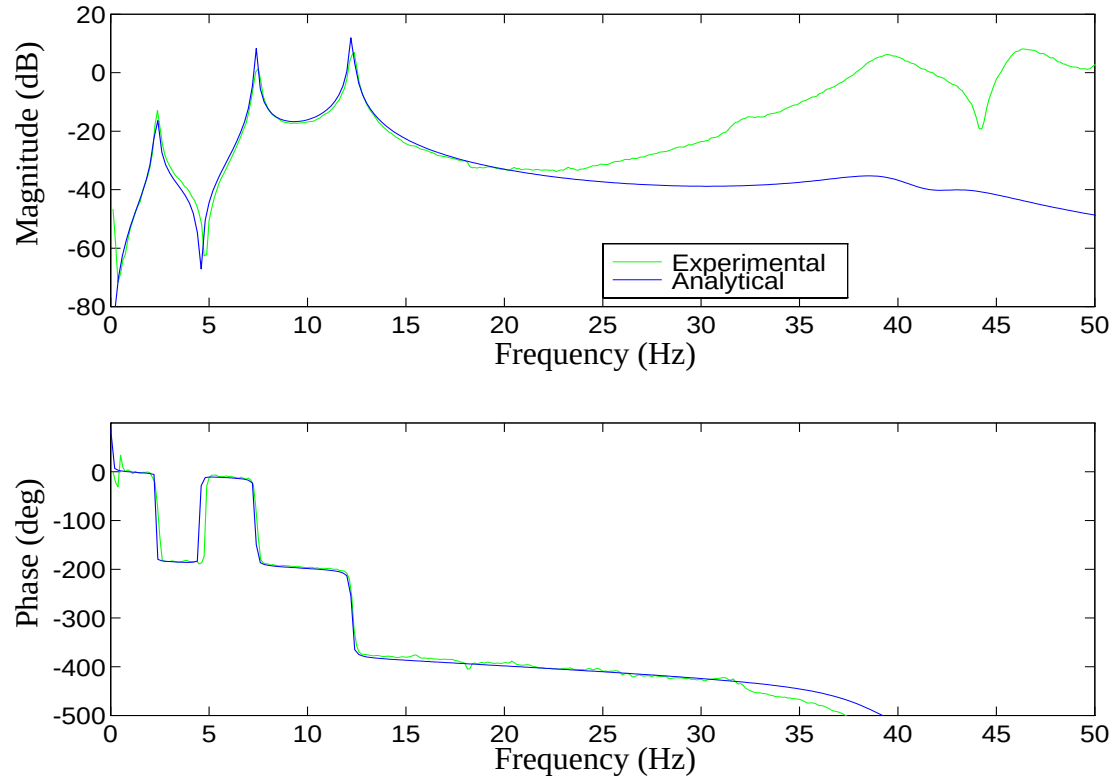

Figure 5.12 Comparison of Reduced-Order Model and Experimental Transfer Function: Actuator Command to the Second Floor Absolute Acceleration.

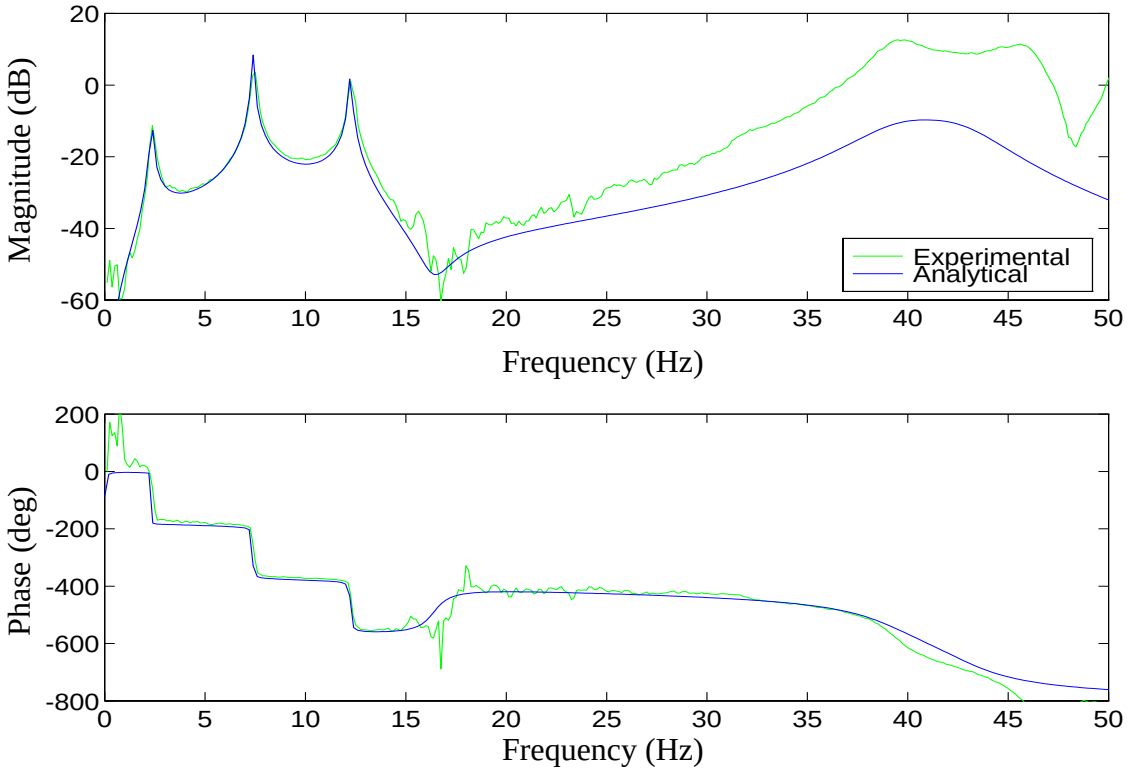

Figure 5.13 Comparison of Reduced-Order Model and Experimental Transfer Function: Actuator Command to the Third Floor Absolute Acceleration.

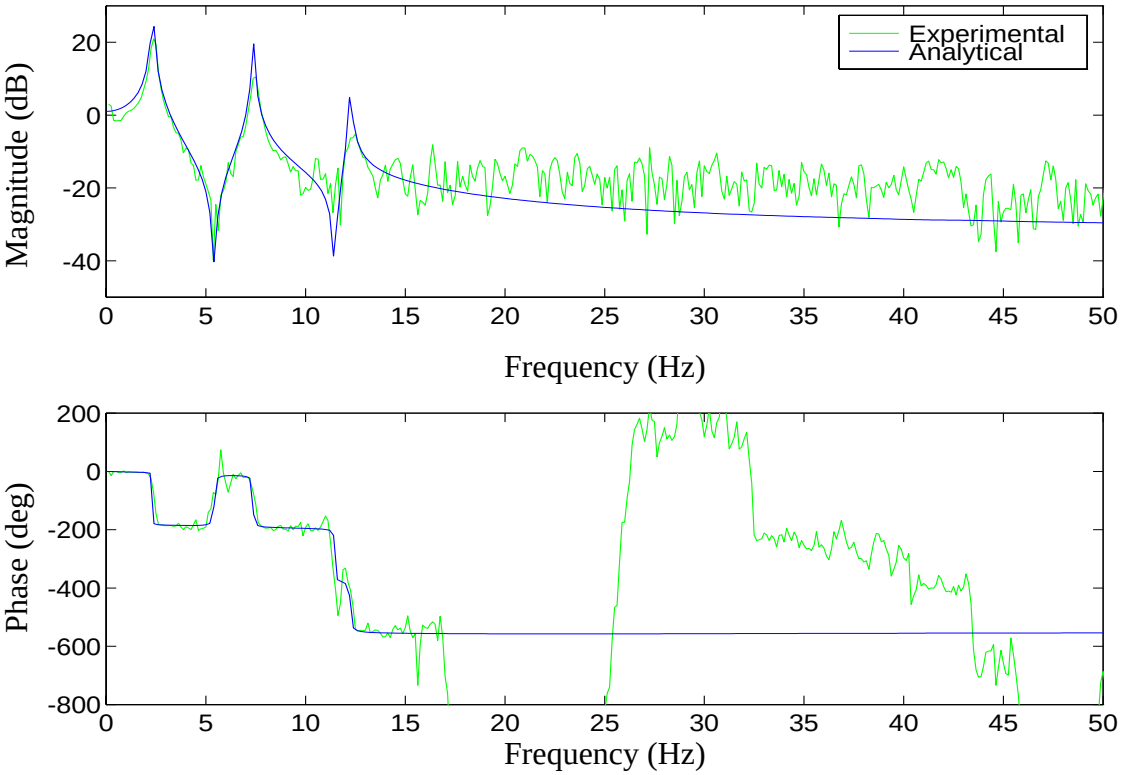

Figure 5.14 Comparison of Reduced-Order Model and Experimental Transfer Function: Ground Acceleration to the Actuator Displacement.

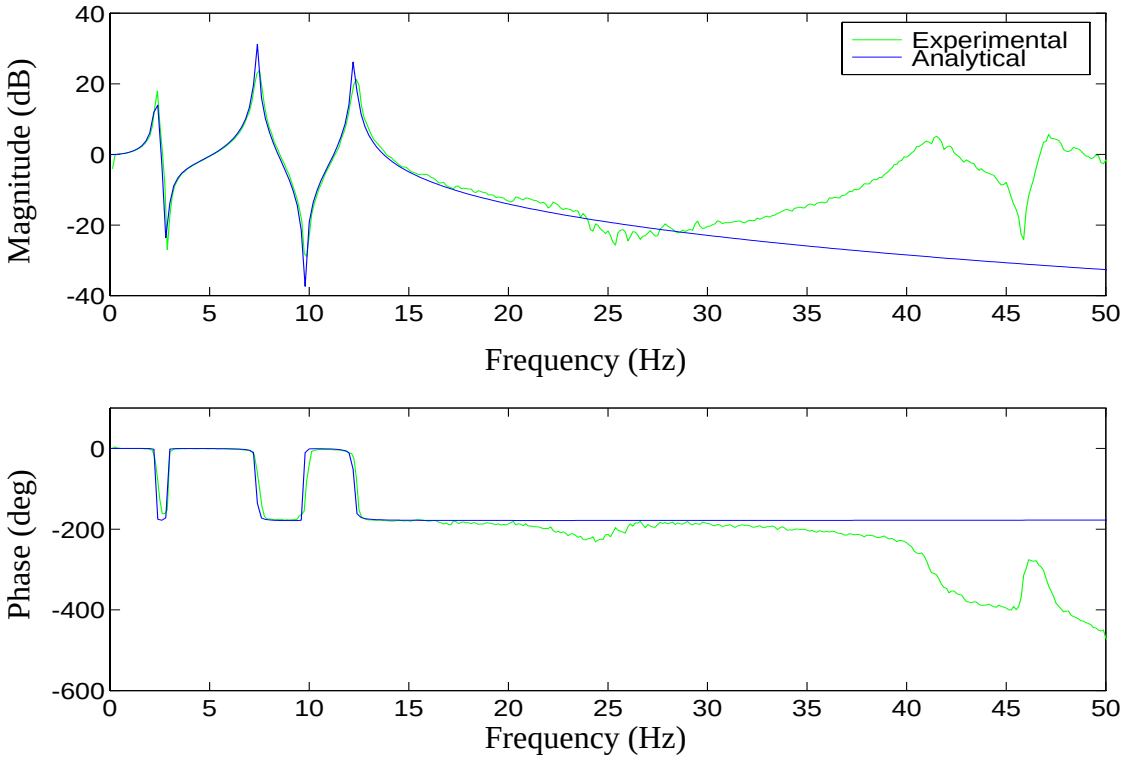

Figure 5.15 Comparison of Reduced-Order Model and Experimental Transfer Function: Ground Acceleration to the First Floor Absolute Acceleration.

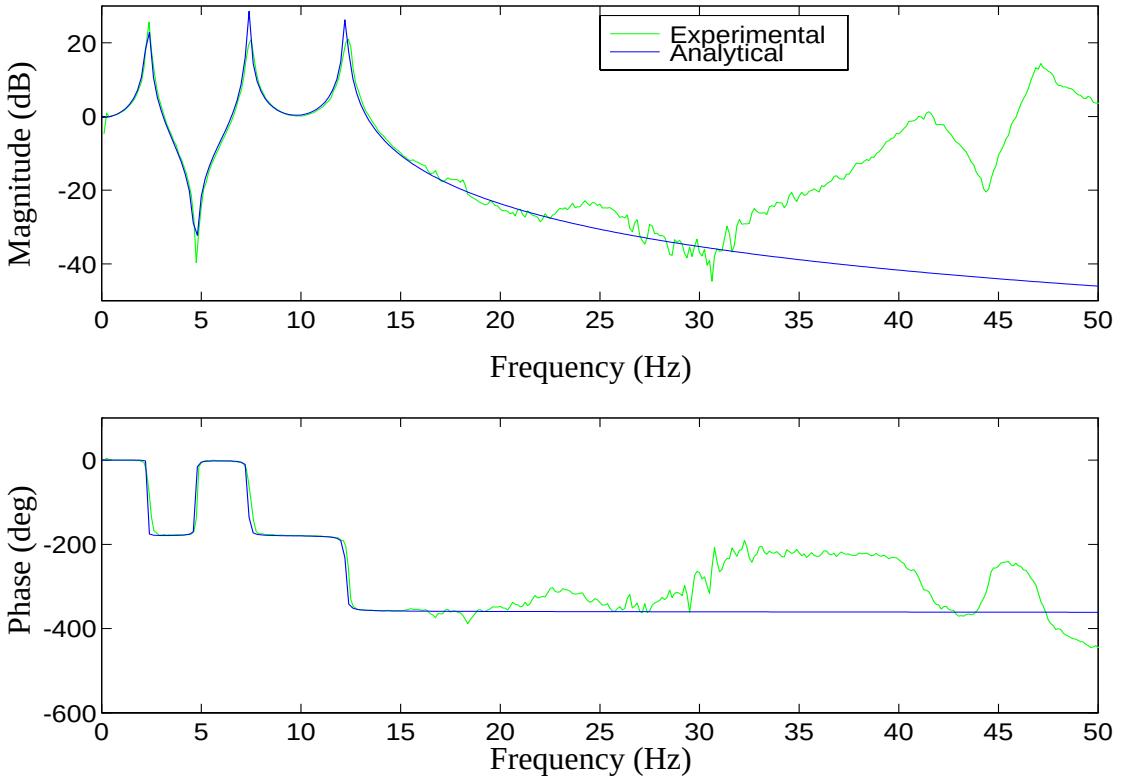

Figure 5.16 Comparison of Reduced-Order Model and Experimental Transfer Function: Ground Acceleration to the Second Floor Absolute Acceleration.

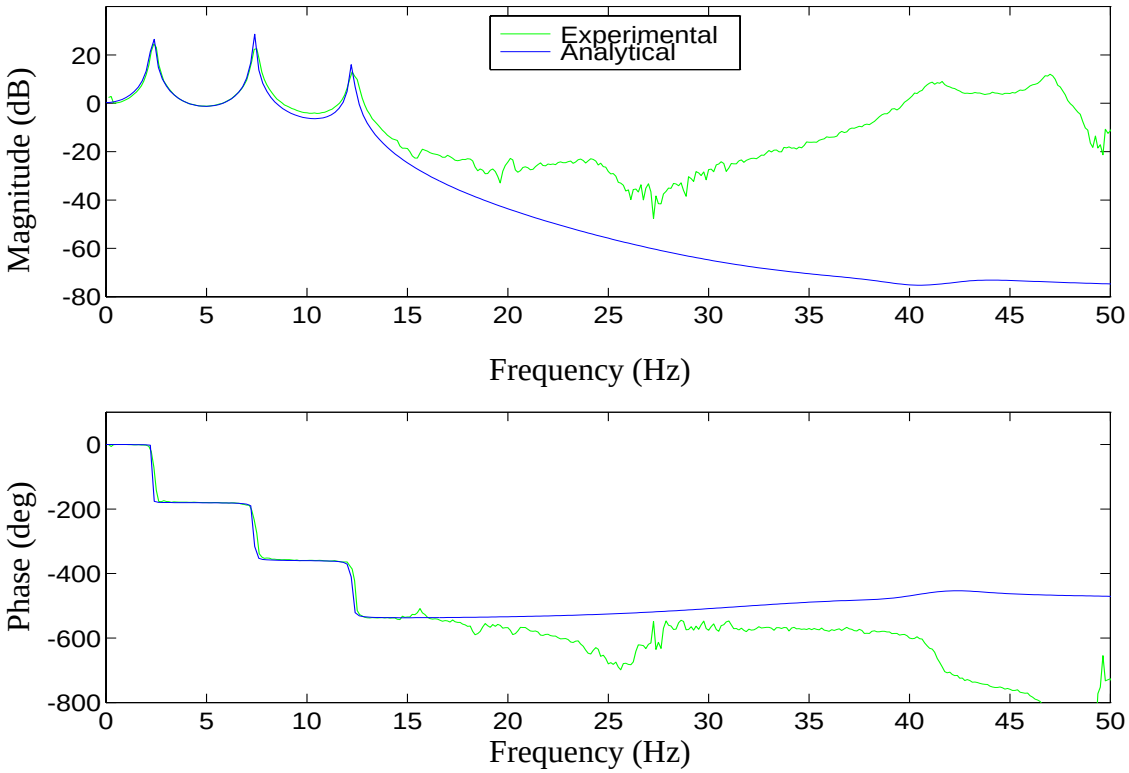

Figure 5.17 Comparison of Reduced-Order Model and Experimental Transfer Function: Ground Acceleration to the Third Floor Absolute Acceleration.

5.3 Control Design and Experimental Results

After the data that was used for system identification was collected, a period of several weeks elapsed until the controllers were actually implemented. Before implementing the controllers, the transfer functions of the system were again determined to verify that the system model on which the controller designs were based was still valid. During the time between the system identification tests and implementation of the control designs the structural system *softened*, resulting in approximately a 1% decrease in the frequencies of the first three modes. However, the control designs were robust enough to account for the slight differences. All of the twenty-one control designs which were implemented produced a significant reduction in the responses. Ten of the controllers were thoroughly tested with various excitations, and the results of five representative controllers are provided.

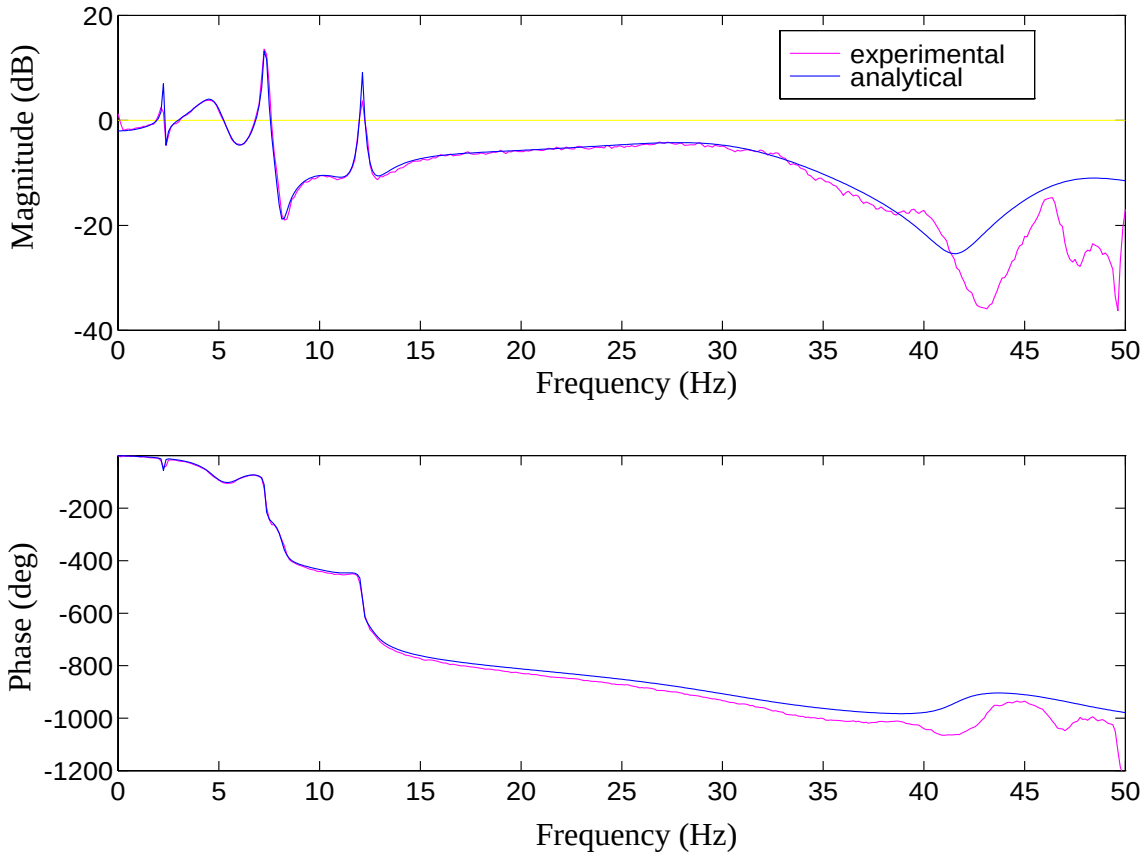

Figure 5.18 Experimental and Analytical Loop Gain for Controller E.

Extensive testing was conducted for all components of the control hardware and software before the experiments were performed to control the structure. One of the final tests was to experimentally determine the loop gain transfer function by attaching the measured outputs from the building to the inputs of the controller (*i.e.*, the DSP board). The loop gain transfer function was then calculated by exciting the actuator command input with a broadband excitation and measuring the controller output. Figure 5.18 compares the experimental and analytical loop gain transfer functions for one of the test controllers (Controller E as defined in Table 5.1). The two transfer functions are nearly identical below 40 Hz, indicating that the controller was working as expected and the system model was accurate.

Two different types of tests were conducted on the earthquake simulator to verify the control designs. A band-limited white noise ground excitation (0-10 Hz) was first used to excite the structure to observe the ability of the controllers to reduce the *rms* values of the structural responses. In the second type of test, the earthquake simulator reproduced a recorded accelerogram to determine the ability of the controllers to reduce the peak structural responses. For this test, two earthquakes were chosen for controller verification: 1) an El Centro earthquake excitation (N-S component), and 2) a Taft earthquake excitation (North 21 East component). The magnitude of the earthquakes were reduced to one-quarter (El Centro) and one-half (Taft) of the recorded intensity to reduce the possibility of damaging the structure. Also, because the test structure was a scaled model of a prototype structure, similitude relations dictated that both earthquakes be reproduced at double the speed of the recorded earthquakes.

5.3.1 Development and Validation of Simulation Model

As discussed previously, the characteristics of the system changed slightly between the time that the original data (used for control design) was taken and the controllers were implemented. After completion of the experiments, a revised simulation model was developed based on the data taken when the control experiments were conducted. This was the model used in all comparisons between the analytical and experimental results. Using the eigenvectors of the system matrix for the original model, and modified values for the eigenvalues from the new data, a revised system matrix was formed.

By exciting the model with the measured base accelerations, a simulation of the uncontrolled system was performed to verify the new model of the structural system. *Uncontrolled*, in this context, refers to the structural system with the tendons in place and the actuator command set to zero. In Figs. 5.19a-c and 5.20a-c, the experimental and sim-

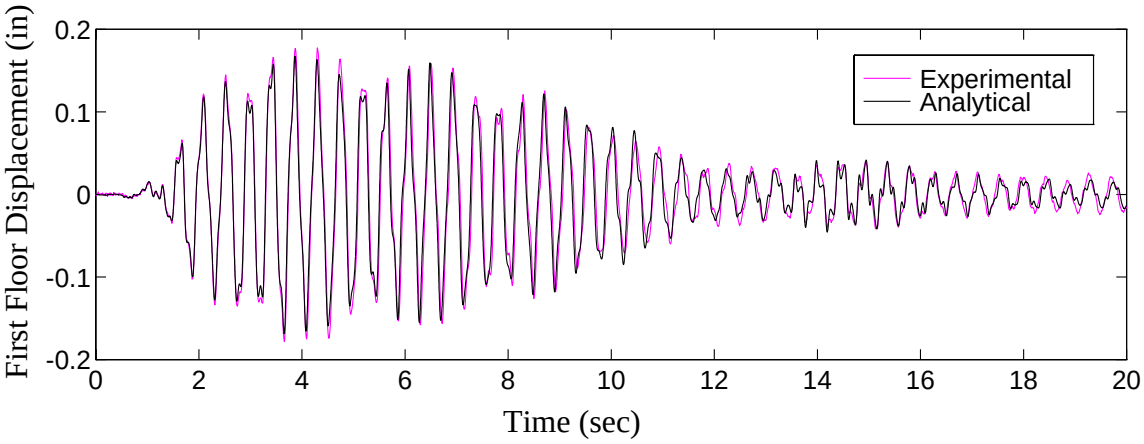

a) First Floor Relative Displacement

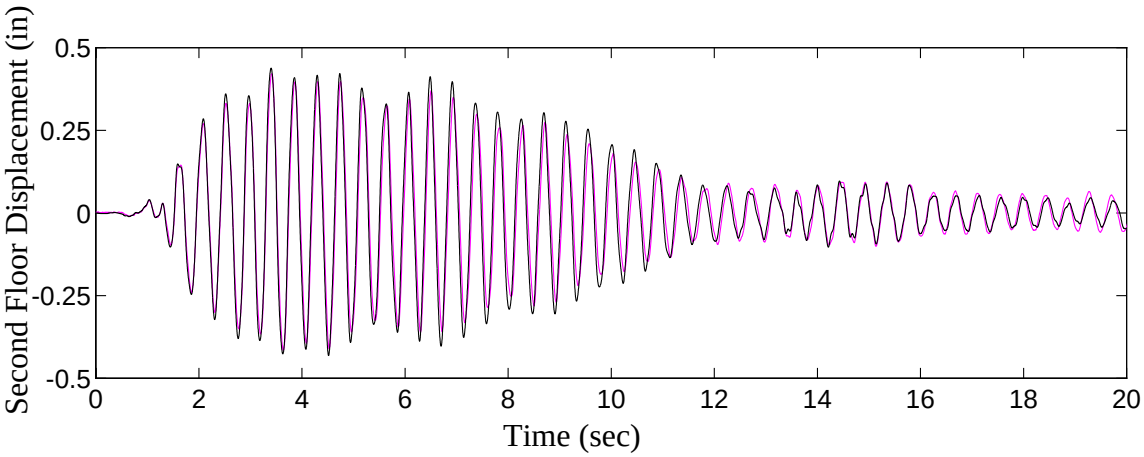

b) Second Floor Relative Displacement

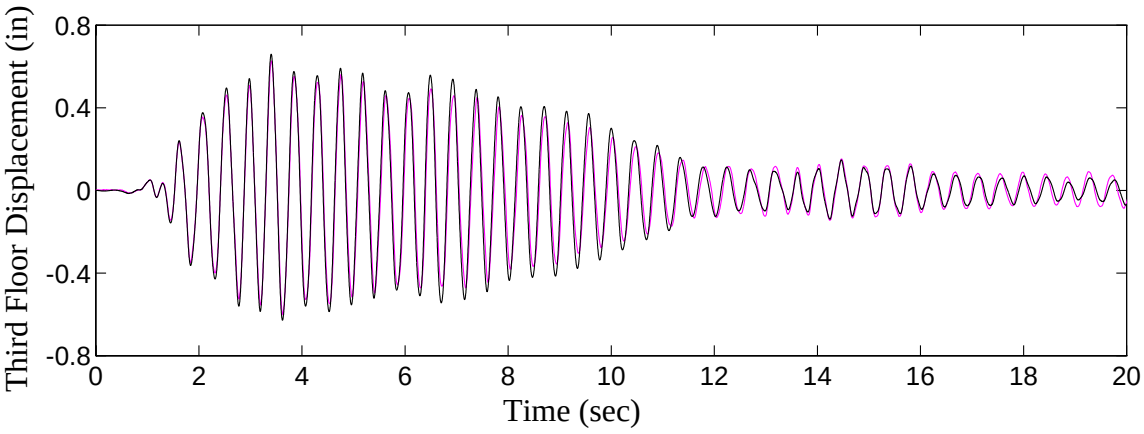

c) Third Floor Relative Displacement

Figure 5.19 Uncontrolled Experimental and Simulated Relative Displacements with Scaled El Centro Excitation.

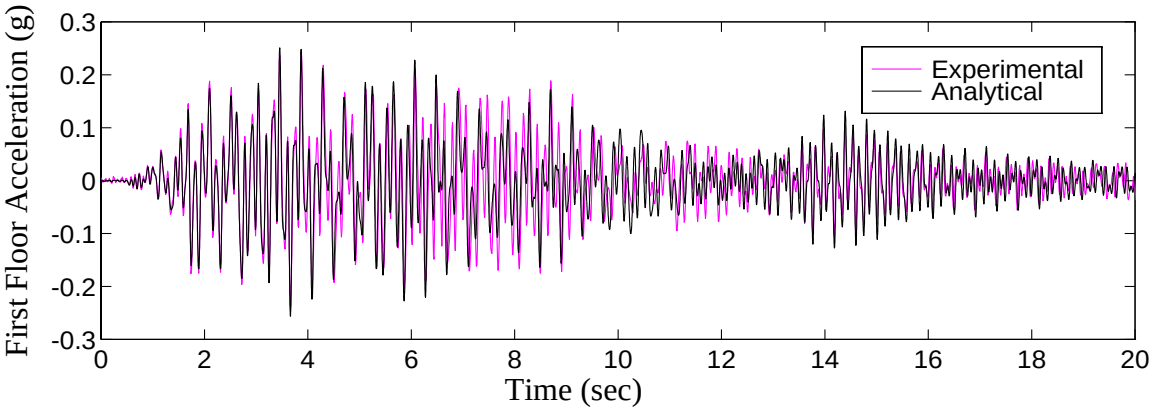

a) First Floor Absolute Acceleration

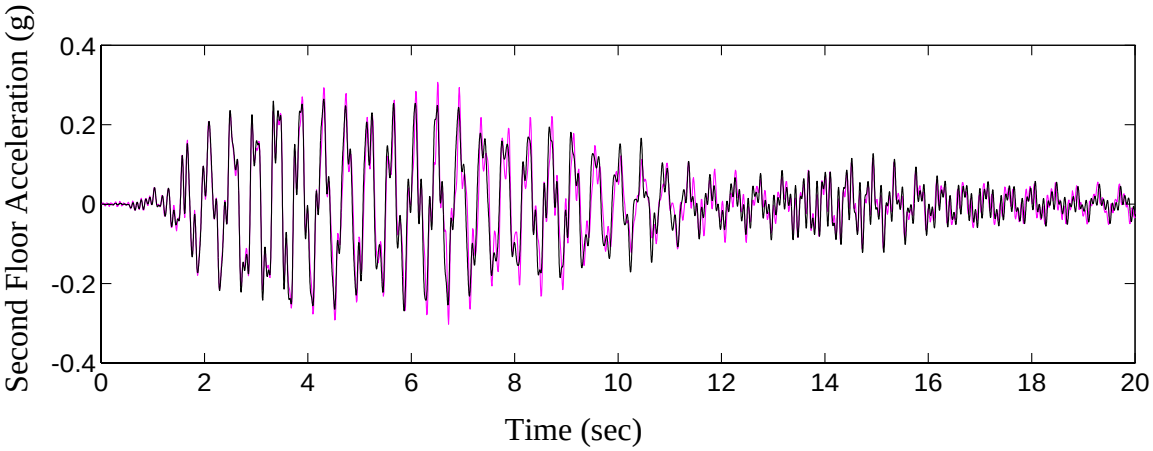

b) Second Floor Absolute Acceleration

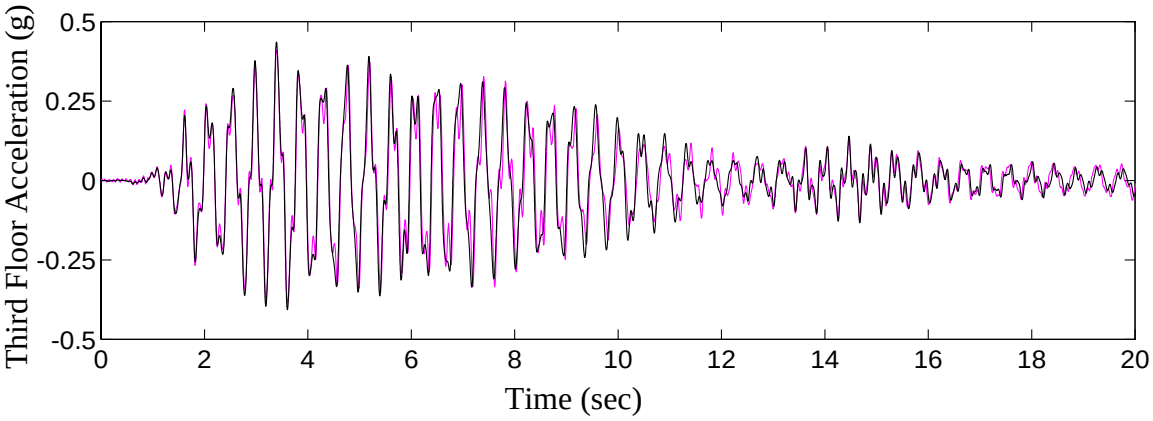

c) Third Floor Absolute Acceleration

Figure 5.20 Uncontrolled Experimental and Simulated Absolute Accelerations with Scaled El Centro Excitation.

ulated time responses of the first, second and third floor relative displacements and absolute accelerations for a quarter scale El Centro excitation are compared for verification of the simulation model. In all cases, the experimental and analytical responses matched well, indicating that the simulation model is quite accurate. In addition, the analytical loop gain shown in Fig. 5.18 corresponds to this model. The analytical and experimental loop gains match well, indicating that the controller was operating as expected. Again, notice that the experimental and analytical loop gains match well in the frequency range of interest, indicating that the model is accurate and the control system is behaving as expected.

5.3.2 Discussion of Results and Comparison to Simulation

Twenty-one control designs were implemented, all of which were designed based on the original model. In all of the controller designs considered, the weighting function on the regulated output, $\mathbf{W}$, was a constant matrix (*i.e.*, independent of frequency). The earthquake filter **F** is modeled based on the Kanai–Tajimi spectrum. The performance of all of the candidate controllers is evaluated analytically and experimentally. Each controller performed well and none resulted in unstable systems.

Ten of the control designs were chosen for further study. The results of five representative control designs, designated A–E, are presented herein. Table 5.1 lists the five controllers with a description of the corresponding control strategy employed for each design. The performance objective in the design of Controller A was to minimize the relative displacements of the structure. This was achieved by weighting the three displacements equally and applying a smaller weighting to the actuator displacement. Controller B was designed to minimize the interstory displacements. In this case a weighting matrix was chosen which corresponded to weighting the three interstory displacements and a smaller weighting was applied to the actuator displacement. The performance objective in the

Table 5.1 Description of Control Strategies for Each Design.

Controller	*Control Strategy*
A	*Equal weighting on all three relative displacements and small weighting on the actuator displacement*
B	*Weighting on the interstory displacements and small weighting on the actuator displacement*
C	*Equal weighting on all three absolute accelerations*
D	*Weighting on third floor absolute acceleration*
E	*Weighting on third floor absolute acceleration and measurement of ground excitation*

design of Controller C was to minimize the absolute accelerations of the structure. This was achieved by placing equal weighting on all three absolute accelerations. Controller D was designed by weighting only the absolute acceleration of the third floor. Since the largest response in the fundamental mode is at the third floor, this approach serves to minimize all the structural responses in the fundamental mode. In Controller E an additional measurement, the base acceleration, was included in the measurement vector, and the absolute acceleration of the third floor was weighted.

The experimental and simulated responses for Controllers A–E are provided in Tables 5.2, 5.3 and 5.4. Table 5.2 provides *rms* responses of each controlled system to a broadband excitation (0-10 Hz) and Tables 5.3 and 5.4 report peak responses to the scaled El Centro and Taft excitations, respectively. Values for the absolute accelerations, $\ddot{x}_{ai}$, relative displacements, x_i, interstory displacements, actuator displacement, x_a, and control signal, u_c, are provided. The results include *rms* responses in the case of the band-limited white noise excitation and peak responses for the scaled El Centro and Taft excitations. The percent reduction of each controlled response relative to the corresponding uncontrolled response is given in parentheses. Note the excellent agreement between the results predicted by the simulation and those obtained in the experiment. The force in the tendons

Table 5.2 *RMS* Responses of Controlled System to Broadband Excitation (0–10 Hz).

Controller	$\ddot{x}_{a1}, \frac{in}{s^2}$	$\ddot{x}_{a2}, \frac{in}{s^2}$	$\ddot{x}_{a3}, \frac{in}{s^2}$	x_1, *in*	x_2, *in*	x_3, *in*	$x_2 - x_1$ *in*	$x_3 - x_2$ *in*	*f, lbf*	x_a, *in*	u_c *Volts*
Experimental *RMS* Responses for Bandlimited White Noise Ground Excitation											
uncontrolled	36.1	39.7	53.0	0.065	0.161	0.228	0.097	0.071	444.0	0.002	—
A	20.5 (43.2)	18.2 (54.0)	23.8 (55.1)	0.026 (60.8)	0.061 (61.9)	0.087 (61.9)	0.037 (61.5)	0.029 (59.1)	183.6 (58.6)	0.008	0.162
B	17.7 (51.0)	18.2 (54.1)	24.4 (53.9)	0.028 (57.0)	0.070 (56.4)	0.100 (56.2)	0.043 (55.7)	0.032 (55.1)	205.6 (53.7)	0.006	0.125
C	14.1 (61.0)	15.1 (62.0)	20.3 (61.6)	0.025 (61.2)	0.062 (61.7)	0.087 (61.8)	0.037 (61.7)	0.027 (62.0)	170.1 (61.7)	0.008	0.168
D	13.7 (62.0)	13.8 (65.3)	18.2 (65.6)	0.024 (64.0)	0.055 (65.9)	0.077 (66.4)	0.033 (66.5)	0.024 (66.6)	147.2 (66.8)	0.010	0.210
E	13.5 (62.7)	13.3 (66.4)	17.5 (67.0)	0.023 (65.0)	0.053 (67.2)	0.074 (67.7)	0.031 (67.9)	0.023 (68.1)	141.3 (68.2)	0.011	0.220
Simulation *RMS* Responses for Bandlimited White Noise Ground Excitation											
uncontrolled	34.7	39.5	52.5	0.059	0.160	0.225	0.104	0.071	413.6	0.002	—
A	19.7 (43.2)	18.6 (52.9)	22.7 (56.9)	0.025 (57.8)	0.062 (61.3)	0.087 (61.4)	0.040 (61.4)	0.029 (58.7)	175.4 (57.6)	0.009	0.187
B	17.0 (50.8)	18.7 (52.7)	24.3 (53.8)	0.027 (54.1)	0.072 (54.9)	0.102 (54.7)	0.047 (54.7)	0.033 (54.3)	195.3 (52.8)	0.007	0.141
C	13.5 (61.0)	15.3 (61.2)	20.2 (61.6)	0.025 (57.3)	0.064 (60.2)	0.089 (60.6)	0.040 (61.1)	0.027 (61.9)	157.9 (61.8)	0.010	0.195
D	13.1 (62.1)	13.9 (64.9)	17.7 (66.4)	0.024 (59.5)	0.056 (64.9)	0.077 (65.7)	0.035 (66.6)	0.023 (67.3)	134.0 (67.6)	0.013	0.250
E	12.9 (62.9)	13.4 (66.1)	16.9 (67.9)	0.023 (60.1)	0.054 (66.1)	0.074 (67.2)	0.033 (68.2)	0.022 (68.9)	132.8 (67.9)	0.013	0.266

Table 5.3 Peak Responses of Controlled System for Quarter Scale El Centro Excitation.

Controller	$\ddot{x}_{a1}, \frac{in}{s^2}$	$\ddot{x}_{a2}, \frac{in}{s^2}$	$\ddot{x}_{a3}, \frac{in}{s^2}$	x_1, *in*	x_2, *in*	x_3, *in*	$x_2 - x_1$ *in*	$x_3 - x_2$ *in*	*f, lbf*	x_a, *in*	u_c *Volts*
Experimental Peak Responses for Scaled El Centro Earthquake Excitation.											
uncontrolled	93.0	118.7	158.6	0.178	0.421	0.627	0.273	0.209	1156	0.005	—
A	68.3 (26.6)	64.6 (45.5)	97.7 (38.4)	0.100 (44.1)	0.221 (47.6)	0.318 (49.4)	0.140 (48.9)	0.115 (44.8)	629.6 (45.5)	0.031	0.625
B	67.2 (27.7)	68.2 (42.6)	94.6 (40.3)	0.102 (42.6)	0.263 (37.5)	0.388 (38.1)	0.167 (38.9)	0.127 (39.2)	698.9 (39.5)	0.024	0.500
C	55.9 (39.9)	57.8 (51.3)	84.1 (47.0)	0.095 (46.6)	0.230 (45.5)	0.333 (46.9)	0.142 (47.9)	0.104 (50.5)	584.0 (49.5)	0.034	0.688
D	57.3 (38.5)	56.5 (52.3)	82.2 (48.2)	0.094 (47.2)	0.211 (50.0)	0.293 (53.3)	0.129 (52.9)	0.095 (54.5)	495.2 (57.2)	0.041	0.824
E	51.7 (44.4)	53.3 (55.0)	78.4 (50.6)	0.093 (47.8)	0.206 (51.1)	0.284 (54.7)	0.125 (54.3)	0.091 (56.3)	927.5 (19.8)	0.044	0.284
Simulation Peak Responses for Scaled El Centro Earthquake Excitation.											
uncontrolled	99.1	103.9	168.5	0.169	0.438	0.660	0.309	0.221	1194	0.006	—
A	64.1 (35.3)	66.1 (36.4)	93.7 (44.4)	0.098 (41.7)	0.225 (48.8)	0.327 (50.4)	0.153 (50.5)	0.116 (47.6	622.2 (47.9)	0.035	0.700
B	64.1 (35.3)	70.9 (31.8)	95.6 (43.3)	0.097 (42.4)	0.265 (39.5)	0.390 (40.8)	0.183 (40.8)	0.126 (42.9)	692.1 (42.0)	0.027	0.538
C	52.7 (46.8)	59.4 (42.8)	81.3 (51.7)	0.093 (44.6)	0.236 (46.1)	0.341 (48.3)	0.158 (48.9)	0.106 (52.1)	553.2 (53.7)	0.039	0.770
D	52.9 (46.6)	56.8 (45.4)	76.2 (54.8)	0.095 (43.5)	0.214 (51.1)	0.299 (54.6)	0.140 (54.7)	0.097 (56.3)	474.9 (60.2)	0.048	0.953
E	48.7 (50.9)	51.8 (50.2)	72.9 (56.8)	0.094 (44.2)	0.207 (52.9)	0.287 (56.4)	0.133 (56.9)	0.093 (58.0)	459.8 (61.5)	0.051	1.026

Table 5.4 Peak Response of Controlled System to One-Half Scale Taft Earthquake Excitation.

Controller	$\ddot{x}_{a1}, \frac{in}{s^2}$	$\ddot{x}_{a2}, \frac{in}{s^2}$	$\ddot{x}_{a3}, \frac{in}{s^2}$	x_1, *in*	x_2, *in*	x_3, *in*	$x_2 - x_1$ *in*	$x_3 - x_2$ *in*	*f, lbf*	x_a, *in*	u_c *Volts*
Experimental Peak Responses for Scaled Taft Earthquake Excitation.											
uncontrolled	102.7	104.5	146.4	0.165	0.408	0.585	0.248	0.187	1079	0.005	—
A	55.9 (45.5)	55.6 (46.8)	98.9 (32.4)	0.086 (48.0)	0.222 (45.6)	0.341 (41.8)	0.146 (41.1)	0.122 (34.9)	576.2 (46.6)	0.029	0.617
B	57.3 (44.2)	60.9 (41.7)	102.9 (29.7)	0.099 (39.9)	0.260 (36.2)	0.390 (33.4)	0.169 (32.1)	0.134 (28.4)	657.4 (39.0)	0.023	0.492
C	49.4 (51.8)	52.1 (50.1)	84.8 (42.1)	0.083 (49.4)	0.224 (45.1)	0.333 (43.2)	0.144 (42.0)	0.112 (40.2)	562.9 (47.8)	0.031	0.629
D	44.5 (56.7)	48.2 (53.8)	75.3 (48.6)	0.072 (56.0)	0.190 (53.5)	0.282 (51.8)	0.123 (50.3)	0.097 (48.3)	473.3 (56.1)	0.036	0.741
E	43.5 (57.7)	46.4 (55.6)	71.8 (50.9)	0.070 (57.2)	0.184 (54.8)	0.273 (53.4)	0.121 (51.2)	0.094 (49.7)	460.4 (57.3)	0.038	0.786
Simulation Peak Responses for Scaled Taft Earthquake Excitation.											
uncontrolled	89.6	109.9	144.3	0.149	0.417	0.601	0.272	0.191	1054	0.005	—
A	57.1 (36.3)	59.0 (46.3)	94.0 (34.8)	0.079 (46.8)	0.216 (48.2)	0.310 (43.2)	0.161 (40.8)	0.125 (34.5)	602.0 (42.8)	0.032	0.668
B	57.9 (35.4)	61.6 (44.0)	102.9 (28.7)	0.090 (39.9)	0.262 (37.1)	0.363 (33.5)	0.188 (31.1)	0.137 (28.2)	604.1 (42.7)	0.025	0.528
C	46.0 (48.7)	54.8 (50.1)	84.9 (41.2)	0.077 (48.7)	0.222 (46.9)	0.336 (44.1)	0.158 (41.9)	0.114 (40.4)	516.0 (51.0)	0.033	0.685
D	42.7 (52.3)	49.9 (54.6)	71.9 (50.2)	0.066 (55.6)	0.180 (56.8)	0.276 (54.1)	0.130 (52.4)	0.096 (49.9)	479.8 (54.5)	0.040	0.805
E	40.7 (54.6)	47.7 (56.6)	69.0 (52.2)	0.068 (54.3)	0.175 (58.0)	0.242 (55.7)	0.125 (54.1)	0.091 (52.3)	478.5 (54.6)	0.042	0.863

(above the pretensioned value), *f*, was also measured during the experiment and is included in each table. Notice that the measured force in the tendons during the controlled tests was less than the force during the uncontrolled test for all control designs.

Comparing Controllers A and B, it is evident that no particular advantage was gained by weighting interstory displacements in this experiment. In all response categories except the first floor displacement, Controller A consistently performed better than Controller B. In the first floor relative displacement response, Controller B produced slightly better results than Controller A. However, Controller A reduced the remaining interstory displacements (*i.e.*, $x_2 - x_1$ and $x_3 - x_2$) 5-10% more than Controller B. Also, Controller A reduced the *rms* relative displacements of each floor by almost 62% and reduced the peak relative displacement responses by approximately 45-50%, whereas Controller B could only produce a 56% reduction in the *rms* relative displacements.

Comparing Controllers C and D, which both weight various accelerations of the structure, Controller D performs significantly better. In the design of Controller D, the absolute acceleration of the third floor was weighted heavily, which forced the controller to concentrate most of its efforts on the fundamental mode of the structure. In the design of Controller C, the absolute acceleration of each floor was weighted equally, and the controller had less of an effect in the fundamental mode. Choosing to weight only the absolute acceleration of the third floor also made it possible to design a higher authority controller. Therefore, application of Controller D resulted in a moderate increase in the ability of the controller to reduce the acceleration responses and a significant increase in the ability of the controller to reduce all of the displacement responses as compared to Controller C.

In all response categories, Controller E performed best, achieving a 62-68% reduction in all *rms* responses to a broadband disturbance. Controller E performed best because it had the advantage of measuring the ground acceleration, in addition to the structural accel-

erations and actuator displacement. Including the disturbance as a measurement produced moderately better results than Controller D, which had the same performance objective, but did not measure the ground acceleration. With Controller E the peak relative displacement of the third floor due to the scaled El Centro and Taft earthquakes was reduced by 55% and 53%, respectively, indicating that a significant reduction in the response in the fundamental mode was achieved.

Damping ratios for the first three modes were also determined for each controlled system. These values are provided in Table 5.5 for each of the controllers mentioned above. The results exhibit the same trends as the *rms* and peak responses discussed above. Again, Controller E performed best, increasing the damping in the fundamental mode from 1.0% to 11.1%. Comparing Controllers C and D, one observes that Controller D has a significant effect on the damping ratio of the fundamental mode of the system. Therefore, weighting only the third floor absolute acceleration had the intended effect on the responses of the system in the fundamental mode. Generally, the control strategies which weighted the absolute accelerations of the structure (Controllers C, D, and E) resulted in higher damping ratios than those weighting relative displacements (Controllers A and B).

Table 5.5 Estimated Damping Ratios of Structural Modes.

Controller	Mode 1 (%)	Mode 2 (%)	Mode 3 (%)
uncontrolled	1.0	0.7	0.4
A	6.7	5.0	1.1
B	4.9	3.5	1.5
C	7.6	6.6	2.0
D	10.6	6.4	1.7
E	11.1	6.8	1.9

The experimental relative displacement and absolute acceleration responses of the closed-loop system formed with the best control design, Controller E, are compared to the experimental uncontrolled responses for the scaled El Centro excitation in Figs. 5.21a-c and 5.22a-c, respectively. Clearly, the controller has a significant effect on the magnitude of the system responses and on the damping characteristics. The experimental transfer functions of the uncontrolled system are compared to the experimental transfer functions of the controlled system (using Controller E) in Figs. 5.23-5.28. The experimental and simulated closed-loop responses are compared in Figs. 5.29a-c and 5.30a-c. Notice the excellent agreement between the simulated and experimental responses, indicating that the model is very accurate and there were no unforeseen problems in the implementation of the controller.

Notice from the results that by weighting the absolute accelerations, both the absolute accelerations and relative displacements are significantly reduced. However, weighting the relative displacements does not effectively minimize the absolute accelerations. This observation can be explained by considering the relationship between the relative displacements and absolute accelerations. In the relative displacement responses, the fundamental mode accounts for the largest component of the responses. Therefore, a controller which concentrates on the response in this mode will cause a significant reduction in the relative displacements. However, because the higher modes contribute significantly to the acceleration responses, and these modes are not significantly affected by the controller, the accelerations will not be reduced as greatly as the displacements. By placing weighting on the absolute accelerations, the response in all modes is affected, thus reducing the displacements as well as the accelerations.

Finally, as empirical evidence of robustness of the controllers, it should be mentioned that during one of the controlled experiments a sensor was left disconnected. Neverthe-

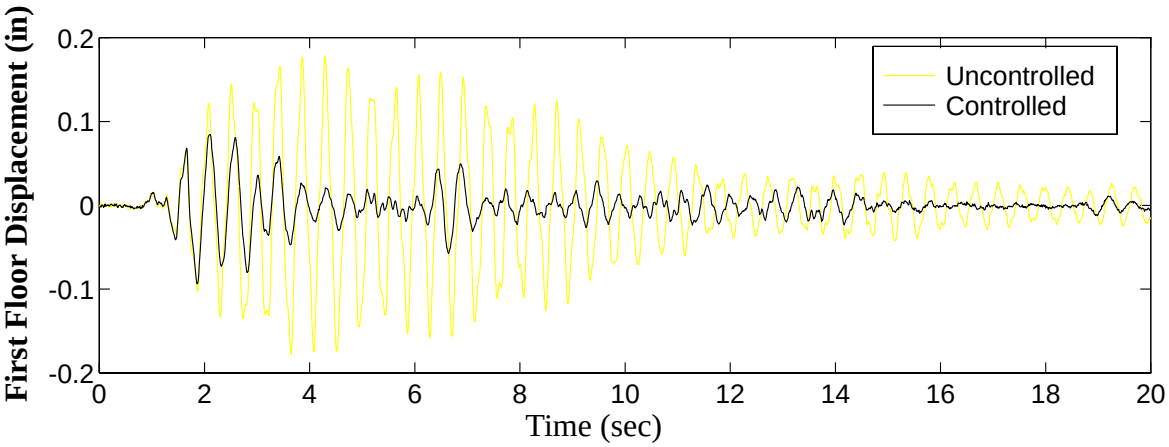

a) First Floor Relative Displacement

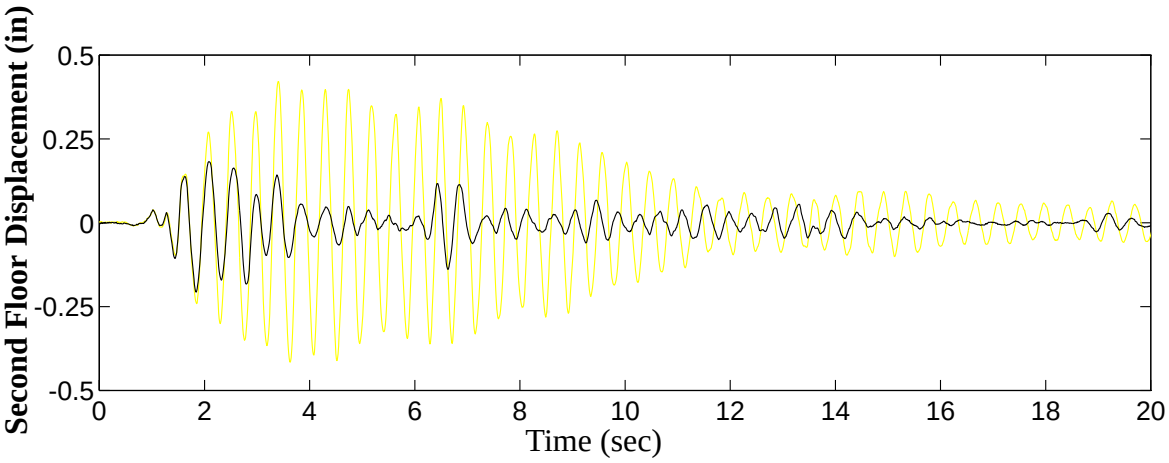

b) Second Floor Relative Displacement

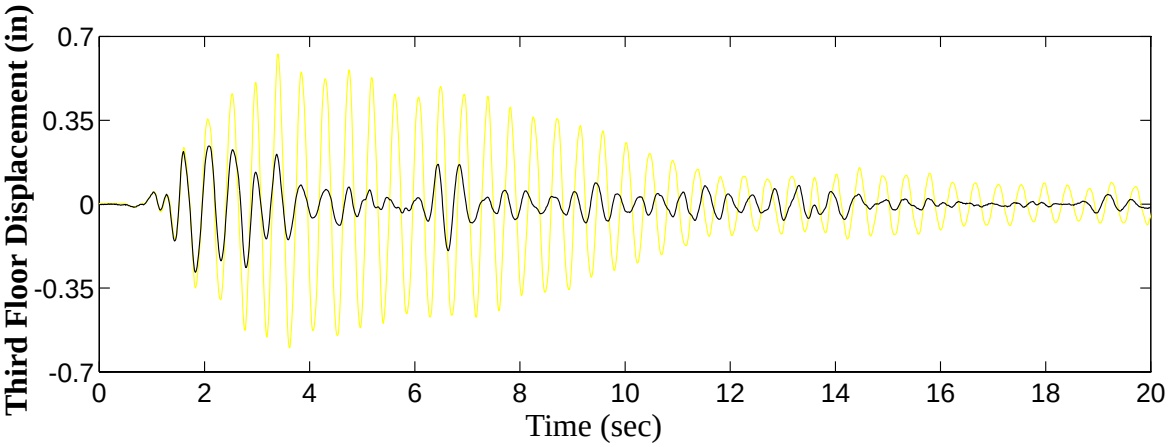

c) Third Floor Relative Displacement

Figure 5.21 Uncontrolled and Controlled Experimental Relative Displacements (Controller E).

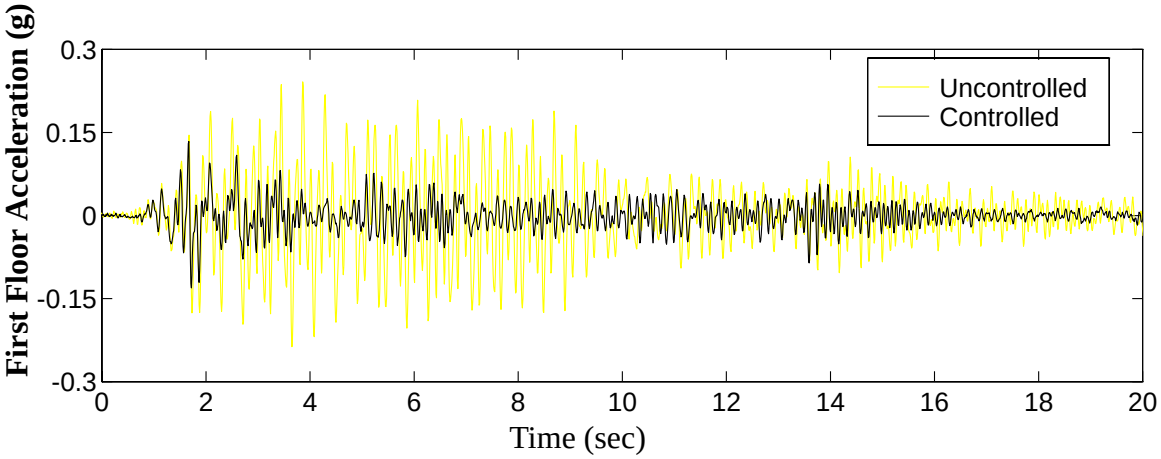

a) First Floor Absolute Acceleration

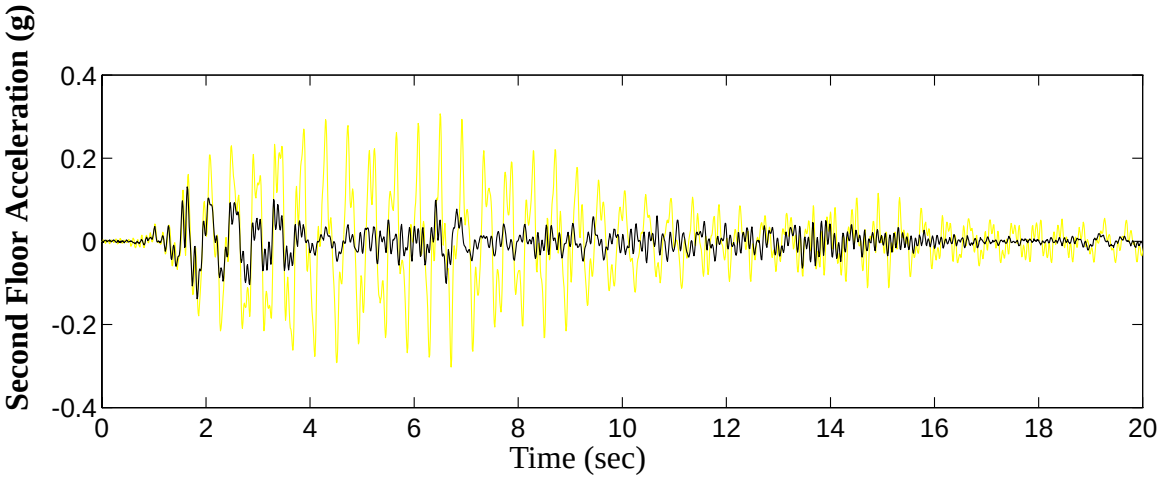

b) Second Floor Absolute Acceleration

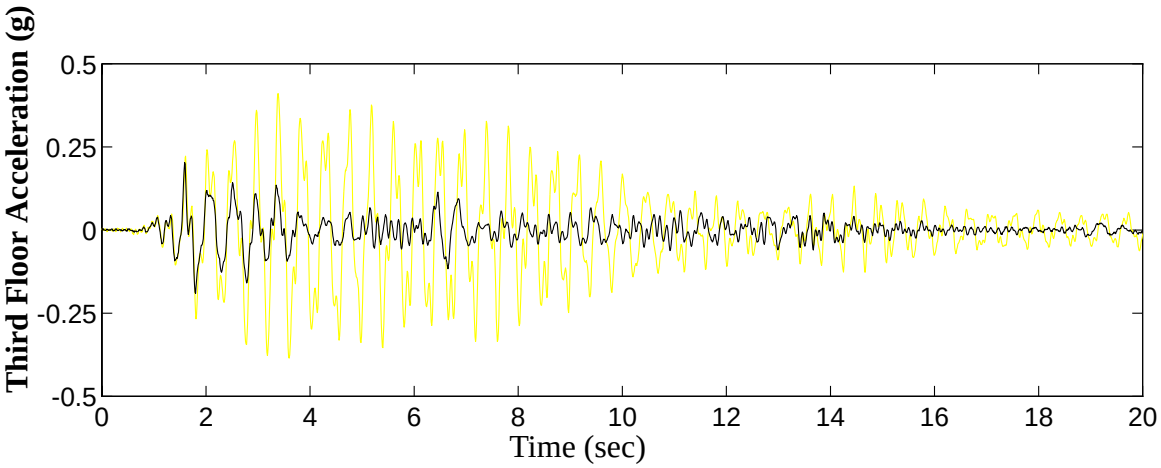

c) Third Floor Absolute Acceleration

Figure 5.22 Uncontrolled and Controlled Experimental Absolute Accelerations (Controller E).

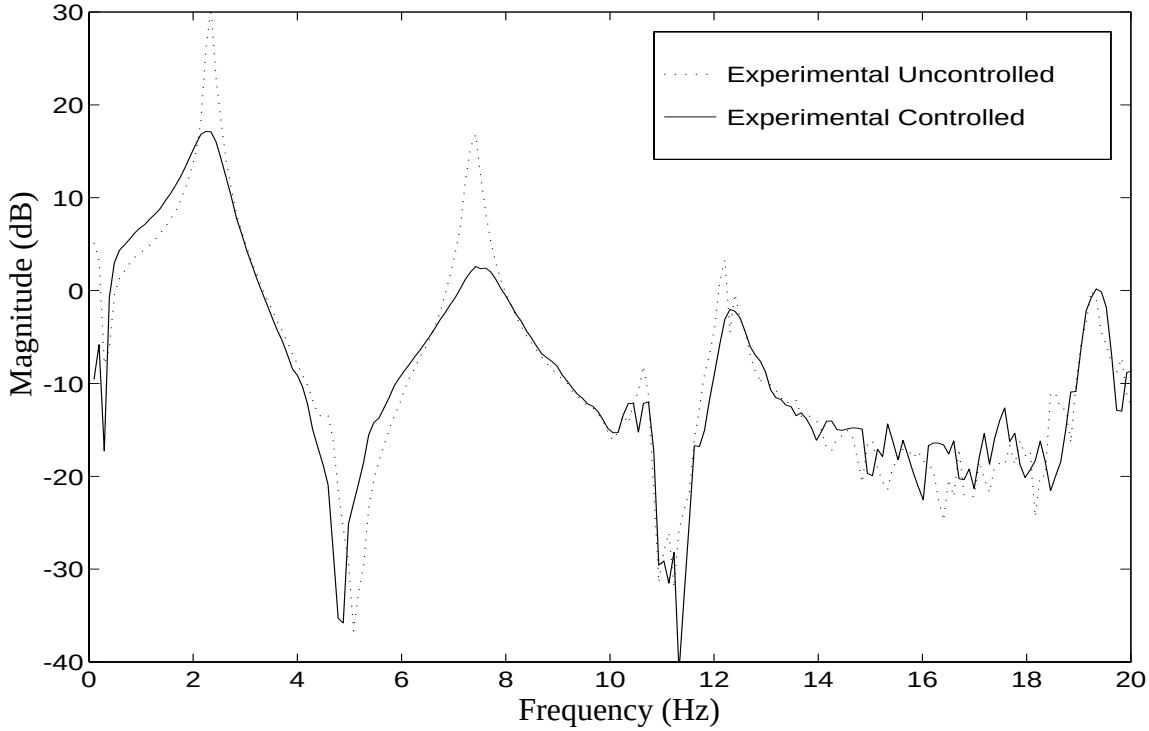

Figure 5.23 Comparison of Uncontrolled and Controlled Transfer Functions: Ground Acceleration to the First Floor Relative Displacement.

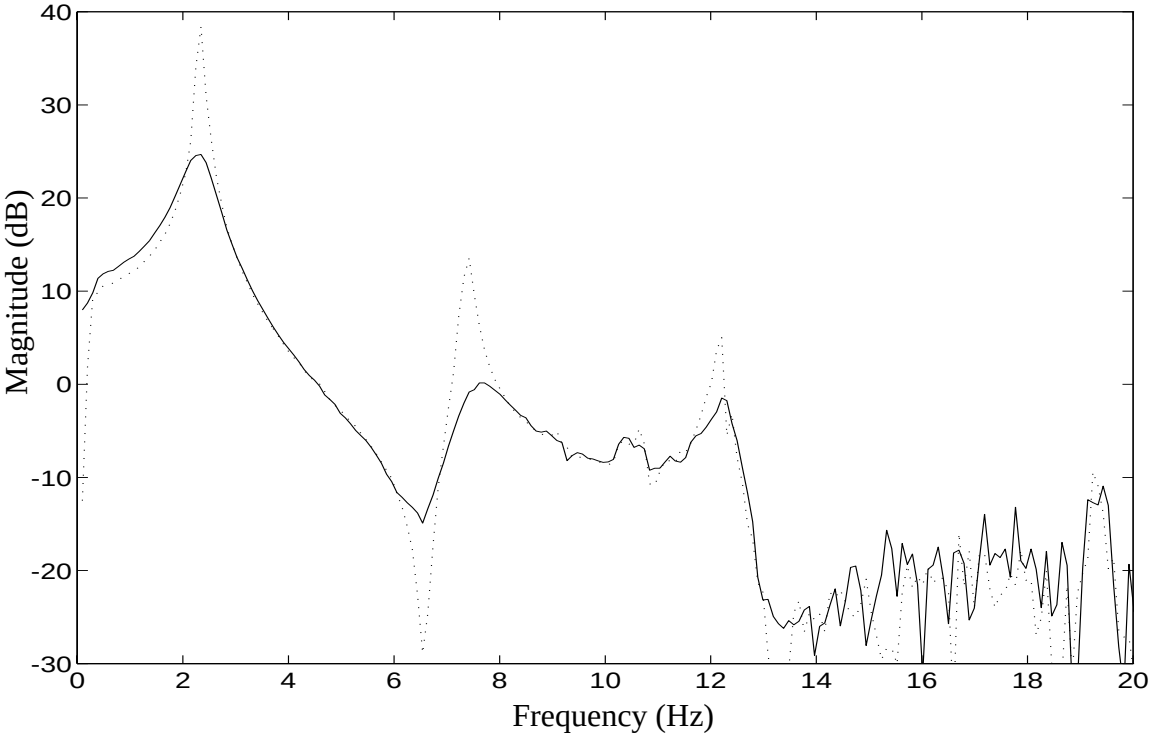

Figure 5.24 Comparison of Uncontrolled and Controlled Transfer Functions: Ground Acceleration to the Second Floor Relative Displacement.

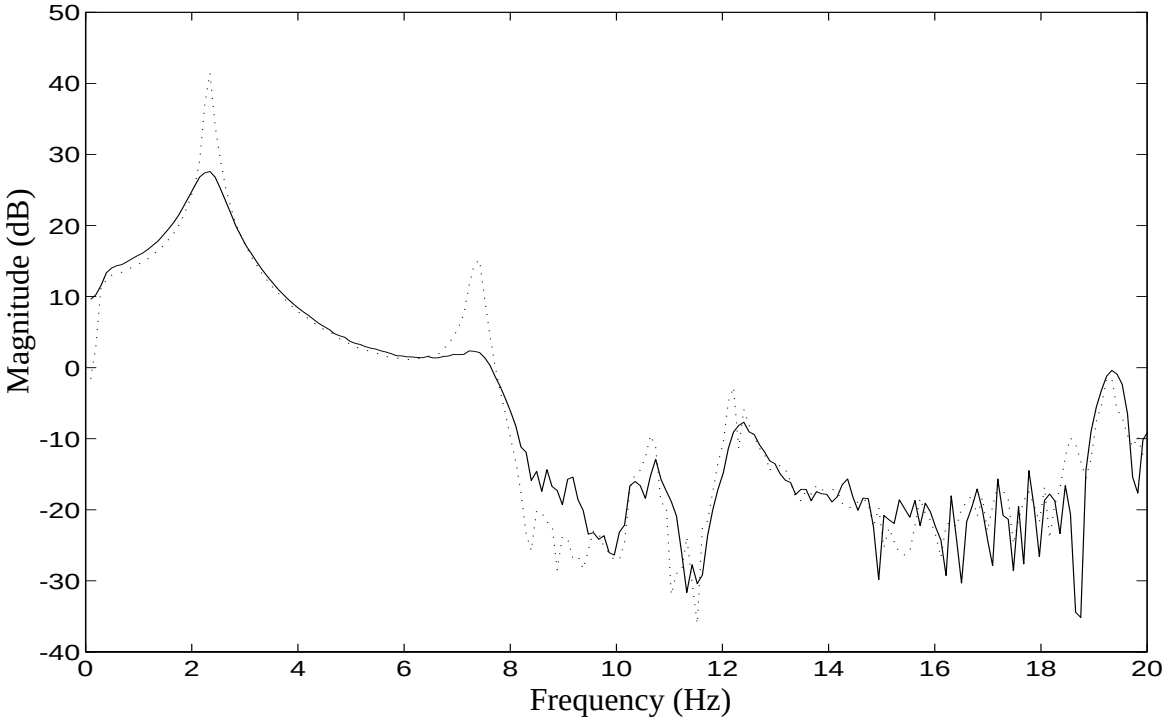

Figure 5.25 Comparison of Uncontrolled and Controlled Transfer Functions: Ground Acceleration to the Third Floor Relative Displacement.

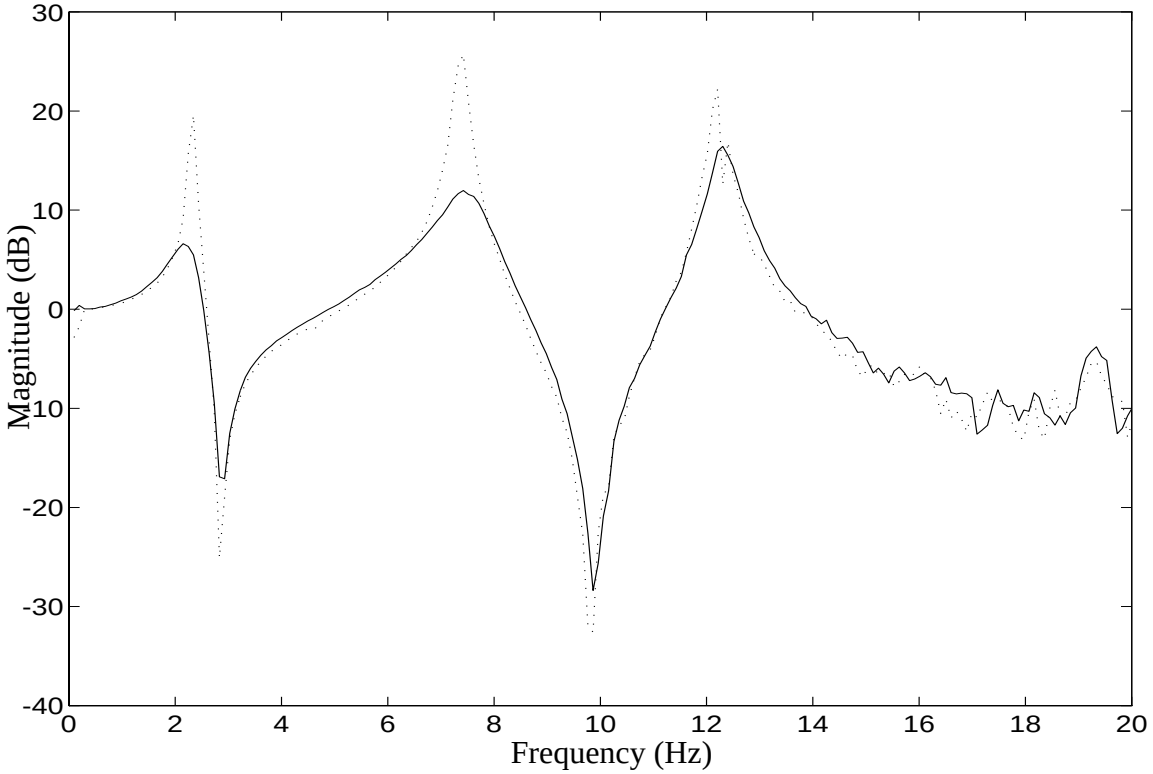

Figure 5.26 Comparison of Uncontrolled and Controlled Transfer Functions: Ground Acceleration to the First Floor Absolute Acceleration.

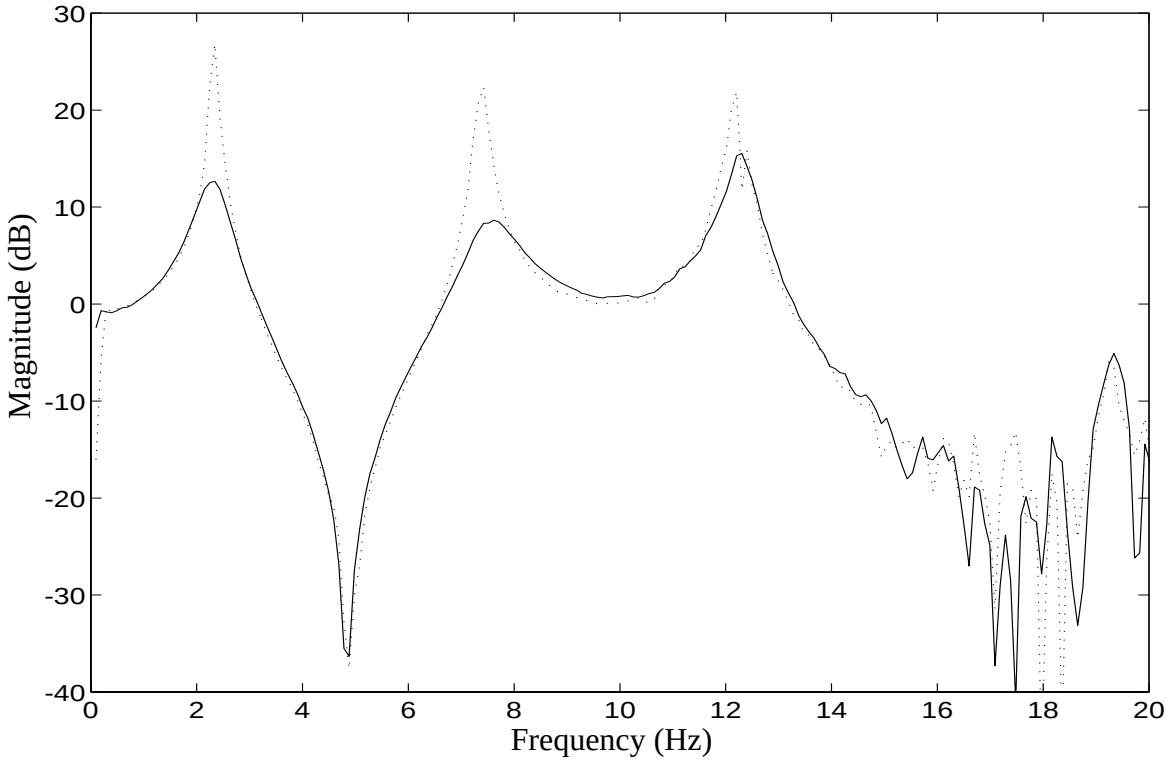

Figure 5.27 Comparison of Uncontrolled and Controlled Transfer Functions from the Ground Acceleration to the Second Floor Absolute Acceleration.

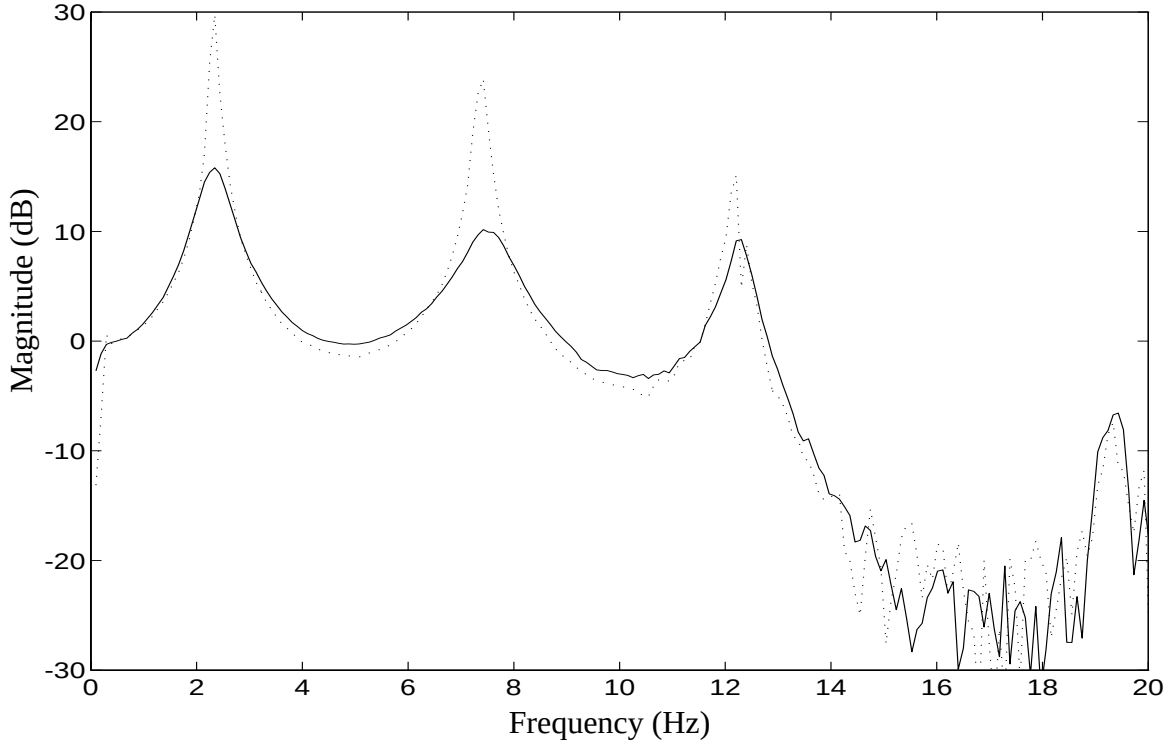

Figure 5.28 Comparison of Uncontrolled and Controlled Transfer Functions: Ground Acceleration to the Third Floor Absolute Acceleration.

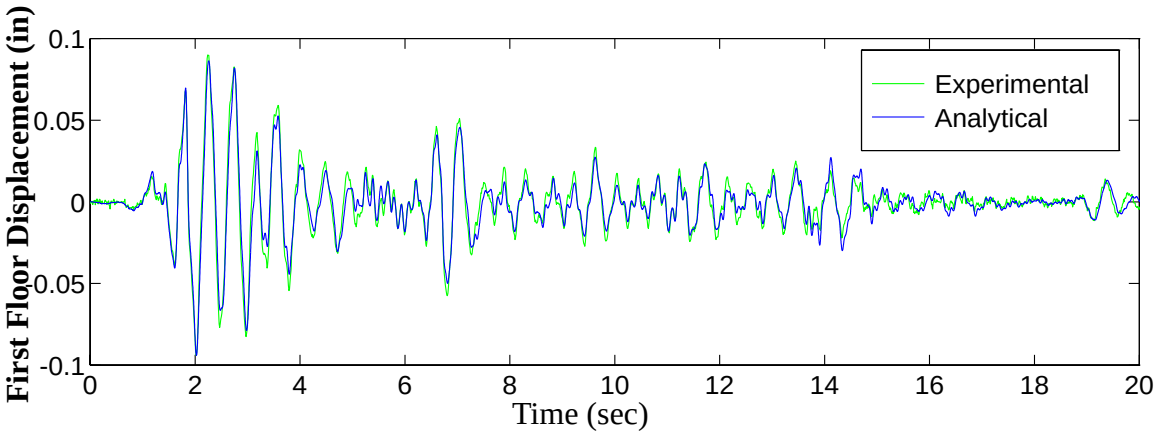

a) First Floor Relative Displacement

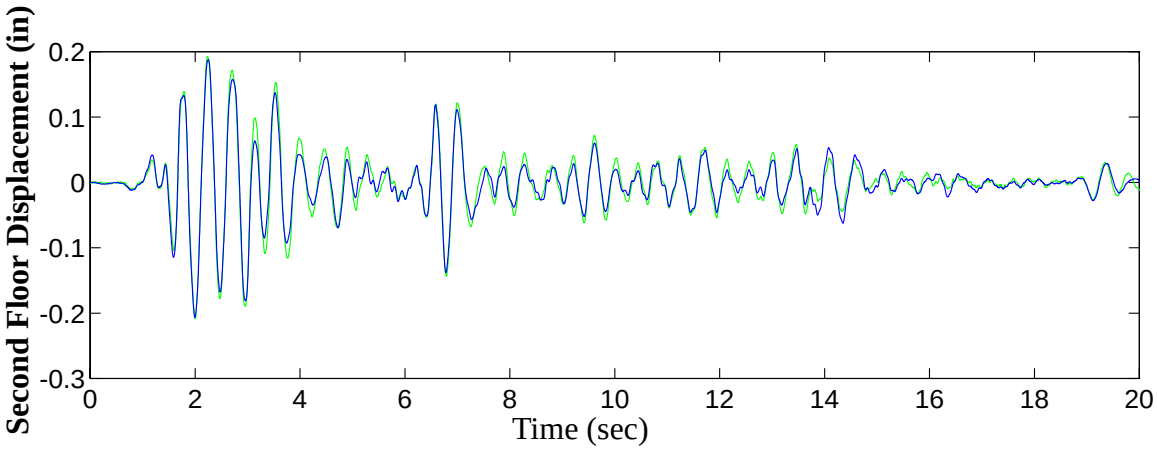

b) Second Floor Relative Displacement

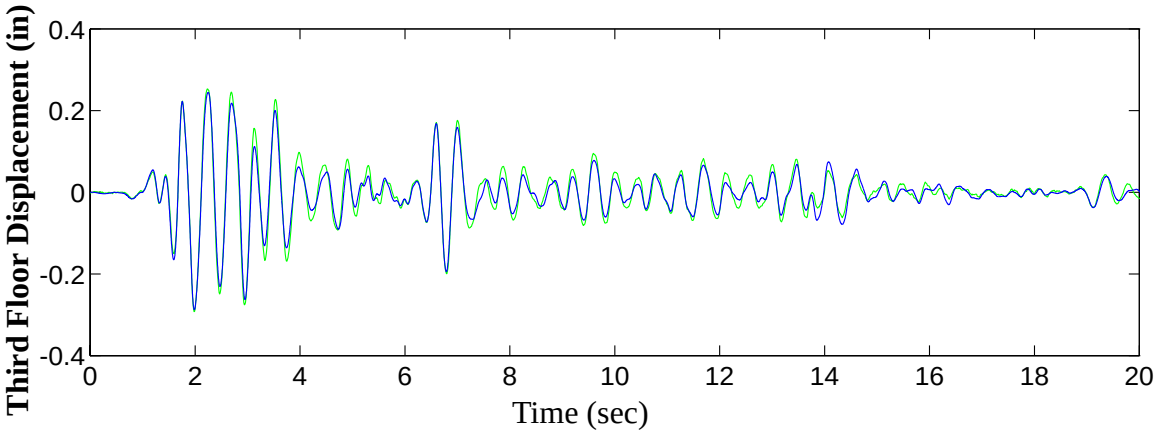

c) Third Floor Relative Displacement

Figure 5.29 Comparison of Experimental and Simulated Controlled Relative Displacement Responses (Controller E).

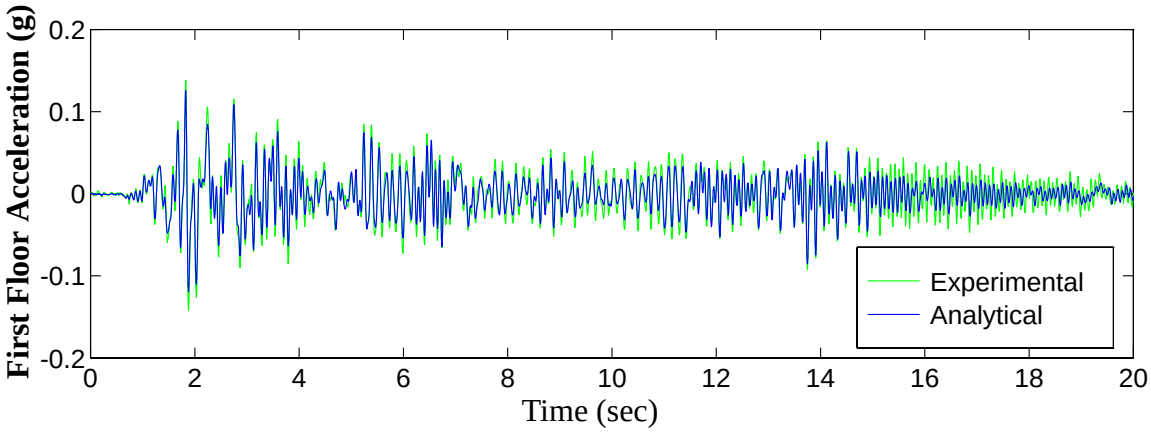

a) First Floor Absolute Acceleration

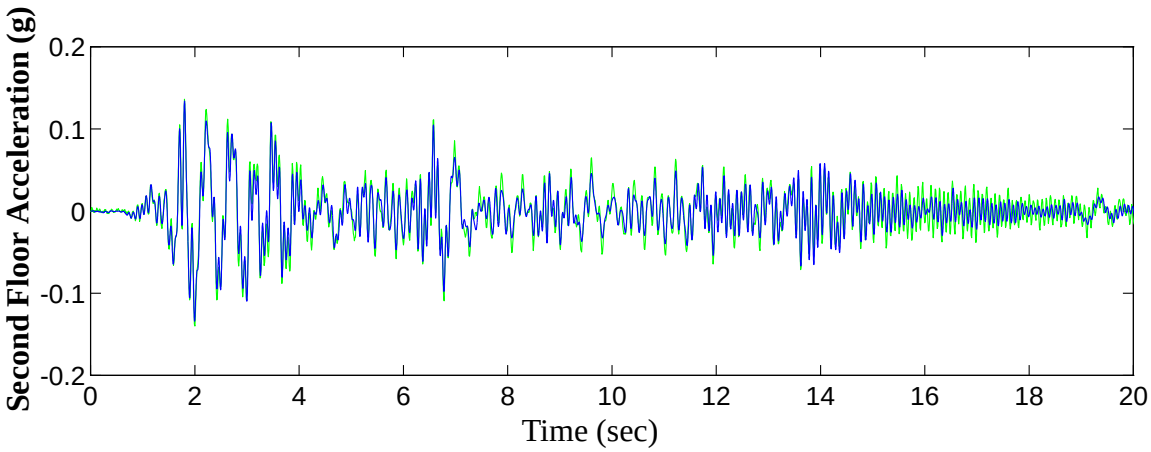

b) Second Floor Absolute Acceleration

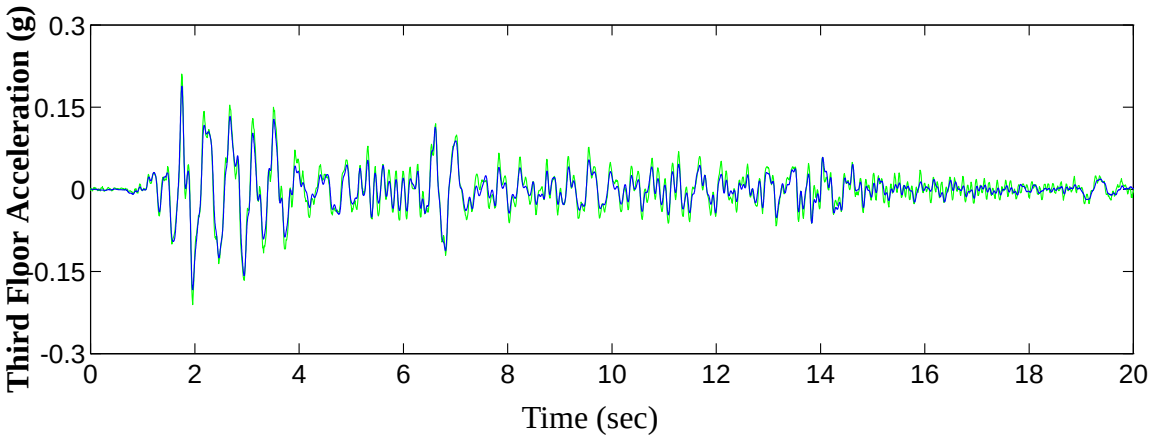

c) Third Floor Absolute Acceleration

Figure 5.30 Comparison of Experimental and Simulated Controlled Absolute Acceleration Responses (Controller E).

less, the resulting structural responses were reduced, although not as greatly as when all sensors were connected.

5.4 Summary of the Active Tendon Experiment

Active control designs based on acceleration feedback have been successfully implemented and verified on a tendon-controlled, MDOF test structure at the National Center for Earthquake Engineering Research at SUNY, Buffalo. The effects of actuator dynamics and control-structure-interaction were incorporated into the system identification procedure. The identified ten-state model reproduced the experimental results well in both the frequency domain and the time domain. Experimental results indicate that effective and robust controllers can be designed using an acceleration feedback control strategy, and full state feedback performance can be recovered.

Using H_2/LQG control design techniques, many different controllers were designed, each with a different performance objective. Some controllers were designed to minimize the three relative displacements of the structure while others minimized the absolute acceleration of the third floor. The best control design, which was designed to minimize the third floor acceleration and included the ground acceleration as an additional measurement (Controller E), achieved a 60-68% reduction in all *rms* displacement and acceleration measurements. Similarly, a 55% and 53% reduction in the peak response of the third floor displacement under the scaled El Centro earthquake and Taft excitations, respectively, was achieved. Comparable reductions were obtained for the other peak responses. In all cases, including the ground acceleration as an additional measurement resulted in a better control system. Additionally, excellent agreement was obtained between the simulations based on the identified analytical model and the experimental results.

By comparing the various control designs it was observed that weighting the displacements of the structure did not effectively reduce the acceleration responses. However, by weighting the accelerations in the control design, both the displacements and accelerations were efficiently reduced.

CHAPTER 6

Active Mass Driver Experiment

Because of the large number of full-scale implementations of active and hybrid mass drivers, a final active control experiment to verify acceleration feedback control strategies was performed at the Structural Dynamics and Control/Earthquake Engineering Laboratory (SDC/EEL) at the University of Notre Dame. The three story test structure employed in the active bracing experiment and described in Chapter 4, was reconfigured with an active mass driver (AMD) system. Control-structure interaction models were incorporated into the analysis and frequency domain H_2/LQG optimal control strategies were applied to achieve the control objectives. The results indicate that AMD systems employing acceleration feedback strategies are effective for reduction of structural responses during seismic activity and that response reduction can be achieved in all three modes of the structural system.

6.1 Experimental Setup

Tests were conducted at the Structural Dynamics and Control/ Earthquake Engineering Laboratory (SDC/EEL) at the University of Notre Dame using the three-story scale model building described in Chapter 4. A simple implementation of an active mass driver (AMD) was placed on the third floor of this test structure for control purposes. The AMD consisted of a high pressure hydraulic actuator with steel masses attached to each end of the piston rod (Fig. 6.3). The hydraulic cylinder, manufactured by Nopak, had a 3.8 cm

(1.5 in) diameter and a 30.5 cm (12 in) stroke. A Dyval servo-valve was employed that had an operational frequency range of 0–45 Hz. This hydraulic actuator was fitted with low-friction Teflon seals to reduce nonlinear frictional effects. For this experiment, the moving mass for the AMD weighed 5.2 kg (11.5 lbs) and consisted of the piston, piston rod and the steel disks bolted to the end of the piston rod. The total mass of the structure, including the frame and the AMD, was 300 kg (660 lbs). Thus, the moving mass of the AMD was 1.7% of the total mass of the structure. Because hydraulic actuators are inherently open loop unstable, position feedback was employed to stabilize the control actuator. The position of the actuator was obtained with an LVDT (linear variable differential transformer) rigidly mounted between the piston rod and the third floor.

As shown in Fig. 6.1, accelerometers positioned on each floor of the structure and on the AMD provided measurements of the absolute accelerations of the model, and an accelerometer located on the base measured the ground excitation. The displacement of the AMD relative to the third floor was measured using the LVDT mentioned previously. Only the three floor acceleration measurements and the absolute acceleration of the AMD were employed for purposes of control force determination (see Fig. 6.1).

6.2 System Identification and Model Validation

A block diagram of the structural system to be identified (*i.e.*, in Figs. 6.1 and 6.2) is shown in Fig. 6.4. The two inputs are the ground excitation $\ddot{x}_g$ and the command signal to the actuator u. The four measured system outputs include the absolute acceleration of the moving mass, $\ddot{x}_{am}$, and the absolute accelerations, $\ddot{x}_{a1}$, $\ddot{x}_{a2}$, $\ddot{x}_{a3}$, of the three floors of the test structure (*i.e.*, $\mathbf{y} = [\ddot{x}_{am} \;\; \ddot{x}_{a1} \;\; \ddot{x}_{a2} \;\; \ddot{x}_{a3}]'$). Thus, a 4×2 transfer function matrix (*i.e.*, eight input/output relations) must be identified to describe the characteristics of the system in Fig. 6.4.

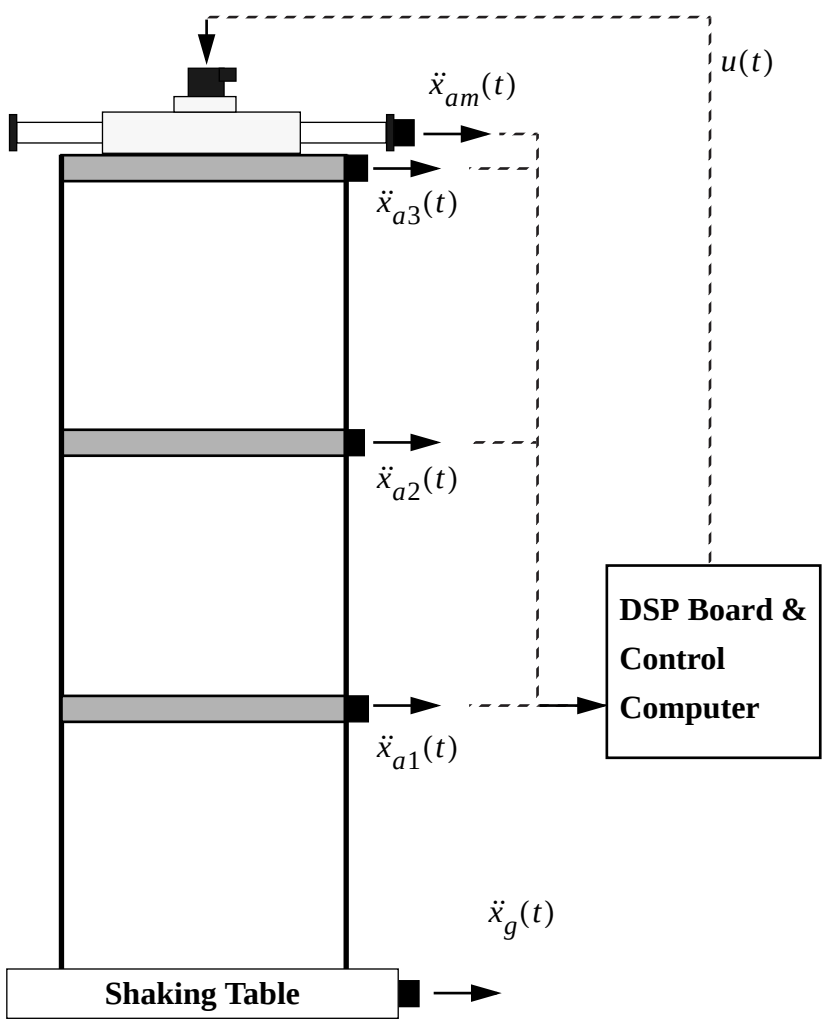

Figure 6.1 Schematic of Experimental Setup.

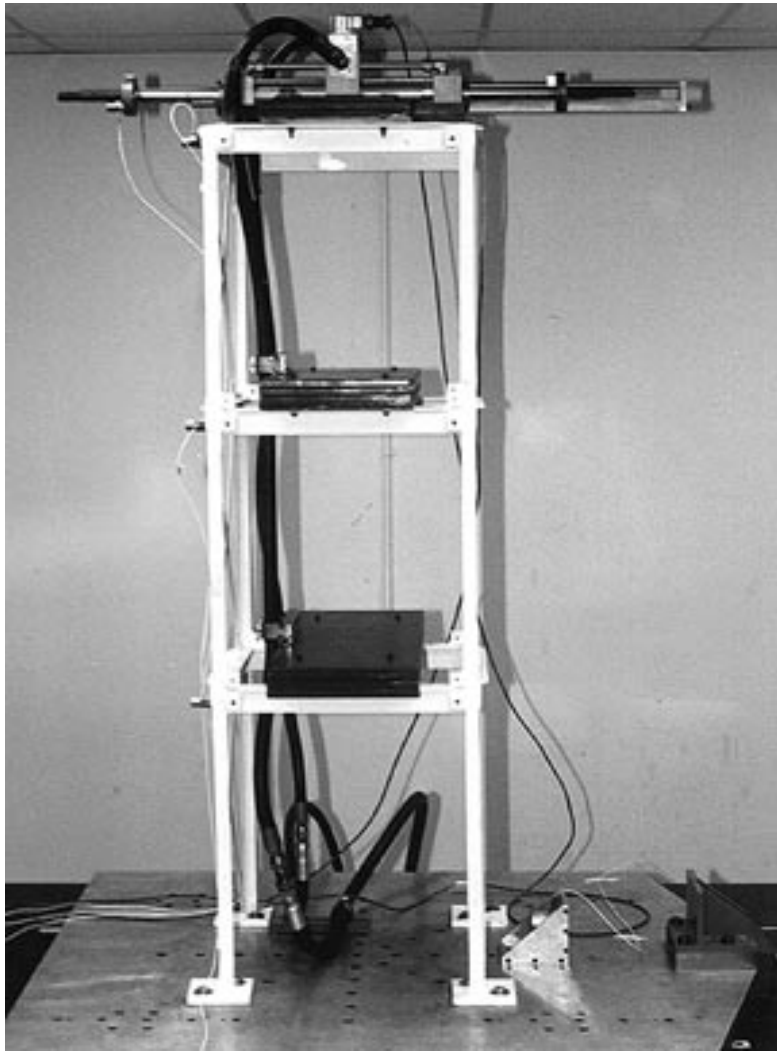

Figure 6.2 Three-Degree-of-Freedom Test Structure with an Active Mass Driver.

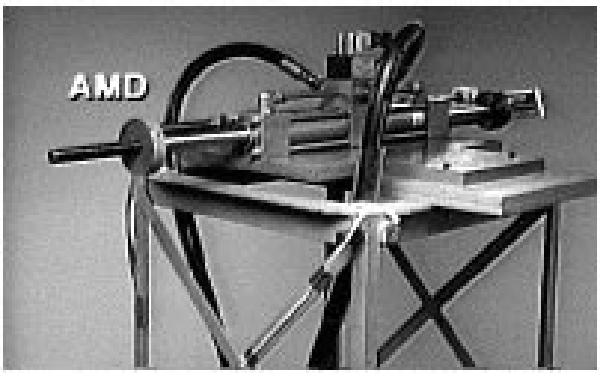

Figure 6.3 Active Mass Driver.

The procedure outlined in Chapter 2 was applied to determine a model of this 2-input/ 4-output structural system. The data acquisition system was employed to record the time responses and the eight experimental transfer functions for the system shown in Fig. 6.4 were then calculated in MATLAB (1994). The transfer functions from the ground acceleration to each of the four measured responses were obtained by exciting the structure with a band-limited white noise ground acceleration (0-100 Hz) with the AMD in place and the actuator command set to zero. Similarly, the experimental transfer functions from the actuator command signal to each of the measured outputs were determined by applying a band-limited white noise (0-100 Hz) to the actuator command while the ground was held fixed.

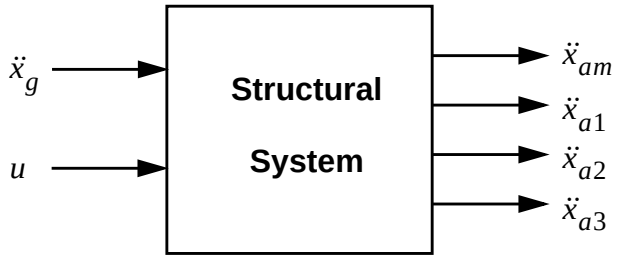

Figure 6.4 Block Diagram Representation of the Active Tendon System.

Three representative experimental transfer functions are shown in Fig. 6.5–6.7. Twenty averages (*i.e.*, $M = 20$ in Eqs. (2.7–2.8)) were used to obtain these transfer functions. Figure 6.5 presents the transfer function from the ground acceleration to the absolute acceleration of the third floor. Figures 6.6 and 6.7 present the transfer functions from the actuator command signal to the absolute acceleration of the third floor and to the absolute acceleration of the actuator, respectively.

Once the experimental transfer functions have been obtained, the next step in the system identification procedure is to model the transfer functions as a ratio of two polynomials in the Laplace variable *s*. Again, the effects of control-structure interaction should be incorporated into the model. Notice the near pole/zero cancellation in the actuator transfer function (Fig. 6.7) resulting from the control-structure interaction. This behavior is predicted by the models in Chapter 3 which employ the model of the hydraulic actuator.

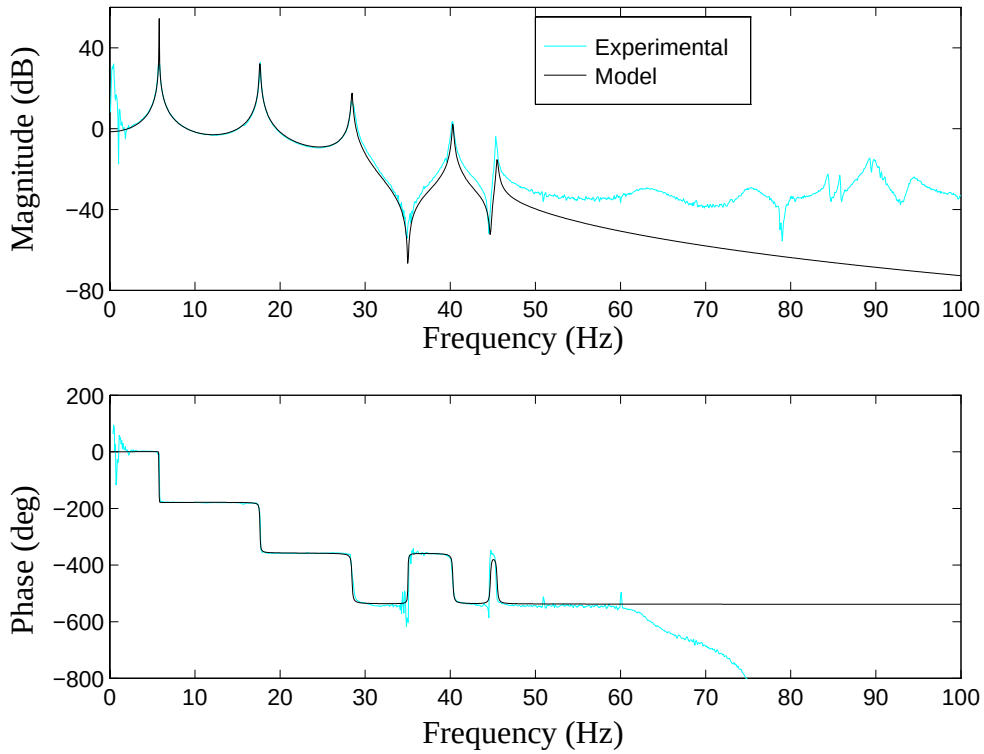

Figure 6.5 Transfer Function from Ground Acceleration to Third Floor Absolute Acceleration.

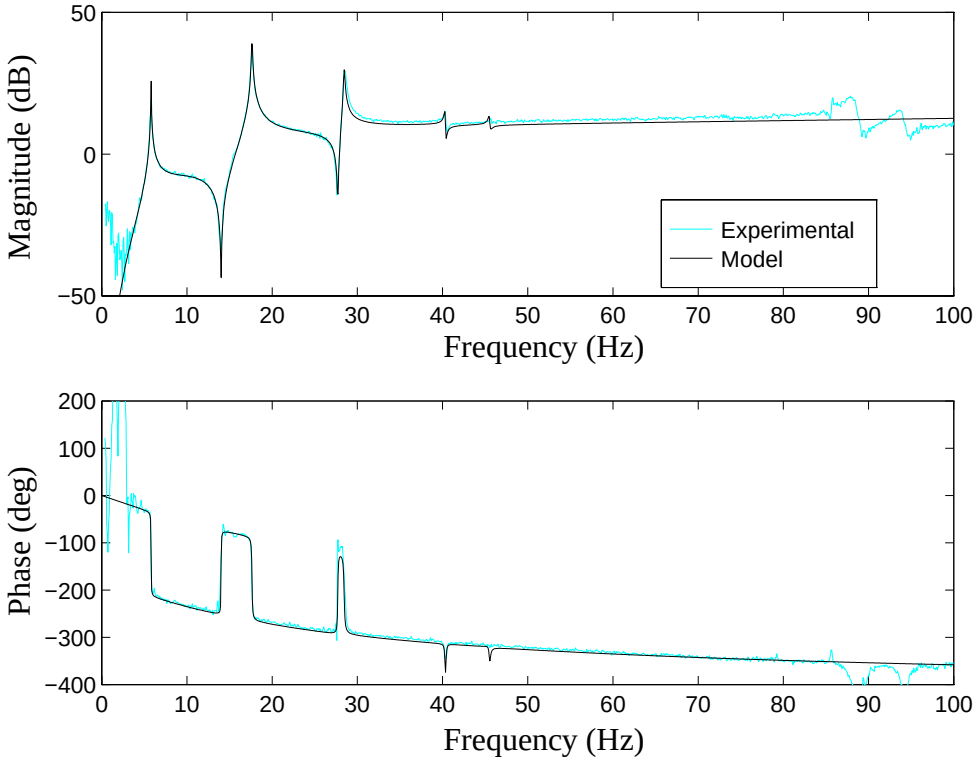

Figure 6.6 Transfer Function from Actuator Command to Third Floor Absolute Acceleration.

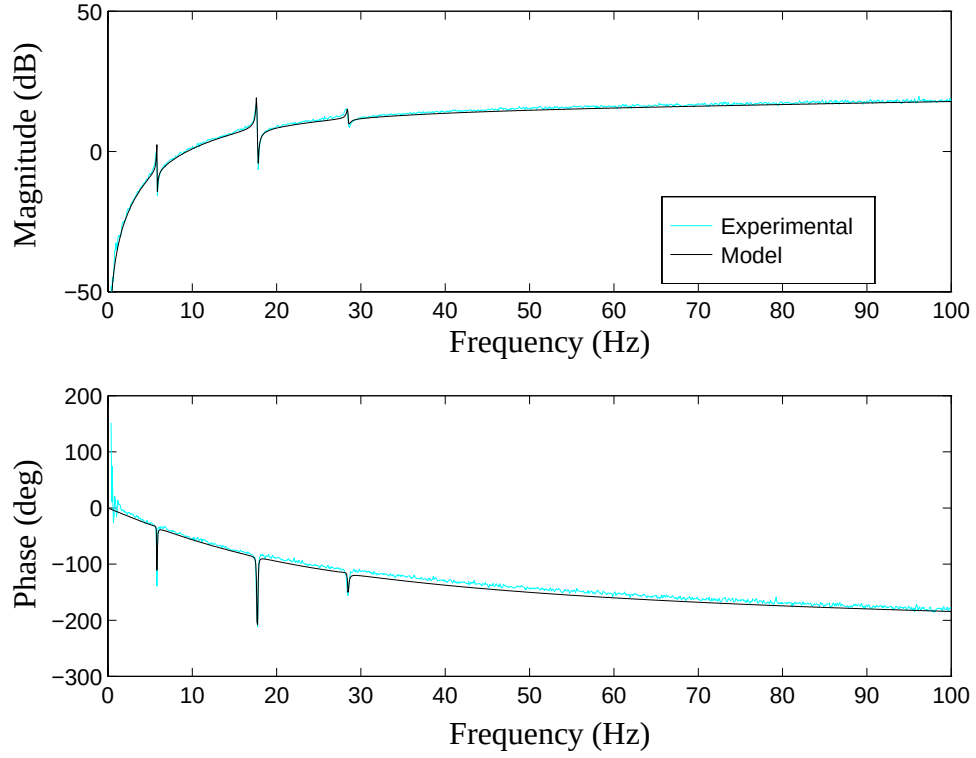

Figure 6.7 Transfer Function from Actuator Command to Actuator Acceleration.

For this experiment, the decision was made to focus control efforts on the reduction of the structural responses in the first three vibrational modes; thus, the model was required to be accurate below 35 Hz. To achieve an accurate model over this frequency range, the first five modes of the structural system were included in the model. Therefore, significant control effort should not be applied at frequencies above 35 Hz. The techniques used to roll-off the control effort at higher frequencies were presented previously in Chapter 2.

The resulting mathematical models of the transfer functions are overlaid in Figs. 6.5-6.7. The quality of the mathematical models for the remaining transfer functions was similar to that depicted in Figs. 6.5-6.7.

Next, the model was assembled in state space form. Again, the transfer functions from the ground to the structural responses were dominated by the dynamics of the structure, so the system related to the ground acceleration input (Eq. 2.11) required ten states corresponding to the first five modes of the test structure. The second state equation, modeling the relationship between the actuator command and the structural responses (Eq. 2.12), required fourteen states corresponding to the poles identified previously. Once each of the two state space systems were assembled, the states of the individual systems were stacked, as described in Chapter 2, to form a combined system. The model reduction procedure was applied, and the twenty-four state system was reduced to a fourteenth-order system. The ten eliminated states corresponded to ten redundant states corresponding to the building dynamics.

To ensure that information was not lost in the model reduction, the transfer functions of the reduced order system were compared to the transfer functions of the original model. All of the eight input/output relationships matched the original model well. A representative comparison of the reduced order model and the original model is shown in Figs. 6.8

(transfer function from actuator command to the first floor absolute acceleration) and 6.9 (transfer function from ground acceleration to the first floor absolute acceleration). In Fig. 6.9 the two transfer functions are indiscernible, indicating that no significant information was lost in the reduction. This control design model was used as a basis for the control designs. All of the experimental transfer functions are compared to the reduced order model in Figs. 6.10 through 6.17.

6.3 Control Design and Experimental Results

To offer a basis for comparison, a number of candidate controllers were designed using H_2/LQG control design techniques, each employing a different performance objective. Designs which minimize the three relative displacements, interstory displacements, and various combinations of three absolute accelerations of the structure and the absolute acceleration of the AMD were considered. In all of the controller designs considered, the

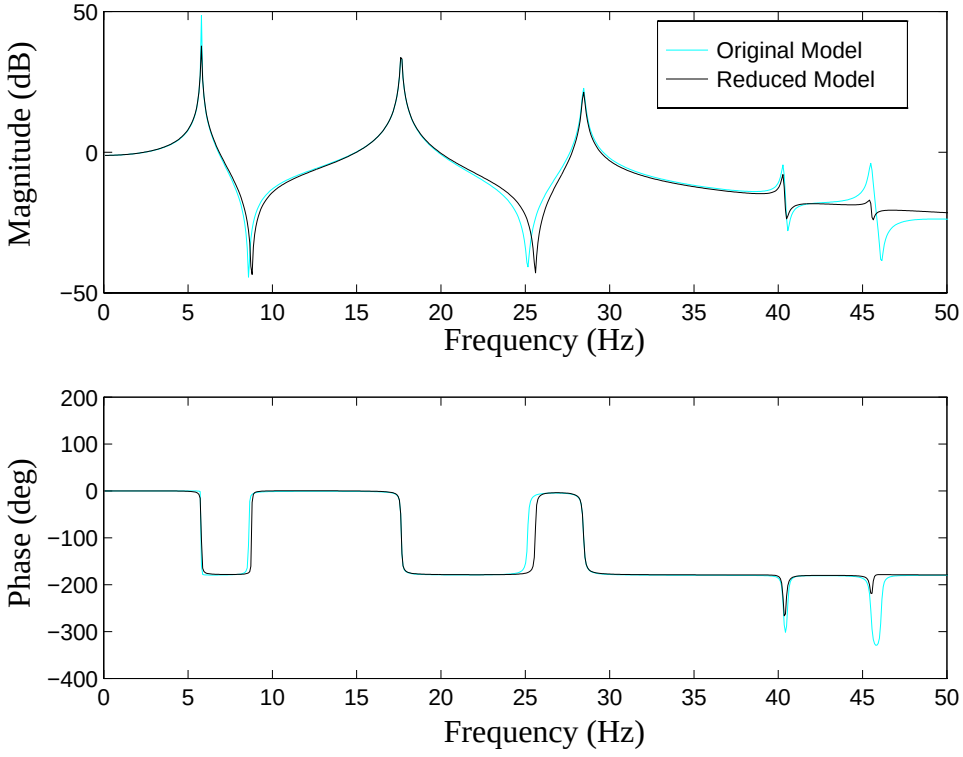

Figure 6.8 Comparison of the Reduced Order Model and the Original Model: Ground Acceleration to the First Floor Acceleration.

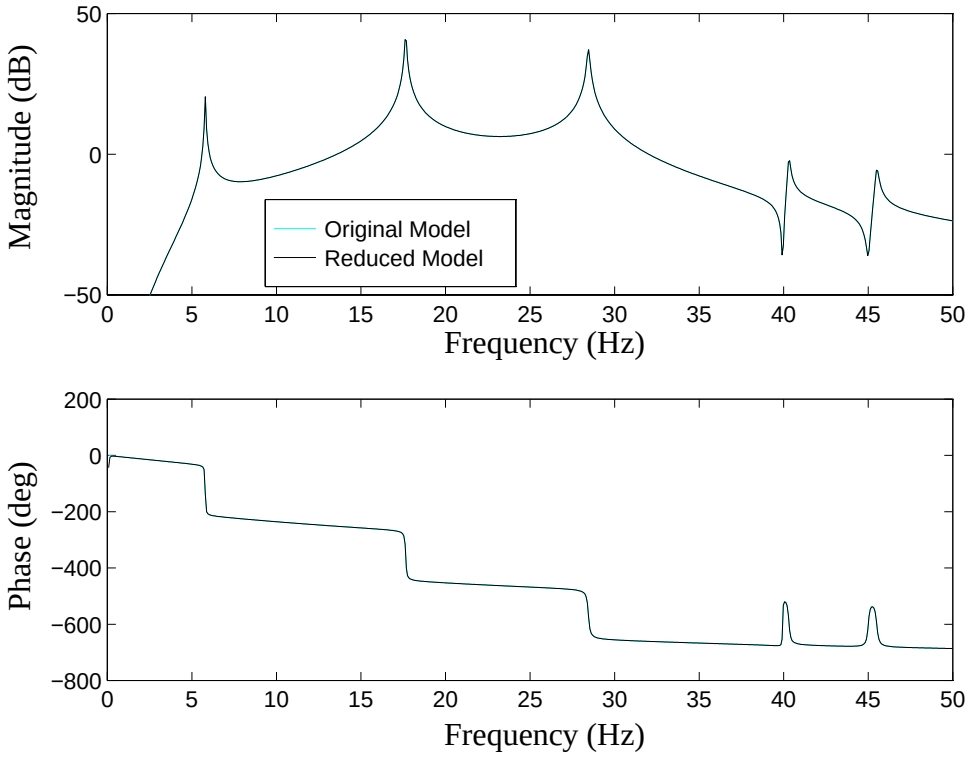

Figure 6.9 Comparison of the Reduced Order Model and the Original Model: Actuator Command to the First Floor Acceleration.

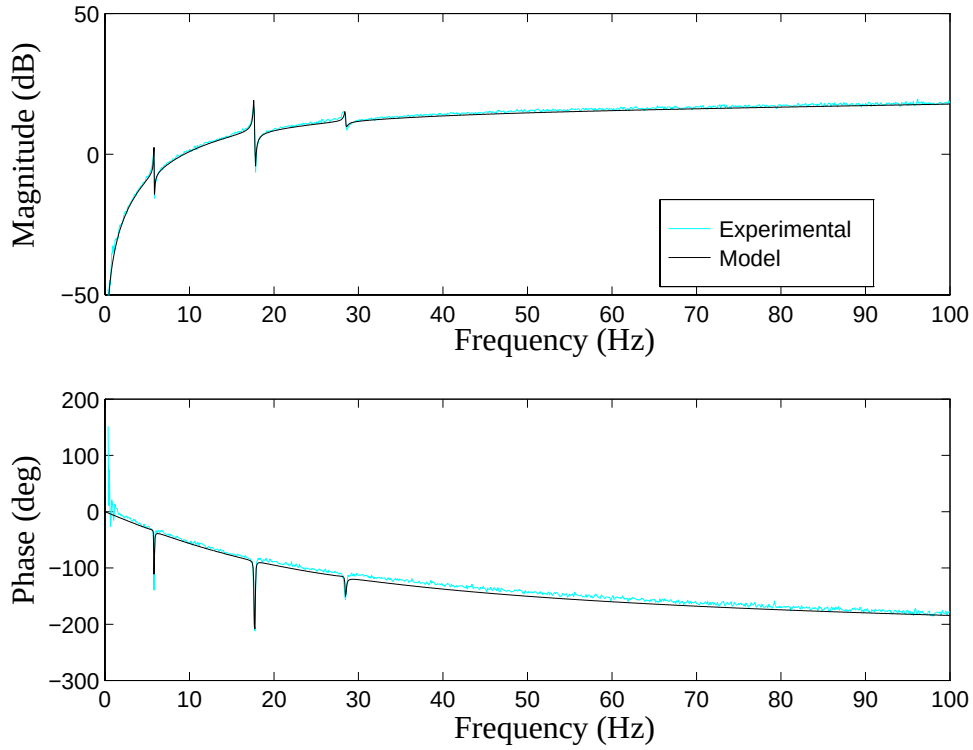

Figure 6.10 Comparison of Reduced-Order Model and Experimental Transfer Function: Actuator Command to Actuator Absolute Acceleration.

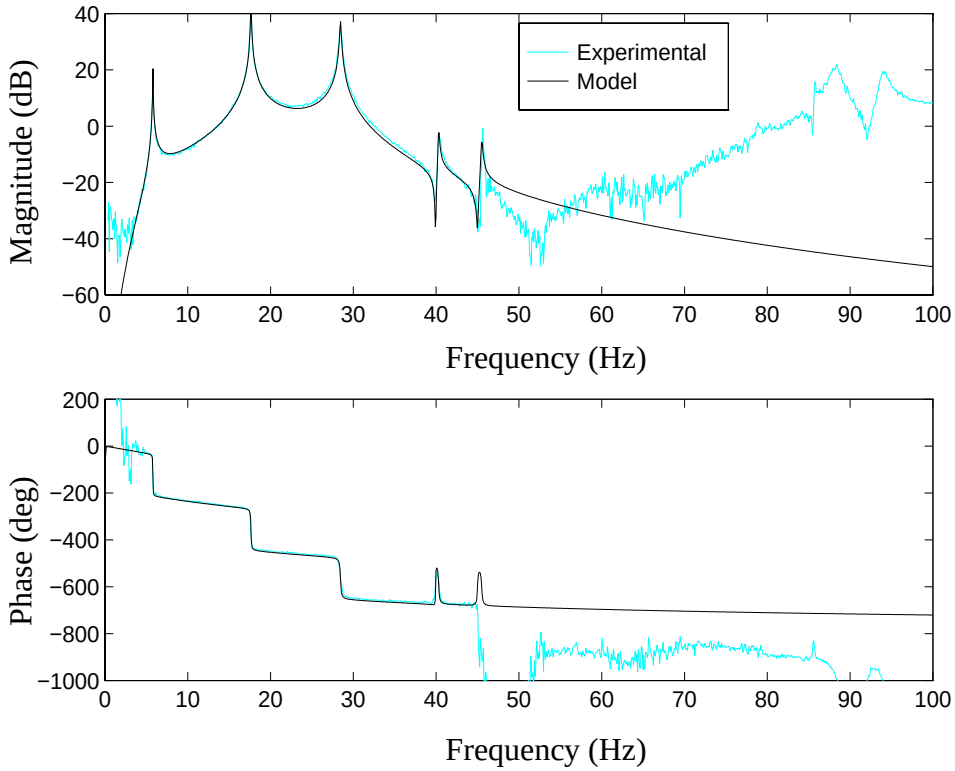

Figure 6.11 Comparison of Reduced-Order Model and Experimental Transfer Function: Actuator Command to First Floor Absolute Acceleration.

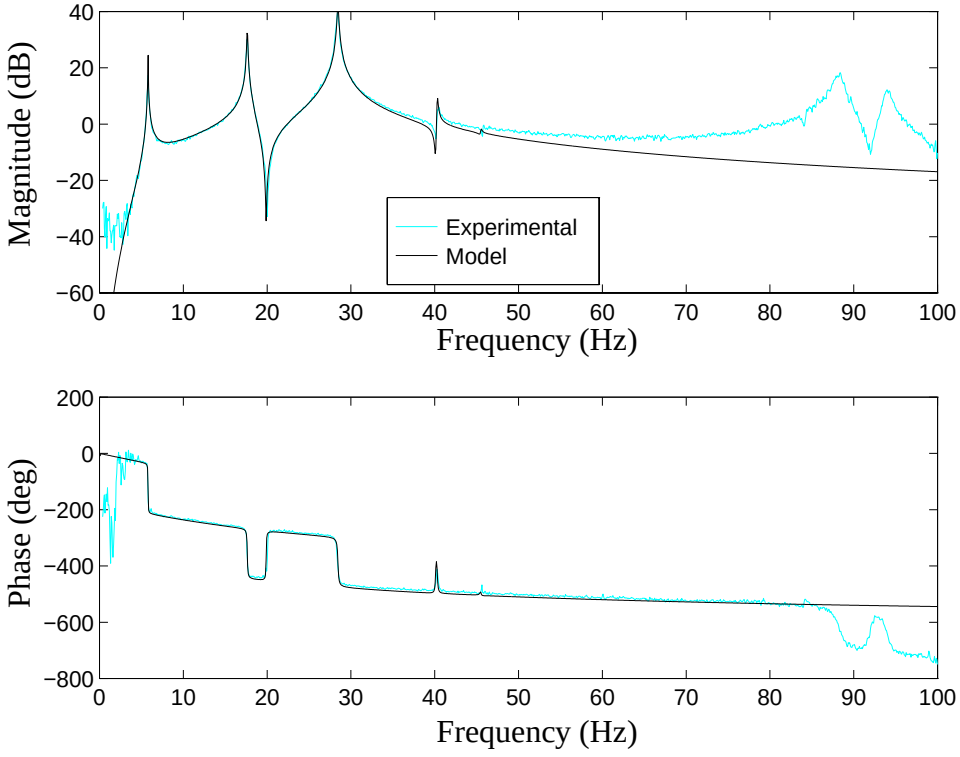

Figure 6.12 Comparison of Reduced-Order Model and Experimental Transfer Function: Actuator Command to Second Floor Absolute Acceleration.

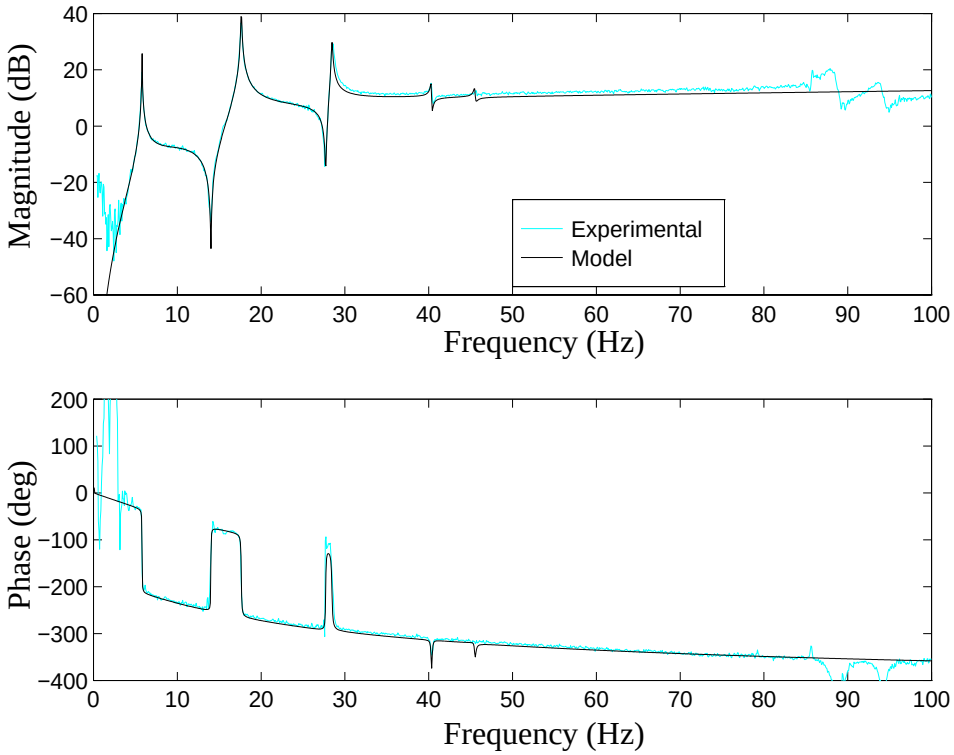

Figure 6.13 Comparison of Reduced-Order Model and Experimental Transfer Function: Actuator Command to Third Floor Absolute Acceleration.

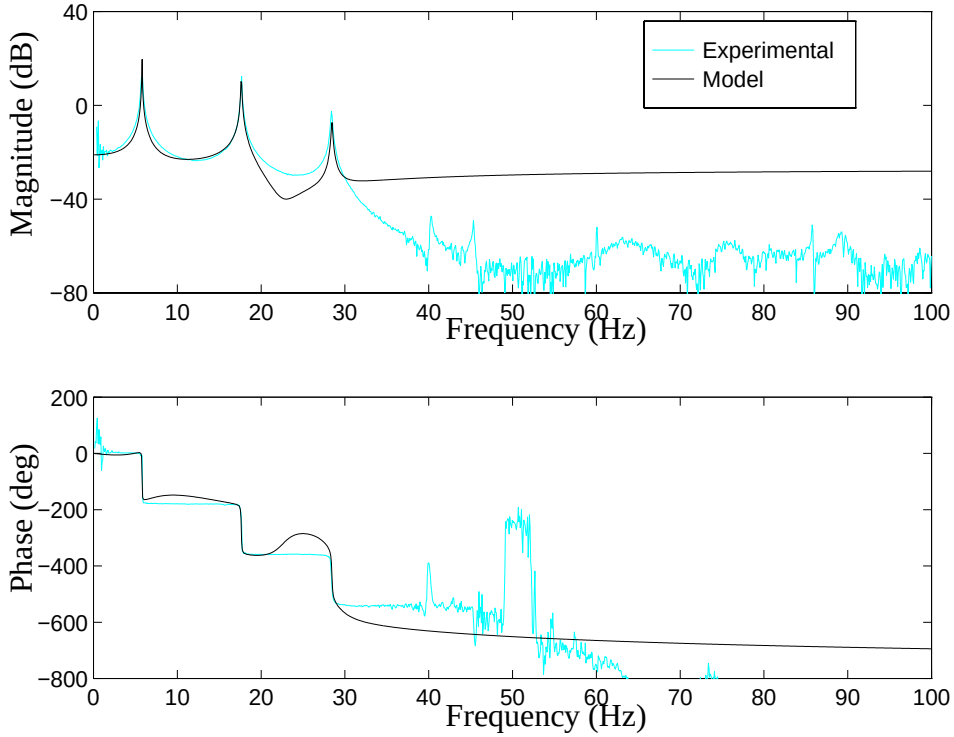

Figure 6.14 Comparison of Reduced-Order Model and Experimental Transfer Function: Ground Acceleration to Actuator Absolute Acceleration.

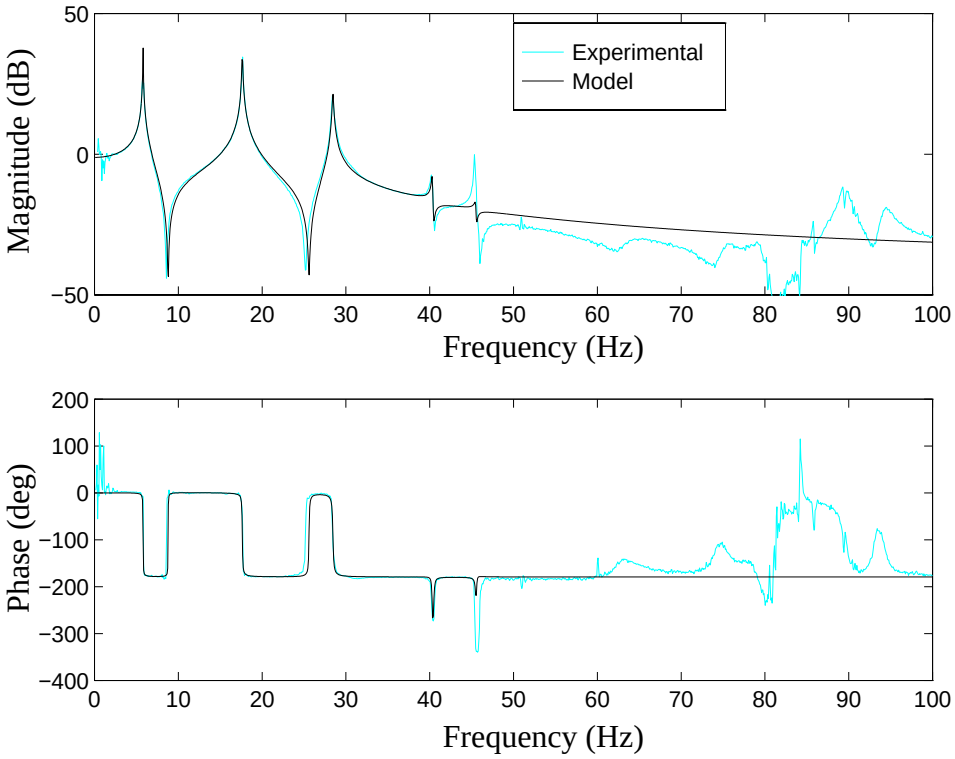

Figure 6.15 Comparison of Reduced-Order Model and Experimental Transfer Function: Ground Acceleration to First Floor Absolute Acceleration.

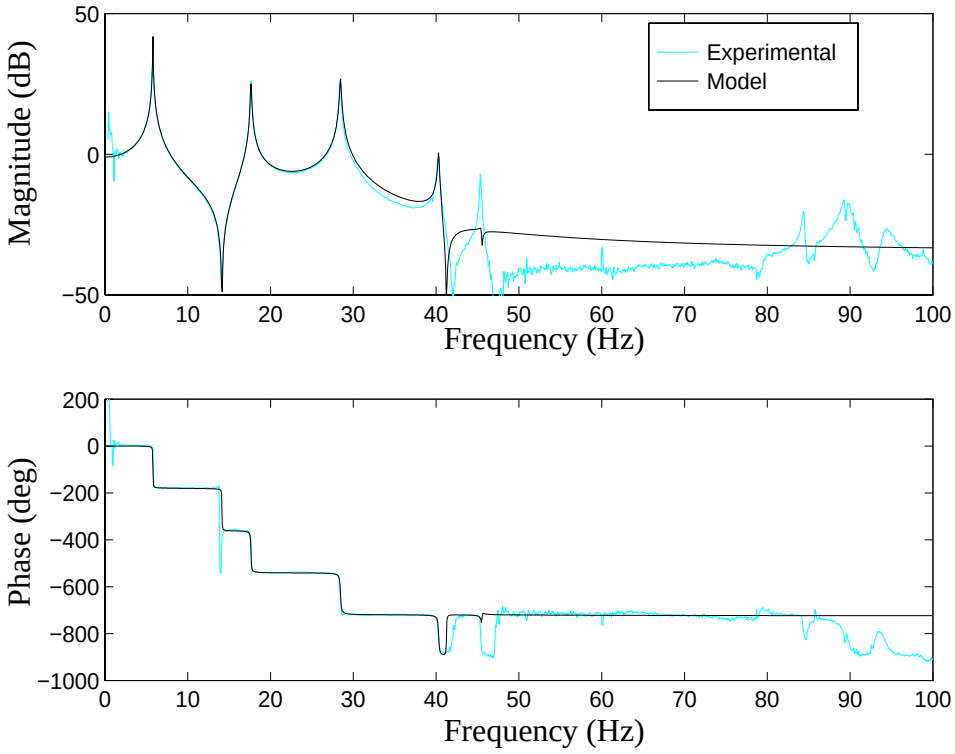

Figure 6.16 Comparison of Reduced-Order Model and Experimental Transfer Function: Ground Acceleration to Second Floor Absolute Acceleration.

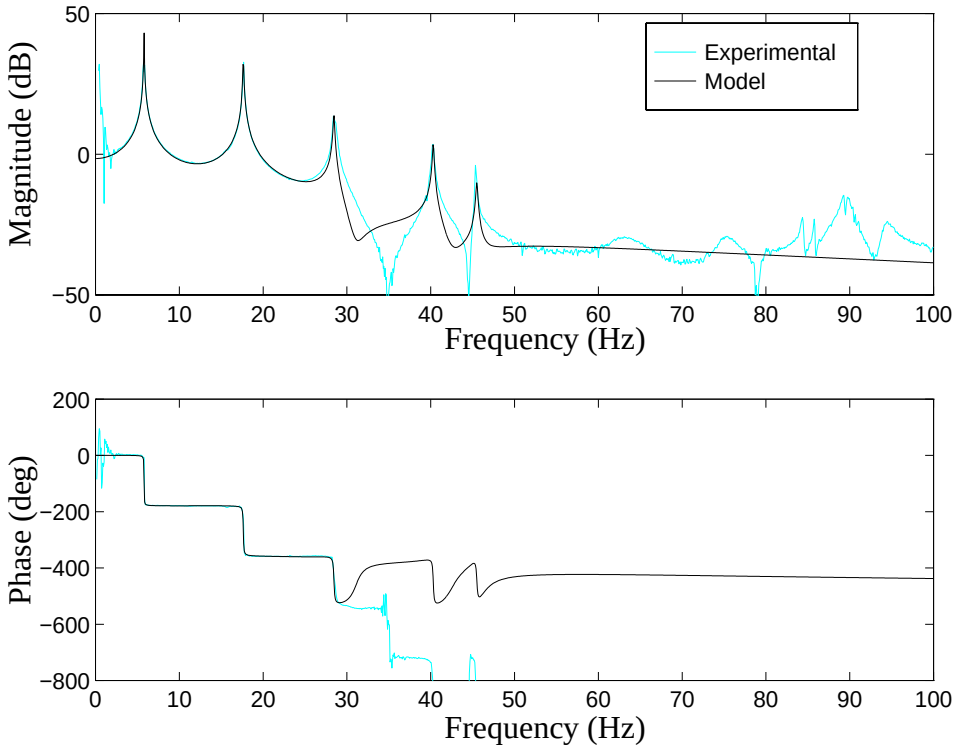

Figure 6.17 Comparison of Reduced-Order Model and Experimental Transfer Function: Ground Acceleration to Third Floor Absolute Acceleration.

weighting function on the regulated output, $\mathbf{W}$, was a constant matrix (*i.e.*, independent of frequency), and the earthquake filter **F** is modeled based on the Kanai–Tajimi spectrum.

Previously, the control design model was shown to be acceptably accurate below 35 Hz. However, significant modeling errors may occur at higher frequencies due to unmodeled dynamics. If one tries to affect high authority control at frequencies where the system model is poor, degraded or unstable controlled performance may result. Thus, for the structural system under consideration, no significant control effort was allowed above 35 Hz. Loop shaping techniques were used to roll-off the control effort in the high frequency regions where the system model was not accurate.

The loop gain transfer function was examined in assessing the various control designs to provide an indication of the closed-loop stability when the controller is implemented on

the physical system. For this experiment, the loop gain should be less than one at the frequencies above 35 Hz. Herein, a control design was considered to be acceptable for implementation if the magnitude of the loop gain at high frequencies was less than -5 dB at frequencies greater than 35 Hz.

The results of two representative control designs is presented herein. The first design (Controller A) was designed by placing an equal weighting on the absolute accelerations of the top two floors of the structure. The second controller (Controller B) was designed using the same weighting matrix as Controller A, but in addition used loop shaping techniques to roll-off the control effort at higher frequencies. A summary of the control designs is presented in Table 6.1. The loop gains for these two controllers are compared to

Table 6.1 Description of Control Strategies for Each Design.

Controller	*Control Strategy*
A	*Equal weighting on second and third floor absolute accelerations*
B	*Equal weighting on second and third floor absolute accelerations and control effort rolled off at high frequencies*

the experimentally obtained loop gains in Figs. 6.18 and 6.19. In both cases, the analytical loop gains match the experimental results very well, indicating that the mathematical model of the system is sufficiently accurate and the controller is operating as expected. The magnitude of the analytical loop gains is compared for the two controllers in Fig. 6.20. Here one can see that with Controller B the loop gain has been rolled-off significantly at high frequencies, and the controller is designed to concentrate most of its efforts on the first three modes of the system.

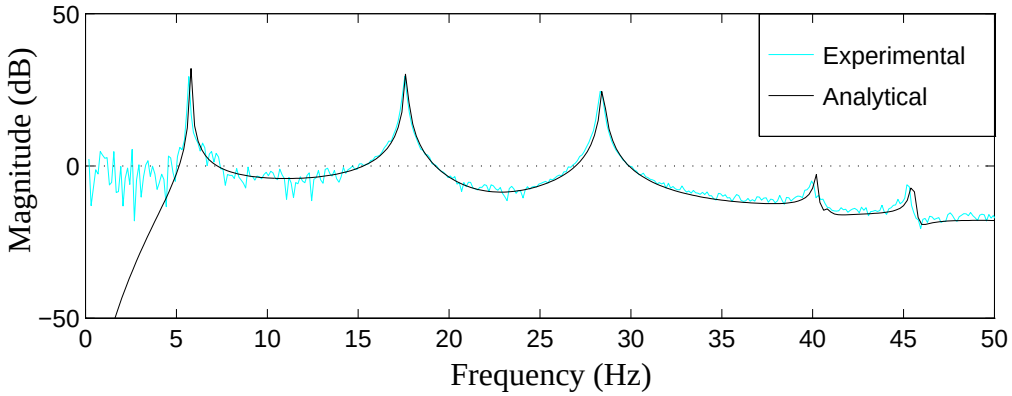

Figure 6.18 Experimental and Analytical Loop Gain Transfer Function Formed with Controller A.

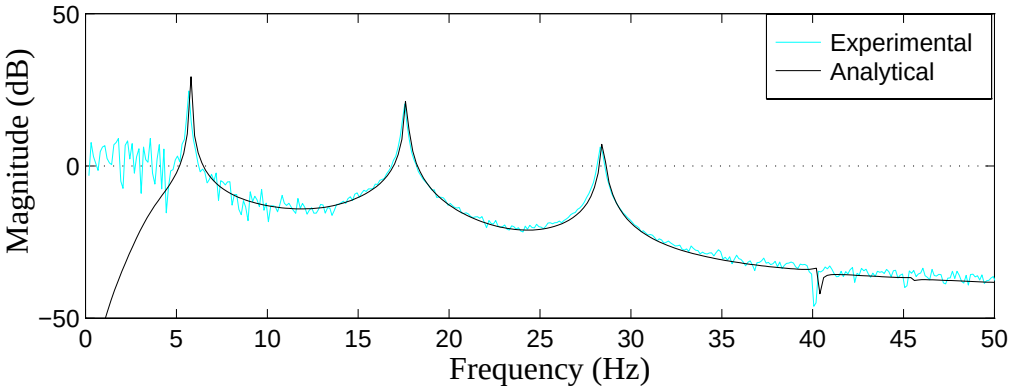

Figure 6.19 Experimental and Analytical Loop Gain Transfer Function Formed with Controller B.

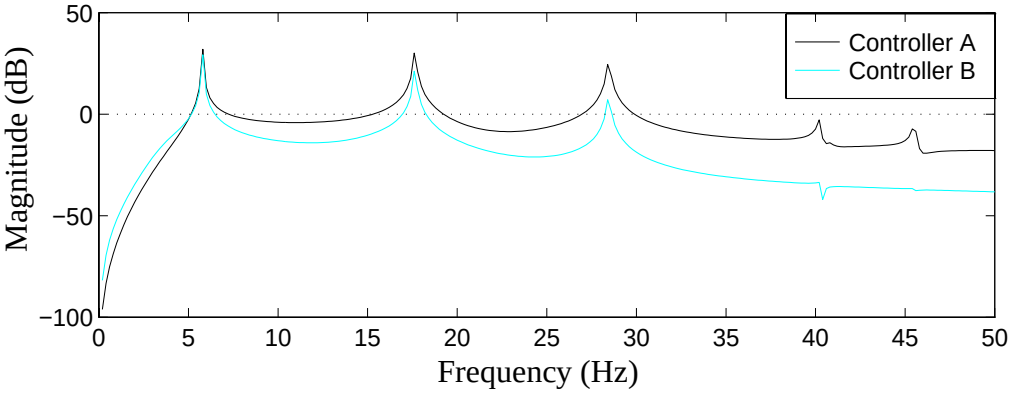

Figure 6.20 Comparison of Two Analytical Loop Gains with Controllers A and B.

Two series of experimental tests were conducted to evaluate the performance of the control designs. First a broadband signal (0–50 Hz) was used to excite the structure and rms responses were calculated. In the second series of tests an earthquake-type excitation was applied to the structure and peak responses were determined.

For the broadband disturbance tests, the *rms* responses for the two controllers are compared to the uncontrolled responses in Table 6.2. The percent reductions are indicated in parentheses. For this experiment, *uncontrolled* refers to the case in which the AMD was attached to the structure and the command signal was set equal to zero. Both controllers were able to achieve at least an 80% reduction in the third floor *rms* absolute acceleration. Notice that Controller A was able to achieve moderately better results than those of Controller B, but the *rms* acceleration of the actuator was almost twice that of Controller B while the *rms* displacements remained approximately the same. This difference is due to the loop shaping used in the design of Controller B, which resulted in less control effort being applied at the higher frequencies.

Table 6.2 RMS Responses for Broadband Disturbance Tests (0–50 Hz).

controller	$\ddot{x}_{a1}$ *(in/s²)*	$\ddot{x}_{a2}$ *(in/s²)*	$\ddot{x}_{a3}$ *(in/s²)*	x_a *(in)*	$\ddot{x}_{am}$ *(in/s²)*	u *(V)*
Uncontrolled	51.4	61.6	76.0	—	75.6	—
Controller A	11.6 (77.4)	12.0 (80.5)	13.2 (82.6)	.0903	202	.057
Controller B	14.0 (72.7)	14.5 (76.5)	15.1 (80.1)	.0808	101	.055

The experimentally obtained closed loop transfer functions for the two control designs are compared to the uncontrolled transfer functions in Figs. 6.21–6.26. Notice that all three of the first modes are significantly reduced. The analytical closed loop transfer

functions are also presented in these graphs for comparison to the experimental data. The closed loop analytical transfer functions are very close to the experimentally obtained transfer functions, again indicating that the model accurately represents the behavior of the system and that the controller is operating correctly. Figs. 6.27–6.29 provide a comparison of the experimental closed loop transfer functions for the two controllers. Here, one sees that Controller A and B reduce the vibrational response in the first mode to a similar level. However, Controller A more effectively reduces the structural responses in the second and third vibrational mode. Because the control action was rolled-off at higher frequencies, the local vibrational modes above 35 Hz are not greatly affected by either controller.

The measured ground acceleration record that was generated by the simulator for the earthquake tests is shown in Fig. 6.30. For these tests, Table 6.3 presents the peak responses for the two controllers are compared to the uncontrolled responses. The third

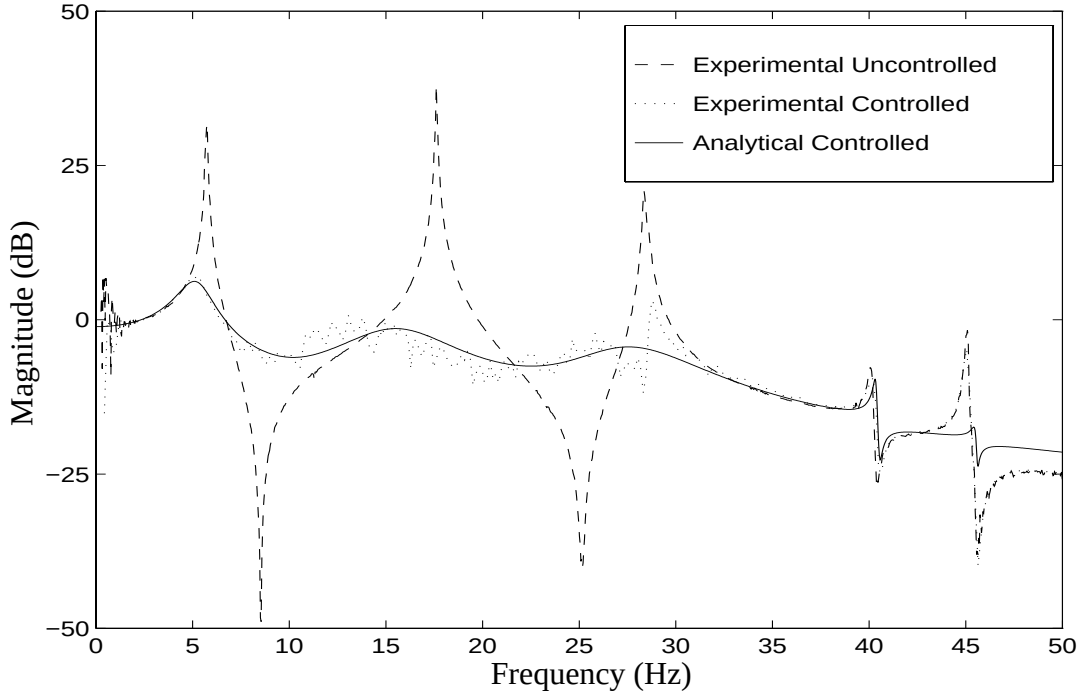

Figure 6.21 Transfer Function from the Ground Acceleration to the First Floor Absolute Acceleration with Controller A.

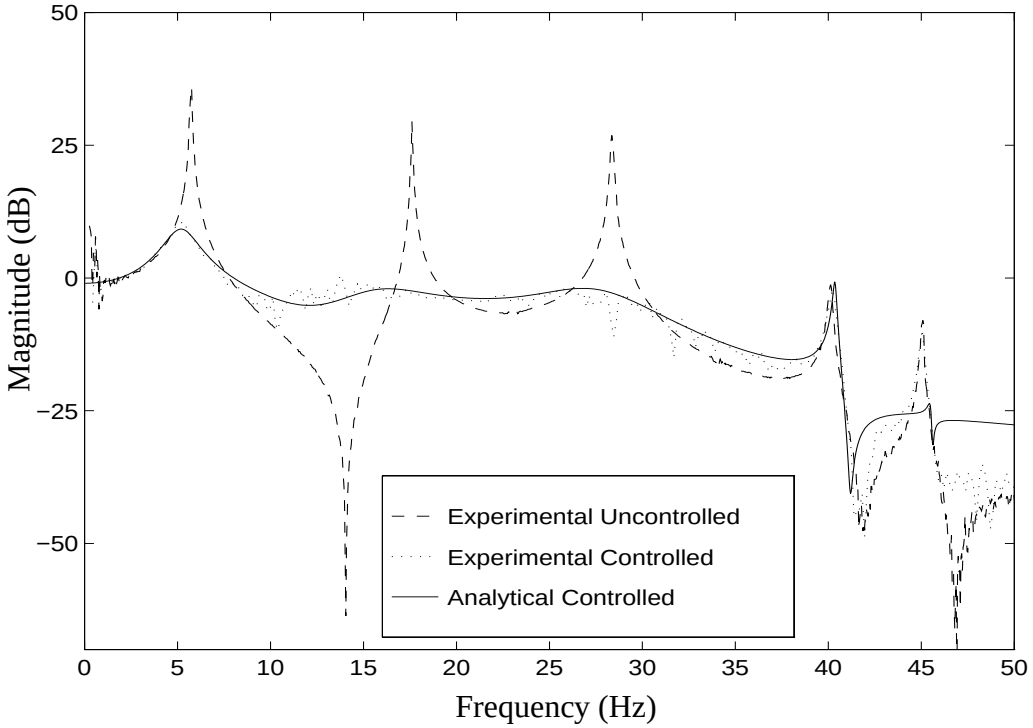

Figure 6.22 Transfer Function from the Ground Acceleration to the Second Floor Absolute Acceleration with Controller A.

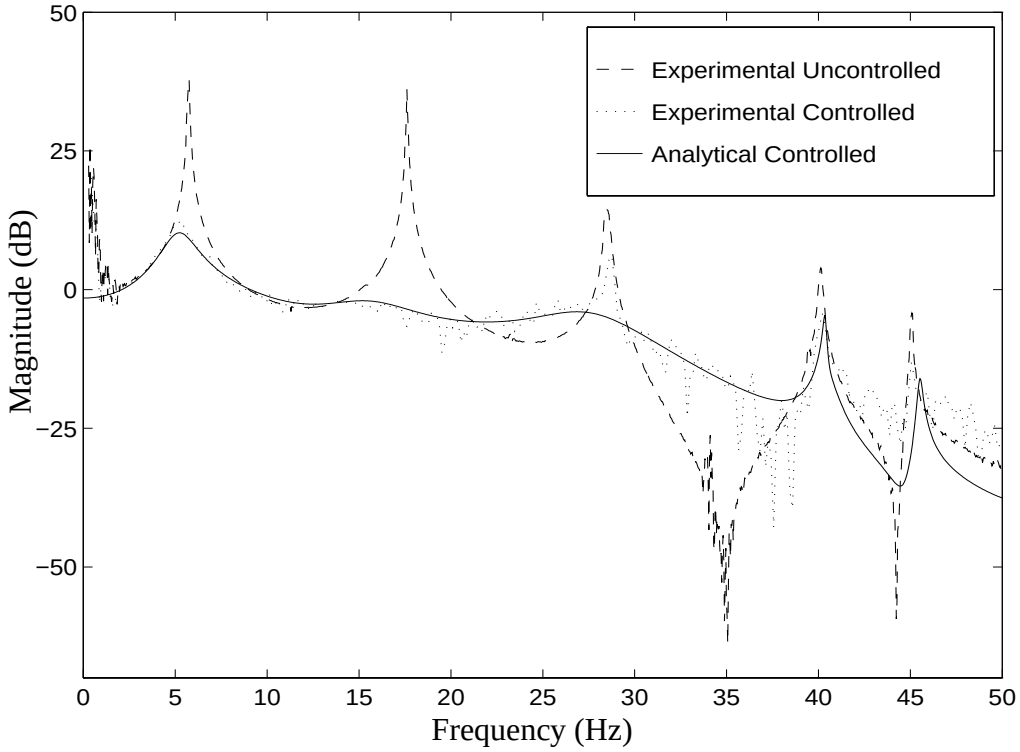

Figure 6.23 Transfer Function from the Ground Acceleration to the Third Floor Absolute Acceleration with Controller A.

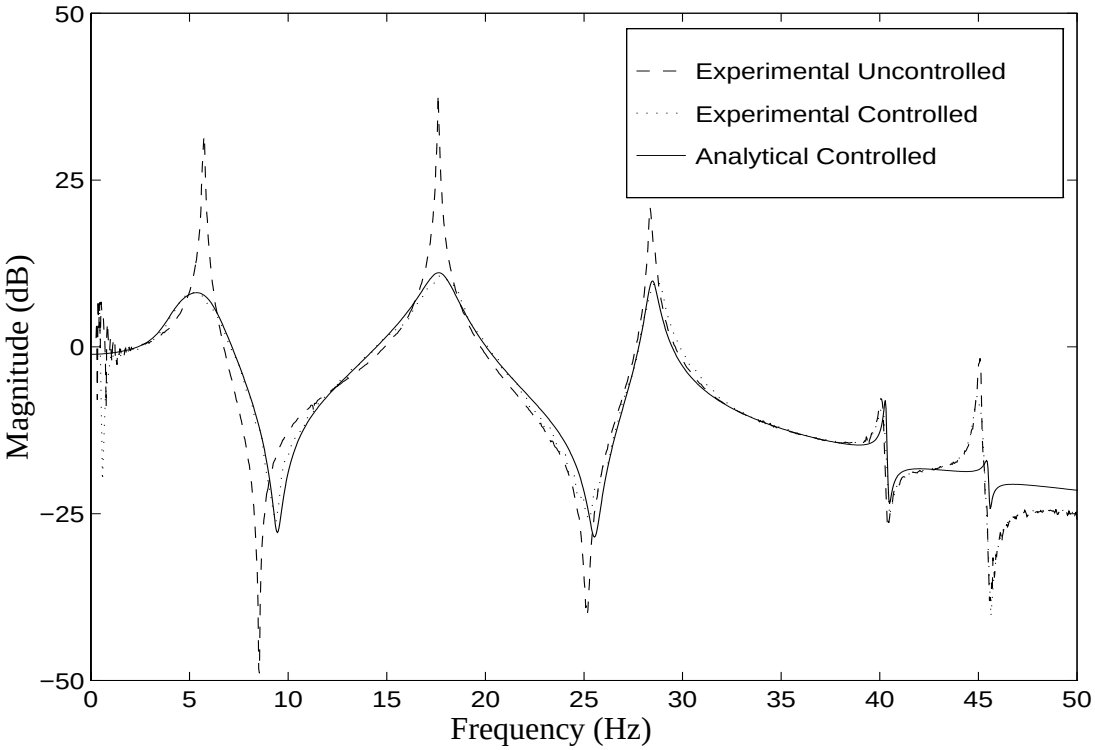

Figure 6.24 Transfer Function from the Ground Acceleration to the First Floor Absolute Acceleration with Controller B.

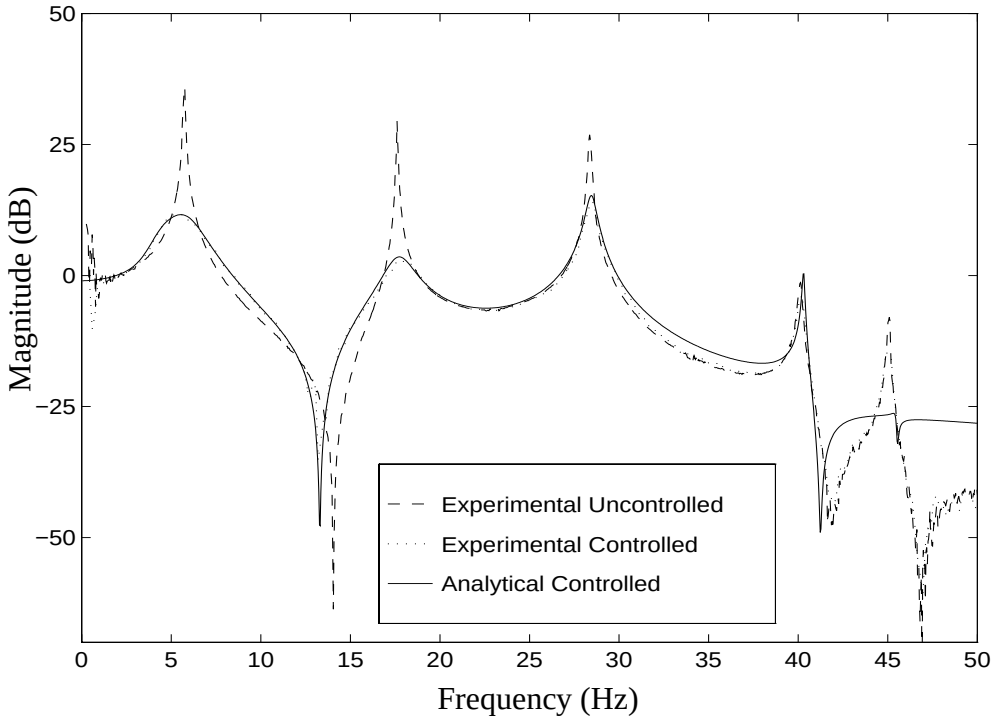

Figure 6.25 Transfer Function from the Ground Acceleration to the Second Floor Absolute Acceleration with Controller B.

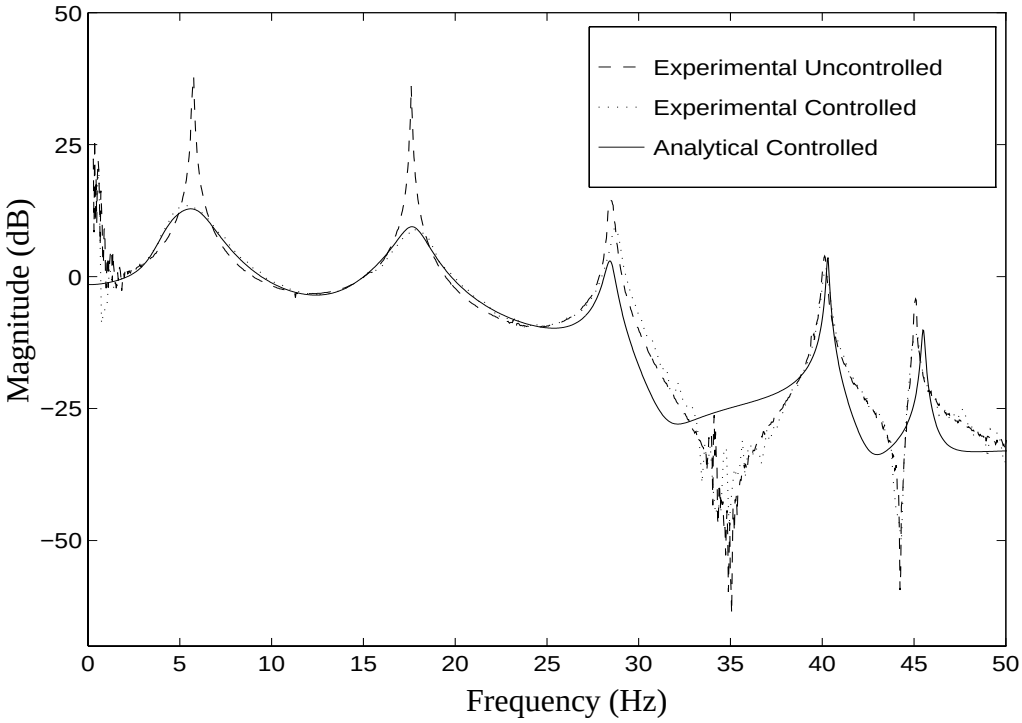

Figure 6.26 Transfer Function from the Ground Acceleration to the Third Floor Absolute Acceleration with Controller B.

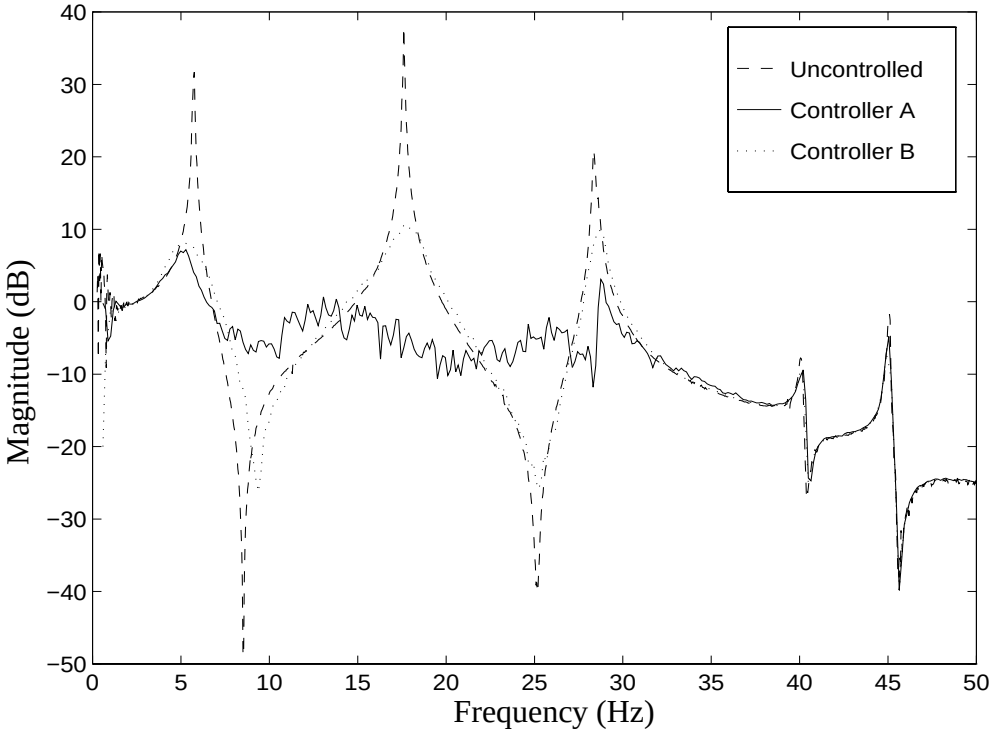

Figure 6.27 Comparison of Experimental Closed Loop Transfer Functions from Ground Acceleration to First Floor Acceleration.

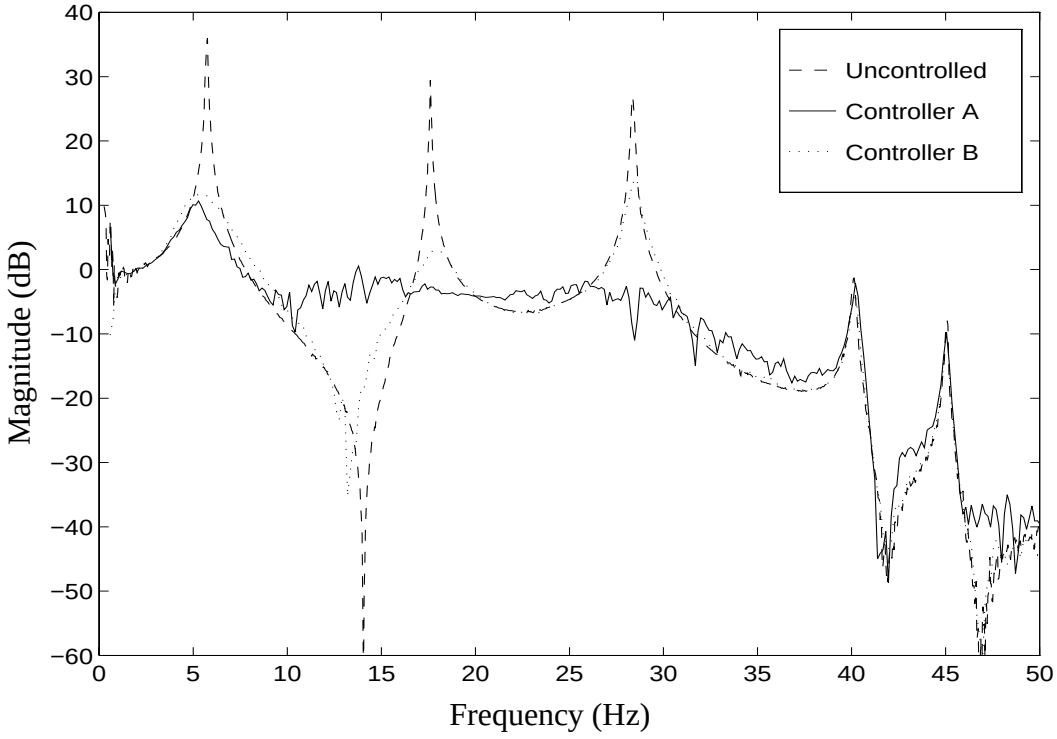

Figure 6.28 Comparison of Experimental Closed Loop Transfer Functions from Ground Acceleration to Second Floor Acceleration.

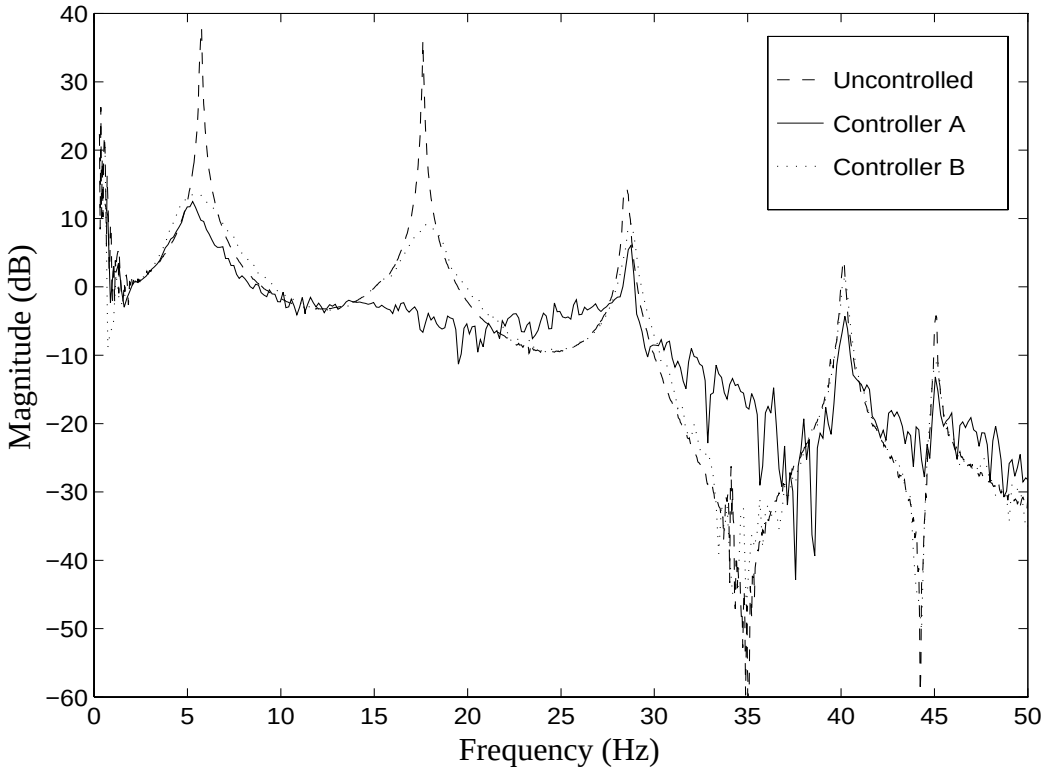

Figure 6.29 Comparison of Experimental Closed Loop Transfer Functions from Ground Acceleration to Third Floor Acceleration.

floor absolute acceleration time response is compared to the uncontrolled response in Figs. 6.31 (Controller A) and 6.34 (Controller B). Controller A was able to reduce the peak acceleration of the third floor by 65.0% and Controller B was able to reduce this peak acceleration by 55.2%. The absolute acceleration of the actuator for the two controllers is shown in Figs. 6.32 (Controller A) and 6.35 (Controller B). The corresponding displacement of the actuator relative to the third floor is given in Figs. 6.33 (Controller A) and 6.36 (Controller B). As indicated in Figs. 6.27–6.29, the high-frequency content of the actuator motion for Controller A is greater than it is for Controller B. Notice again from these graphs and from the peak values in Table 6.3 that the peak acceleration of the actuator for Controller A was significantly larger than that of Controller B, while the peak displacements remained approximately the same.

6.4 Summary of the Active Mass Driver Experiment

In this experiment, acceleration feedback control strategies were successfully implemented and verified on a three-story, single-bay test structure controlled with an active

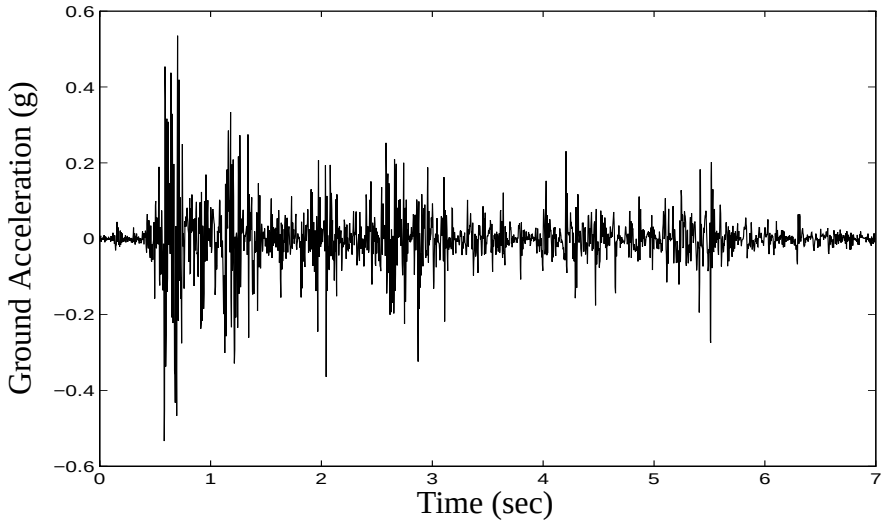

Figure 6.30 Measured Ground Acceleration Used for Earthquake Tests.

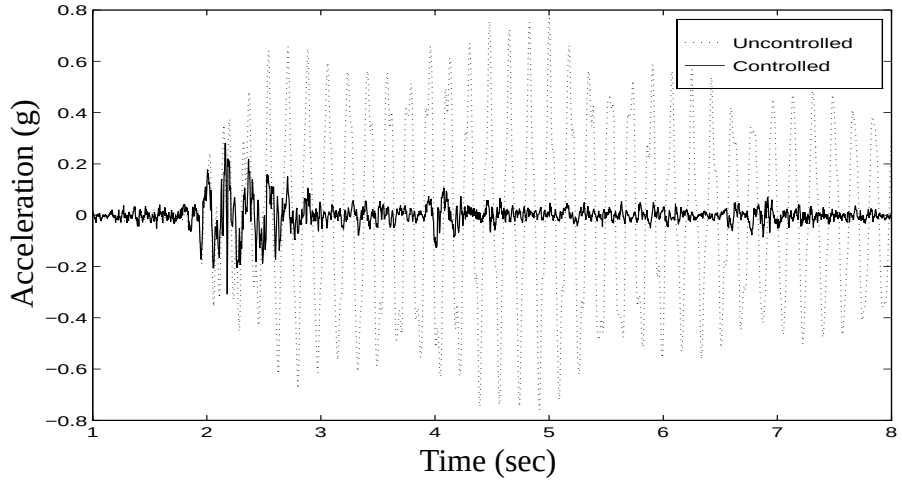

Figure 6.31 Comparison of Uncontrolled and Controlled Absolute Acceleration of the Third Floor with Controller A.

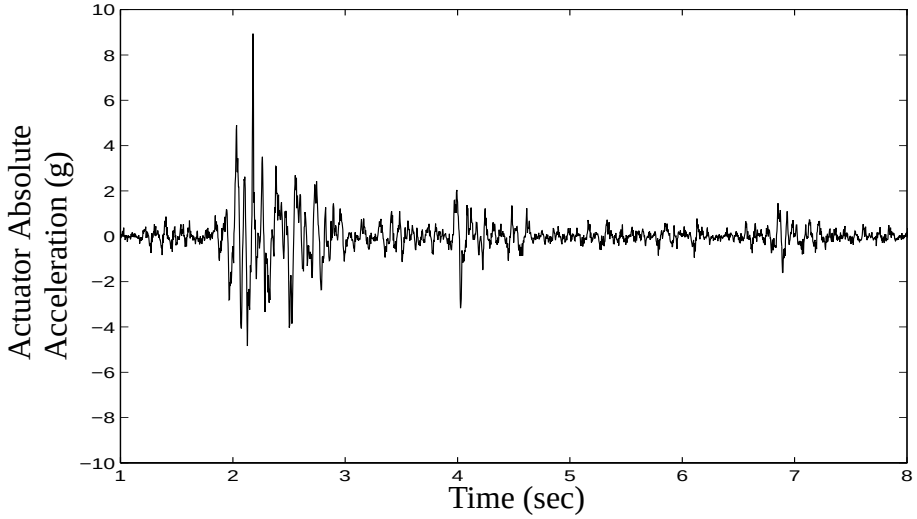

Figure 6.32 Absolute Acceleration of the Actuator with Controller A.

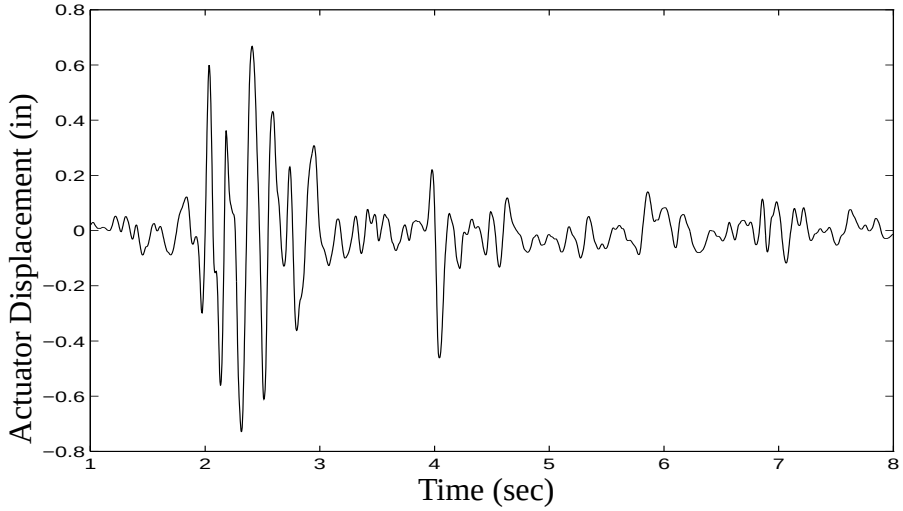

Figure 6.33 Displacement of the Actuator with Controller A.

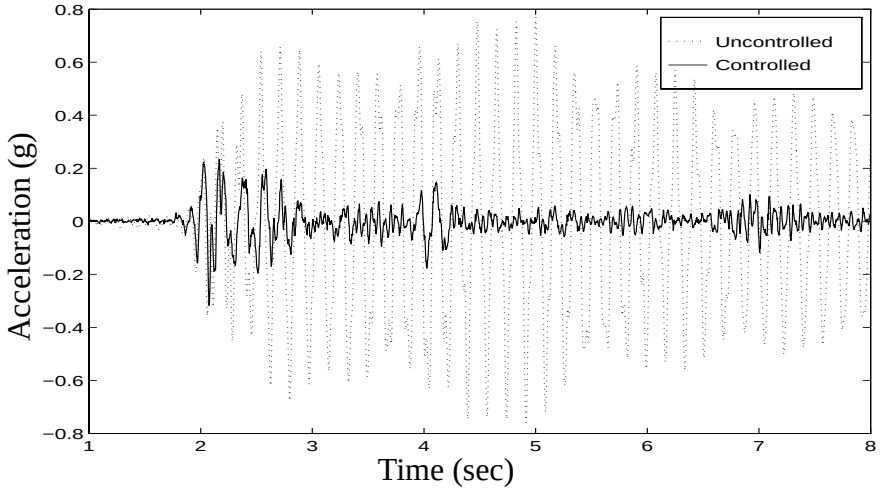

Figure 6.34 Comparison of Uncontrolled and Controlled Absolute Acceleration of the Third Floor with Controller B.

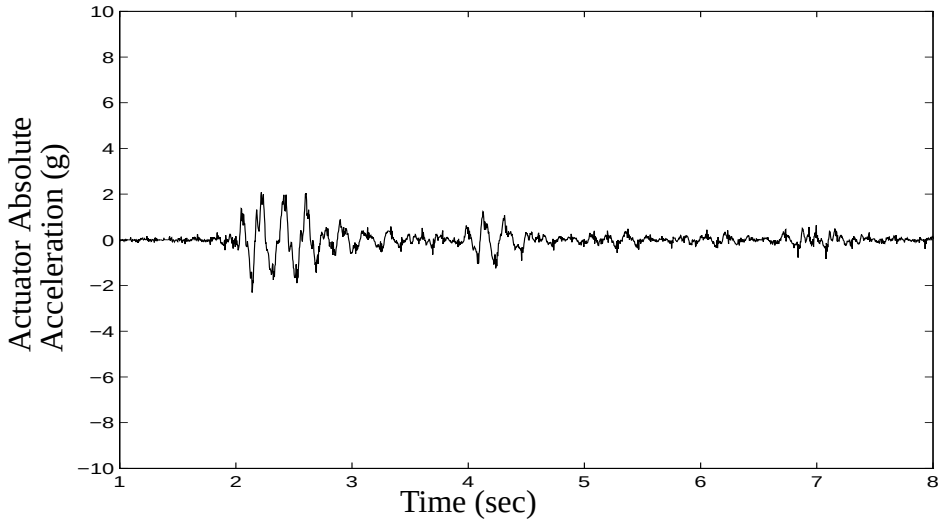

Figure 6.35 Absolute Acceleration of the Actuator with Controller B.

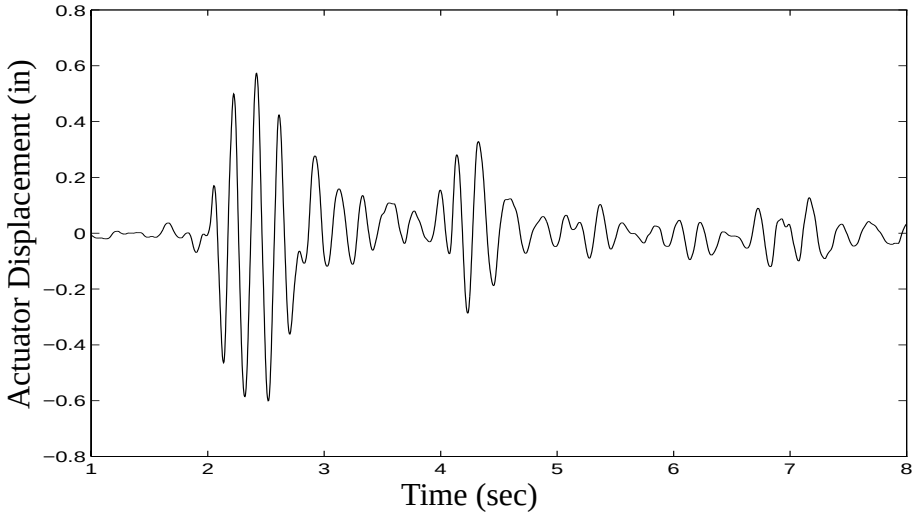

Figure 6.36 Displacement of the Actuator with Controller B.

Table 6.3 Peak Responses for Earthquake Excitation Tests.

Controller	$\ddot{x}_{a1}$, *(in/s²)*	$\ddot{x}_{a2}$, *(in/s²)*	$\ddot{x}_{a3}$, *(in/s²)*	x_a, *(in)*	$\ddot{x}_{am}$, *(in/s²)*	u, *(V)*
Uncontrolled	192	258	297	—	298	—
Controller A	113 (39.3)	123 (49.9)	96.0 (65.0)	0.720	3060	0.444
Controller B	99.3 (46.7)	103 (58.2)	123 (55.2)	0.606	890	0.373

mass driver. A model was identified for the structural system which included the first five modes of the system. The effects of actuator dynamics and control-structure interaction were incorporated into the system identification procedure and the resulting fourteen state model was found to be effective for control design.

H_2/LQG control design techniques were used to successfully design a number of controllers and the results of two control designs were presented. Under a broadband excitation, the AMD controller was able to achieve approximately an 80% reduction in *rms* acceleration responses and a significant response reduction was achieved in all three modes of the system. When excited by an earthquake disturbance, the reduction in the peak response of the third floor absolute acceleration was 65.0%. Based on these results, acceleration feedback control strategies should be regarded as viable and effective for mitigation of structural responses due to seismic excitations.

The experimental results indicate that AMD systems employing acceleration feedback strategies are effective for reduction of structural responses during seismic activity and that response reduction can be achieved in all three modes of the structural system.

CHAPTER 7

Modeling of a Semi-Active Magnetorheological Damper

The focus of the remaining chapters of the dissertation is the verification of acceleration feedback strategies for semi-active control systems. Because semi-active control systems combine the best features of passive and active control, they appear to have significant potential to advance the acceptance of structural control as a viable means for dynamic hazard mitigation. In contrast to active control devices, semi-active control devices do not have the potential to destabilize the structure (in the bounded input – bounded output sense), and most require little power to operate. Moreover, preliminary studies indicate that the semi-active dampers have the potential to achieve the performance of fully active systems, thus allowing for the possibility of effective response reduction during both moderate and strong seismic activity. One particularly promising class of semi-active control devices for seismic response reduction is found in magnetorheological (MR) dampers. These devices offer mechanical simplicity, low operating power requirements, environmental robustness, and demonstrated potential for developing forces sufficient for full-scale applications.

A prototype magnetorheological (MR) damper has been obtained from the Lord Corporation of Cary, North Carolina to evaluate the usefulness of MR devices in response reduction for civil engineering structures. To develop control algorithms that take maxi-

mum advantage of the unique features of the damper and to evaluate its effectiveness of for structural control applications, a model must be developed that can adequately characterize the damper's intrinsic nonlinear behavior. Following a description of the MR damper, a review of several idealized mechanical models for controllable fluids and fluid dampers is presented, and a new model is proposed that can effectively portray the behavior of a typical MR damper. Comparison with experimental results for a prototype damper indicates that the model is accurate over a wide range of operating conditions and is appropriate for control design and analysis.

7.1 Magnetorheological Fluid and Damper

MR fluids are the magnetic analogs of electrorheological (ER) fluids which have also been considered for structural control applications. The essential characteristic of these controllable fluids is their ability to reversibly change from a free-flowing, linear, viscous fluid to a semi-solid in milliseconds when exposed to a magnetic (or electric in the case of ER fluids) field. Recently developed MR fluids have high strength, low viscosity, and low power requirements, are stable over a broad temperature range and are insensitive to impurities commonly introduced during manufacturing (see Table 1.1). Because there are no moving parts, other than the piston itself, damping devices that take advantage of controllable fluids are simpler and more reliable than semi-active dampers based on electromechanical devices. Furthermore, the MR damper is expected to be quite inexpensive to build and operate, and preliminary tests indicate that it will be capable of generating the required forces for civil engineering applications. However, semi-active control devices are also intrinsically nonlinear, making it a challenging task to develop system identifica-

tion techniques and appropriate control strategies that can optimally exploit their unique features.

The MR damper consists of a fixed orifice damper filled with a magnetorheological fluid as shown in Fig. 7.1. The MR fluid is a proprietary formulation, VersaFlo^{TM} MRX-135GD developed by the Lord Corporation, that consists of micron-size, magnetically-soft iron randomly dispersed in a hydrocarbon oil along with additives that promote homogeneity and inhibit gravitational settling. The fluid has a density of 3.28 g/cm^3.

The damper is 21.5 cm long in its extended position, and the main cylinder is 3.8 cm in diameter. The main cylinder houses the piston, the magnetic circuit, an accumulator and

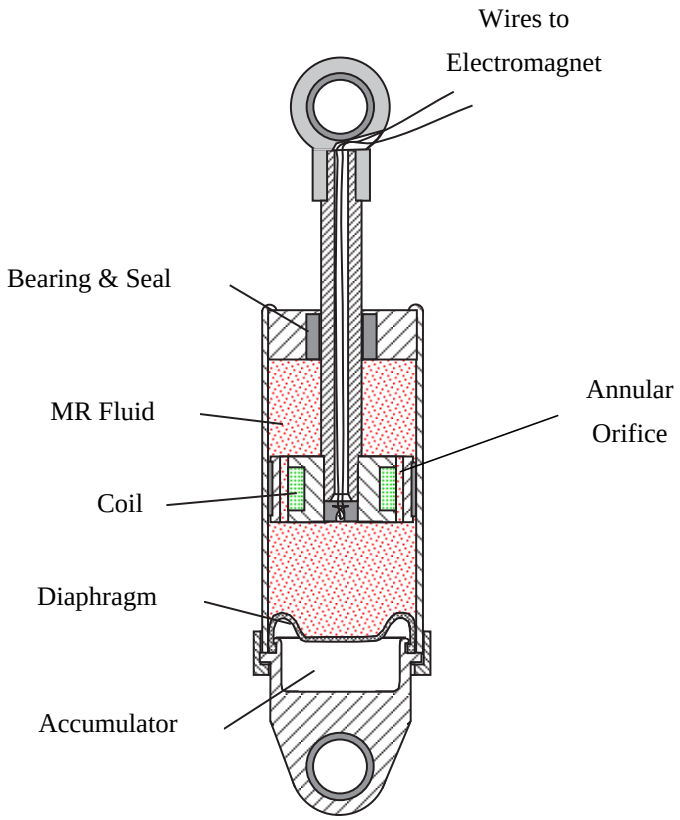

Figure 7.1 Schematic of MR Damper.

50 ml of MR fluid, and the damper has a ±2.5 cm stroke. As shown in Fig. 7.1, the MR fluid valve is contained within the damper piston and consists of an annular flow channel having an inner diameter of 27 mm and an outer diameter of 28 mm. The magnetic field is applied radially across the resulting 0.5 mm dimension, perpendicular to the direction of fluid flow. The total axial length of the flow channel is 15 mm of which 7 mm is exposed to the applied magnetic field. Thus, the total volume of fluid that sees the magnetic field at any instant is about 0.3 ml. The magnetic field can be varied from 0 to 200kA/m for currents of 0 to 1 amp in the electromagnet coil, which has a resistance of 4 Ω. The total inductance of the MR fluid valve is 40 mH, resulting in an L/R time constant of 10 msec. The peak power required is less than 10 watts, which would allow the damper to be operated continuously for more than an hour on a small camera battery. For this example, the current for the electromagnet is supplied by a linear current driver running off of 120 volts AC and generates a 0 to 1 amp current that is proportional to a commanded DC input voltage in the range 0–3 V. With this power supply, the damper typically reaches rheological equilibrium in less than 6.5 msec after applying the magnetic field (Carlson and Weiss 1994). Forces of up to 3000 N can be generated with devices of this size, with small variations over a broad temperature range (varying less than 10% in the range of –40 to 150 degrees Celsius).

7.2 Behavior of a Magnetorheological Damper

To take full advantage of the unique features of the MR damper in control applications, a model must be developed that can accurately reproduce the behavior of the MR damper. The load frame shown in Fig. 7.2 was designed and built for the purpose of obtaining the MR damper response data necessary for identification studies. In this setup, a double-ended hydraulic actuator, manufactured by Nopak, was employed to drive the

damper. The actuator had a 3.8 cm diameter cylinder and a 30.5 cm stroke and was fitted with low-friction Teflon seals to reduce nonlinear effects. A servo-valve, made by Dynamic Valves, Inc., with a nominal operational frequency range of 0–45 Hz was used to control the actuator. A Schaevitz linear variable differential transformer (LVDT) was used to measure the displacement of the piston-rod of the MR damper, and an Omega load cell with a range of $\pm$ 4540 N was included in series with the damper to measure the output force. Using this experimental setup, dynamic responses of the damper can be measured for a wide range of prescribed displacement wave forms, including sine, step, triangle and pseudo random.

Using the setup depicted in Fig. 7.2, a series of preliminary tests was conducted to measure the response of the damper under various loading conditions. In each test, the hydraulic actuator was driven with a sinusoidal signal with a fixed frequency, and the voltage applied to the prototype MR damper was held at a constant level. A wide range of frequencies, amplitudes and voltage levels were considered. The data was sampled at 256 Hz. The velocity response was calculated from the measured displacements via a central difference approximation.

The response of the MR damper due to a 2.5 Hz sinusoid with an amplitude of 1.5 cm is shown in Fig. 7.3 for four constant voltage levels, 0 V, 0.75 V, 1.5 V, and 2.25 V, being applied to the power amplifier for the device. These voltages correspond to 0 A, 0.25 A,

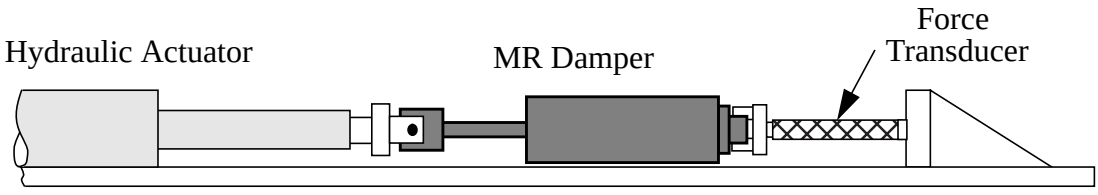

Figure 7.2 Test Setup for MR Damper Identification.

0.5 A and 0.75 A, respectively. The force generated as a function of time is shown in Fig. 7.3a, the force-displacement loop is shown in Fig. 7.3b and the force-velocity loop is shown in Fig. 7.3c. Note that the force-displacement loops in Fig. 7.3b progress along a clockwise path with increasing time, whereas the force-velocity loops in Fig. 7.3c progress along a counter-clockwise path with increasing time.

In Fig. 7.3, the effects of changing the magnetic field are readily observed. At 0 V the MR damper primarily exhibits the characteristics of a purely viscous device (*i.e.*, the force-displacement relationship is approximately elliptical, and the force-velocity relationship is nearly linear). However, as the voltage increases, the force required to yield the MR fluid in the damper increases and produces behavior associated with a plastic material

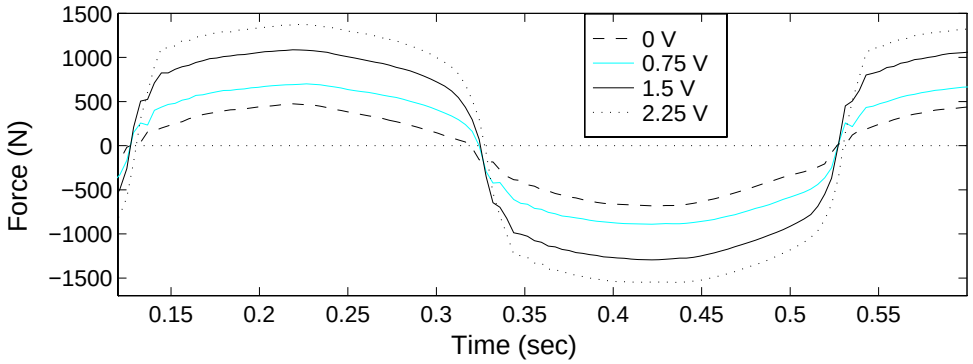

a) Force vs. Time

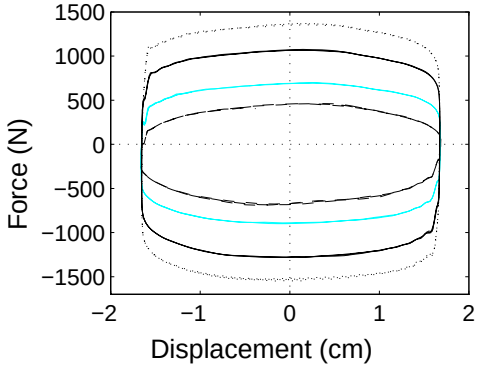

b) Force vs. Displacement

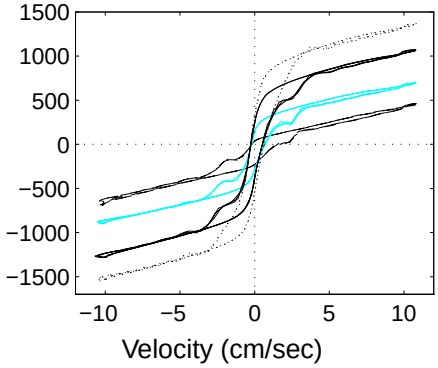

c) Force vs. Velocity

Figure 7.3 Experimentally Measured Force for 2.5 Hz Sinusoidal Excitation with an Amplitude of 1.5 cm.

in parallel with a viscous damper, *i.e.*, Bingham plastic behavior (Shames and Cozzarelli 1992). Also, notice that the increase in force for a given increase in the applied voltage is approximately linear for voltages between 0–2.25 V. For the particular damper tested, saturation of the MR effect occurs above 2.25 V.

From Fig. 7.3, observe that the force produced by the damper is not centered at zero. This effect is due to the presence of an accumulator in the MR damper, which consists of a bladder within the main cylinder (see Fig. 7.1) that is filled with nitrogen pressurized at 300 psi. The accumulator helps prevent cavitation in the fluid during normal operation and accounts for the volume of fluid displaced by the piston rod as well as thermal expansion of the fluid. From a phenomenological perspective, the accumulator acts like a spring in the damper. In the experimental data provided in Fig. 7.3, the presence of the accumulator produces an offset in the measured damper force and a slight vertical widening of the response loops in the force-velocity plot. To obtain an effective model of the MR damper, the stiffness associated with the accumulator must be taken into account.

Another interesting feature of the data that is important to note is seen in the force-velocity responses shown in Fig. 7.3c. Focusing attention on the upper branch of the force-velocity curve, which corresponds to decreasing velocities (*i.e.*, negative accelerations, and therefore positive positions), for large positive velocities, the force in the damper varies linearly with velocity. However, as the velocity decreases and before it becomes negative, the force-velocity relationship is no longer linear, decreasing rapidly and smoothly. This roll-off in the force at small velocities is due to bleed or blow-by of fluid between the piston and the cylinder and is necessary to eliminate harshness from the subjective feel of the damper in vehicular applications. This type of behavior will be sought in a model of the MR damper.

7.3 Mechanical Model Formulation

Both nonparametric and parametric models have been considered to model the observed behavior of controllable fluid dampers. Ehrgott and Masri (1994) presented a nonparametric approach for modeling ER fluid dampers by assuming that the damper force could be written in terms of Chebychev polynomials in the damper velocity and acceleration. McClamroch and Gavin (1995) followed a similar approach in modeling an ER device. One of the difficulties in this approach is that the resulting models are often quite complex. Using basic mechanics, Kamath and Wereley (1996) and Makris, *et al.* (1996) have developed parametric models to characterize ER fluids and fluid devices. Alternatively, parametric models based on simple mechanical idealizations have been considered by Stanway, *et al.* (1985, 1987) and Gamota and Filisko (1991) to describe the behavior of controllable fluids and fluid dampers. Such an approach is advocated herein. Next the effectiveness of several idealized mechanical models for predicting the response of the prototype MR damper are examined, and a new model is proposed that addresses a number of shortcomings associated with these models.

The Bingham viscoplastic model (Shames and Cozzarelli, 1992) is often used to describe the stress-strain behavior of MR (and ER) fluids. In this model, the plastic viscosity is defined as the slope of the measured shear stress versus shear strain rate data. Thus, for positive values of the shear rate, $\dot{\gamma}$, the total stress is given by

$$\tau = \tau_{y(field)} + \eta\dot{\gamma} \tag{7.1}$$

where $\tau_{y(field)}$ is the yield stress induced by the magnetic (or electric) field and η is the viscosity of the fluid.

Based on the Bingham model, Stanway, *et al.* (1985, 1987) proposed an idealized mechanical model, denoted the Bingham model, for the behavior of an ER damper. The Bingham model consists of a Coulomb friction element placed in parallel with a viscous

damper, as shown in Fig. 7.4. In this model, for nonzero piston velocities, $\dot{x}$, the force generated by the device given by

$$f = f_f sgn(\dot{x}) + c_0\dot{x} + f_0 \tag{7.2}$$

where c_0 is the damping coefficient and f_f is the frictional force, which is related to the fluid yield stress. An offset in the force f_0 is included to account for the nonzero mean observed in the measured force due to the presence of the accumulator. Note that if at any point the velocity of the piston is zero, the force generated in the frictional element is equal to the applied force.

To assess its ability to predict the behavior of the MR damper, the model in Eq. (7.2) was fit to the 2.5 Hz sinusoidal response data shown in Fig. 7.3 for the case in which the command voltage to the current driver was a constant 1.5 V. The parameters chosen are f_f = 670 N, c_0 = 50 N·sec/cm and f_0 = –95 N. Fig. 7.5 shows a comparison between the predicted and experimentally obtained responses. Although the force-displacement behavior appears to be reasonably modeled, examination of the force-velocity response and the temporal variation of the force shows that the behavior of the damper is not captured, especially for velocities that are near zero. In particular, this model does not exhibit the nonlinear force-velocity response observed in the data for the case when the acceleration and velocity have opposite signs (or alternatively, when the velocity and the

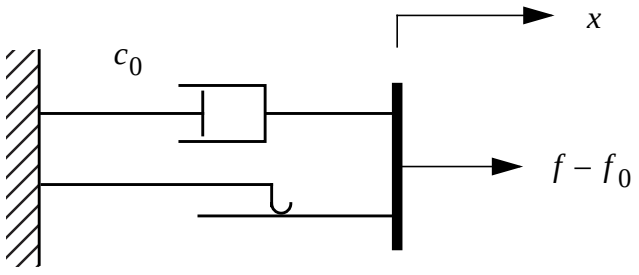

Figure 7.4 Bingham Model of a Controllable Fluid Damper (Stanway, *et al*. 1985, 1987).

displacement have the same sign) and the magnitude of the velocities are small. While this model may be adequate for response analysis, it is not adequate for control analysis. Notice that the model predicts a one-to-one relationship between the force and velocity, but the experimentally obtained data is not one-to-one. Furthermore, at zero velocity, the measured force has a positive value when the acceleration is negative (positive displacements), and a negative value when the acceleration is positive (negative displacement). This behavior must be captured in a mathematical model to adequately characterize the device for control applications.

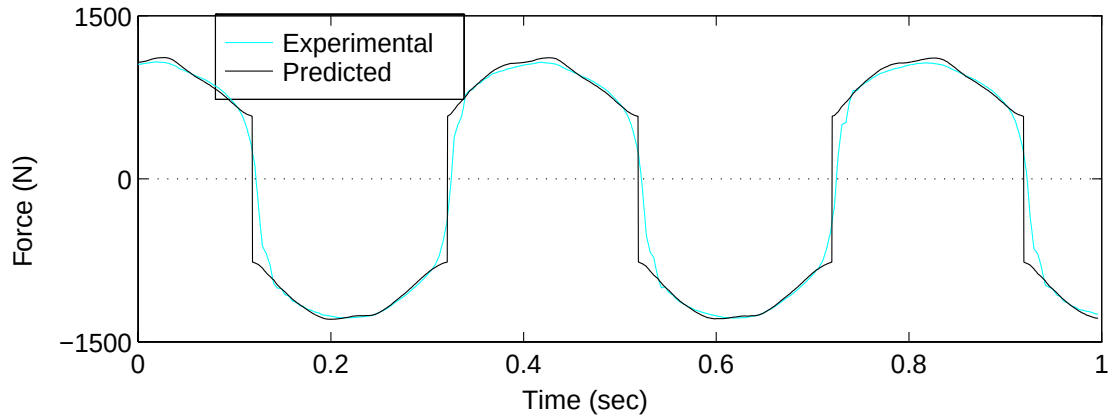

a) Force vs. Time

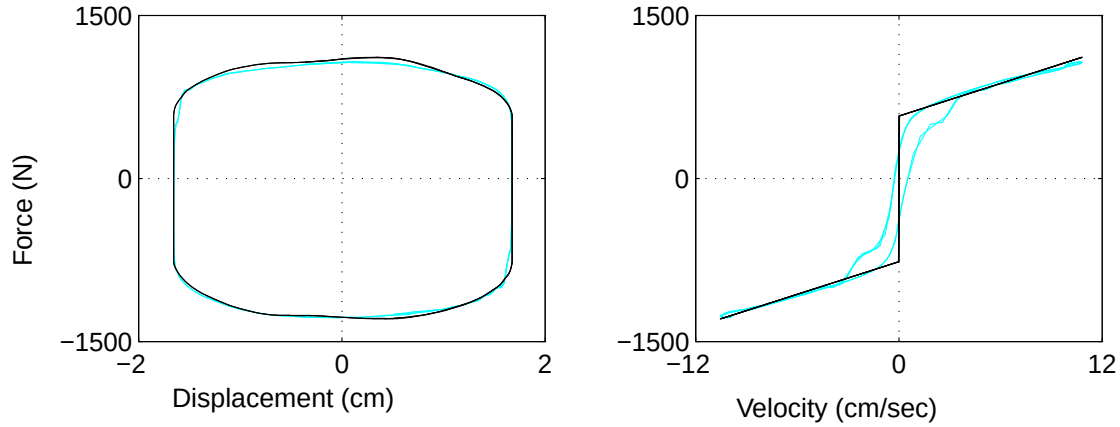

b) Force vs. Displacement

c) Force vs. Velocity

Figure 7.5 Comparison Between the Predicted and Experimentally Obtained Responses for the Bingham Model.

Focusing on predicting the behavior of ER materials, Gamota and Filisko (1991) proposed an extension of the Bingham model, which is given by the viscoelastic-plastic model shown in Fig. 7.6. The model consists of the Bingham model (*i.e.*, a frictional element in parallel with a dashpot) in series with a standard model of a linear solid (Shames and Cozzarelli, 1992). The governing equations for this model are given by

$$\left.\begin{aligned} f &= k_1(x_2 - x_1) + c_1(\dot{x}_2 - \dot{x}_1) + f_0 \\ &= c_0\dot{x}_1 + f_f\, sgn(\dot{x}_1) + f_0 \\ &= k_2(x_3 - x_2) + f_0 \end{aligned}\right\}, \qquad |f| > f_f \tag{7.3}$$

$$\left.\begin{aligned} f &= k_1(x_2 - x_1) + c_1\dot{x}_2 + f_0 \\ &= k_2(x_3 - x_2) + f_0 \end{aligned}\right\}, \qquad |f| \le f_f \tag{7.4}$$

where c_0 is the damping coefficient associated with the Bingham model and k_1, k_2 and c_1 are associated with the linear solid material. Note that when $|f| \le f_f$, $\dot{x}_1 = 0$.

Again, parameters for the model in Eqs. (7.3, 7.4) were determined to fit the 2.5 Hz data shown in Fig. 7.3 for the case where the voltage to the current driver was 1.5 V. The parameters chosen are $f_f = 670$ N, $c_0 = 5000$ N·sec/cm, $c_1 = 1300$ N·sec/cm, $k_1 = 5 \times 10^4$ N/cm, $k_2 = 2 \times 10^6$ N/cm and $f_0 = -95$ N. A comparison between the predicted responses and the corresponding experimental data is provided in Fig. 7.7. As might be expected, this model can portray the force-displacement behavior of the damper well. In addition, it possesses force-velocity behavior that more closely resembles the

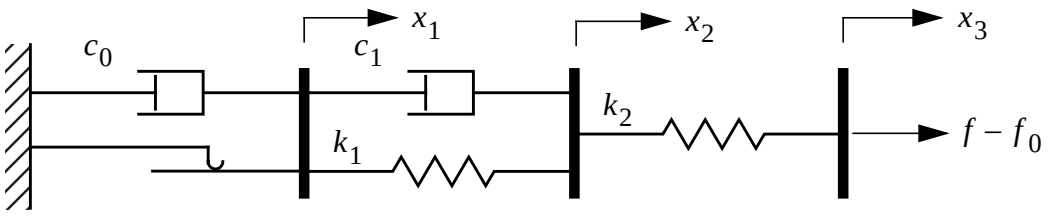

Figure 7.6 Model proposed by Gamota and Filisko (1991).

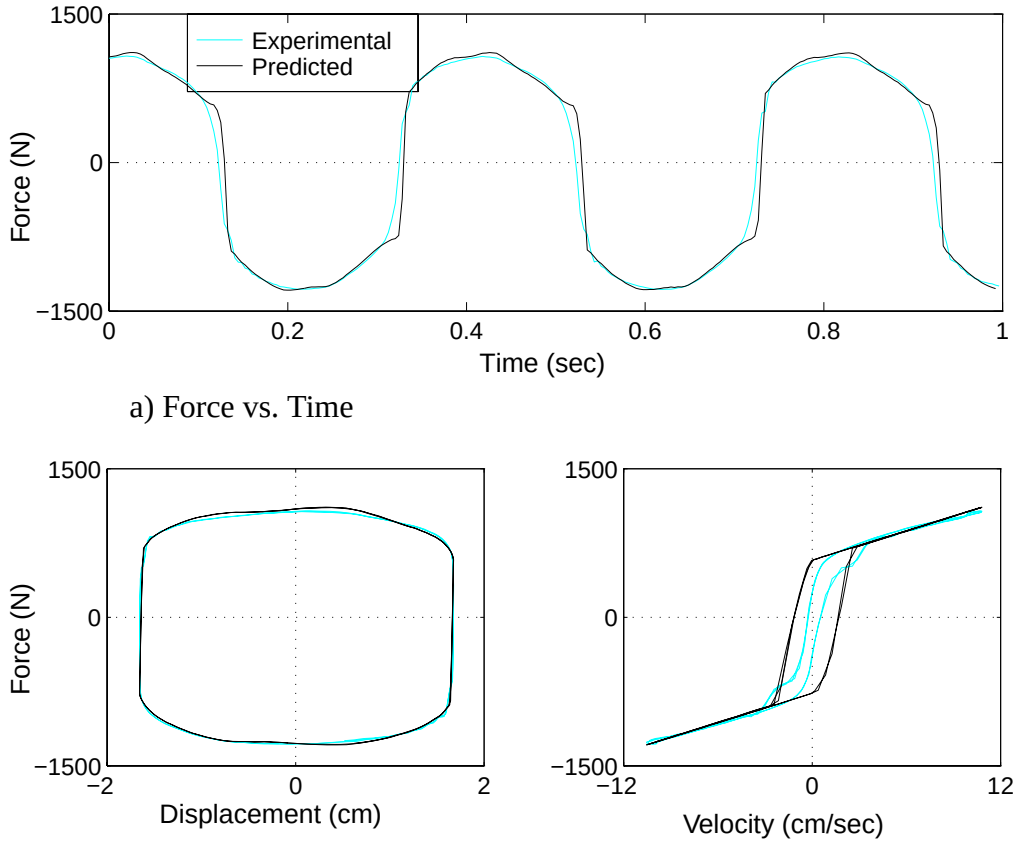

a) Force vs. Time

b) Force vs. Displacement

c) Force vs. Velocity

Figure 7.7 Comparison Between the Predicted and Experimentally Obtained Responses for the Gamota and Filisko Model.

experimental data. However, the governing equations (7.3, 7.4) are extremely stiff, making them difficult to deal with numerically. Numerical integration of Eq. (7.3, 7.4) for the parameters given previously required a time step on the order of 10^{-6} sec. Note that a decrease in the damping, c_1, can produce the nonlinear roll-off observed in the experimental force-velocity relationship as the velocity approaches zero, but then even smaller time steps are required to simulate the system. The numerical challenges of this model constitute its main shortcoming, which was also noted in Ehrgott and Masri (1994).

One model that is numerically tractable and has been used extensively for modeling hysteretic systems is the Bouc-Wen model (Wen 1976). The Bouc-Wen model is

extremely versatile and can exhibit a wide variety of hysteretic behavior. A schematic of this model is shown in Fig. 7.8. The force in this system is given by

$$f = c_0\dot{x}_d + k_0(x_d - x_0) + \alpha z \tag{7.5}$$

where the evolutionary variable z is governed by

$$\dot{z} = -\gamma|\dot{x}_d|z|z|^{n-1} - \beta\dot{x}_d|z|^n + A\dot{x}_d . \tag{7.6}$$

By adjusting the parameters of the model γ, β and A, one can control the linearity in the unloading and the smoothness of the transition from the pre-yield to the post-yield region. In addition, the force f_0 due to the accumulator can be directly incorporated into this model as an initial deflection x_0 of the linear spring k_0.

A set of parameters was determined to fit the response of the Bouc-Wen model to the experimentally measured response of the MR damper shown in Fig. 7.3 (2.5 Hz sinusoidal displacement and a constant applied voltage of 1.5V). The parameters for the model in Eq. (7.5, 7.6) were chosen to be α = 880 N/cm, c_0 = 50 N·sec/cm, k_0 = 25 N/cm, γ = 100 cm^{-2}, β = 100 cm^{-2}, n = 2, A = 120 and x_0 = 3.8 cm. A comparison between the predicted responses and the corresponding experimental data is provided in

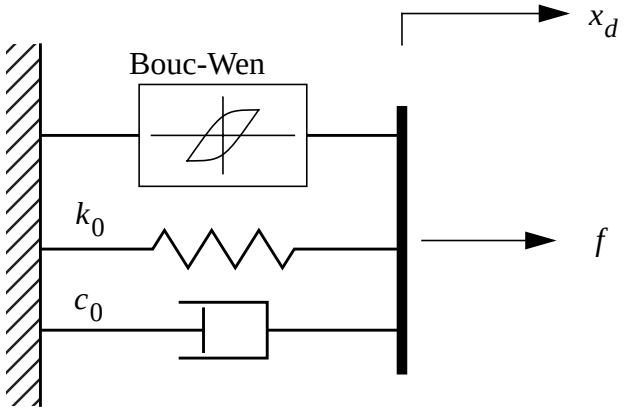

Figure 7.8 Bouc-Wen Model of the MR Damper.

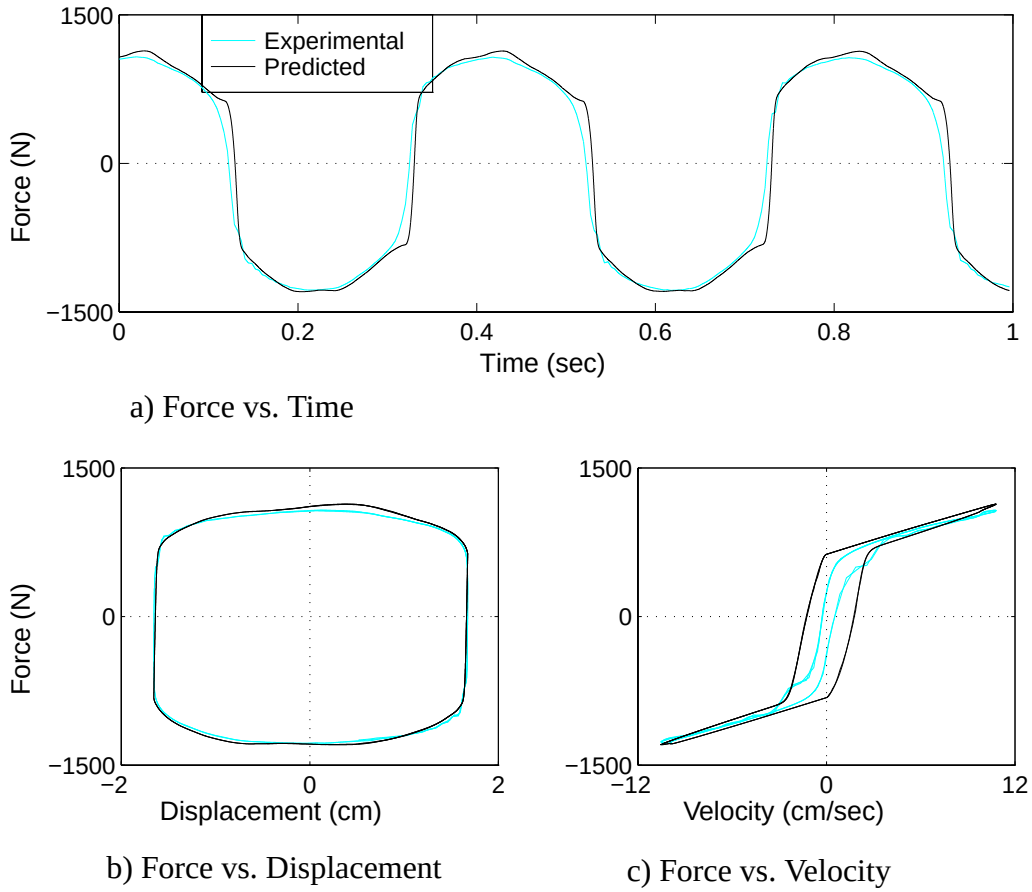

a) Force vs. Time

b) Force vs. Displacement

c) Force vs. Velocity

Figure 7.9 Comparison Between the Predicted and Experimentally Obtained Responses for the Bouc-Wen Model.

Fig. 7.9. The Bouc-Wen model predicts the force-displacement behavior of the damper well, and it possesses force-velocity behavior that more closely resembles the experimental data. However, similar to the Bingham model, the nonlinear force-velocity response of the Bouc-Wen model does not roll-off in the region where the acceleration and velocity have opposite signs and the magnitude of the velocities are small. To better predict the damper response in this region, a modified version of the system in Fig. 7.8 is proposed, as shown in Fig. 7.10. To obtain the governing equations for this model, consider only the upper section of the model. The forces on either side of the rigid bar are equivalent; therefore,

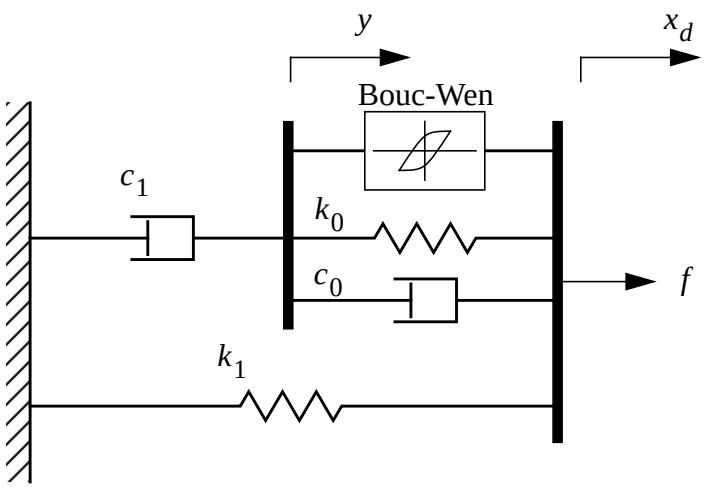

Figure 7.10 Proposed Mechanical Model of the MR Damper.

$$c_1\dot{y} = \alpha z + k_0(x_d - y) + c_0(\dot{x}_d - \dot{y}) \tag{7.7}$$

where the evolutionary variable z is governed by

$$\dot{z} = -\gamma\left|\dot{x}_d - \dot{y}\right|z|z|^{n-1} - \beta(\dot{x}_d - \dot{y})|z|^n + A(\dot{x}_d - \dot{y}). \tag{7.8}$$

Solving (7.7) for $\dot{y}$ results in

$$\dot{y} = \frac{1}{(c_0 + c_1)}\{\alpha z + c_0\dot{x}_d + k_0(x_d - y)\}. \tag{7.9}$$

The total force generated by the system is then found by summing the forces in the upper and lower sections of the system in Fig. 7.10, yielding

$$f = \alpha z + c_0(\dot{x}_d - \dot{y}) + k_0(x_d - y) + k_1(x_d - x_0) \tag{7.10}$$

From Eq. (7.7), the total force can also be written as

$$f = c_1\dot{y} + k_1(x_d - x_0). \tag{7.11}$$

In this model, the accumulator stiffness is represented by k_1 and the viscous damping observed at larger velocities is represented by c_0. A dashpot, represented by c_1, is

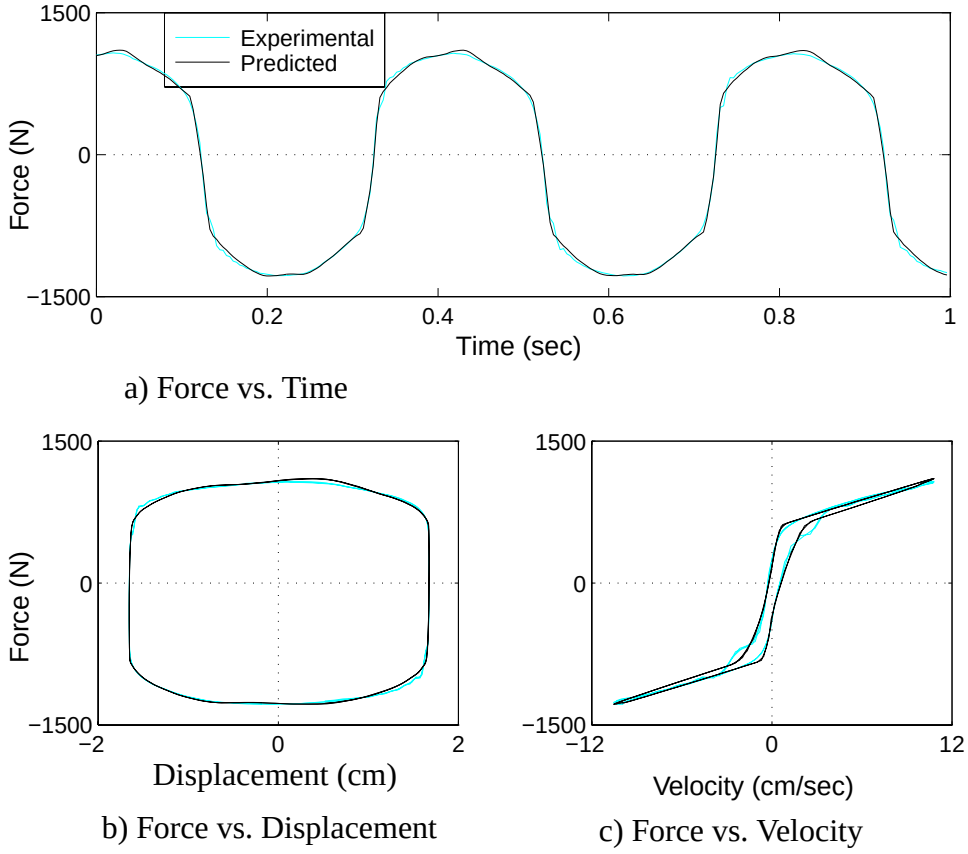

a) Force vs. Time

b) Force vs. Displacement

c) Force vs. Velocity

Figure 7.11 Comparison Between the Predicted and Experimentally Obtained Responses for the Proposed Model.

included in the model to produce the roll-off that was observed in the experimental data at low velocities, k_0 is present to control the stiffness at large velocities, and x_0 is the initial displacement of spring k_1 associated with the nominal damper force due to the accumulator.

The parameters for the model in Eq. (7.9, 7.10) were chosen to be $\alpha = 963$ N/cm, $c_0 = 53$ N $\cdot$ sec/cm, $k_0 = 14$ N/cm, $c_1 = 930$ N $\cdot$ sec/cm, $k_1 = 5.4$ N/cm, $\gamma = 200$ cm^{-2}, $\beta = 200$ cm^{-2}, $n = 2$, $A = 207$, and $x_0 = 18.9$ cm, which fit the response of the proposed model to the 2.5 Hz data shown in Fig. 7.3 for the case where the voltage to the current driver was 1.5 V. A comparison between the predicted responses and the corresponding experimental data is provided in Fig. 7.11. The proposed model for the damper

predicts the behavior of the damper very well in all regions, including in the region where the acceleration and velocity have opposite signs and the magnitude of the velocities are small.

In addition to the graphical evidence of the superiority of the proposed model, a quantitative study of the errors between each of the models and the experimental data. For each of the models considered here, the error between the predicted force and the measured force has been calculated as a function of time, displacement and velocity over two complete cycles. The following expressions have been used to represent the errors

$$E_t = \frac{\varepsilon_t}{\sigma_f}, \qquad E_x = \frac{\varepsilon_x}{\sigma_f}, \qquad E_{\dot{x}} = \frac{\varepsilon_{\dot{x}}}{\sigma_f} \tag{7.12}$$

where

$$\varepsilon_t^2 = \frac{1}{T}\int_0^T (f_{exp} - f_{pre})^2 \, dt \tag{7.13}$$

$$\varepsilon_x^2 = \frac{1}{T}\int_0^T (f_{exp} - f_{pre})^2 \left|\frac{dx_d}{dt}\right| dt \tag{7.14}$$

$$\varepsilon_{\dot{x}}^2 = \frac{1}{T}\int_0^T (f_{exp} - f_{pre})^2 \left|\frac{d\dot{x}_d}{dt}\right| dt \tag{7.15}$$

$$\sigma_f^2 = \frac{1}{T}\int_0^T (f_{exp} - \mu_F)^2 \, \mathrm{dt}. \tag{7.16}$$

The resulting error norms are given in Table 7.1. In all cases, the error norms calculated for the proposed model are considerably smaller than those calculated for the other models considered, indicating that the proposed model is superior to the other models for the MR damper considered.

Table 7.1 Error Norms for MR Damper Models.

Model	E_t	E_x	$E_{\dot{x}}$
Bingham Model	0.154	0.0398	0.133
Gamota and Filisko Model	0.196	0.0717	0.300
Simple Bouc-Wen Model	0.167	0.0585	0.135
Proposed Bouc-Wen Model	0.0351	0.0228	0.0445

Because of its flexibility and numerical tractability for sinusoidal displacement and constant magnetic field, the proposed mechanical model will be used to predict the behavior of the MR damper. In the next section, a generalization will be considered to model the device when the magnetic field and the prescribed displacements are arbitrary functions of time.

7.4 Generalization for Fluctuating Magnetic Fields

All of the data that we have examined previously has been based on the response of the MR damper when the applied voltage, and hence the magnetic field, was held at a constant level. However, optimal performance of a control system which utilizes this device is expected to be achieved when the magnetic field is continuously varied based on the measured response of the system to which it is attached. To use the damper in this way, a model must be developed which is capable of predicting the behavior of the MR damper for a fluctuating magnetic field.

To determine a model that is valid for fluctuating magnetic fields, the functional dependence of the parameters on the applied voltage (or current) must be determined. For instance, the yield stress of the MR fluid is directly dependent on the magnetic field strength, so the parameter α in Eqs. (7.9–7.11) is assumed to be a function of the applied voltage. From the experimental results shown in Fig. 7.3, the steady state yield level

appears to vary linearly with the applied voltage, and have a nonzero initial value (*i.e.*, at 0 V). This nonzero initial value is due in part to the fluid which by design has a small yield strength at zero field for stability against gravitational settling, and in part due to friction in the piston rod seal. The viscous damping constants also vary linearly with the applied voltage. Therefore, the following relations are proposed

$$\alpha = \alpha(u) = \alpha_a + \alpha_b u, \qquad c_1 = c_1(u) = c_{1a} + c_{1b} u$$

$$\text{and} \qquad c_0 = c_0(u) = c_{0a} + c_{0b} u \tag{7.17}$$

where the dynamics involved in the MR fluid reaching rheological equilibrium are accounted for through the first order filter

$$\dot{u} = -\eta(u - v) \tag{7.18}$$

and v is the voltage applied to the current driver. Optimal values of a total of fourteen parameters (c_{0a}, c_{0b}, k_0, c_{1a}, c_{1b}, k_1, x_0, α_a, α_b, γ, β, n, η and A) must be determined for the prototype MR damper.

A constrained nonlinear optimization was used to obtain these parameters. The optimization was performed using a sequential quadratic programming algorithm available in MATLAB (1994). Table 7.2 provides the optimized parameters for the generalized model that were determined to best fit the data in a variety of representative tests, including: 1) step response, 2) constant voltage/random displacement, and 3) random displacement/random voltage. In the following paragraphs these tests will be described, and a comparison made between the data and the responses predicted by the proposed model using the parameters given in Table 7.2. Simulations were performed in SIMULINK (1994) using the experimentally determined displacement x_d and calculated velocity $\dot{x}_d$ of the piston-rod in determining the force generated in the damper model.

Table 7.2 Parameters for the Generalized Model

Parameter	Value	Parameter	Value
c_{0a}	21.0 N·sec/cm	α_a	140 N/cm
c_{0b}	3.50 N·sec/cm·V	α_b	695 N/cm·V
k_0	46.9 N/cm	γ	363 cm^{-2}
c_{1a}	283 N·sec/cm	β	363 cm^{-2}
c_{1b}	2.95 N·sec/cm·V	A	301
k_1	5.00 N/cm	n	2
x_0	14.3 cm	η	190 sec^{-1}

The step response tests consisted of applying a triangular displacement to the damper, resulting in regions in which the velocity is nearly constant, and applying a step change in the applied voltage from 0 to 2.25 V as the damper passes through the middle of the stroke ($x_d \approx 0$). The measured displacement and applied voltage are shown in Fig. 7.12. The measured force is expected to jump to a new value and remain there when the step in the voltage occurs. Figure 7.13 compares the predicted results to the experimental data for the input signals shown in Fig. 7.12. The model effectively predicts the behavior of the device. The error norms given in Eq. (7.12) were calculated to be $E_t = 0.101$, $E_x = 0.051$, and $E_{\dot{x}} = 0.107$ for this test. This test also verified that the damper reaches rheological equilibrium within approximately 6 msec after the step voltage is applied. Note that the sampling rate was increased to 3 kHz in this test to capture the higher frequency content of the measured responses.

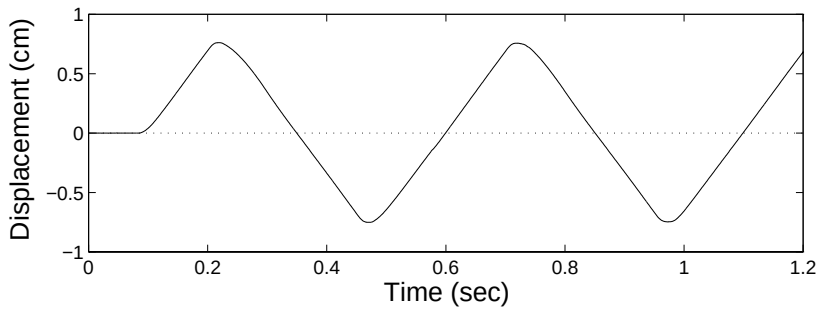

a) Displacement vs. Time

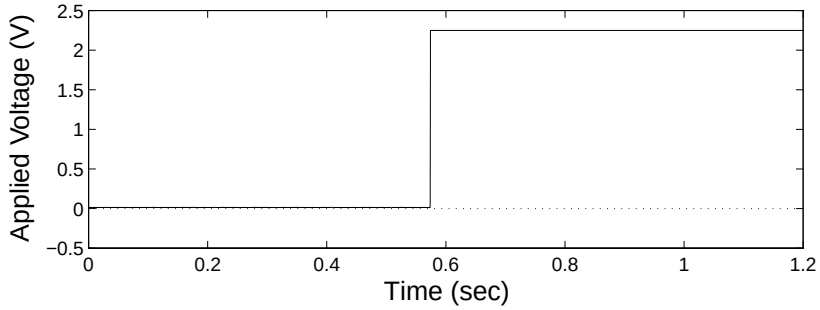

b) Applied Voltage vs. Time

Figure 7.12 Inputs Applied to the MR Damper in the Step Response Test.

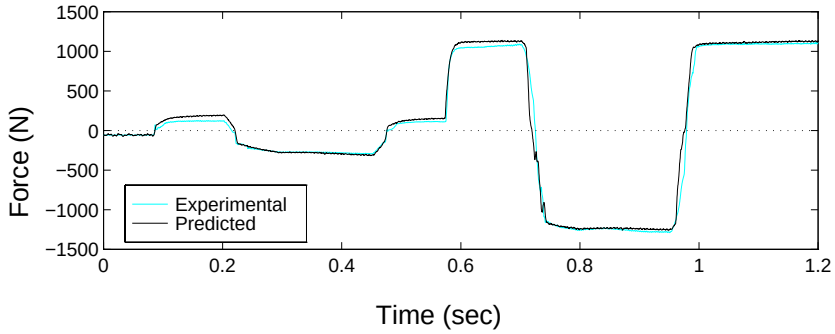

a) Force vs. Time

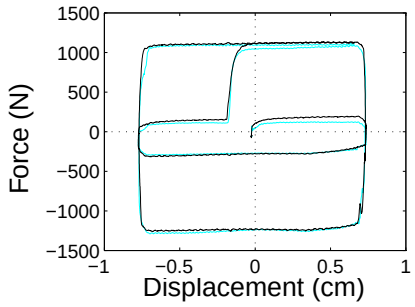

b) Force vs. Displacement

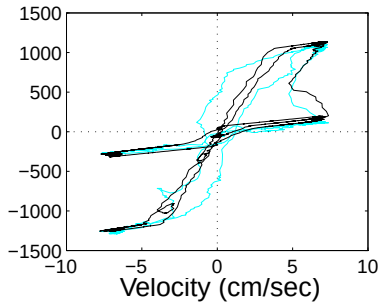

c) Force vs. Velocity

Figure 7.13 Comparison of Predicted Response and Experimental Data for Step Response Tests.

In the second test to verify the model, the damper was excited with a 15 second random displacement record based on an El Centro earthquake acceleration record. A portion of the displacement record of the damper is shown in Fig. 7.14. The voltage applied to the current driver was a constant 2.25 V. The sampling rate was set at 2 kHz. The simulated force is compared to the experimental data in Fig. 7.15. As seen here, the model accurately predicts the behavior of the damper. For this test, the error norms given in Eq. (7.12) were determined to be $E_t = 0.286$, $E_x = 0.118$, and $E_{\dot{x}} = 0.260$.

For the final verification test, the inputs to the device were chosen to be characteristic of the operating conditions the MR damper will experience when it is applied to a structure in a semi-active control system. In Chapter 8, a clipped-optimal control strategy is proposed for controlling a three story model structure with an MR damper. A controlled simulation was performed based on the numerical example therein. The input control signal and displacement of the MR damper determined from this simulation are shown in Figure 7.16. This sample displacement and control input history were applied simultaneously to the MR damper. A comparison between the experimental results and the predicted behavior of the damper is shown in Figure 7.17. Again, excellent agreement is found between the experimental and model responses. For this test, the error norms given in Eq. (7.12) were determined to be $E_t = 0.188$, $E_x = 0.164$, and $E_{\dot{x}} = 0.188$.

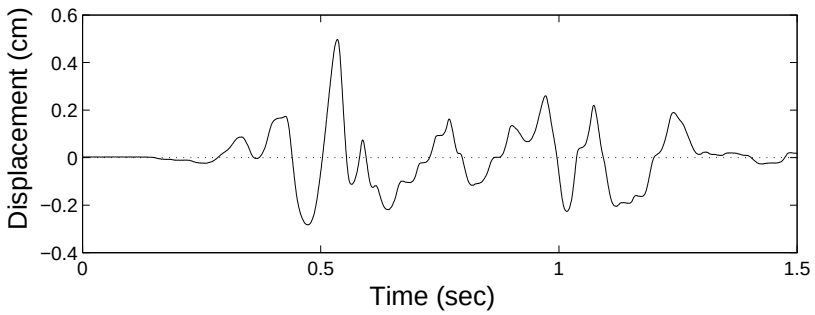

Figure 7.14 Displacement Input Applied to MR Damper in Constant Voltage, Random Displacement Test.

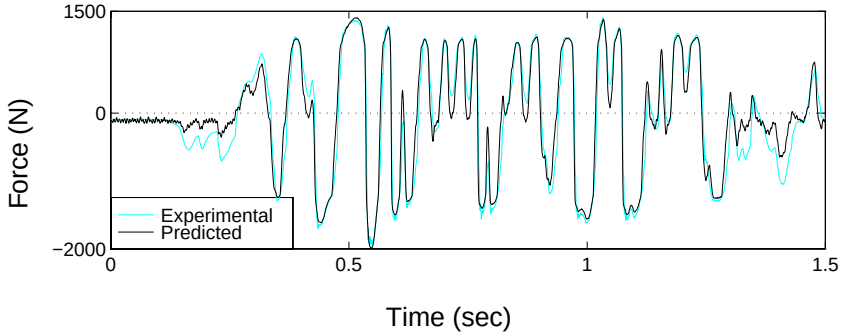

a) Force vs. Time

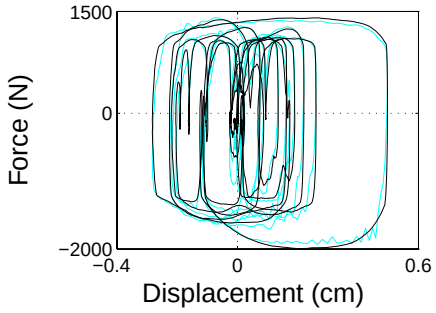

b) Force vs. Displacement

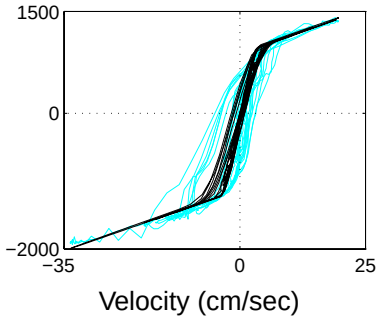

c) Force vs. Velocity

Figure 7.15 Comparison of the Model Results and the Experimental Data for the Constant Voltage, Random Displacement Tests.

7.5 Summary

To take full advantage of the unique features of the MR damper, a high fidelity model has been developed for control design and analysis. A review of several idealized mechanical models for controllable fluid dampers has been presented. Subsequently, a new model has been proposed that overcomes a number of the shortcomings of these models and can effectively portray the behavior of a typical magnetorheological damper. This phenomenological model is based on a Bouc–Wen hysteresis model, which is numerically tractable and is capable of exhibiting a wide variety of hysteretic behaviors. A dashpot has been added in series with the Bouc–Wen model which creates the nonlinear roll-off observed in the force as the velocity approaches zero; and an additional spring is incorporated into the

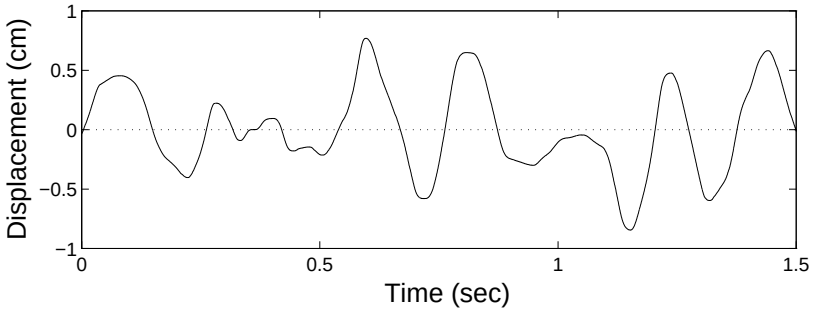

a) Displacement vs. Time

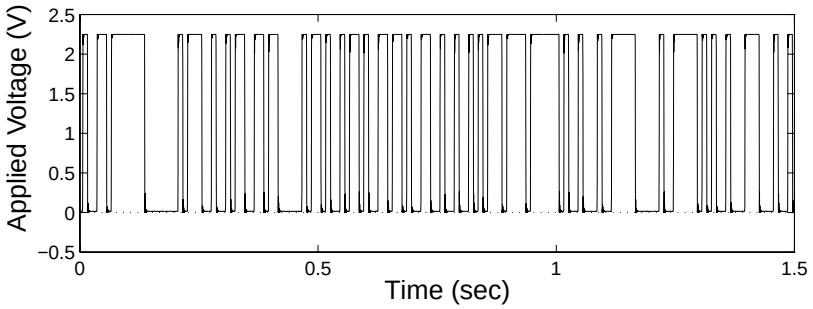

b) Applied Voltage vs. Time

Figure 7.16 Inputs to MR Damper for the Control Simulation Test.

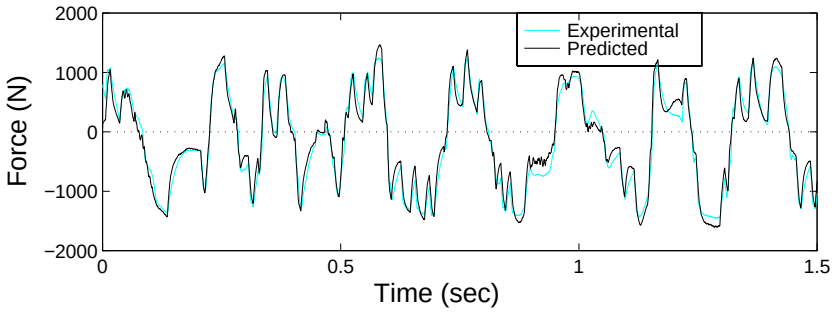

a) Force vs. Time

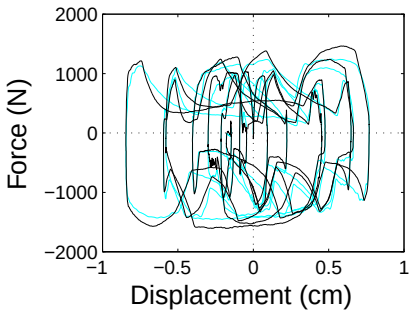

b) Force vs. Displacement

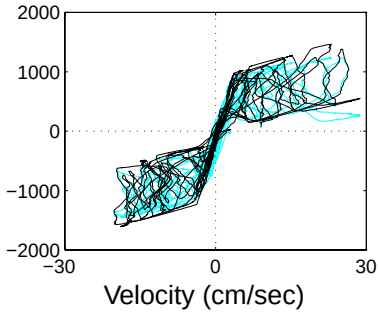

c) Force vs. Velocity

Figure 7.17 Comparison of the Model Results and the Experimental Data for the Control Simulation Test.

model to account for the stiffness of the accumulator present in the prototype MR damper. To obtain a model that reproduces the behavior of the damper with fluctuating magnetic fields, three parameters are assumed to vary with the applied voltage. Additionally, a first order filter has been incorporated into the model to account for the dynamics involved in the MR fluid reaching rheological equilibrium. When compared with experimental data, the resulting model was shown to accurately predict the response of the MR damper over a wide range of operating conditions, including step voltage, random displacement/constant voltage, and random displacement/random voltage tests. These results indicate that the model can be effectively used for control algorithm development and system evaluation.

CHAPTER 8

Semi-Active Control Algorithm

As discussed in Chapter 7, MR dampers, like most semi-active control devices, are intrinsically nonlinear, making it challenging to develop control strategies that can optimally exploit their unique features. Many of the approaches to control of semi-active systems that have been proposed either use only local information in the control algorithm or are based on state feedback (Leitmann and Reithmeier, 1993; McClamroch and Gavin 1995; Inaudi, *et al*., 1996). While local controllers can be effective, their ability to achieve global response reduction is limited. Moreover, the use of state feedback is generally viewed as being impracticable for civil engineering structures. However, as already demonstrated in the previous chapters for active systems, control strategies based on acceleration measurements are viable for structural control. In this chapter, a type of clipped-optimal controller based on acceleration feedback is proposed for semi-active control systems and shown to be effective for civil engineering applications through numerical simulation.

8.1 Clipped Optimal Control Algorithm Development

Although semi-active control systems use a fraction of the power required by a fully active controller, these devices have the potential to approach, and even surpass, the performance of the active systems (Ivers and Miller, 1989; Miller, 1988; Patten *et al.*, 1994; Tseng and Hedrick, 1994; Dyke, *et al.*, 1996c–f). Because semi-active control devices are

inherently stable (in a bounded input - bounded output sense), high authority control strategies may be designed and implemented, which, in practice, may result in performances that may even surpass that of an actively controlled structure.

Consider a seismically excited structure controlled with a single MR damper. Assuming that the forces provided by the MR damper are adequate to keep the response of the primary structure from exiting the linear region, then the equations of motion can be written as

$$\dot{\mathbf{z}} = \mathbf{A}\mathbf{z} + \mathbf{B}f + \mathbf{E}\ddot{x}_g \tag{8.1}$$

where $\ddot{x}_g$ is a one-dimensional ground acceleration, f is the measured force generated between the structure and the MR damper (*e.g.*, Eq. 7.10 or 7.11), and $\mathbf{z}$ is the state vector. The measurement equation is given by

$$\mathbf{y} = \mathbf{C}\mathbf{z} + \mathbf{D}f + \mathbf{v} \tag{8.2}$$

where $\mathbf{y}$ is the vector of measured outputs, and $\mathbf{v}$ is the measurement noise vector. In this application, the measurements typically available for control force determination include the acceleration of selected points on the structure, the displacement x of the MR damper and the measurement of the control force f provided by the MR damper.

The approach proposed here is to append a force feedback loop (Ivers and Miller, 1989) to induce the MR damper to produce approximately a desired control force f_c. A linear optimal controller $\mathbf{K}_c(s)$ is then designed that provides the desired control force f_c based on the measured responses $\mathbf{y}$, and the measured force f, *i.e.*,

$$f_c = \mathcal{L}^{-1}\left\{-\mathbf{K}_c(s)\left(\begin{bmatrix}\mathbf{y}\\ f\end{bmatrix}\right)\right\} \tag{8.3}$$

where $\mathcal{L}\{\cdot\}$ is the Laplace transform. Although the controller $\mathbf{K}_c(s)$ can be obtained from a variety of synthesis methods, the H_2/LQG strategies are advocated herein because

of the stochastic nature of earthquake ground motions and because of their successful application in previous studies.

The force generated by the MR damper cannot be commanded; only the voltage v applied to the current driver for the MR damper can be directly changed. To induce the MR damper to generate approximately the desired optimal control force f_c, the command signal v is selected as follows. When the MR damper is providing the desired optimal force (*i.e.*, $f = f_c$), the voltage applied to the damper should remain at the present level. If the magnitude of the force produced by the damper is smaller than the magnitude of the desired optimal force and the two forces have the same sign, the voltage applied to the current driver is increased to the maximum level so as to increase the force produced by the damper to match the desired control force. Otherwise, the commanded voltage is set to zero. The algorithm for selecting the command signal is graphically represented in Fig. 8.1 and can be concisely stated as

$$v = V_{\max} H\{(f_c - f) f\} \tag{8.4}$$

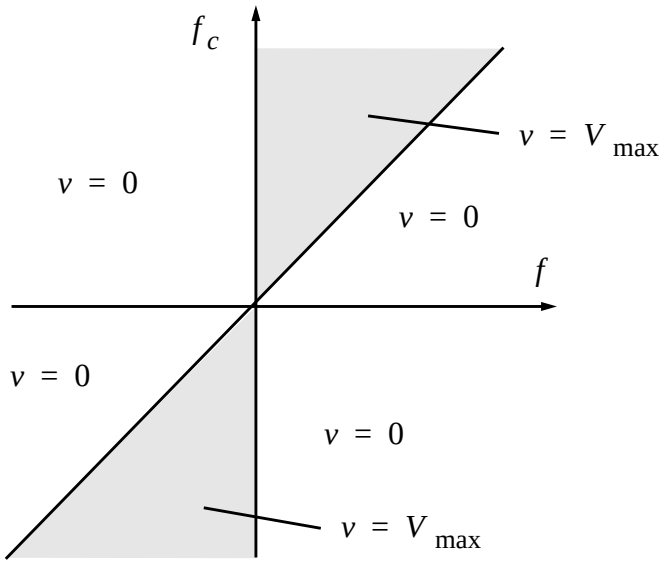

Figure 8.1 Graphical Representation of Algorithm for Selecting the Command Signal.

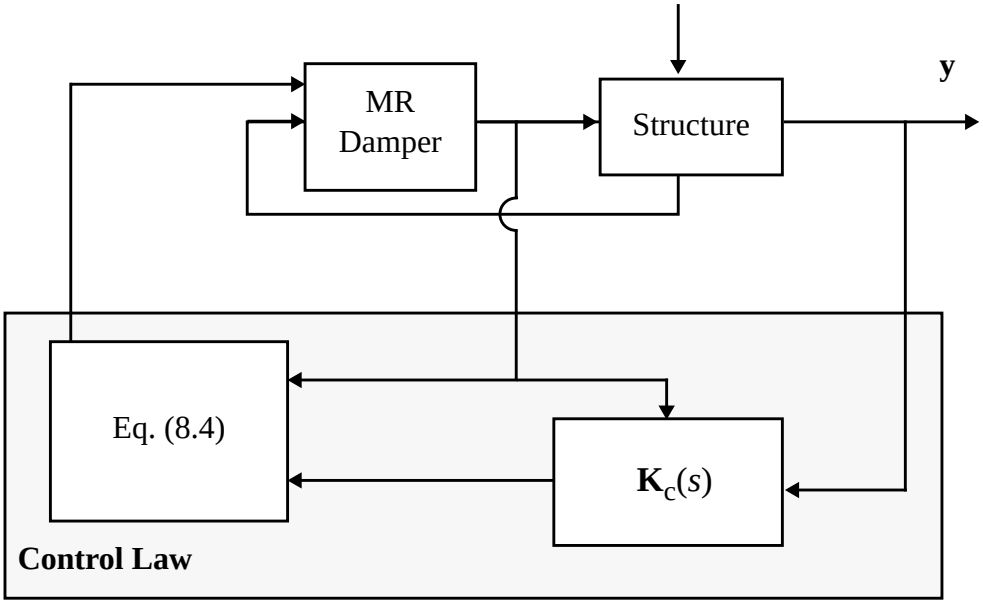

Figure 8.2 Block Diagram of the Semi-Active Control System.

where $V_{\max}$ is the voltage to the current driver associated with saturation of the magnetic field in the MR damper, and $H(\cdot)$ is the Heaviside step function. A block diagram of this semi-active control system is shown in Fig. 8.2.

8.2 Numerical Example

The performance of the clipped-optimal control algorithm presented in section 8.1 is now evaluated through numerical simulation. A model of a three-story building configured with a single MR damper is considered. The MR damper is rigidly connected between the ground and the first floor of the structure. A diagram of the MR damper implementation is shown in Fig. 8.3. The equations of motion of the structure are given by

$$\mathbf{M}_s\ddot{\mathbf{x}} + \mathbf{C}_s\dot{\mathbf{x}} + \mathbf{K}_s\mathbf{x} = \Gamma f - \mathbf{M}_s\Lambda\ddot{x}_g \tag{8.5}$$

where f is the measured control force, defined by Eqs. (7.7–7.11, 7.17, 7.18), $\mathbf{x} = [x_1 \;\; x_2 \;\; x_3]'$ is a vector of the displacements of the three floors of the structure relative to the ground. The system matrices are

$$\mathbf{M}_s = \begin{bmatrix} 98.3 & 0 & 0 \\ 0 & 98.3 & 0 \\ 0 & 0 & 98.3 \end{bmatrix} \text{kg}, \qquad \mathbf{C}_s = \begin{bmatrix} 175 & -50 & 0 \\ -50 & 100 & -50 \\ 0 & -50 & 50 \end{bmatrix} \frac{\text{N} \cdot \text{sec}}{\text{m}}$$

$$\mathbf{K}_s = 10^5 \begin{bmatrix} 12.0 & -6.84 & 0 \\ -6.84 & 13.7 & -6.84 \\ 0 & -6.84 & 6.84 \end{bmatrix} \frac{\text{N}}{\text{m}}, \qquad \mathtt{G} = \begin{bmatrix} -1 \\ 0 \\ 0 \end{bmatrix}, \qquad \mathtt{L} = \begin{bmatrix} 1 \\ 1 \\ 1 \end{bmatrix}$$

This system is a simple model of the scaled, three-story, test structure at the Structural Dynamics and Control / Earthquake Engineering Laboratory (SDC/EEL) at the University

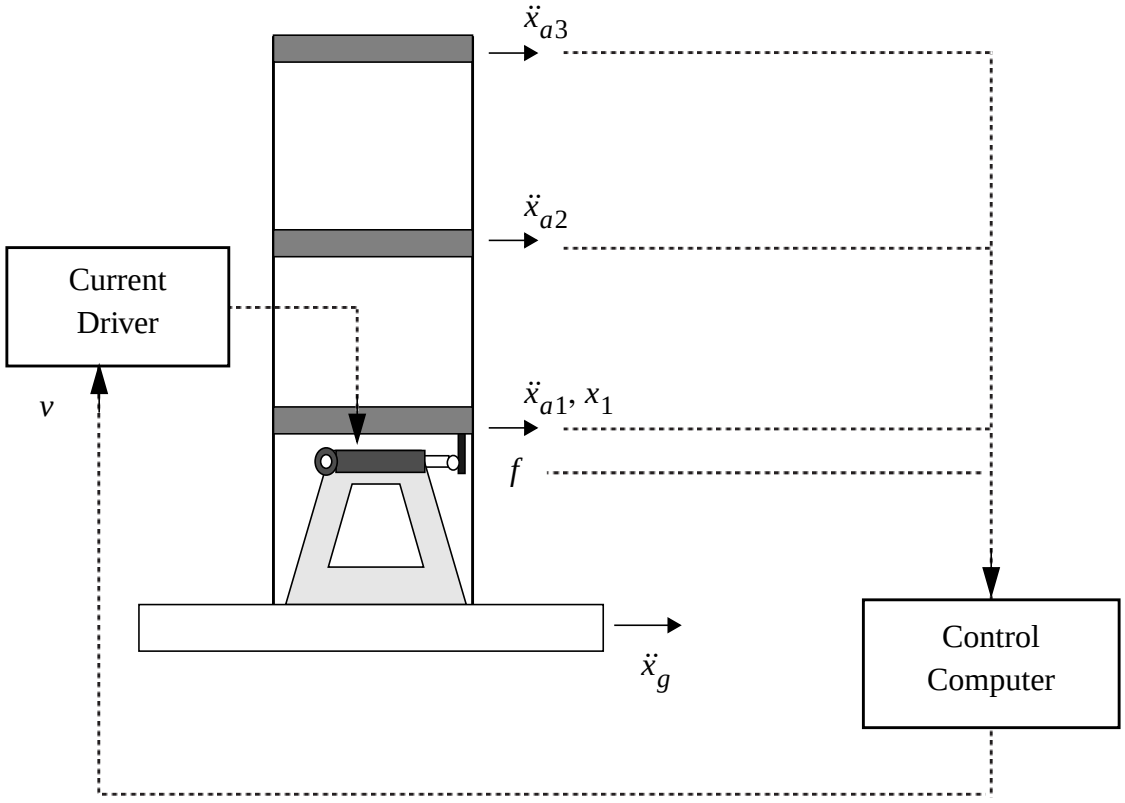

Figure 8.3 Diagram of MR Damper Implementation.

of Notre Dame. Because the MR damper is attached between the first floor and the ground, its displacement is equal to the displacement of the first floor of the structure relative to the ground, *i.e.*, $x = x_1$ in Eqs. (7.7–7.11).

The structural measurements used for calculating the desired control force f_c include the absolute accelerations of the three floors of the structure, and the displacement of the MR damper (*i.e.*, $\mathbf{y} = [\ddot{x}_{a1} \ \ddot{x}_{a2} \ \ddot{x}_{a3} \ x_1]'$). Thus, Eq. (8.5) can be written in the form of Eqs. (8.1–8.2) by defining

$$\mathbf{A} = \begin{bmatrix} \mathbf{0} & \mathbf{I} \\ -\mathbf{M}_s^{-1}\mathbf{K}_s & -\mathbf{M}_s^{-1}\mathbf{C}_s \end{bmatrix}, \quad \mathbf{B} = \begin{bmatrix} \mathbf{0} \\ \mathbf{M}_s^{-1}\mathsf{G} \end{bmatrix}, \quad \mathbf{E} = -\begin{bmatrix} \mathbf{0} \\ \mathsf{L} \end{bmatrix} \tag{8.6}$$

$$\mathbf{C} = \begin{bmatrix} -\mathbf{M}_s^{-1}\mathbf{K}_s & -\mathbf{M}_s^{-1}\mathbf{C}_s \\ 1\ 0\ 0 \quad 0\ 0\ 0 \end{bmatrix}, \quad \mathbf{D} = \begin{bmatrix} \mathbf{M}_s^{-1}\mathsf{G} \\ 0 \end{bmatrix} \tag{8.7}$$

The MR damper parameters given in Table 7.2 are used for the simulation studies, except that an appropriate translation of coordinates is made to cancel the initial offset caused by the accumulator in the MR damper (*i.e.*, x_0 was set at zero). The essential effect was to eliminate the need to consider asymmetry in the results.

Acceleration feedback control strategies are employed to design the optimal controller $\mathbf{K}_c(s)$ in Eq. (8.3) for the system in Eq. (8.5).

For the control design, the absolute acceleration of the ground, $\ddot{x}_g$, is taken to be a stationary white noise, and an infinite horizon performance index is chosen that weights the acceleration of the third floor, *i.e.*,

$$J = \lim_{\tau \to \infty} \frac{1}{\tau} \mathrm{E}\left[\int_0^{\tau} \left\{ (\mathbf{C}\mathbf{z})'\mathbf{Q}(\mathbf{C}\mathbf{z}) + r f_c^{\,2} \right\} dt \right] \tag{8.8}$$

where $r = 10^{-17}$, and all of the elements of the weighting matrix $\mathbf{Q}$ are zero, except for

$Q_{33} = 1$. Further, the measurement noise is assumed to be identically distributed, statistically independent Gaussian white noise processes, and $S_{\ddot{x}_g\ddot{x}_g}/S_{v_iv_i} = \gamma = 50$. The controller is

$$\mathbf{K}_c(s) = \mathbf{K}[s\mathbf{I} - (\mathbf{A} - \mathbf{LC})]^{-1}\hat{\mathbf{B}} \tag{8.9}$$

where $\hat{\mathbf{B}} = [\mathbf{L} \quad \mathbf{B} - \mathbf{LD}]$. Here, $\mathbf{K}$ is the full state feedback gain matrix for the deterministic regulator problem given by

$$\mathbf{K} = \mathbf{B}'\mathbf{P}/r \tag{8.10}$$

where $\mathbf{P}$ is the solution of the algebraic Ricatti equation given by

$$\mathbf{0} = \mathbf{PA} + \mathbf{A}'\mathbf{P} - \mathbf{PB}'\mathbf{BP}/r + \mathbf{C}'\mathbf{QC} \tag{8.11}$$

and

$$\mathbf{L} = (\mathbf{CS})' \tag{8.12}$$

where $\mathbf{S}$ is the solution of the algebraic Ricatti equation given by

$$\mathbf{0} = \mathbf{SA}' + \mathbf{AS} - \mathbf{SC}'\mathbf{CS} + \gamma\mathbf{EE}' \tag{8.13}$$

Calculations to determine $\mathbf{K}$ and $\mathbf{L}$ were performed using the control toolbox in MATLAB (1994).

In simulation, the model of the structure is subjected to the NS component of the 1940 El Centro earthquake shown in Fig. 8.4. Because the system under consideration is a scaled model, the earthquake must be reproduced at five times the recorded rate. The maximum structural responses to the El Centro earthquake are presented in Table 8.1. Here, x_i is the displacement of the ith floor relative to the ground, d_i is the interstory drift (*i.e.*, $x_i - x_{i-1}$), $\ddot{x}_{ai}$ is the absolute acceleration of the ith floor, and f is the applied control force.

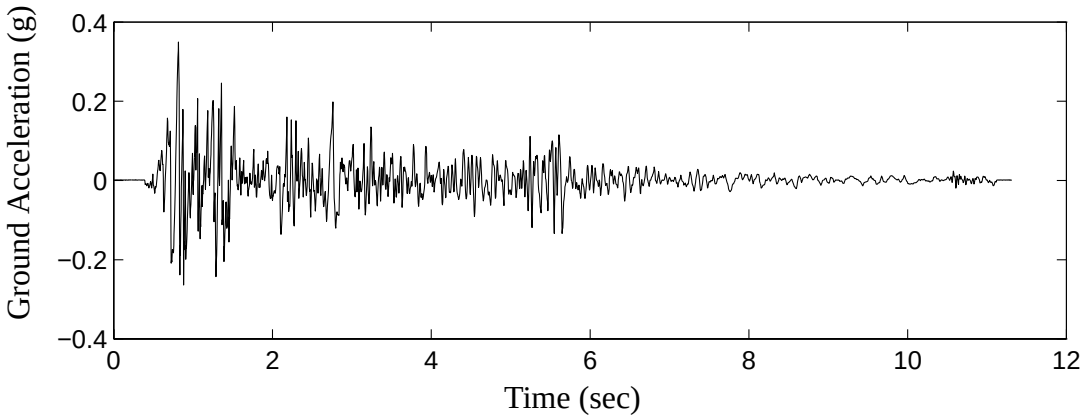

Figure 8.4 Time Scaled NS Component of the Ground Acceleration for the 1940 El Centro Earthquake.

Table 8.1 Peak Responses due to the El Centro Earthquake.

Control Strategy	Uncontrolled	Passive-Off	Passive-On	Clipped-Optimal Control (MR Damper)	Ideal Active Control
x_i (cm)	0.538 0.820 0.962	0.211 0.357 0.455	0.076 0.196 0.306	0.114 0.185 0.212	0.108 0.154 0.236
d_i (cm)	0.538 0.319 0.201	0.211 0.153 0.103	0.076 0.158 0.110	0.114 0.090 0.101	0.108 0.132 0.082
$\ddot{x}_{ai}$ (cm/sec^2)	856 1030 1400	420 480 717	281 494 767	696 739 703	445 393 569
f (N)	–	258	979	941	941

In this study, two cases are considered in which the MR damper is employed in a passive mode. In the first case, designated *passive-off*, the command voltage to the MR damper is held at 0 V. The second passive case the voltage to the MR damper is held at the maximum voltage level (2.25 V) and is denoted as *passive-on*. The results for these two cases indicate that both of the passive systems are able to achieve a reasonable level of performance. As shown in Table 8.1, the passive-off system reduces the maximum relative displacement of the third floor by 52.7% of the uncontrolled values, and the passive-on system achieves a 68.1% reduction. Both passive systems reduce the upper story absolute accelerations and interstory displacements by approximately 50%. However, as compared to the passive-off case, notice that the passive-on controller increases both the absolute accelerations and the interstory displacements of the upper floors. Apparently, choosing a passive device that produces the largest damping forces may not always be the most effective approach to protective system design.

Using the control law in Eq. (8.4), the closed loop semi-active system is simulated. Because the MR damper has the ability to dynamically modify its properties, the performance of the system employing a clipped-optimal controller (*i.e.*, semi-actively controlled) surpasses that of both passive systems. The time responses for the third floor relative displacement and the third floor absolute acceleration are shown in Fig. 8.5. Notice that the MR damper is able to reduce the structural responses, even during the first few cycles of the response. The peak structural responses to the El Centro earthquake are given in Table 8.1. The clipped-optimal controller reduces the peak third floor relative displacement by an additional 30.7% and reduces the maximum peak interstory displacement by an additional 27.8%, as compared to the best passive responses. Notice that these performance gains are achieved by the semi-active controller while requiring smaller control forces than are required in the passive-on case. In addition, the semi-active controller

reduces the maximum peak absolute floor acceleration more than the passive-on case, although not quite as well as for the passive-off case.

Insight into how the semi-active system achieves improved performance over the passive system is seen by examining Fig. 8.6, which compares the control forces produced by the MR damper for the strong motion portion of the El Centro earthquake operating in both the semi-active and passive-on modes. A scaled version of the commanded voltage to the MR damper is superimposed on the figure. The ability of the MR damper to quickly respond to changes in the commanded voltage are clearly seen here. The peak in the structural responses occurs at approximately 0.8 seconds. At this time the semi-active force increases and then sharply rolls off much faster than the force produced in the passive-on

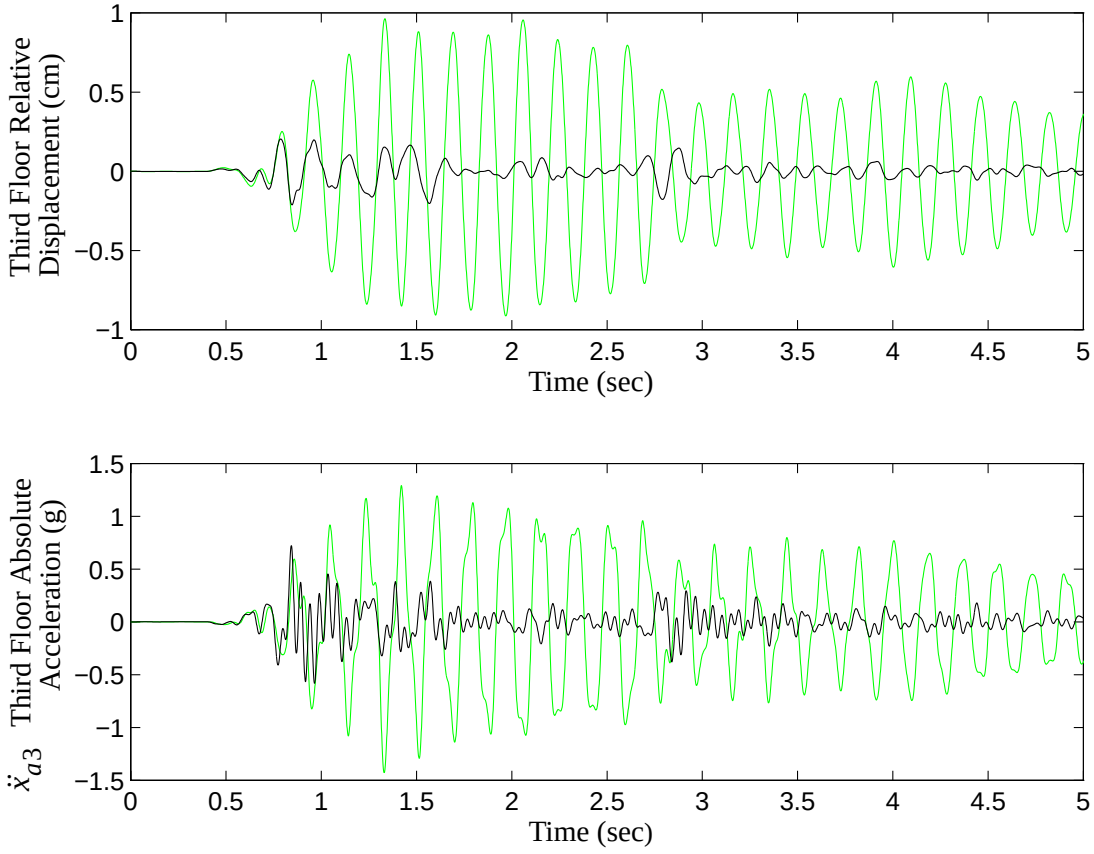

Figure 8.5 Structural Responses of Uncontrolled and Semi-Actively Controlled Systems Due to the El Centro Earthquake.

mode. Interestingly, the forces applied by the MR damper operating in semi-active mode are often smaller than those corresponding to the damper operating in the passive-on mode, again indicating that larger damping forces do not always produce better results.

As a final study, an assessment is made of the ability of the MR damper to achieve the performance of a comparable fully active control system. To this end, the active controller is assumed to be ideal, in that actuator/sensor dynamics are not considered. As discussed in Chapter 3, actuator/sensor dynamics often limit achievable performance. Moreover, the forces generated by an actuator can be highly dependent on the corresponding response of the structure, particularly for lightly damped system. In this study, the actuator used to generate the control forces is considered to be nondynamic and capable of generating the required control forces instantaneously; no interaction is allowed between the structure and the actuator. With these assumptions, the active control case considered herein is designated an *ideal* controller and represents an upper bound on active control system performance for an appropriately sized actuator.

To have a basis for comparison of the active and semi-active control systems, a linear active controller is designed such that the peak control force is the same as that of the

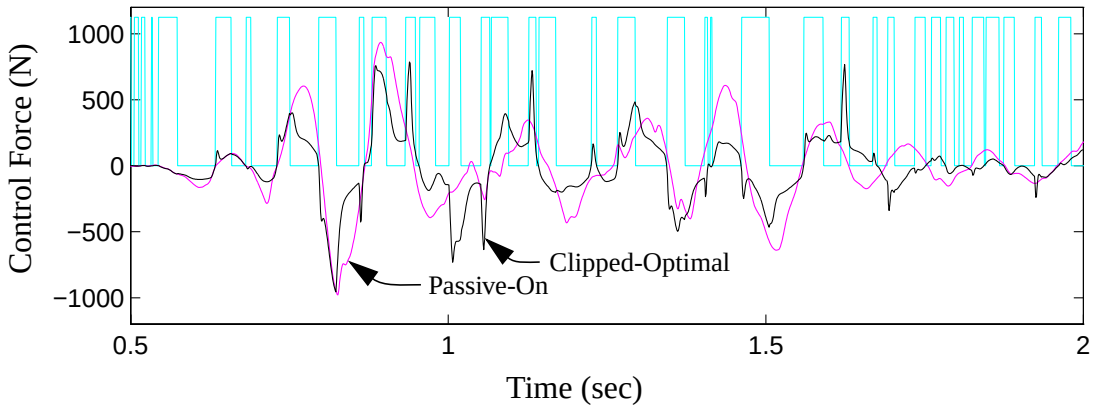

Figure 8.6 Command Signal and Control Force Applied in the Clipped-Optimal Case, and Reaction Force for the Passive-On Case Due to the El Centro Earthquake.

semi-active controller. Thus, the same capacity actuator would be required to implement either control strategy. An H_2/LQG optimal active controller is designed by weighting both the third floor absolute acceleration and the third floor relative displacement.

The peak responses for the actively controlled structure are provided in Table 8.1. The ideal active control system is also very effective in reducing the structural responses due to the El Centro earthquake. Interesting, the peak third floor relative displacement was 10% smaller for the clipped optimal controller than for the active system. The maximum of the peak interstory displacements is also 15% smaller with the clipped-optimal controller than with the active control. This result is quite remarkable given that the MR damper uses only a small fraction of the power required to operate the active control system. This result may be attributed in part to the fact that semi-active devices are inherently stable, allowing high authority control strategies to be effectively designed and implemented.

8.3 Summary

The effectiveness of the MR damper using the proposed clipped-optimal control law has been demonstrated through numerical example. Excellent results were obtained when this strategy was applied to control a model of a seismically excited three-story scaled building model. Because the semi-active system has the ability to vary its properties to more effectively control the structure, the clipped optimal controller performed better than both the passive-off and passive-on, and even a comparably designed ideal active control system. One of the attractive features of this control strategy is the fact that the feedback for the controller is based readily obtainable acceleration measurements, thus making them quite implementable. In addition, the proposed control design does not require a model for the MR damper. In the following chapters the clipped-optimal control strategy will be experimentally verified.

CHAPTER 9

Magnetorheological Damper Experiment

The focus of this chapter is to present experimental verification of the acceleration feedback control strategies for semi-actively controlled structures presented in Chapter 8 and demonstrate the effectiveness of the MR damper for structural control applications. Following a description of the experimental setup, the system identification procedure for semi-actively controlled structures, presented in Chapter 2, is applied to identify a model of the MR damper/structure system and the integrated system model is verified. Based on this identified model, controllers are designed and implemented on the three-story test structure. The experimental results reported herein indicate that high performance can be obtained with a semi-active control system using acceleration feedback control strategies.

9.1 Experimental Setup

Experimental verification of the acceleration feedback control strategies for the semi-active control system employing the MR damper were performed on the test structure at the Structural Dynamics and Control / Earthquake Engineering Laboratory at the University of Notre Dame. Figure 9.1 is a diagram of the semi-actively controlled, three-story, model building. A single MR damper is installed between the ground and the first floor, as

shown in Fig. 9.1. The MR damper employed here is the prototype device described in Chapter 7.

Sensors are installed in the model building for use in determining the control action. Accelerometers located on each of the three floors provide measurements the absolute accelerations $\ddot{x}_{a1}$ $\ddot{x}_{a2}$ $\ddot{x}_{a3}$, an LVDT measures the displacement x_d of the MR damper, and a force transducer is placed in series with the MR damper to measure the control force f being applied to the structure. Note that only these five measurements are used in the control algorithm. However, to evaluate the performance of the control strategies, LVDTs are attached to the base and to each floor of the structure to measure the relative displacements of the structure.

Implementation of the discrete controller was performed using the Spectrum Signal Processing Real-Time Digital Signal Processor (DSP) System described in Chapter 2.

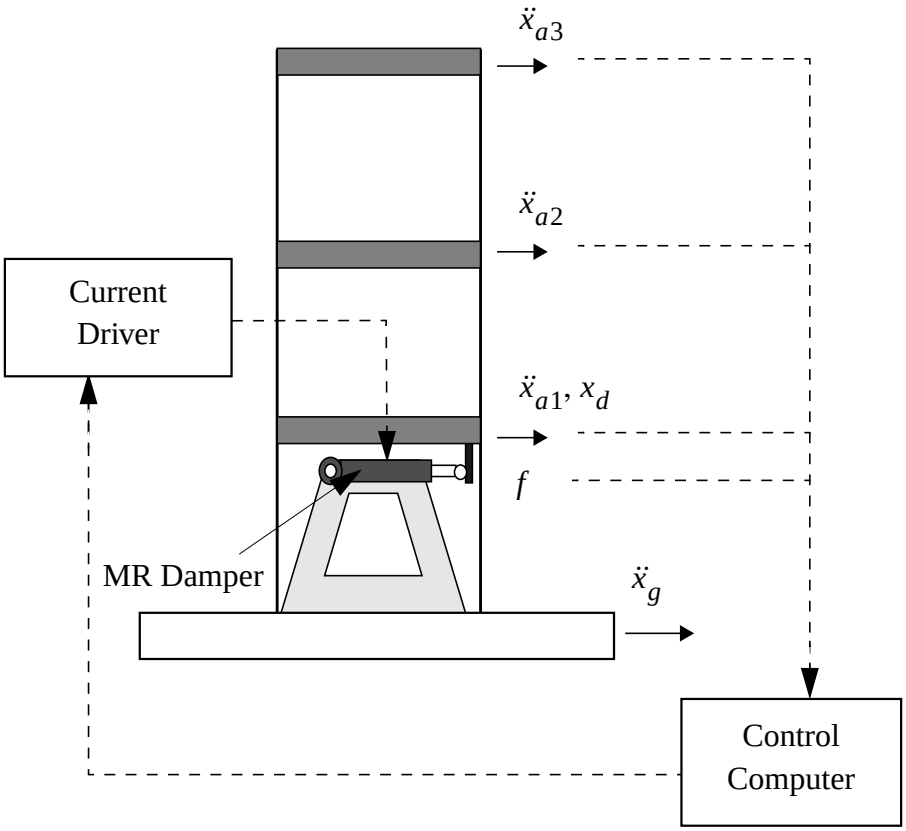

Figure 9.1 Diagram of MR Damper Implementation.

9.2 System Identification and Model Validation

To identify a model of the integrated MR damper/structure system, the approach to system identification of semi-actively controlled structures outlined in section 2.2.2 is employed. The first step in the identification process is to develop an input/output model for the MR damper. In Chapter 7 a mechanical model was proposed and shown to accurately predict the behavior of the prototype MR damper over a broad range of inputs. A set of optimized parameters was determined to fit the response of the MR damper to the experimentally obtained response in a series of displacement-controlled tests in which the MR damper was driven with a hydraulic actuator. In the following sections, the remaining steps of the system identification procedure for the integrated system are discussed.

9.2.1 Identification of the Structure

The second step in identifying a model of the integrated system is to determine an input/output model of the structure. Because the structure itself is assumed to remain in the linear region, the frequency domain approach to linear system identification discussed in section 2.2.1 is used to identify a mathematical model of the test structure.

A block diagram of the structural system to be identified is shown in Fig. 9.2. The two inputs are the ground excitation $\ddot{x}_g$ and the applied control force f. The four measured system outputs include the displacement x_d of the structure at the attachment point of the MR damper, and the absolute accelerations, $\ddot{x}_{a1}$, $\ddot{x}_{a2}$, $\ddot{x}_{a3}$, of the three floors of the test structure (*i.e.*, $\mathbf{y} = [x_d \quad \ddot{x}_{a1} \quad \ddot{x}_{a2} \quad \ddot{x}_{a3}]'$). Thus, a 4×2 transfer function matrix must be identified to describe the characteristics of the system in Fig. 9.2.

According to the procedure outline in Chapter 2, the first step in the identification of the structure is to experimentally determine the transfer functions from each of the system inputs to each of the outputs. The Tektronix Fourier analyzer was employed to obtain the

experimental transfer functions for the structure. The transfer functions from the ground acceleration to each of the measured responses were obtained by exciting the structure with a band-limited white noise ground acceleration (0-50 Hz). During this test, the MR damper is not connected to the structure, making $f = 0$. Similarly, the experimental transfer functions from the applied control force to each of the measured outputs are determined. To this end, the MR damper is replaced with a hydraulic actuator to apply a band-limited white noise (0-50 Hz) force to the structure while the ground acceleration $\ddot{x}_g$ is set equal to zero. The force transducer, mentioned previously, is placed in series with the hydraulic actuator to directly measure the applied force.

Figures 9.3–9.7 show representative magnitude and phase plots for the experimentally determined transfer functions obtained using twenty averages. The three distinct, lightly-damped peaks occurring at 5.88, 17.5, and 28.3 Hz correspond to the first three modes of the structural system. The errors near the peaks in the transfer functions from the control force to the structural responses are due to the effects of control-structure interaction. As discussed in Chapter 3, in the case of a lightly damped structure, the hydraulic actuator used to apply the force is unable to apply significant forces at the natural frequencies of the structure. The forces in this frequency range are very small and within the noise level of the Tektronix instrument.

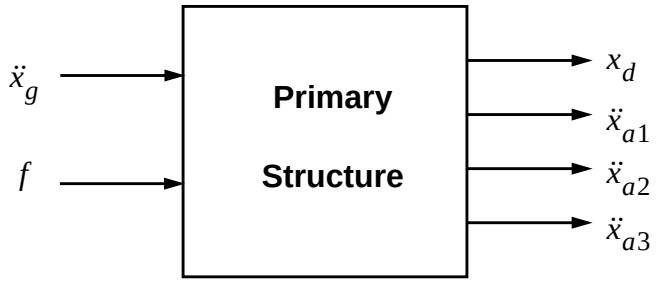

Figure 9.2 System Identification Block Diagram.

Once the experimental transfer functions have been obtained, the next step in the system identification procedure is to model the transfer functions as a ratio of two polynomials in the Laplace variable *s*. The decision was made to focus control efforts on reduction of the structural responses in the first three modes. Thus, the model was required to be accurate below 35 Hz. Six poles were necessary to model the input/output behavior of each of the transfer functions in the frequency range of interest.

The system was then assembled in state space form using the analytical representation of the transfer functions (*i.e.*, the poles, zeros and gain). Because all of the transfer functions required six states, the combined system had a total of twelve poles. The model reduction procedure was applied and the twelve state system was reduced to a six state system. A comparison of the reduced-order model to the experimental transfer functions is shown in Figs. 9.3–9.7.

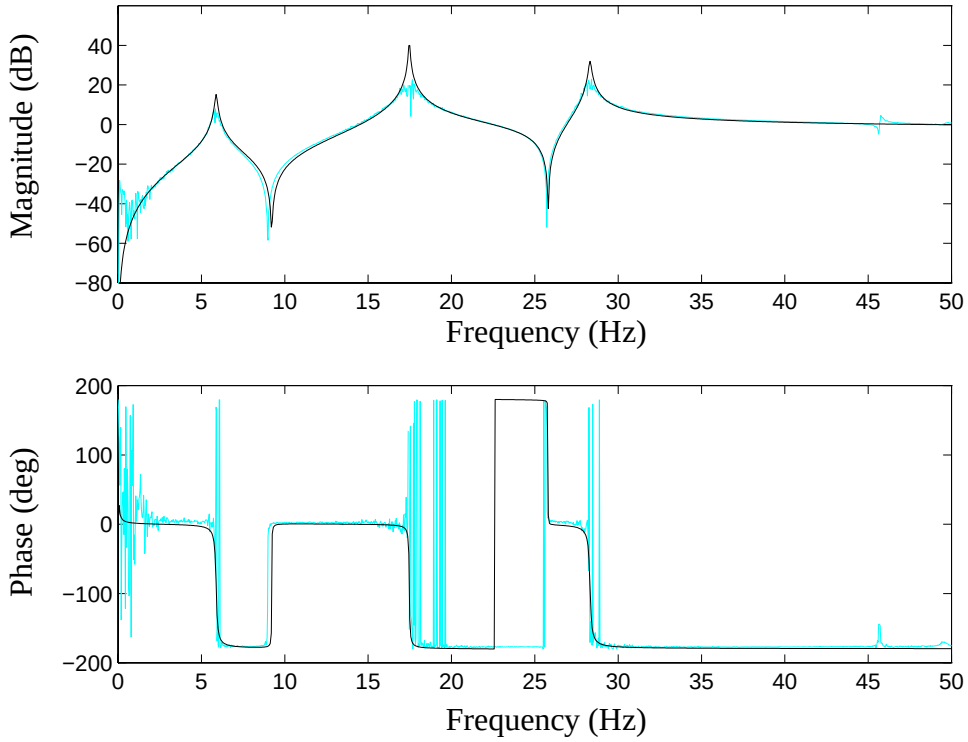

Figure 9.3 Comparison of Reduced-Order Model and Experimental Transfer Function: Control Force to First Floor Absolute Acceleration.

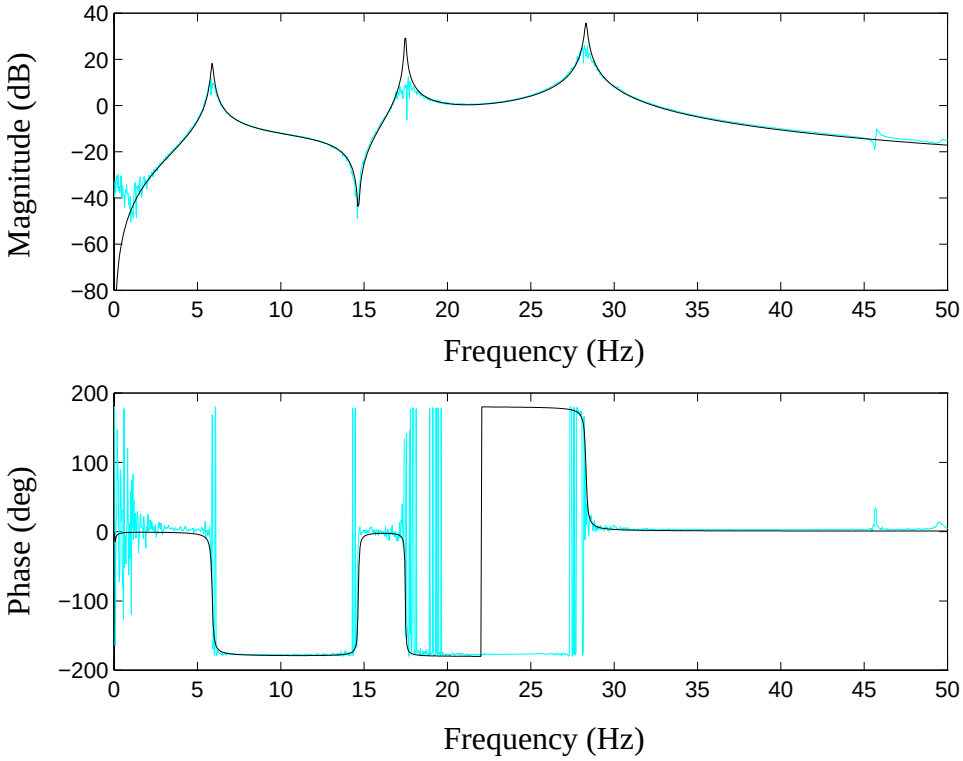

Figure 9.4 Comparison of Reduced-Order Model and Experimental Transfer Function: Control Force to Second Floor Absolute Acceleration.

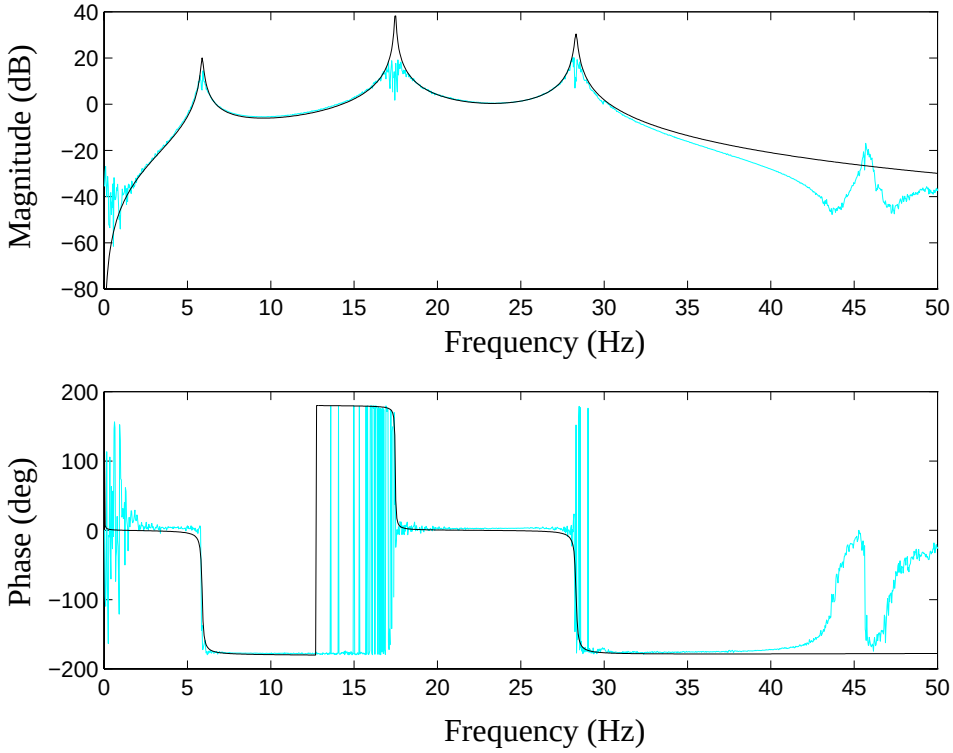

Figure 9.5 Comparison of Reduced-Order Model and Experimental Transfer Function: Control Force to Third Floor Absolute Acceleration.

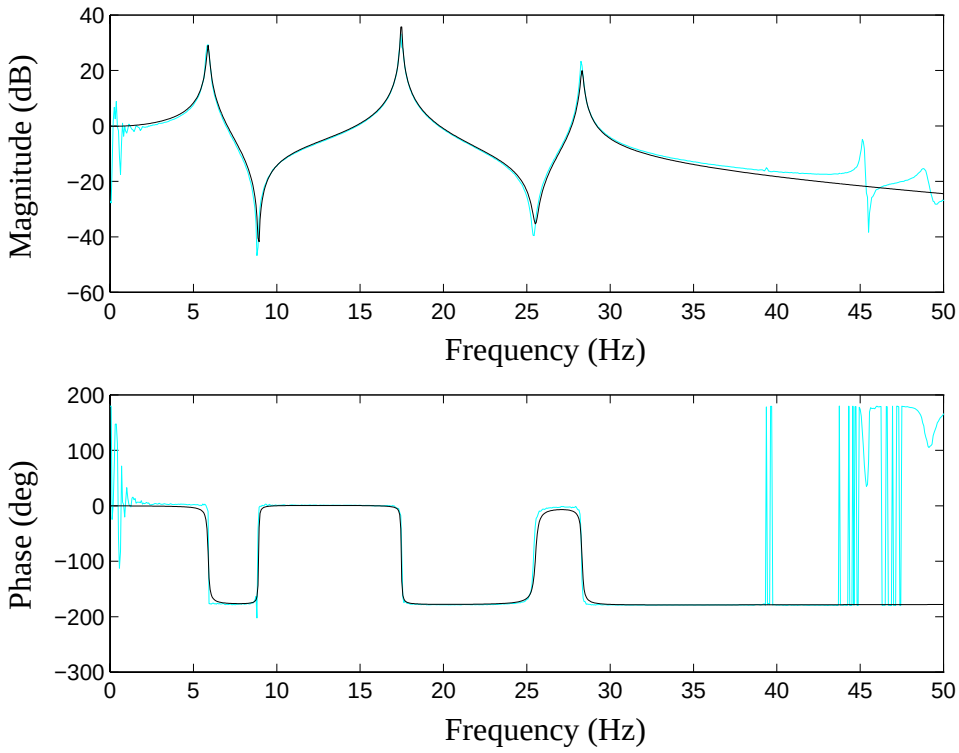

Figure 9.6 Comparison of Reduced-Order Model and Experimental Transfer Function: Ground Acceleration to First Floor Absolute Acceleration.

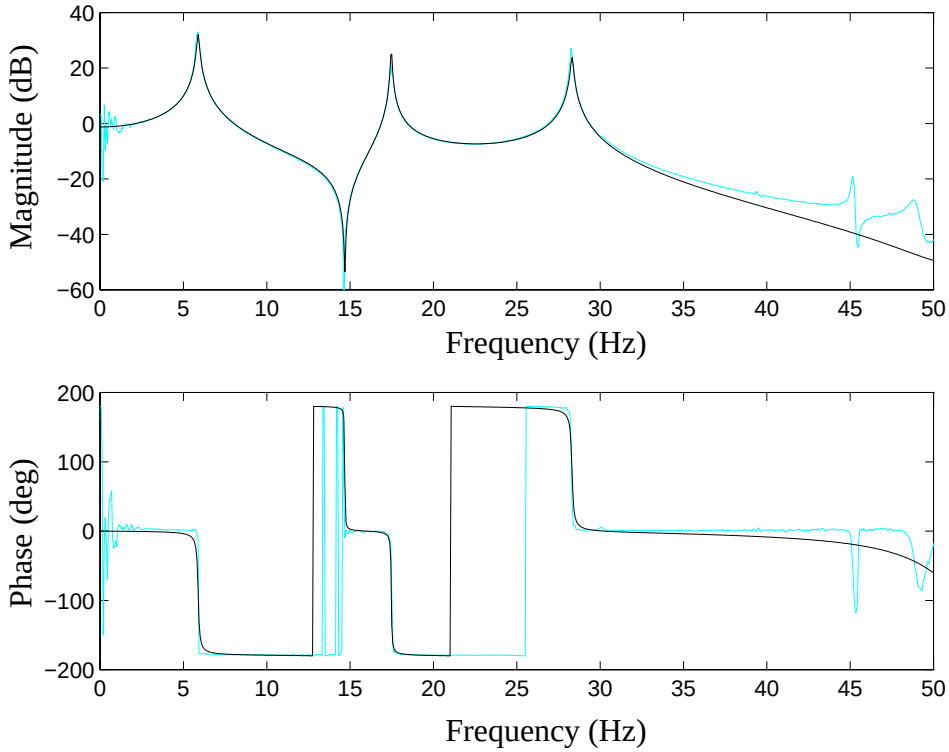

Figure 9.7 Comparison of Reduced-Order Model and Experimental Transfer Function: Ground Acceleration to Second Floor Absolute Acceleration.

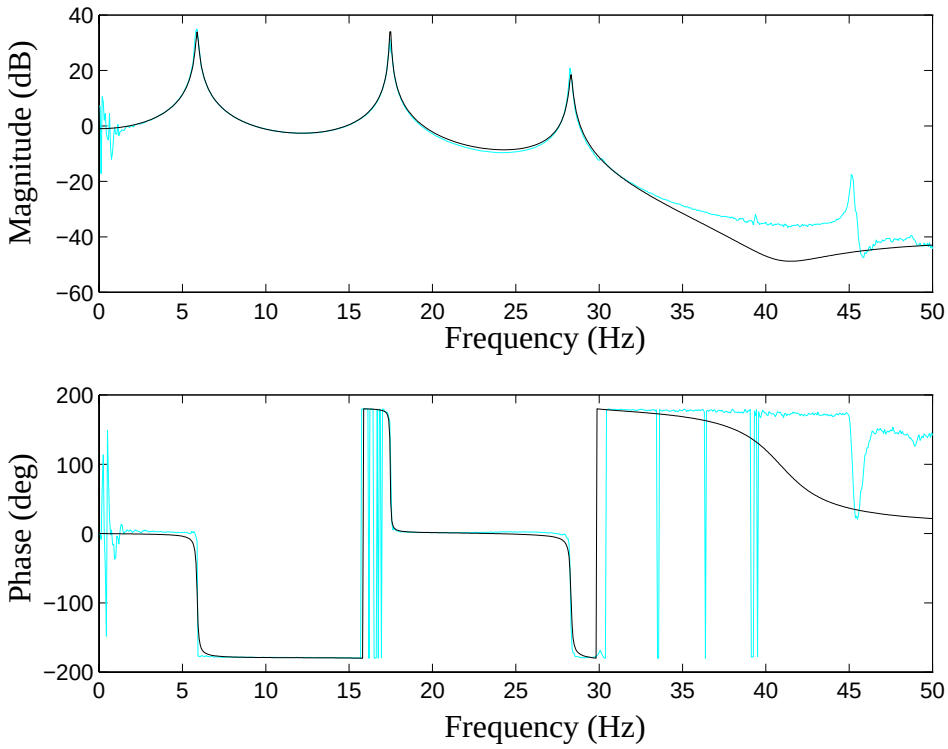

Figure 9.8 Comparison of Reduced-Order Model and Experimental Transfer Function: Ground Acceleration to Third Floor Absolute Acceleration.

9.2.2 Development of an Integrated System Model

The next step is to optimize the set of parameters for the MR damper model (given in Eqs. 7.7–7.11, 7.17 and 7.18) for the case when it is installed in the test structure, and combine the models of the device and structure to form the integrated system model (shown in Fig. 9.9). It is necessary to update the parameters of the MR damper model because when the MR damper is employed in the test structure it may be functioning at a different operating point than in the initial tests in which the damper was driven with a hydraulic actuator.

To identify a new set of parameters, a series of tests was conducted to measure the response of the system with the MR damper in place. In these tests, the base of the structure was excited and various commanded voltages v were applied to the MR damper,

including two constant voltage levels (0 V, 2.25 V) and a step function voltage (0 to 2.25 V). The recorded system responses included the force generated in the MR damper, absolute accelerations of the floors of the structure, displacement of the structure at the MR damper attachment point, displacement of the base, and displacement of the three floors of the structure.

A least-squares output-error method was employed in conjunction with a constrained nonlinear optimization to obtain the updated 14 model parameters required to model the MR damper. The optimization was performed using the sequential quadratic programming algorithm available in MATLAB (1994). Optimized parameters were determined to fit the generalized model of the MR damper to the experimental data. The resulting parameters are provided in Table 9.1.

The integrated system model is then formed by connecting the models of the MR damper and structure as shown in Fig. 9.9. Verification of this integrated system model is provided in the following section.

9.2.3 Verification of the Integrated System Model

To verify that the identified model is adequate for control synthesis and analysis, the predicted response and experimental response were compared in one controlled case

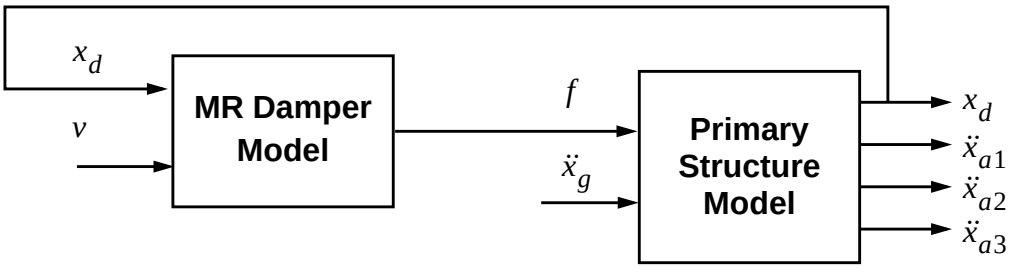

Figure 9.9 Block Diagram of the Integrated Structural System.

Table 9.1 Updated Parameters for the Generalized Model.

Parameter	Value	Parameter	Value
c_{0a}	8.0 N·sec/cm	α_a	100 N/cm
c_{0b}	6.0 N·sec/cm·V	α_b	450 N/cm·V
k_0	50 N/cm	γ	363 cm^{-2}
c_{1a}	290 N·sec/cm	β	363 cm^{-2}
c_{1b}	5.0 N·sec/cm·V	A	301
k_1	12 N/cm	n	2
x_0	14.3 cm	η	190 sec^{-1}

(Controller A as described in the following section). A comparison of the experimental controlled responses and the predicted responses is shown in Figs. 9.10 and 9.11 for a broadband excitation (0-20 Hz) with an rms ground acceleration of 0.20 *g*. Good agreement is obtained.

9.3 Control Design and Experimental Results

To evaluate the performance of the semi-active control system employing the MR damper, eight controllers with various performance objectives were designed based on the identified model of the integrated structure/MR damper system, and implemented in the laboratory. The acceleration feedback control strategies based on H_2/LQG methods, discussed in Chapter 8, were employed to design the optimal controller $\mathbf{K}_c(s)$.

The results of four semi-active control designs, denoted A–D, are presented herein. Controller A was designed by placing a high weighting on the third floor relative displacement. Controllers B, C, and D were designed by placing a low, medium, and high weighting, respectively, on the third floor acceleration. A summary of the control designs is provided in Table 9.2.

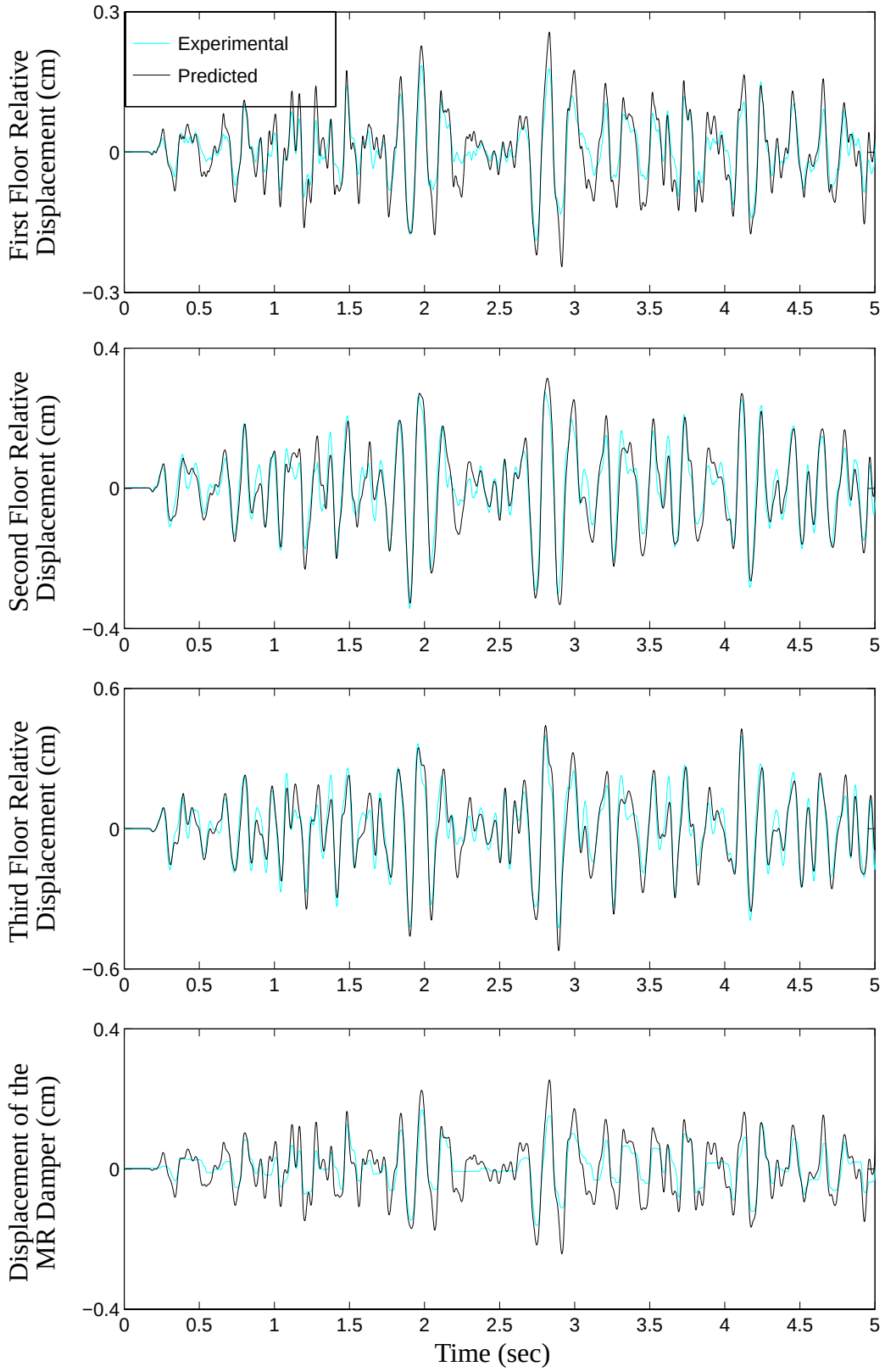

Figure 9.10 Experimental and Predicted Responses of the Semi-Actively Controlled System (Controller A): Floor Displacements and MR Damper Displacement.

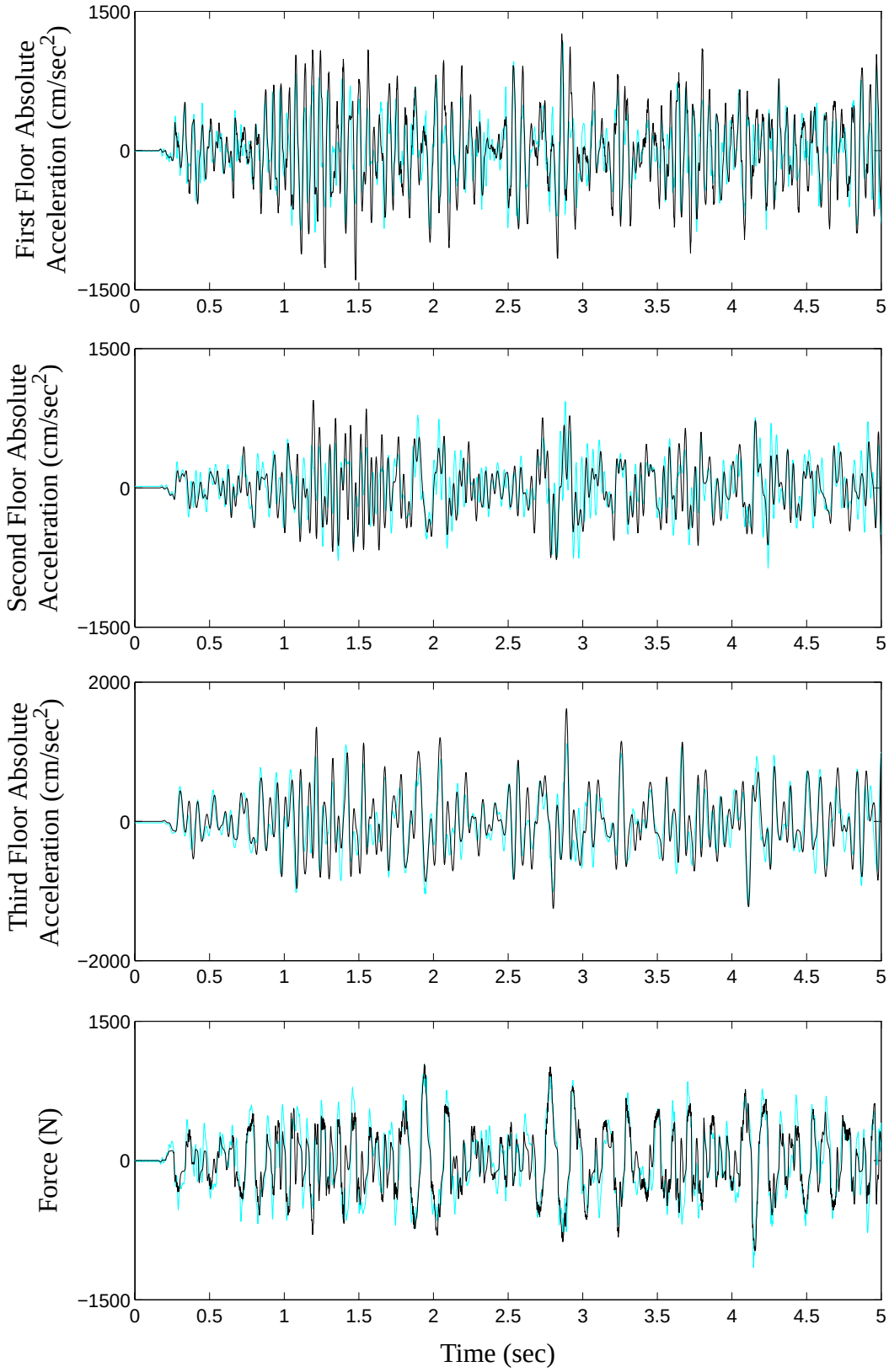

Figure 9.11 Experimental and Predicted Responses of the Semi-Actively Controlled System (Controller A): Floor Accelerations and Control Force.

Table 9.2 Description of Control Strategies for Each Design.

Controller	*Control Strategy*
A	*High Weighting on the Third Floor Displacement*
B	*Low weighting on the Third Floor Absolute Acceleration*
C	*Medium Weighting on the Third Floor Absolute Acceleration*
D	*High Weighting on the Third Floor Absolute Acceleration*

Two types of experimental tests were conducted to evaluate the performance of the control designs. First the three story model structure was subjected to a scaled version of the 1940 El Centro earthquake and the measured responses were recorded. To satisfy the similitude relations, the earthquake must be reproduced at five times the recorded speed. Because the MR damper is a nonlinear device, it is expected to perform differently at various excitation amplitudes. Thus, the tests were performed at two different excitation amplitudes (80% and 120% of the recorded El Centro earthquake). In the second set of tests, the three story model structure was subjected to a 200 second broadband signal (0–20 Hz) and *rms* values of the measured responses were calculated. The tests were conducted at three different excitation amplitudes including excitations with *rms* values of 0.06 *g* (low), 0.13 *g* (medium), and 0.20 *g* (high).

Tables 9.3 and 9.4 provide summaries of the peak structural responses for the high and low amplitude El Centro earthquake excitation tests, respectively. In addition to the results for semi-active controllers, two passive cases are reported. *Passive-off* and *passive-on* refer to the cases in which the voltage to the MR damper is held at a constant value of $V = 0$ and $V = V_{\max} = 2.25$ Volts, respectively. The *uncontrolled* response refers to the case in which the MR damper is not attached to the structure. Here, x_i is the displacement of the ith floor relative to the ground, d_i is the interstory drift (*i.e.*, $x_i - x_{i-1}$), $\ddot{x}_{ai}$ is the absolute acceleration of the ith floor, and f is the measured control force.

Because the excitation levels used in the passive and controlled tests were considerable for the test structure, exciting the uncontrolled structure with the same magnitude excitation could have been destructive. Therefore, the uncontrolled results presented herein were obtained by exciting the structure with excitations that were 50% of those used in the passive and controlled tests, and appropriately scaling the uncontrolled results to the same magnitude excitation. Thus the uncontrolled results optimistically represent the response of the structure if it were to remain linear throughout the tests.

The results of the earthquake tests indicate that the passive systems are able to achieve a reasonable level of performance at both excitation levels. One might assume that because the MR damper produces larger damping forces in the passive-on case, that the responses would be smaller. At high excitation levels (Table 9.3), the passive-on controller is able to achieve a larger reduction in the third floor displacement than the passive-off case, but a modest increase in the third floor absolute acceleration is observed. In the case of the low amplitude (80%) El Centro earthquake, most of the passive-on responses are actually larger than the passive-off case. The third floor displacement, maximum interstory displacement, and maximum floor acceleration of the passive-on system are 11.3%, 10.9% and 19.0% larger, respectively, than the responses of the passive-off system.

Figure 9.12 shows the uncontrolled and semi-actively controlled structural responses (using Controller A) for the high amplitude El Centro excitation. The effectiveness of the proposed control strategy is clearly seen, with peak third floor displacement being reduced by 74.5% and the peak third floor acceleration being reduced by 47.6%.

All of the semi-active control systems perform significantly better than both of the passive systems. At high amplitudes (Table 9.3) Controller A achieves a 24.3% reduction in the peak third floor displacement and a 29.1% reduction in the maximum interstory displacement over the best passive case. Furthermore, these results were obtained while

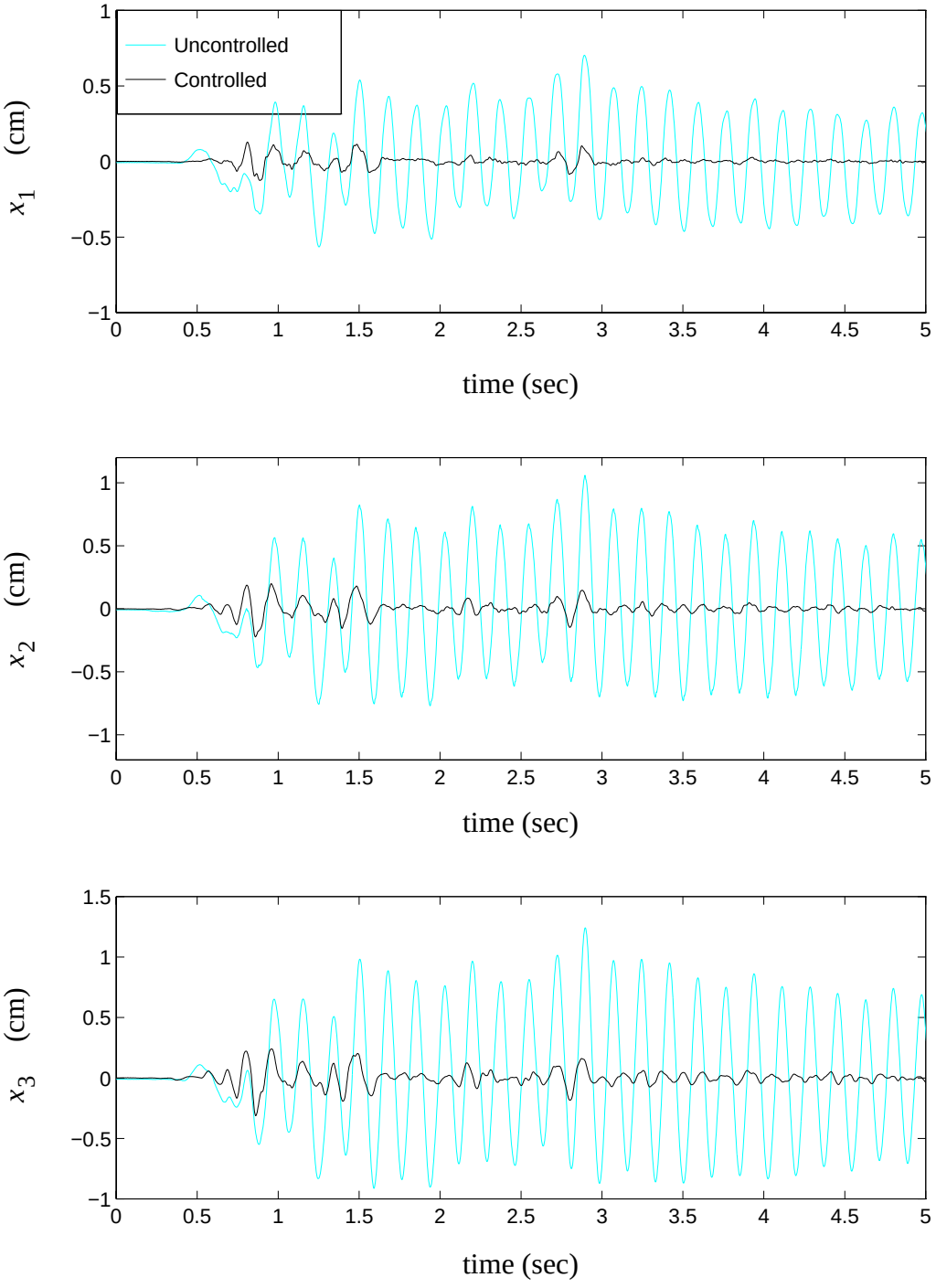

Figure 9.12 Controlled and Uncontrolled Structural Displacement Responses Due to El Centro Earthquake (Controller A).

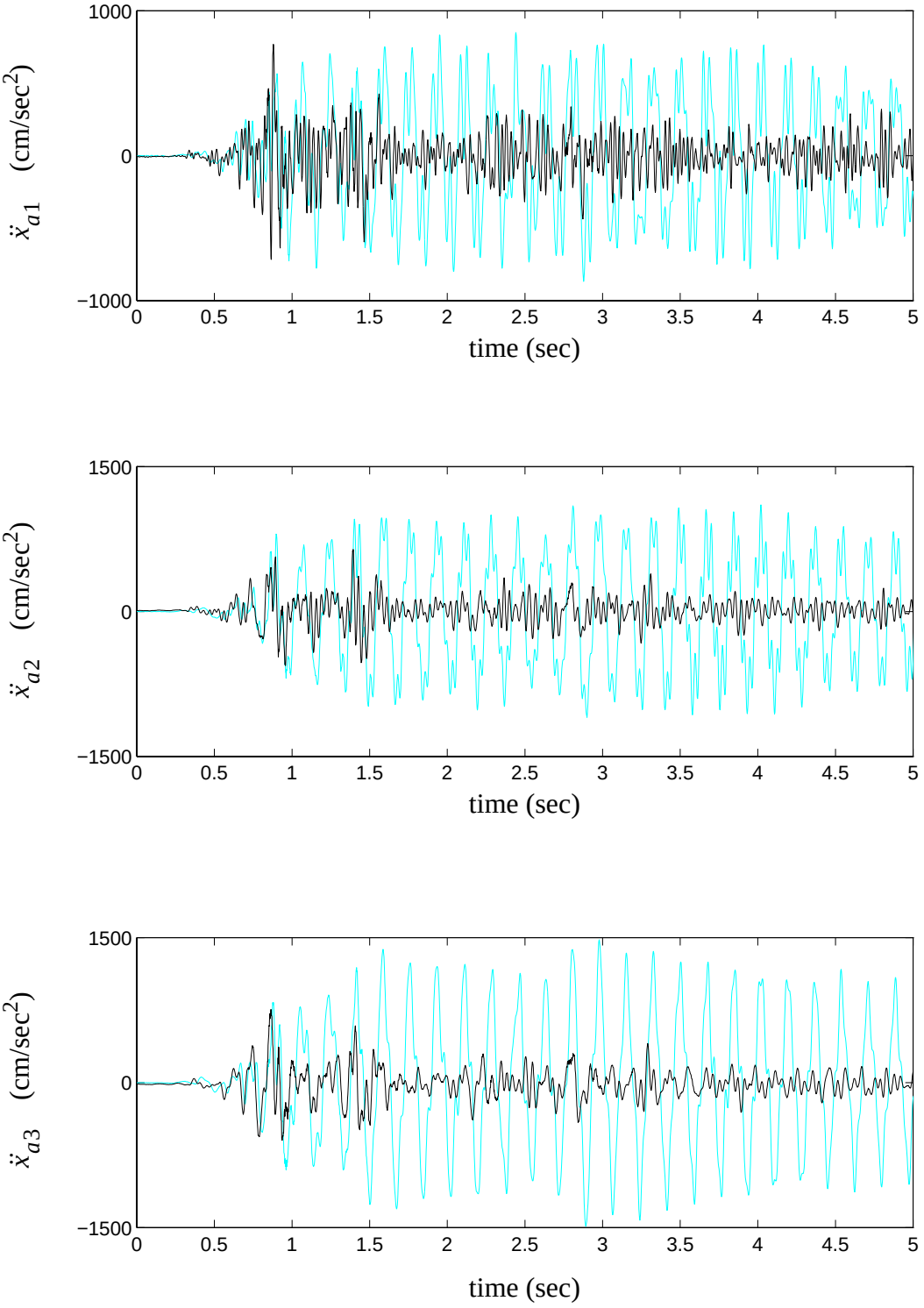

Figure 9.13 Controlled and Uncontrolled Structural Acceleration Responses Due to El Centro Earthquake (Controller A).

achieving a modest reduction in the maximum acceleration over that of the passive response. Additional reduction in the peak third floor relative displacement over the best passive case is achieved with Controllers C (32.6%) and D (33.3%), although at an increase in the maximum floor absolute acceleration. Notice that for all of the semi-actively controlled systems, these performance gains are achieved while requiring smaller control forces than are required in the passive-on case.

At low excitation amplitudes (Table 9.4), the reductions are not as great as in the previous case, but the semi-active controllers continue to perform better than the best passive case. Controller A achieves a 11.3% reduction in the peak third floor relative displacement, a 27.8% reduction in maximum interstory displacement, and a 3.6% reduction in the maximum floor absolute acceleration over the best passive responses. Additional reduction in the peak third floor relative displacement is achieved with controllers B (20%), C (23.8%), and D (23.3%), although, again, the acceleration responses are increased with these controllers.

The *rms* responses for the three random excitation tests are provided in Tables 9.5 (high amplitude), 9.6 (medium amplitude), and 9.7 (low amplitude). Again, at all excitation levels, the passive systems are able to achieve reasonable performance compared to the uncontrolled responses. In the high amplitude tests, most of the *rms* responses of the passive-on system are better than those of the passive-off system. However, at lower excitation levels, the *rms* responses of the passive-on system are often larger than those of the passive-off system. For instance, in both the low and medium amplitude tests, the *rms* third floor absolute acceleration is larger in the passive-on case than in the passive-off case and in the low amplitude test, the maximum interstory displacement and third floor relative displacement are increased.

Table 9.3 Experimental Peak Responses Due to the 120% El Centro Earthquake.

Control Strategy	Uncontrolled	Passive-Off	Passive-On	Clipped-Optimal Controller A	Clipped-Optimal Controller B	Clipped-Optimal Controller C	Clipped-Optimal Controller D
x_i (cm)	0.710 1.068 1.249	0.236 0.362 0.436	0.126 0.312 0.420	0.127 0.229 0.318	0.157 0.264 0.335	0.153 0.215 0.283	0.151 0.213 0.280
d_i (cm)	0.710 0.362 0.205	0.236 0.167 0.106	0.126 0.196 0.110	0.127 0.139 0.092	0.157 0.139 0.081	0.153 0.124 0.089	0.151 0.123 0.087
$\ddot{x}_{ai}$ (cm/sec^2)	879 1110 1500	666 714 804	920 808 897	711 642 786	874 673 653	936 932 766	957 859 748
x_d (cm)	–	0.214	0.095	0.112	0.133	0.129	0.133
f (N)	–	258	1030	696	668	769	754

Table 9.4 Experimental Peak Responses Due to the 80% El Centro Earthquake.

Control Strategy	Uncontrolled	Passive-Off	Passive-On	Clipped-Optimal Controller A	Clipped-Optimal Controller B	Clipped-Optimal Controller C	Clipped-Optimal Controller D
x_i (cm)	0.473 0.712 0.833	0.119 0.197 0.240	0.074 0.196 0.267	0.084 0.157 0.213	0.087 0.148 0.192	0.087 0.134 0.183	0.089 0.136 0.184
d_i (cm)	0.473 0.241 0.137	0.119 0.099 0.067	0.074 0.132 0.083	0.084 0.086 0.066	0.087 0.085 0.060	0.087 0.076 0.060	0.089 0.077 0.059
$\ddot{x}_{ai}$ (cm/sec^2)	586 740 1000	388 481 500	595 546 594	462 457 482	542 579 521	647 739 538	657 759 545
x_d (cm)	–	0.112	0.049	0.063	0.071	0.070	0.071
f (N)	–	224	768	537	580	615	630

In the random excitation tests, the semi-active systems perform significantly better than the passive systems at reducing the *rms* structural responses. All of the semi-active controllers are able to reduce not only the *rms* third floor relative displacements and interstory displacements, but also the maximum *rms* floor accelerations, below those obtained with the passive systems. For all excitation levels, Controller B achieves the best performance of the four semi-active control designs. In the high amplitude tests (Table 9.5), Controller B attains a 14.6% reduction in third floor relative displacement, a 26.5% reduction in maximum interstory displacement, and a 23.6% reduction in the maximum floor absolute acceleration over the best passive case. At medium amplitudes (Table 9.6), Controller B achieves a 17.8%, 30.0% and 8.0% reduction in these responses, respectively. Even at low amplitudes (Table 9.7), a modest reduction in the structural responses is observed. Again, notice that the semi-active controllers achieve these performance levels while using significantly less force than the passive-on system.

Table 9.5 Experimental *RMS* Responses Due to the High Amplitude Random Excitation.

Control Strategy	Uncontrolled	Passive-Off	Passive-On	Clipped-Optimal Controller A	Clipped-Optimal Controller B	Clipped-Optimal Controller C	Clipped-Optimal Controller D
x_i (cm)	0.250 0.382 0.467	0.070 0.112 0.139	0.027 0.070 0.103	0.036 0.066 0.091	0.036 0.065 0.088	0.038 0.066 0.089	0.038 0.066 0.089
d_i (cm)	0.250 0.156 0.123	0.070 0.048 0.035	0.027 0.049 0.036	0.036 0.039 0.031	0.036 0.036 0.027	0.037 0.036 0.029	0.038 0.036 0.029
$\ddot{x}_{ai}$ (cm/sec^2)	1020 576 999	274 184 292	226 178 292	228 159 250	209 153 223	228 179 244	225 176 241
x_d (cm)	–	0.066	0.020	0.033	0.032	0.034	0.034
f (N)	–	112	311	219	209	223	220

Table 9.6 Experimental *RMS* Responses Due to the Medium Amplitude Random Excitation.

Control Strategy	Uncontrolled	Passive-Off	Passive-On	Clipped-Optimal Controller A	Clipped-Optimal Controller B	Clipped-Optimal Controller C	Clipped-Optimal Controller D
x_i (cm)	0.164 0.248 0.304	0.036 0.059 0.077	0.018 0.049 0.073	0.022 0.043 0.062	0.022 0.043 0.060	0.023 0.043 0.061	0.023 0.044 0.061
d_i (cm)	0.163 0.101 0.080	0.036 0.028 0.022	0.018 0.035 0.026	0.022 0.028 0.022	0.022 0.026 0.020	0.023 0.027 0.021	0.023 0.027 0.021
$\ddot{x}_{ai}$ (cm/sec^2)	663 374 649	168 112 176	162 134 208	154 115 174	149 113 162	161 127 172	161 126 172
x_d (cm)	–	0.031	0.010	0.018	0.019	0.020	0.020
f (N)	–	105	237	174	161	171	170

Table 9.7 Experimental *RMS* Responses Due to the Low Amplitude Random Excitation.

Control Strategy	Uncontrolled	Passive-Off	Passive-On	Clipped-Optimal Controller A	Clipped-Optimal Controller B	Clipped-Optimal Controller C	Clipped-Optimal Controller D
x_i (cm)	0.075 0.115 0.140	0.013 0.026 0.035	0.009 0.026 0.037	0.009 0.024 0.034	0.010 0.023 0.033	0.010 0.023 0.033	0.010 0.023 0.033
d_i (cm)	0.075 0.047 0.037	0.013 0.016 0.012	0.009 0.020 0.014	0.009 0.017 0.012	0.010 0.016 0.012	0.010 0.017 0.012	0.010 0.017 0.012
$\ddot{x}_{ai}$ (cm/sec^2)	306 173 300	88.3 68.3 92.5	114 88.1 113	102 78.3 102	102 76.8 95.6	105 78.4 96.8	105 78.7 96.9
x_d (cm)	–	0.017	0.007	0.010	0.012	0.014	0.014
f (N)	–	85.0	140	121	111	113	113

9.4 Summary

In this chapter, the efficacy of the clipped-optimal control strategy based on acceleration feedback has been experimentally verified on a semi-actively controlled structure employing a magnetorheological (MR) damper. First, a model of the integrated structure/MR damper system was identified using the procedure outlined in Chapter 2. The integrated model was then verified by comparing the predicted response of the controlled system with the experimentally obtained response for a broadband excitation.

Four different controllers were tested. These controllers were designed with the objective of minimizing either the third floor relative displacement or the third floor absolute acceleration. The ability of the system to reduce both the peak responses, in the case of the earthquake excitation, and *rms* response, in the case of the broadband excitation, were studied. Excellent results were obtained with the semi-active system. In the large amplitude El Centro excitation tests, the best controller achieved a 74.5% and 47.6% reduction in the peak third floor relative displacement and peak third floor absolute acceleration, respectively, over the uncontrolled values. The response of the system was also measured for two passive cases, designated passive-off and passive-on. All of the semi-active controllers performed significantly better than both of the passive systems in reducing the peak responses.

The response of the semi-active system to a 0–20 Hz broadband excitation was also measured. When the system was excited with a broadband excitation, the responses of the semi-actively controlled system were significantly smaller than those of the uncontrolled and passive systems. In the high amplitude broadband tests, as compared to the best passive results, the best controller reduced the 14.6% reduction in the third floor displacement, a 26.5% reduction in the maximum interstory displacement, and a 23.6% reduction

in the third floor absolute acceleration. The semi-active controllers achieve these performance gains while using smaller control forces than in the passive-on system.

The capabilities of the MR damper have been shown to mesh well with the requirements and constraints associated with seismic response reduction in civil engineering structures.

CHAPTER 10

Conclusions and Recommendations

In this dissertation, acceleration feedback strategies have been developed and experimentally verified for seismically excited structures employing both active and semi-active control systems. Accelerations are readily available and provide inexpensive and reliable measurements of the responses of a structure. Thus, in contrast to state feedback methods, acceleration feedback control strategies are practically implementable.

First, the effects of actuator dynamics and control-structure interaction in structural control systems were investigated. Typically, the dynamics of control actuators are closely linked to the dynamics of the structure being controlled. A model of a hydraulic actuator, typical of those used in control studies, was developed. Simulations were performed which demonstrated the potential consequences of neglecting actuator dynamics and control-structure interaction. The effects of actuator dynamics and control-structure-interaction were found to be highly important and must be incorporated into the structural model to achieve high quality controllers.

The acceleration feedback control strategies have been successfully implemented and verified for three different control system configurations: (i) active bracing, (ii) active tendon, and (iii) active mass driver. A frequency domain approach was employed to identify linear models for the structural systems in each experiment. To consistently incorporate actuator dynamics and control-structure interaction into the system models, the actuator

was included in the structural system to be identified. H_2/LQG control strategies were applied to design controllers which primarily used the accelerations of the structure in determining the control action. The ability of the control systems to reduce both peak responses, in the case of transient excitations, and *rms* responses, in the case of random excitations, was tested. In each of the three active control experiments, a significant reduction in the structural responses was achieved. The main conclusions of each experiment are summarized in the following paragraphs.

The first successful implementation of acceleration feedback strategies was conducted using an active bracing system in which the control actuator was rigidly connected between the ground and first floor of the test structure. The controller, designed to minimize the absolute accelerations of the floors of the structure, achieved a 37.8%, 56.4%, and 61% reduction in the *rms* values of the floor accelerations when excited with a 0–100 Hz broadband excitation. Additionally, a significant reduction was observed in all three modes of the structure.

In the second experiment, acceleration feedback strategies were verified for a larger scale test structure at the National Center for Earthquake Engineering Research in Buffalo, N.Y. The most effective controller, which was designed by weighting the accelerations of the structure and included the ground acceleration as an additional measurement, achieved a 62–68% reduction in the *rms* structural responses to a 0–10 Hz broadband excitation, a 44–56% reduction in the peak responses due to the El Centro earthquake, and a 50–57% reduction in the peak responses to the Taft earthquake. The damping ratios of the first three modes of the structural system were increased to 11.1%, 6.8%, and 1.9%, respectively. The results of the five control designs presented also indicated that weighting the displacement in the control design resulted in a controller which was able to effectively

reduce primarily the structural displacements, while weighting the acceleration served to minimize both the absolute accelerations and relative displacements of the structure.

Because of the number of full-scale implementations of active and hybrid mass driver systems, the final validation of acceleration feedback control strategies for active control systems was conducted using the three-story test structure at the Structural Dynamics and Control Laboratory equipped with an active mass driver. Two similar controllers were studied, both designed with the objective of minimizing the absolute accelerations of the top two floors. The primary difference between the two control designs was that one controller was designed to roll-off the control effort at higher frequencies where the modeling errors were significant. The design that was not designed to roll-off the control effort had the best performance, achieving a 77.4%, 80.5%, and 82.6% reduction in the absolute accelerations of the three floors. Although the controller which rolled-off the control effort did not perform quite as well (72.7%, 76.5%, and 80.1% reduction in the floor accelerations), this controller required only 50%of the *rms* actuator acceleration and 29% of the peak actuator acceleration required by the other controller. Thus, for the controllers examined in this experiment, small performance gains required significantly larger control forces.

The results of these three active control experiments indicate that effective, robust, and practically implementable controllers can be developed using acceleration feedback control strategies.

In the latter portion of this dissertation, a new semi-active control device called a MR damper, was evaluated for use in structural response reduction to seismic loads. Because of its mechanical simplicity, low operating power requirements, environmental robustness, and demonstrated potential for developing forces sufficient for full-scale applications, it is a particularly promising device for structural response reduction. A prototype

damper was obtained from the Lord Corporation of Cary, North Carolina, for laboratory testing. First, a mechanical model for the MR damper, based on the Bouc-Wen model, was developed and shown to effectively portray the intrinsic nonlinear behavior of a typical magnetorheological damper.

This model was then used to investigate, through simulation, the efficacy of a clipped-optimal control algorithm based on acceleration feedback. The approach is to append a force feedback loop to induce the MR damper to produce approximately a desired control force. Although a variety of methods may be used to obtain the desired control force, H_2/LQG methods have been applied because of the stochastic nature of earthquake ground motions and because of their successful application in previous studies. In these simulations, the MR damper was employed to control a model of a three-story structure subjected to an El Centro earthquake. The semi-active control system reduced the third floor relative displacement by 77.9% and the third floor absolute acceleration by 49.8%. The performance of the semi-active system surpassed that of two passive systems considered (designated passive-off and passive-on) while utilizing smaller control forces. Additionally, the semi-active system performed significantly better than a comparable ideal active control system using the same control forces. These performance gains are attributed in part to the fact that the MR damper can quickly respond to changes in the command voltage, and because the device is inherently stable, allowing high authority control strategies to be effectively designed and implemented.

The performance of the MR damper was experimentally verified on the three-degree-of-freedom test structure at the SDC/EEL. A single MR damper, rigidly attached between the ground and the first floor of the structure, was used to control the structure. First, a novel approach for the nonlinear identification of semi-actively controlled structures was applied to identify the integrated MR damper/structure system. Then, four clipped-optimal

controllers were designed and implemented on the test structure. The MR damper performed well in reducing both peak structural responses to the El Centro earthquake and *rms* responses to a random excitation. In the large amplitude El Centro excitation tests, the best controller achieved a 74.5% and 47.6% reduction in the peak third floor relative displacement and peak third floor absolute acceleration, respectively, over the uncontrolled values. Because the MR damper has the ability to dynamically modify its properties, the performance of the semi-active system surpassed that of the two different passive systems considered. In the high amplitude broadband tests, as compared to the best passive results, the best controller reduced the 14.6% reduction in the third floor displacement, a 26.5% reduction in the maximum interstory displacement, and a 23.6% reduction in the third floor absolute acceleration.

The experimental results reported indicate that high performance can be attained with a semi-active control system using acceleration feedback control strategies and the characteristics of the MR damper meet the requirements associated with seismic response reduction in civil engineering structures.

Future Studies

Some recommendations for future studies related to this work are:

- Acceleration feedback strategies have been verified for control systems employing a single control actuator or a single semi-active MR damper. Control systems which use multiple control devices, as is likely for full-scale implementations, should be investigated and implemented in the laboratory.
- Throughout this dissertation the structural system was assumed to remain in the linear region, but the structure will inevitably become nonlinear at some point due

to excessive excitation levels. Methods of analyzing and controlling the structures in these situations must be developed.

- Semi-active structural control devices appear to be particularly promising in addressing a number of questions about structural control systems and advancing the acceptance of structural control as a viable technology. However, these devices are intrinsically nonlinear, making modeling and control design challenging tasks. Standarized analysis techniques, system identification methods, and evaluation procedures must be established to study these devices for structural control applications.
- One of the attractive features of the clipped-optimal control strategy employed in the semi-active systems is that it does not require a model for the MR damper, although the model of the damper is important to system analysis. However, control algorithms that explicitly incorporate actuator dynamics and control-structure interaction into the design process may offer additional performance gains and should be investigated.
- Preliminary tests indicate that MR dampers, such as the one studied in this research, may be scaled up to create devices that are capable of generating the forces required in full-scale structural control applications. Full-scale MR dampers must be designed, built, and tested to confirm the scaleability of these devices. Furthermore, these devices must be modeled.
- Before structural control systems are implemented in full-scale structures, guidelines and codes will be necessary for the design of structures which employ control systems. The requirements of these guidelines and codes should be considered.
- Because the MR damper is a nonlinear device, the response of the device is dependent on the amplitude of the inputs. Thus, to achieve high performance levels in

the controlled system, studies should be conducted to observe and model the variation in the response of the device at various amplitudes and to develop a procedure which can be used to size the device properly for a structure being controlled.

- Although the procedure used herein for the identification of linear systems yields high quality models, more systematic methods are sought that are capable of identifying real poles and/or zeros typically introduced due to the dynamics of the actuators.

References

Abdel-Rohman, M. and Leipholz, H.H. (1978a). "Active Control of Flexible Structures." *Journal of the Structural Division*, ASCE, Vol. 104, No. 8, pp. 1251-1266.

Abdel-Rohman, M. and Leipholz, H.H. (1978b). "Structural Control by Pole Assignment Method." *Journal of the Structural Division*, ASCE, Vol. 104, No. 5, pp. 1159-1175.

Abdel-Rohman, M. and Leipholz, H.H. (1983). "Active Control of Tall Buildings." *Journal of the Structural Division*, ASCE, Vol. 109, No. 3, pp. 628-645.

Abdel-Rohman, M. (1984). "Optimal Control of Tall Buildings by Appendages." *Journal of the Structural Engineering*, ASCE, Vol. 110, pp. 937-947.

Abdel-Rohman, M. and Nayfeh, A.H. (1987). "Active Control of Nonlinear Oscillations in Bridges." *Journal of the Engineering Mechanics*, Vol. 113, No. 3, pp. 335-348.

Adhikari, R. and Yamaguchi, H. (1994). "Adaptive Control of Nonstationary Wind-Induced Vibration of Tall Building." *Proc. of the First World Conference on Structural Control*, pp. TA4:43–52.

Akbay, Z. and Aktan, H.M. (1990). "Intelligent Energy Dissipation Devices." *Proc. of the Fourth U.S. National Conference on Earthquake Engineering*, Vol 3, No. 4. pp. 427-435.

Akbay, Z. and Aktan, H.M. (1991). "Actively Regulated Friction Slip Devices." *Proc. of the 6th Canadian Conference on Earthquake Engineering*, pp. 367-374.

Antoniou, Andreas. 1993. *Digital Filters: Analysis, Design, and Applications*, McGraw-Hill, Inc., New York, pp. 444–446.

Asano, K. and Nakagawa, H. (1993). "Seismic Random Response of Elasto-Plastic Systems Under Active Saturation Control Force." *Proceedings of the U.S. National Workshop on Structural Control Research*, USC Publications No. M9013, University of Southern California, Los Angeles, October 25–26, pp. 40–48.

Astrom, K.J. and Wittenmark, B. (1990). *Computer-Controlled Systems: Theory and Design*, Prentice Hall, Englewood Cliffs, New Jersey.

ATC 17-1, (1993), *Proceedings on Seismic Isolation, Passive Energy Dissipation, and Active Control*, Applied Technology Council, Redwood City, California.

Bergland, G.D. (1969). A Guided Tour of the Fast Fourier Transform. *IEEE Spectrum*, vol. 6, pp. 41–52, July.

Bendat, J.S. and Piersol, A.G. (1980). *Engineering Applications of Correlation and Spectral Analysis*, John Wiley & Sons, Inc., New York.

Bendat, J.S. and Piersol, A.G. (1986). *Random Data: Analysis and Measurement Procedures*, John Wiley & Sons, Inc., New York.

Bendat, J.S. and Piersol, A.G. (1990). *Nonlinear System Analysis and Identification from Random Data*, John Wiley & Sons, Inc., New York.

Billings, S.A. (1984).“Identification of Nonlinear Systems.” *Non-Linear System Design*, (S.A. Billings, J.O. Gray and D.H. Owens, eds., Peter Peregrinus, London).

Bossis, G. and Lemaire, E. (1991). “Yield Stresses in Magnetic Suspensions,” *Journal of Rheology*, Vol 35(7), pp. 1345–1354.

Boyd, S.P. and C.H. Barratt, (1991). *Linear Controller Design - Limits of Performance*, Prentice-Hall, Englewood Cliffs, New Jersey.

Buckle, I.G. and Mayes, R.L. (1990). “Seismic Isolation History, Application and Performance--A World View.” *Earthquake Spectra*, Vol. 6, No. 2, 161–201.

Burton, S.A., Makris, N., Konstantopoulos, I. and Antsaklis, P.J. (1996). “Modeling the Response of an Electrorheological Damper: Phenomenology and Emulation,” *J. Engrg. Mech., ASCE*, in press.

Casciati, F. Faravelli, L. and Venini, P. (1993). “A Neural-Network Performance-Function Selection in Active Structural Control,” *Proc. of the Int. Workshop on Structural Control*, Univ. of Southern California, pp. 55–64.

Casciati, F. and Yao, T., (1994). “Comparison of Strategies for the Active Control of Civil Structures,” *Proc. of the First World Conference on Structural Control*, Pasadena, CA, pp. WA:1–12.

Carlson, J.D. (1994). “The Promise of Controllable Fluids.” *Proc. of Actuator 94* (H. Borgmann and K. Lenz, Eds.), AXON Technologie Consult GmbH, pp. 266–270.

Carlson, J.D. and Weiss, K.D. (1994). “A Growing Attraction to Magnetic Fluids,” *Machine Design*, August, pp. 61–64.

Carlson, J.D., Catanzarite, D.M. and St. Clair, K.A. (1995). “Commercial Magneto-Rheological Fluid Devices,” *Proceedings of the 5th International Conference on ER Fluids, MR Fluids and Associated Technology*, U. Sheffield, UK.

Carlson, J.D. and Chrzan, M.J., U.S. Patent #5,277,281, “Magnetorheological Fluid Dampers,” 1994.

Carlson, J.D. Chrzan, M.J., and James, F.O., U.S. Patent #5,398,917, “Magnetorheological Fluid Devices,” 1995.

Chameau, J., Reed, D.A., and Yao, J.T.P., (1991). “Intelligent Systems in Civil Engineering,” *Proc. Int. Fuzzy Systems Assoc.*, Brussels, Belgium.

Chang, J. and Soong, T.T. (1980). “Structural Control Using Active Tuned Mass Dampers.” *Journal of the Engineering Mechanics Division*, ASCE, Vol. 106, No. 6, pp. 1091-1098.

Cheng, W., Qu, W. and Li, A. (1994). “Hybrid Vibration Control of Nanjing TV Tower under Wind Excitation.” *Proc. of the First World Conference on Structural Control*, pp. WP2:32–41.

Cherry, S. (1994). “Research on Friction Damping at the University of British Columbia.” *Proceedings of the International Workshop on Structural Control*, USC Publication Number CE-9311, pp. 84-91.

Chung, L.L., Reinhorn, A.M. and Soong, T.T., (1988), “Experiments on Active Control of Seismic Structures,” *Journal of Engineering Mechanics, ASCE*, Vol. 114, pp. 241-256.

Chung, L.L., Lin, R.C., Soong, T.T., and Reinhorn, A.M., (1989), “Experiments on Active Control for MDOF Seismic Structures,” *Journal of Engineering Mechanics, ASCE*, Vol. 115, No. 8, pp. 1609–1627.

Constantinou, M.C. and Symans, M.D. (1992). "Experimental and Analytical Investigation of Seismic Response of Structures with Supplemental Fluid Viscous Dampers," *Nat. Center for Earthquake Engrg. Res., Tech. Report NCEER-92-0032*, Buffalo, N.Y.

Constantinou, M.C., Symans, M.D., Tsopelas, P. and Taylor, D.P. (1993). “Fluid Viscous Dampers in Application of Seismic Energy Dissipation and Seismic Isolation.” *Proc. of ATC-17-1 Seminar of Seismic Isolation, Passive Energy Dissipation, and Active Control*, Vol. 2, pp. 581-591.

Constantinou, M.C. and Symans, M.D., (1994). “Semi-Active Fluid Viscous Dampers for Seismic Response Control.” *Proc. of the First World Conference on Structural Control*, Pasadena, CA.

Demchuk, S.A. (1993). “Heat Transfer in Narrow Gaps Filled with Magnetorheological Suspensions.” *Journal of Magnetism and Magnetic Materials*, Vol. 122, No. 1 / 3, p. 312.

DeSilva, Clarence W., (1989). *Control Sensors and Actuators*, Prentice Hall, Inc., Englewood Cliffs, New Jersey, pp. 390-405.

Dowdell, D.J and Cherry, S. (1994). “Semi-Active Friction Dampers for Seismic Response Control of Structures,” *Proc., Fifth US Nat. Conf. on Earthquake Engrg.*, Vol. 1, pp. 819–828.

Dowdell, D.J. and Cherry, S. (1994). "Structural Control Using Semi-Active Friction Dampers," *Proc., First World Conf. on Struct. Control*, FA1:59–68.

Dyke, S.J., B.F. Spencer Jr., P. Quast & M.K. Sain. (1993). "Protective System Design: The Role of Control-Structure Interaction." *Proc. of the Int. Workshop on Structural Control*, Univ. of Southern California, pp. 100–114.

Dyke, S.J., Spencer Jr., B.F., Quast, P., Sain, M.K., Kaspari Jr., D.C. and Soong, T.T. (1994). "Experimental Verification of Acceleration Feedback Control Strategies for An Active Tendon System," *Nat. Center for Earthquake Engrg. Res., Tech. Report NCEER-94-0024*, Buffalo, N.Y.

Dyke, S.J., Spencer B.F. Jr., Quast, P., and Sain,M.K. (1995). "The Role of Control-Structure Interaction in Protective System Design." *Journal of Engineering Mechanics, ASCE*, Vol. 121 No. 2, pp. 322–38, 1995.

Dyke, S.J., Spencer Jr., B.F., Quast, P., Kaspari Jr. and Sain, M.K. (1996a). "Implementation of an AMD Using Acceleration Feedback Control," *Microcomputers in Civil Engrg.*, (in press).

Dyke, S.J., Spencer Jr., B.F., Quast, P., Sain, M.K., Kaspari Jr., D.C. and Soong, T.T. (1996b). "Acceleration Feedback Control of MDOF Structures," *J. of Engrg. Mech, ASCE*, (in press).

Dyke, S.J., B.F. Spencer, Jr., M.K. Sain, and Carlson, J.D. (1996c). "A New Semi-Active Control Device for Seismic Response Reduction," *Proc. 11th ASCE Engrg. Mech. Spec. Conf.*, Ft. Lauderdale, Florida, pp. 886–889.

Dyke, S.J., B.F. Spencer, Jr., M.K. Sain, and Carlson, J.D. (1996d). "Seismic Response Reduction Using Magnetorheological Dampers." *Proc. of the IFAC World Congress*, San Francisco, California, Vol. L, pp. 145–150.

Dyke, S.J., Spencer Jr., B.F., Sain, M.K. and Carlson, J.D. (1996e). "Modeling and Control of Magnetorheological Dampers for Seismic Response Reduction." *Smart Structures and Materials*, in press.

Dyke, S.J., Spencer Jr., B.F., Sain, M.K. and Carlson, J.D. (1996f). "Experimental Verification of Semi-Active Structural Control Strategies Using Acceleration Feedback," *Proc., 3rd Int. Conf. on Motion and Vibr. Control*, Chiba, Japan.

Ehrgott, R.C. and Masri, S.F. (1992). "Modelling of Oscillatory Dynamic Behavior of Electrorheological Materials in Shear." *Smart Materials and Structures*, Vol. 4, pp. 275–285.

Ehrgott, R.C. and Masri, S.F. (1994). "Structural Control Applications of an Electrorheological Device." *Proceedings of the International Workshop on Structural Control*, USC Publication Number CE-9311, pp. 115-129.

Fedorov, V. A. (1992). “Features of Experimental Research into the Characteristics of Magnetorheological and Electrorheological Shock Absorbers on Special Test Stands.” *Magnetohydrodynamics*, Vol. 28, No. 1, p. 96.

Feng, Q. and Shinozuka, M. (1990). “Use of a Variable Damper for Hybrid Control of Bridge Response under Earthquake.” *Proc. of the U.S. National Workshop on Structural Control Research*. USC Publication No. CE-9013, pp. 107–112.

Feng, M. Q., Shinozuka, M., and Fujii, S. (1993). “Friction-Controllable Sliding Isolation System”, *Journal of Engineering Mechanics*, ASCE, Vol. 119 (9), pp. 1845–1864.

Friedlander, B. (1982). Lattice Filters for Adaptive Processing. *Proc. of the IEEE*, 70(3).

Fujino, Y., Soong, T.T. and Spencer Jr., B.F. (1996). “Structural Control: Basic Concepts and Applications,” *Proc. ASCE Struct. Cong.*, Chicago, Illinois, pp. pp. 361–370.

Fujino, Y. (1994). “Recent Research and Developments on Control of Bridges under Wind and Traffic Excitations in Japan.” *Proc. Int. Workshop on Struct. Control*, pp. 144–150.

Fujino, Y. and Yamaguchi, H. (1994). “Implemented Examples of Structural Response Control for Civil Structures with Emphasis on Active Control.” *Japan Soc. Steel Const.*, 12, pp. 16–22.

Fujita, T., Kamada, T., Masaki, N. and Suizu, Y. (1994a). “Development of Hybrid Mass Damper with Convertible Active and Passive Modes Using Hydraulic Actuator and Multi-stage Rubber Bearing.” *Proc. of the First World Conference on Structural Control*, FA4:43–52.

Fujita, T., Kamada, T., Teramoto, T., Kitamura, H., Suizu, Y., Masaki, N., Kanno, T. and Kawachi, H. (1994b). “Application of Hybrid Mass Damper Using Hydraulic Actuator and Multistage Rubber Bearing to High-Rise Building.” *Proc. of the First World Conference on Structural Control*, FA4:53–62.

Fujita, T., Shimazaki, M., Hayamizu, Y., Aizawa, S., Higashino, M. and Haniuda, N. (1994c). “Semiactive Seismic Isolation using Controllable Friction Damper,” *Bull. of Earthquake Resist. Struct. Res. Ctr.*, Univ. of Tokyo. No. 27, pp. 21–31.

Furuta, H., Okanan, H., Kaneyoshi, M., and Tanaka, H., (1994). “Application of Genetic Algorithms to Self-Tuning of Fuzzy Active Control for Structural Vibration,” *Proc. of the First World Conference on Structural Control*, Pasadena, CA, pp. WP:1–12.

Gamota, D.R. and Filisko, F.E. (1991). “Dynamic Mechanical Studies of Electrorheological Materials: Moderate Frequencies.” *Journal of Rheology*, Vol. 35, pp. 399–425.

Gattulli, V. and Soong, T.T. (1994). “Nonlinear Control Laws for Enhancement the Structural Control Effectiveness.” *Proc. 5th U.S. National Conference on Earthquake Engineering*, Chicago, IL.

Gavin, H.P., Ortiz, D.S. and Hanson, R.D. (1994). “Testing and Modeling of a Prototype ER Damper for Seismic Structural Response Control.” *Proceedings of the International Workshop on Structural Control*, USC Publication Number CE-9311, pp. 166-180.

Gavin, H.P., Hose, Y.D., and Hanson, R.D. (1994). “Design and Control of Electrorheological Dampers.” *Proc. of the First World Conference on Structural Control*, Pasadena, CA, August 3-5, Vol. 1, pp. WP3-83 through WP3-92.

Gavin, H.P. (1994). “Electrorheological Dampers for Structural Vibrations Suppression.” Ph.D. Dissertation, The University of Michigan, Department of Civil and Environmental Engineering.

Gordaninejad, F., Ray, A. and Bindu, R., (1994). Vibration Control of Structures Using Hybrid ER/Viscous Dampers, *Proc., First World Conf. on Struct. Control*, pp. TA2:41–49.

Grasselli, Y., Bossis, G. and Lemaire, E. (1993). “Field-Induced Structure in Magnetorheological Suspensions.” *Progress in Colloid & Polymer Science*, Vol. 93, p. 175.

Haroun, M.A., Pires, J.A. and Won, A.Y.J. (1994). “Active Orifice Control in Hybrid Liquid Dampers,” *Proc., First World Conf. on Struct. Control*, FA1:69–78.

Harris, F.J. (1978). “On the Use of Windows for Harmonic Analysis with Discrete Fourier Transforms.” *Proc. of the IEEE,* 66(1), pp. 51–83.

Higashino, M. and S. Aizawa. (1993). “The Application of Active Mass Damper System in Actual Buildings.” *Proc. of the Int. Workshop on Struct. Control*, Univ. of Southern California, pp. 194–205.

Hirai, Jun, Abiru Hisanori, and Eiichi Tsuji. (1993). “Study on Tuned Active Damper for Control Tower of Kansai International Airport.” *Proc. of the Int. Workshop on Struct. Control*, Univ. of Southern California, pp 206–13.

Horvath, D. and Kopcansky, P. (1993). “Magnetic Dimer Motion Effects in Rotating Magnetic Field (A Qualitative Model of Magnetoviscosity and Permittivity in Magnetorheological Suspensions).” *Czechoslovak Journal of Physics*, Vol. 43, No. 6, p. 671.

Housner, G.W. and Masri, S.F. (Eds.). (1990). *Proceedings of the U.S. National Workshop on Structural Control Research*, USC Publications No. M9013, University of Southern California, Los Angeles, October 25–26.

Housner, G.W. and Masri, S.F. (Eds.). (1993) *Proceedings of the International Workshop on Structural Control*, USC Publication No. CE–9311, Univ. of Southern California.

Housner, G.W., Masri, S.F. and Chassiakos, A.G. (Eds.), (1994a). *Proceedings of the First World Conference on Structural Control*, Pasadena, CA, August 3-5.

Housner, G.W., Soong, T.T., and Masri, S.F., (1994b). “Second Generation of Active Structural Control in Civil Engineering,” *Proceedings of the First World Conference on Structural Control*, Pasadena, CA, August 3-5.

Hrovat, D., Barak, P. and Rabins, M. (1983). “Semi-Active Versus Passive or Active Tuned Mass Dampers for Structural Control,” *J. Engrg. Mech.*, Vol. 109, No. 3, pp. 691–705.

Iemura, H., and Izuno, K., (1994). “Development of the Self-Oscillating TMD and Shaking Table Tests.” *Proc. of the First World Conference on Structural Control*, pp. WP2:42–51.

Imai, H., Maruyama, O., Shinozuka, M. and Yun, C -B. (1989). “Fundamentals of System Identification in Structural Dynamics.” *Probabilistic Engineering Mechanics*, Vol. 4, No. 4, pp. 162-173.

Inaudi, J.A., Kelly, J.M., and Pu, J.P., (1993). “Optimal Control and Frequency Shaping Techniques for Active Isolation,” *Proc. of ATC Seminar of Seismic Isolation, Passive Energy Dissipation, and Active Control*, San Francisco, Vol. 2, pp. 787–798.

Inaudi, J.A., Hayen, J.C. and Iwan, W.D., “A Semi-Active Damping Brace System,” *J. of Engrg. Mech., ASCE*, submitted.

Inaudi, J.A. and Kelly, J.M. (1994) "Experiments on Tuned Mass Dampers Using Viscoelastic, Frictional and Shape-Memory Alloy Materials.” *Proceedings of the First World Conference on Structural Control*, Pasadena, CA, August 3-5, Vol. 2, pp. TP3-107.

Inaudi, J.A., “Modulated Homogeneous Friction (MHF),” *Earthquake Engrg. and Struct. Dyn.*, submitted.

Inaudi, J.A., Hayen, J.C. and Iwan, W.D. “A Semi-Active Damping Brace System,” *J. of Engrg. Mech., ASCE*, submitted.

Indrawan, B. and Higashihara, H. (1993). “Active Vibration Control with 1efExplicit Treatment of Actuator’s Limit,” *Proceedings on Seismic Isolation, Passive Energy Dissipation, and Active Control*, Applied Technology Council, Redwood City, California, pp. 715–726.

Inoue, Y., E. Tachibana, and Y. Mukai. (1993). “Recent Developments in Active Structural Control of Buildings in Japan.” *Proc. of the Int. Workshop on Struct. Control*, Univ. of Southern California, pp. 239–47.

Ivers, D.E. and Miller, L.R. (1991). "Semi-Active Suspension Technology: An Evolutionary View." *DE-Vol. 40, Advanced Automotive Technologies*, (S.A. Velinsky, R.H. Fries and D. Wang, Eds.), ASME Book No. H00719, pp. 327-346.

Kabakov, A.M. and Pabat, A.I. (1990). “Development and Investigation of Control Systems of Magnetorheological Dampers.” *Soviet Electrical Engineering*, Vol. 61, No. 4, p. 55.

Kamagata, S. and Kobori, T.: (1994). “Autonomous Adaptive Control of Active Variable Stiffness System for Seismic Ground Motion,” *Proc., First World Conf. on Struct. Control*, pp. TA4:33–42.

Kamath, G.M., and Wereley, N.M. (1996). “A Nonlinear Viscoelastic-Plastic Model for Electrorheological Fluids.” *Smart Materials and Structures*, (submitted).

Kannan, S. Uras, H.M. and Aktan, H.M. (1995). “Active Control of Building Seismic Response by Energy Dissipation,” *Earthquake Engrg. and Struct. Dyn.*, Vol. 24, No. 5, pp. 747–759.

Kareem, A. (1994). “The Next Generation of Tuned Liquid Dampers,” *Proc., First World Conf. on Struct. Control*, FP5:19–28.

Kashevskii, B.E. (1990). “Relaxation of Viscous Stresses in Magnetorheological Suspensions.” *Magnetohydrodynamics*, Vol. 26, No. 2, p. 140.

Kawatani, M., Yamada, Y., Shimono, M. and Mori, A. (1994). “Hybrid Control of Traffic-Induced Vibration of Girder Bridges.” *Proc. of the First World Conference on Structural Control*, pp. TA2:3–10.

Kawashima, K., Unjoh, S. and Shimizu, K. (1992). “Experiments on Dynamics Characteristics of Variable Damper.” *Proc. of the Japan National Symposium on Structural Response Control*, Tokyo, Japan, p.121.

Kawashima, K., Unjoh, S. and Mukai, H., (1994). “Seismic Response Control of Highway Bridges by Variable Dampers,” *Proc., Fifth US Nat. Conf. on Earthquake Engrg.*, Vol. 1, pp. 829–838.

Kelly, J.M. (1981). “Aseismic Base Isolation: Its History and Prospects.” *Proceedings of the First World Congress on Joints and Bearings*, ACI–SP–70, Vol. 1, 549–586.

Kelly, J.M. (1986). “Aseismic Base Isolation: Review and Bibliography.*” Soil Dynamics and Earthquake Engineering*, Vol. 5, No. 3, pp. 202–216.

Kobori, T., Koshika, N., Yamada, K., and Ikeda, Y. (1991a). “Seismic -Response-controlled structure with active mass driver system. Part 1: Design.” *Earthquake Engineering and Structural Dynamics*, Vol. 20, pp. 133–149.

Kobori, T., Koshika, N., Yamada, K., and Ikeda, Y. (1991b). “Seismic -response-controlled structure with active mass driver system. Part 2: Verification.” *Earthquake Engineering and Structural Dynamics*, Vol. 20, pp. 151–166.

Kobori, T., Takahashi, M., Nasu, T., Niwa, N. and Ogasawara, K. (1993). “Seismic Response Controlled Structure with Active Variable Stiffness System.” *Earthquake Engineering and Structural Dynamics*, Vol. 22, pp. 925–941.

Kobori, T. (1994). “Future Direction on Research and Development of Seismic-Response-Controlled Structure,” *Proc. 1st World Conf. on Struct. Control*, Panel:19–31.

Koike, Y., Murata, T., Tanida, K., Kobori, T., Ishii, K., and Takenaka, Y. (1994). “Development of V-Shaped Hybrid Mass Damper and Its Application to High-Rise Buildings.” *Proc. of the First World Conference on Structural Control*, FA2:3–12.

Kordonsky, W.I. (1993a). “Elements and Devices Based on Magnetorheological Effect.” *Journal of Intelligent Material Systems and Structures*, Vol. 4, No. 1, p. 65.

Kordonsky, W.I. (1993b). “Magnetorheological Effect as a Base of New Devices and Technologies.” *Journal of Magnetism and Magnetic Materials*, Vol. 122, No. 1 / 3, p. 395.

Kordonsky, W.I. Shulman, Z.P., Gorodkin, S.R., Demchuk, S.A., Prokhorov, I.V., Zaltsgendler, E.A. and Khusid, B.M. (1990). “Physical Properties of Magnetizable Structure-Reversible Media.” *Journal of Magnetism and Magnetic Materials*, Vol. 85, pp. 114–120.

Kordonsky, W.I., Gorodkin, S.P. and Demchuk, S.A. (1993). “Magnetorheological Control of Heat Transfer.” *International Journal of Heat and Mass Transfer*, Vol. 36, No. 11, pp. 2783.

Kurata, N., Kobori, T., Takahashi, M. Niwa, N. and Kurino, H. (1994). “Shaking Table Experiements of Active Variable Damping System.” *Proceedings of the First World Conference on Structural Control*, Pasadena, CA, August 3-5, pp. TP2-108 through TP2-107.

Laub, A.J. (1980). Computation of Balancing Transformations. *Proc. JACC*, Vol. 2, paper FA8-E.

Leitmann, G., and Reithmeier, E. (1993). “Semiactive Control of a Vibrating System by Means of Electrorheological Fluids,” *Dynamics and Control*, Vol. 3, pp. 7–33.

Lemaire, E., Grasselli, Y. and Bossis, G. (1994). “Field Induced Structure in Magneto and Electro-Rheological Fluids.” *Journal de Physique*, Vol. 2, No. 3, p. 359.

Liang, Z., Tong, M. and Lee, G.C. (1995). “Real-Time Structural Parameter Modification (RSPM): Development of Innervated Structures,” *Tech. Report NCEER-95-0012*, National Center for Earthquake Engineering Research, Buffalo, New York.

Lou, J. Y. K., Lutes, L. D. and Li, J. J. (1994). “Active Tuned Liquid Damper for Structural Control,” *Proc., First World Conf. on Struct. Control*, pp. TP1:70–79.

Makris, N., Hill, D., Burton, S. and Jordan, M. (1995). “Electrorheological Fluid Dampers for Seismic Protection of Structures.” *Proc. SPIE Conf. on Smart Struct. and Materials* (I. Chopra, Ed.), San Diego, California, 184–194.

Makris, N., Burton, S.A., Hill, D. and Jordan, M. (1996). “Analysis and Design of an Electrorheological Damper for Seismic Protection of Structures,” *Journal of Engineering Mechanics*, ASCE, (in press).

MATLAB (1994). The Math Works, Inc. Natick, Massachusetts.

McClamroch, N.H. and Gavin, H.P. (1995). "Closed Loop Structural Control Using Electrorheological Dampers." *Proceedings of the American Control Conference*, Seattle, Washington, pp. 4173–4177.

Miller, L.R. (1988). Tuning Passive, Semi-Active, and Fully Active Suspensions. *IEEE, Proceedings of the Conference on Decision and Control*, Paper No. 88CH25312/99/000-2047.

Minagawa, K., Watanabe, T. and Munakata, M. (1994). "A Novel Apparatus for Rheological Measurements of Electro- Magneto-Rheological Fluids." *Journal of Non-Newtonian Fluid Mechanics*, Vol. 52, No. 1, p. 59.

Mizuno, T., Kobori, T., Hirai, J., Matsunaga, Y. and Niwa, N. (1992). "Development of Adjustable Hydraulic Dampers for Seismic Response Control of Large Structure." *ASME PVP Conference*, PVP-Vol. 229, pp. 163–170.

Moore, B.C. (1981). "Principal Component Analysis in Linear Systems: Controllability, Observability, and Model Reduction." *IEEE Trans. on Automatic Control*, pp. 26–31.

Nagarajaiah, S., Feng, M.Q. and Shinozuka, M. (1993). "Control of Structures with Friction Controllable Sliding Isolation Bearings," *Soil Dyn. and Earthquake Engrg.*, Vol. 12, No. 2, pp. 103–112.

Nagarajaiah, S. (1994). "Fuzzy Controller for Structures with Hybrid Isolation System." *Proc. of the First World Conference on Structural Control*, pp. TA2:67–76.

Nakamura, Y., Tanaka, K., Ishii, M., Hirasawa, M., Nakayama, M., Ohyama, H. and Fujita, T. (1994). "Fault Diagnosis Method Using Energy Absorbing Performance for Hybrid Mass Damper for Vibration Control of Tall Buildings." *Proc. of the First World Conference on Structural Control*, FA2:33–42.

Niiya, T., Ishimaru, S., Koizumi, T. and Takai, S. (1994). "A Hybrid System Controlling Large Amplitude Vibrations of High-Rise Buildings." *Proc. of the First World Conference on Structural Control*, FA2:43–52.

Nonami, K., Nishimura, H. and Tian, H. (1994). "H_∞/μ Control-Based Frequency-Shaped Sliding Mode Control for Flexible Structures." *Proc. of the First World Conference on Structural Control*, pp. TP4:110–119.

Nishimura, I., Abdel-Ghaffar, A.M., Masri, S.F., Miller, R.K., Beck, J.L., Caughey, T.K. and Iwan, W.D. (1992). "An Experimental study of the Active Control of a Building Model." *Journal of Intelligent Material Systems and Structures*, Vol. 3, pp. 134–165.

Ohyama, H., Tanaka, K., Arai, N., Ishiguro, Y., Ishii, M., Murakoshi, K., Nakamura, Y., Miyano, H., Hora, H., Fujita, T. (1994). "Practical Application of Hybrid Mass Damper Us-

ing AC-Servomotor for Vibration Control of a Slender Tall Building." *Proc. of the First World Conference on Structural Control*, pp. WP2:62–71.

Ohrui, S., Kobori, T., Sakamoto, M., Koshika, N., Nishimura, I., Sasaki, K. and Kondo, A. and Fukushima, I. (1994). "Development of Active-Passive Composite Tuned Mass Damper and an Application to the High Rise Building." *Proc. of the First World Conference on Structural Control*, pp. TP1:100–109.

Otsuka, S., Shimoda, I., Kawai, N., Inaba, K., Kurimoto, M., Yasui, K., and Mochimaru, M. (1994). "Development and Verification of Active/Passive Mass Damper." *Proc. of the First World Conference on Structural Control*, pp. WP2:72–79.

Pabat, A.I. (1990). "Controlled Magnetorheological Shock Absorbers." *Magnetohydrodynamics*., Vol. 26, No. 2, p. 222.

Patten, W.N., Kuo, C.C., He, Q., Liu, L. and Sack, R.L. (1994a). "Seismic Structural Control via Hydraulic Semiactive Vibration Dampers (SAVD)," *Proc., First World Conf. on Struct. Control*, pp. FA2:83–92.

Patten, W.N., Kuo, C.C., He, Q., Liu, L., and Sack, R.L. (1994b). "Suppression of Vehicle-Induced Bridge Vibration via Hydraulic Semiactive Vibration Dampers." *Proc. of the First World Conference on Structural Control*, Pasadena, CA, August 3–5, pp. FA1-30 through FA1-38.

Petti, L., Soong, T. T. and Palazzo, B. (1994). "Hybrid Mass Dampers for Structural Control against Wind and Earthquakes." *Proc. of the First World Conference on Structural Control*, pp. TP1:110–118.

Quast, P., B.F. Spencer Jr., M.K. Sain and S.J. Dyke (1994). "Microcomputer Implementation of Digital Control Strategies for Structural Response Reduction." *Microcomputers in Civil Engineering: Special Issue on New Directions in Computer Aided Structural System Analysis, Design and Optimization,* Vol. 10, 1995, pp. 13–25.

Rabinow, J. (1948). "The Magnetic Fluid Clutch." *AIEE Transactions*, Vol. 67, pp. 1308–1315.

Reinhorn, A.M., Manolis, G.D. and Wen, C.Y. (1987a). "Active Control of Inelastic Structures." *Journal of the Engineering Mechanics*, Vol. 113, No. 3, pp. 315-333.

Reinhorn, A.M., Soong, T.T. and Wen, C.Y. (1987b). "Base Isolated Structures with Active Control." *Proceedings of the ASME PVD Conference,* San Diego, California.

Reinhorn, A.M., Soong, T.T., Fukao, Y., Lin, R.C., Wang, Y.P., and Nakai, M. (1989a). "Experiments on Active Structural Control Under Seismic Loads." in the *Proceedings of ICOSSAR '89,* April 30-May 4, San Francisco, California.

Reinhorn, A.M., Soong, T.T., Lin, R.C., Wang, Y.P., Fukao, Y., Abe, H., and Nakai, M., (1989b), *1:4 Scale Model Studies of Active Tendon Systems and Active Mass Dampers for Aseismic Protection*, Technical Report NCEER-89-0026.

Reinhorn, A.M., T.T. Soong, M.A. Riley, R.C. Lin, S. Aizawa, & M. Higashino, (1993). "Full Scale Implementation of Active Control. II: Installation and Performance.," *Journal of Structural Engineering*, ASCE, Vol. 119, No. 6, pp. 1935–1960.

Rodellar, J., Barbat, A. H. and Molinares, N. (1994). "Response Analysis of Buildings with a New Nonlinear Base Isolation System." *Proc. of the First World Conference on Structural Control*, pp. TP1:31–40.

Roorda, J. (1975). "Tendon Control in Tall Buildings." *Journal of the Structural Division*, ASCE, Vol. 101, No. 3, pp. 505-521.

Sack, R.L. and Patten, W., (1994). "Semiactive Hydraulic Structural Control." *Proceedings of the International Workshop on Structural Control*, USC Publication Number CE-9311, pp. 417-431.

Sack, R.L., Kuo, C.C., Wu, H.C., Liu, L. and Patten, W.N. (1994). "Seismic Motion Control via Semiactive Hydraulic Actuators." *Proc. of the U.S. Fifth National Conference on Earthquake Engineering*, Chicago, Illinois, Vol. 2, pp. 311–320.

Sakamoto, M. and T. Kobori. (1994). "Practical Applications of Active and Hybrid Response Control Systems." *Proc. of the Int. Workshop on Struct. Control*, Univ. of Southern California, pp. 432–46.

Savost'yanov, A. (1992). "Effects of Magnetomechanical Relaxation in a Magnetorheological Suspension." *Magnetohydrodynamics*, Vol. 28, No. 1, p. 42.

Schoukens, J. and R. Pintelon, (1991). *Identification of Linear Systems, A Pratical Guide to Accurate Modeling*. Pergamon Press. New York, pp. 39–49.

Shames, I.H. and Cozzarelli, F.A. (1992). *Elastic and Inelastic Stress Analysis*. Prentice Hall, Englewood Cliffs, New Jersey, pp. 120-122.

Shiba, K., Tamura, K., Inada, Y., Yamaura, N., (1994). "Vibration Control Characteristics of a Hybrid Mass Dampers System Through Earthquake Observation Records of a Tall Building." *Proc. 1st World Conf. on Struct. Control*, WP2:80–89.

Shing, P.B., Dixon, M., Kermiche, N., Su, R. and Frangopol., D.M. (1994). "Hybrid Control Techniques for Building Structures." *Proc. of the First World Conference on Structural Control*, pp. WP2:100–109.

Shinozuka, M., Constantinou, M.C. and Ghanem, R. (1992). "Passive and Active Fluid Dampers in Structural applications," *U.S./China/Japan Workshop on Structural Control*, Shanghai, China, pp. 507–516.

Shoureshi, R., Bell, M., and Wheeler, M., (1994). “Neural-Based Intelligent Control of Structures,” *Proc. of the First World Conference on Structural Control*, Pasadena, CA, pp. FP4:3–11.

Shulman, Z.P., Kordonsky, W.I. and Zaitsgendler. (1986). “Structure, Physical Properties and Dynamics of Magnetorheological Suspensions.” *International Journal of Multiphase Flow*, Vol. 12, No. 6, pp. 935–955.

Shulman, Z.P., Kordonsky, W.I. and Gorodkin, S.R. (1989). “A Recuperator with a Magnetorheological Coolant.” *Journal of Engineering Physics*, Vol. 56, No. 4, p. 438.

SIMULINK (1994). The Math Works, Inc. Natick, Massachusetts.

Skelton, R.E. (1988). *Dynamic Systems Control: Linear Systems Analysis and Synthesis*. Wiley, New York.

Soong, T.T. and Skinner, G.K. (1981). “Experimental Study of Active Structural Control.” *Journal of Engineering Mechanics Division*, ASCE, Vol. 113, No. 6, pp. 1057-1067.

Soong, T.T. (1990). *Active Structural Control: Theory and Practice*, Longman Scientific and Technical, Essex, England.

Soong, T.T., A.M. Reinhorn, Y.P. Wang, & R.C. Lin, (1991a). “Full Scale Implementation of Active Control. I: Design and Simulation,” *Journal of Structural Engineering*, ASCE, Vol. 117, November, pp. 3516–3536.

Soong, T.T., Masri, S.F. and Housner, G.W. (1991b). “An Overview of Active Structural Control under Seismic Loads.” *Earthquake Spectra*, Vol. 7, No. 3, pp. 483–505.

Soong, T.T., Masri, S.F. and Housner, G.W. (1991c). “An Overview of Active Structural Control under Seismic Loads.” *Earthquake Spectra*, Vol. 7, No. 3, pp. 483–505.

Soong, T.T. and Grigoriu, M., (1992). *Random Vibration of Mechanical and Structural Systems*, Prentice Hall, Englewood Cliffs, New Jersey.

Soong, T.T. and Reinhorn , A.M., (1993). *Proc. of ATC-17-1 Seminar of Seismic Isolation, Passive Energy Dissipation, and Active Control*, Vol. 2, pp. 701–713.

Soong, T.T. and Constantinou, M.C. (eds.) (1994). *Passive and Active Structural Vibration Control in Civil Engineering*, Springer–Verlag, Wien and New York.

Spencer Jr., B.F., P. Quast., S.J. Dyke and M.K. Sain. (1994b). “Digital Signal Processing Techniques for Active Structural Control.” *Proc. of the 1994 ASCE Structures Congress*, Atlanta, Georgia.

Spencer Jr., B.F., Suhardjo, J. and Sain, M.K., (1991), “Frequency Domain Control Algorithms for Civil Engineering Applications.” *Proceedings of the International Workshop on*

Technology for Hong Kong's Infrastructure Development, Hong Kong, December 19-20, 1991, pp. 169-178.

Spencer Jr., B.F., Suhardjo, J. and Sain, M.K., (1994), "Frequency Domain Optimal Control Strategies for Aseismic Protection." *Journal of Engineering Mechanics, ASCE,* Vol. 120, No. 1, pp. 135-159, 1994.

Spencer Jr., B.F., M.K. Sain, C.-H. Won, D. Kaspari, Jr., and P.M. Sain (1994). "Reliability-Based Measures of Structural Control Robustness." *Structural Safety*, (in press).

Spencer Jr., B.F., Dyke, S.J., Sain, M.K. and Carlson, J.D. (1996a) "Phenomenological Model of a Magnetorheological Damper," *J. Engrg. Mech., ASCE*, (in press).

Spencer Jr., B.F., Dyke, S.J., Sain, M.K. and Carlson, J.D. (1996b). "Idealized Model of a Magnetorheological Damper," *Proceedings of the 12th Conference on Analysis and Computation, ASCE*, Chicago, Illinois.

Spencer Jr., B.F. and Dyke, S.J. (1996c). "Semi-Active Structural Control: System Identification for Synthesis and Analysis," *Proc., First Europ. Conf. on Struct. Control*, Barcelona, Spain.

Spencer Jr., B.F., Dyke, S.J., Sain, M.K. and Carlson, J.D. (1996d). "Nonlinear Identification of Semi-Active Control Devices." *11th ASCE Engrg. Mech. Spec. Conf.*, Ft. Lauderdale, Florida, pp. 164–167.

Stanway, R. Sproston, J.L. and Stevens, N.G. (1985). "Non-linear Identification of an Electro-rheological Vibration Damper." *IFAC Identification and System Parameter Estimation*, pp. 195–200.

Stanway, R,. Sproston, J.L. and Stevens, N.G. (1987). "Non-linear Modelling of an Electro-rheological Vibration Damper." *J. Electrostatics*, Vol. 20, pp. 167–184.

Stengel, R.F. (1986). *Stochastic Optimal Control: Theory and Application*. Wiley, New York.

Suhardjo, J. (1990). *Frequency Domain Techniques for Control of Civil Engineering Structures with Some Robustness Considerations*, Ph.D. Dissertation, Univ. of Notre Dame, Dept. of Civil Engineering.

Suhardjo, J., Spencer Jr., B.F. and Kareem, A., (1992), "Frequency Domain Optimal Control of Wind Excited Buildings." *Journal of Engineering Mechanics, ASCE*, Vol. 118, No. 12, pp. 2463–2481.

Sun, L. and Goto, Y. "Application of Fuzzy Theory to Variable Dampers for Bridge Vibration Control." *Proc. of the First World Conference on Structural Control*, pp. WP1:31–40.

Suzuki, T., M. Kageyama and A. Nohata. (1994). “Active Vibration Control System Installed in a High-Rise Building.” *Proc. of the First World Conference on Structural Control*, Univ. of Southern California.

Symans, M.D., Constantinou, M. C., Taylor, D. P. and Garjost, K.D. (1994). “Semi-Active Fluid Viscous Dampers for Seismic Response Control,” *Proc., First World Conf. on Struct. Control*, FA4:3–12.

Symans, M.D. and Constantinou, M.C., (1995). “Development and Experimental Study of Semi-Active Fluid Damping Devices for Seismic Protection of Structures,” *Nat. Center for Earthquake Engrg. Res., Tech. Report NCEER-95-0011* .

Symans, M.D. and Constantinou, M.C. (1996). “Experimental Study of Seismic Response of Structures with Semi-Active Damping Control Systems,” *Proc., Struct. Cong. XIV*, Chicago, IL, April 15–18.

Tanida, K., Y. Koike, K. Mutaguchi, and N. Uno. 1991. “Development of Hybrid Active-Passive Mass Damper.” PVP–Vol. 211, pp. 21–26, *Active and Passive Damping*, The American Society of Mechanical Engineers.

Tanida, K. (1995). “Active Control of Bridge Towers During Erection,” *Proc. 3rd Colloquium on Vibration Control of Structures, JSCE, part A*, 173–184 (in Japanese).

Tamura, K., Shiba, K., Inada, Y., and Wada, A. (1994). “Control Gain Scheduling of a Hybrid Mass Damper System Against Wind Response of Tall Buildings.” *Proc. of the First World Conference on Structural Control*, FA2:13–22.

Tseng, H.E. and J.K. Hedrick (1994). Semi-Active Control Laws–Optimal and Sub-Optimal. *Vehicle System Dynamics*, **23**, 545–569.

Venini, P. and Wen, Y. K. (1994). “Hybrid Vibration Control of MDOF Hysteretic Structures with Neural Networks.” *Proc. of the First World Conference on Structural Control*, pp. TA3:53–62.

Wen, Y.K. (1976). “Method of Random Vibration of Hysteretic Systems.” *Journal of Engineering Mechanics Division, ASCE*, Vol. 102, No. EM2, pp. 249–263.

Winslow, W.M. (1947). “Method and Means for Translating Electrical Impulses Into Mechanical Force.” US Patent No. 2,417,850.

Winslow, W.M. (1949). “Induced Fibration of Suspensions.” *Journal of Applied Physics*, Vol. 20, pp. 1137–1140.

Yamamoto, M. and Aizawa, S. (1994). “Control Effects of Active Mass Damper System Installed on Actual Buildings.” *Proc. of the First World Conference on Structural Control*, FP1:13–22.

Yamazaki, S., et al. (1992). “Tuned Active Dampers Installed in the Minato Mirai (MM) 21 Landmark Tower in Yokohama.” *J. of Wind Engrg. and Aerodyn*. 41–44, 1937–1948.

Yamazaki, S., et al. (1995). “Full Scale Investigation of Performance of Tuned Active Dampers Installed in Landmark Tower in Yokohama,” *Proc. Int. Wind Eng. Conf.*, 1631–1642 (to appear in *J. of Wind Engrg. and Aerodyn.*)

Yang, J.N. Wu, J.C and Hsu, S.Y. (1994a). “Parametric Control of Seismic-Excited Structures,” *Proc., First World Conf. on Struct. Control*, pp. WP1:88–97.

Yang, J.N. Agrawal, A.K., and Wu, J.C, (1994b). “Sliding Mode Control for Structures Subjected to Seismic Loads,” *Proc., First World Conf. on Struct. Control*, pp. WA1:13–22.

Yao, J.T.P., (1972). “Concept of Structural Control,” *Journal of the Structural Division, ASCE*, 98(ST7), 1567–1574.

Yoshida, K., Kang, S. and Kim, T. (1994). “LQG Control and Control of Vibration Isolation for Multi-Degree-of-Freedom Systems.” *Proc. of the First World Conference on Structural Control*, pp. TP4:43–52.